SAPIENZA
UNIVERSITÀ DI ROMA

Searching for new physics in the neighborhood of a black hole: fundamental interactions, plasmas and tests of gravity

Scuola di dottorato Vito Volterra – Dottorato di Ricerca in Fisica
PhD degree in physics (XXXVI cycle)

Enrico Cannizzaro
ID number 1708079

Advisor
Prof. Paolo Pani

Academic Year 2023

Searching for new physics in the neighborhood of a black hole: fundamental interactions, plasmas and tests of gravity
PhD thesis. Sapienza University of Rome

This thesis has been typeset by LaTeX and the Sapthesis class.

Version: February 7, 2024

Author's email: enrico.cannizzaro@uniroma1.it

Abstract

A plethora of theoretical arguments and experimental observations suggest evidence for new physics beyond the standard model and general relativity. A promising way to detect such deviations is to analyze the possible signatures of these theories around compact astrophysical objects. In this spirit, this thesis is devoted to the study of different phenomenological imprints of new physics around black holes.

In the first part of the thesis, I analyze in detail superradiant instabilities, focusing in particular on the role of interactions of the superradiant field with astrophysical plasma. I show that such interactions are pivotal to obtain a detailed description of the systems, and may either lead to promising observables or hamper the instability itself.

In the second part of the thesis, I focus on tests of general relativity using gravitational waves. In particular, I discuss in detail the possible detectability of fundamental dipoles in extreme mass-ratio inspirals, and introduce a formalism to probe theories beyond general relativity using pulsar-timing arrays. In both cases, I adopt a model-agnostic approach, encapsulating different theories in the analysis.

Contents

Preface

The scientific work discussed in this thesis has been carried out at Sapienza University in Rome, in the "Gravity theory and gravitational wave phenomenology group". Part of this work was also performed at the Niels Bohr Institute in Copenhagen, which I kindly thank for the hospitality.

List of publications

The work in this thesis was performed with different collaborators, which I kindly acknowledge, and is based on the following publications:

- Title: Plasma-photon interaction in curved spacetime I: formalism and quasi-bound states around nonspinning black holes
  Journal: Phys.Rev.D 103 (2021) 124018, e-Print: 2012.05114 [gr-qc]
  Authors: **Enrico Cannizzaro**, Andrea Caputo, Laura Sberna, Paolo Pani

- Title: Plasma-photon interaction in curved spacetime II: Collisions, thermal corrections, and superradiant instabilities
  Journal: Phys.Rev.D 104 (2021) 10, 104048, e-Print: 2107.01174 [gr-qc]
  Authors: **Enrico Cannizzaro**, Andrea Caputo, Laura Sberna, Paolo Pani

- Title: Superradiant instabilities by accretion disks in scalar-tensor theories
  Journal: Phys.Rev.D 106 (2022) 2, 024007, e-Print: 2204.09335 [gr-qc]
  Authors: Giuseppe Lingetti, **Enrico Cannizzaro** and Paolo Pani

- Title: Dark photon superradiance quenched by dark matter
  Journal: Phys.Rev.D 106 (2022) 8, 083019, e-Print: 2206.12367 [hep-ph]
  Authors: **Enrico Cannizzaro**, Laura Sberna, Andrea Caputo, Paolo Pani

- Title: Nonlinear photon-plasma interaction and the black hole superradiant instability
  Journal: Under peer review, e-Print: 2306.12490 [gr-qc]
  Authors: **Enrico Cannizzaro**, Fabrizio Corelli, Paolo Pani

- Title: Superradiance: Axionic Couplings and Plasma Effects
  Journal: Phys.Rev.D 108 (2023) 6, 063013, e-Print: 2306.16447 [gr-qc]
  Authors: Thomas Spieksma, **Enrico Cannizzaro**, Taishi Ikeda, Vitor Cardoso, Yifan Chen

- Title: Novel tests of gravity using nano-Hertz stochastic gravitational-wave background signals
  Journal: Under peer review, e-Print: 2307.11665 [gr-qc]
  Authors: **Enrico Cannizzaro**, Gabriele Franciolini, Paolo Pani
- Title: Relativistic perturbation theory for black-hole boson clouds
  Journal: Under peer review, e-Print: 2309.10021 [gr-qc]
  Authors: **Enrico Cannizzaro**, Laura Sberna, Stephen Green, Stefan Hollands
- Title: Extreme mass-ratio inspirals as probes of fundamental dipoles
  Journal: Under peer review, e-Print: 2310.07772 [gr-qc]
  Authors: Jacopo Lestingi, **Enrico Cannizzaro**, Paolo Pani

Acronyms

GR: general relativity
QFT: quantum field theory
(B)SM: (beyond) standard model
(SI)DM: (self-interacting) dark matter
BH: black hole
GW: gravitational wave
QCD: quantum chromodynamics
ALP: axion-like particle
SMBHB: supermassive black hole binary
EMRI: extreme mass ratio inspiral
EM: electromagnetic
PN: post-Newtonian
QNM: quasi-normal modes
QBS: quasi-bound states
ISM: interstellar medium
LISA: laser interferometer space antenna
CMB: cosmic microwave background
ISCO: innermost stable circular orbit
PIC: particle in cell
MHD: magnetohydrodynamics
WB: wave-breaking
DP: dark photon
ADAF: advection-dominated accretion flow
LIGO: laser interferometer gravitational-wave observatory
NANOGrav: North American Nanohertz Observatory for Gravitational Waves
EPTA: European pulsar timing array
PPTA: Parkes Pulsar Timing Array
CPTA: Chinese Pulsar Timing Array
TOA: time of arrival
SGWB: stochastic gravitational wave background
HD: Hellings-Downs
(B)PL: (broken) power-law

Chapter 1

Introduction

The last century dramatically marked the way we understand the Universe, as the two milestones of modern theoretical physics were born and raised: Einstein's General Theory of Relativity (GR) and Quantum Field Theory (QFT). While the former changed at a fundamental level our understanding of gravity and cosmology, the second had a analogous impact for fundamental interactions, and led to the development of the Standard Model (SM) for particle physics. From their very birth, these theories were able to provide an exquisite description of reality and passed every test with flying colours. Nevertheless, a number of theoretical arguments and experimental results gradually led to the conclusion that the actual picture is still incomplete. In particular, there are at least two important problems supporting this incompleteness: I) While GR is a classical theory, a unified picture between QFT and gravity is lacking. Indeed, GR is not renormalisable in the standard QFT sense; II) several gravitational evidences – from galaxy rotation curves to gravitational lensing effects (see e.g. [1, 2, 3, 4, 5, 6, 7]) – showed that only a mere 5% of our Universe is composed of visible matter. The nature of the remaining "dark universe" is one of the most mysterious puzzles in physics. In order to explain astrophysical and cosmological observations, it is believed that the 27% of the energy content in the Universe is made by dark matter (DM), while the remaining 68% is made by dark energy, supposedly responsible for the acceleration of the universe [8]. Motivated by these reasons, in the past decades there have been several attempts to extend GR or the SM with new degrees of freedom at high or low energy. A fair requirement of these theories is to reproduce faithfully the phenomenology of GR and the SM at the energy scales we were able to probe up to now. For this reason, they are expected to interact very weakly with the SM, or, in the case of modified GR, to possess a screening mechanism that "hides" them in the intermediate length scales [9, 10]. For theories beyond the SM (BSM), the feebleness interacting nature of these particles entails the difficulty to detect them with standard particle accelerators, where the energy scales may not be sufficiently high. This motivated theorists in the last decades to search hints of these particles in high-energy astrophysical phenomena, where the energy scales are extreme, and currently unavailable in particle accelerators [11, 12]. In addition, the recent discovery of gravitational waves (GWs) [13] opened a hitherto unexplored window on the strong gravity regime around compact objects, black holes (BHs) and neutron stars, where the regime is highly-relativistic and even the very nature of GR can be put into scrutiny [14, 15, 16, 17, 18]. Hence, the development of precise GW astrophysics allows for the exciting perspective to turn BHs into "natural laboratories" to search for new physics. In this spirit, this thesis is devoted on the study of some of the most energetic phenomena around astrophysical BHs, aimed at the possibility to detect both physics beyond the SM or beyond GR.

1.1 Black Holes and ultralight bosonic fields

Ultralight bosons are ubiquitous in BSM physics. The most famous proposal is the QCD axion, a pseudoscalar particle proposed by Peccei and Quinn to solve the strong charge-parity problem in quantum chromodynamics (QCD) [19]. This particle arises from a spontaneous symmetry breaking of a U(1) symmetry [20] and gains mass due to non-perturbative effects. Interestingly, while the axion was initially proposed to solve the aforementioned problem, in the last decades it also became a very popular candidate for cold DM [21, 22, 23]. A plethora of similar particles, usually called axion-like particles (ALP), also arise from a string theory scenario called "string-axiverse" and they can populate the spectrum down to the Hubble mass ($\approx 10^{-33}$eV)[24, 25]. Another prediction from high-energy theories is the existence of massive spin-1 fields, as the dark photon [26, 27, 28, 29], which supposedly couples with the SM photon through a non-trivial kinetic mixing. Astrophysical BHs offer a unique opportunity to probe the existence of these degrees of freedom, in particular through a phenomenon called superradiance [30]. Due to this phenomenon, ultralight bosonic fields in a wide mass range can extract rotational energy at a continuous level from a spinning BH, leading to the so-called superradiant instability. Due to this energy extraction, the field is amplified and can form a macroscopic cloud around the BH, with an extremely large occupation number. Superradiant instabilities lead to striking observables signatures, and therefore represent a unique tool to probe the existence of these particles.

Up to now, most studies assumed these bosonic fields to be free from interactions, aside from a minimal coupling to gravity. Nevertheless, in this process, number densities in the cloud reach extreme values and the effects of interactions can be crucial even for very feebly interacting fields. In particular, astrophysical BHs are usually surrounded by plasma, either in the form of accretion disks or interstellar medium (see e.g. [31, 32, 33]). Hence, taking into account the effects of interactions and environmental effect is of utmost importance in order to properly understand these systems. In the first part of this work, I shall focus on these aspects and provide a description of superradiant instabilities by different interacting ultralight bosons in the presence of astrophysical plasmic environments.

1.2 Tests of gravity using gravitational waves

The previously mentioned considerations suggest that GR should be corrected both at low energy (cosmological) and high energy scales. The new theory should be viable from a cosmologically point of view and, as already mentioned, it should be consistent with GR in the intermediate length scale $1\mu\text{m} < \ell < 1\text{AU}$, where GR was verified with exquisite precision [17, 34, 35]. Besides these requirements, on a practical point of view, a key question is also *how* to modify GR. The building blocks of GR are enclosed in Lovelock's theorem, that states that GR is the only possible viable theory of gravity in four dimensions under specific assumptions, i.e. I) no additional fields, II) diffeomorphism invariance, III) the field equations contains up to second derivatives of the metric tensor. Relaxing one of these assumptions allows for different classes of modified theories. Examples include scalar-tensor theories [36, 37], where assumption I is violated, and massive gravity [38, 39, 40], which violates assumption II.

As already mentioned, these theories beyond GR usually possess a screening mechanism that "hides" them in the intermediate regime. Thus, it is thus relevant to study the phenomenology of these theories in the strong gravity regime– where deviations from GR might be more dramatic– via GW observables. In this spirit, we discuss in the second part of this thesis how two types of BH binaries, namely supermassive BH binaries (SMBHB) and Extreme Mass Ratio Inspirals (EMRIs) allow for novel test of GR using present and future GW detectors. In both cases, we adopt a *theory-agnostic approach* and encapsule different classes of theories beyond GR in a model-agnostic fashion.

1.3 Outline and General Structure

For the reader's convenience, I summarize in this section the structure of the thesis. Part I focuses on the study of superradiant instabilities around astrophysical BHs. In the first part, I discuss in detail the phenomenology of superradiant instabilities induced by the SM photon in the presence of astrophysical plasma. I show that, while the plasma confinement provides a mechanism to trigger an instability at a linear level, non-linear effects completely alter the plasma behaviour and quench the confinement, rendering the instability ineffective. Afterwards, I discuss some aspects of the superradiant instability of two of the most interesting ultralight bosons beyond the SM: the dark photon and the axion. For the former, I show that the instability, while effective in the minimal scenario, can be completely quenched in the presence of fermionic dark matter charged under this dark $U(1)$ symmetry, as this additional component acts as a dark plasma and provides an effective mass to the dark photon, altering its dispersion relation. As for the axionic case, I discuss in detail a scenario in which the QCD axion is coupled to the SM photon, so that the energy of the axion cloud can be released in the emission of powerful EM bursts, provided the ambient plasma is not too dense. Afterwards, I discuss the phenomenology of superradiant instabilities in scalar-tensor theories, where the matter surrounding the BH provides an effective mass to the scalar degree of freedom of the gravitational sector. Finally, I introduce in the last chapter a relativistic perturbation framework aimed at the study of transitions between energy levels in the BH-cloud system. This framework is meant to replace the standard hydrogenic formalism, valid only in the non-relativistic limit.

In the second part, I discuss novel tests of gravity using GWs. First, I study an EMRI binary where the secondary is endowed with a fundamental scalar dipole and show that the emission of scalar radiation due to the latter is suppressed by the mass ratio with respect to the well-known monopole case. Afterwards, I introduce a model-agnostic formalism to map beyond GR theories into a modified tilt for the Stochastic GW Background (SGWB) spectrum, showing that negative PN corrections (in particular -2PN) can alleviate the tension in the recent pulsar-timing-array data if the detected SGWB is interpreted as arising from supermassive binaries. As a byproduct, I show that adopting this formalism for current data already allows to place strong constrain in some beyond GR theories. In this work I use $G = c = \hbar = 1$ units, unless otherwise stated, and the $(-, +, +, +)$ signature.

Part I
Superradiant Instabilities around astrophysical black holes

"Inseguendo un'altra volta
La grande onda che ritorna! "
Piotta, La Grande Onda (2002)

Chapter 2

Superradiance and plasma physics: an introduction

2.1 Superradiance: Introduction and General Features

Superradiance is a phenomenon that, in generic terms, describes the anomalous amplification of radiation due to dissipation of energy of a given system. The term was introduced by Dicke in 1954, when delving into the study of coherent emission processes from radiating gas in quantum optics [41]. Nevertheless, examples of similar phenomena can be traced back even to a decade before, when Ginzburg and Frank discovered the anomalous Doppler effect [42], and the Klein paradox [43] for charged bosonic fields was analyzed by Hund [44] (see also [45, 46]). Remarkably, in 1971 Zel'dovich discovered a peculiar form of superradiance, known as *rotational superradiance*, where radiation can be amplified by the scattering with an absorbing, rotating object provided that the incident radiation satisfies the following condition:

$$\omega < m\Omega \,, \tag{2.1}$$

where ω and m are the frequency and azimuthal number of the incoming wave while Ω is the angular velocity of the absorbing object. On a physical ground, this condition implies for the angular phase velocity of the wave, ω/m, to be less than the velocity of rotation of the object [47, 48]. Just an year after, in 1972 Teukolsky decoupled the perturbation equation for massless test field on a Kerr background, by exploiting the Newman-Penrose formalism [49]. In the same year, together with Press, he provided the first quantitative study of BH superradiance, proving that Zel'dovich mechanism works remarkably well for spinning BHs [50]. They also predicted that, if superradiant scattering is supported by a confinement of the radiation modes, an instability can develop, and give rise to striking phenomena such as *BH bombs* and *floating orbits*. In the same years, different studies showed that no superradiance is possible for fermionic perturbations, so that the phenomenon is restricted to bosonic ones [51, 52, 53]. Finally, the last piece of the puzzle was provided by Damour, Daruelle and Ruffini – and later refined by Detweiler, Zouros and Eardley – which showed that spinning Kerr BHs are unstable under massive bosonic field perturbation due to superradiance, as the mass of the field can naturally provide confinement of the modes [54, 55, 56]. These studies enshrine this decade as the birth of BH superradiance. In the wake of these studies, BH superradiance has gradually become a flourishing research field, and gained a renewed interest in recent years with the discovery of GWs, which potentially allow a pletohra of observable signatures (see 2.2.4 for details). Finally, it is important to mention that a form of rotational superradiance was recently observed for the first time in an experiment, in the form of plane waves propagating on a water surface and amplified by the scattering with a draining vortex [57].

2.2 Superradiance in BH physics

2.2.1 Features of spinning BHs

In order to introduce relevant quantities that will be extensively used throughout this thesis, let us briefly introduce the geometry of spinning BHs in GR.

Black holes are solutions in vacuum of GR. The No-hair theorem states that, within GR, every black hole is completely characterised by three quantities: mass, angular momentum and electric charge. Nevertheless, in the contest of astrophysical BHs, the charge can always be neglected as several processes, i.e. charge separation of the surrounding plasma, pair production, Hawking radiation, contribute to neutralize the BH by any putative charge in an extremely short timescale [58, 59, 60, 61, 62]. The metric describing the space-time around a rotating, neutral and axially-symmetric black hole was found by Roy Kerr in 1963 [63]. In Boyer-Lindquist coordinates, the solution reads:

$$ds^2 = -dt^2 + \Sigma(\frac{dr^2}{\Delta} + d\theta^2) + (r^2+a^2)\sin^2\theta d\varphi^2 + \frac{2Mr}{\Delta}(a\,\sin^2\theta d\varphi - dt)^2\,, \quad (2.2)$$

where $\Delta = r^2 + a^2 - 2Mr$ and $\Sigma = r^2 + a^2\cos^2\theta$. The metric is stationary and axisymmetric, as it admits two Killing vectors along the t and φ directions, but not static.

In Boyer-Lindquist coordinates, the metric has a coordinate singularity in the submanifold $\Delta = r^2 + a^2 - 2Mr = 0$, i.e. at $r_\pm = M \pm \sqrt{M^2 - a^2}$, which are respectively the outer and inner horizon. However, unlike in the Schwarzschild's case, the horizons do not coincide with the infinite redshift surfaces. In fact, the latter are the solutions of the equation:

$$g_{tt} = -1 + \frac{2Mr}{\Sigma} = 0\,. \quad (2.3)$$

The equation (2.3) has two solutions at:

$$r_{s\pm} = M \pm \sqrt{M^2 - a^2\cos^2\theta}\,. \quad (2.4)$$

The outer horizon coincides with the infinite redshift surface only along the z-axis poles, i.e. at $\theta = 0, \pi$ while in general $r_+ \le r_{s+}$. Thus, there exist a region $r_+ < r < r_{s+}$ *outside* the outer horizon where $g_{tt} > 0$. This region is the ergoregion, and the surface $r = r_{s+}$ is called ergosurface. Notably, a particle could cross the ergosurface, enter the ergoregion and then cross the ergosphere in the opposite direction escaping at infinity without violating causality. Nevertheless, no static *observer* is allowed inside the ergoregion as the time-oriented Killing vector is spacelike in this region. Finally, a crucial quantity that defines the Kerr geometry is the BH horizon angular velocity:

$$\Omega_H = \frac{a}{r_+^2 + a^2}\,, \tag{2.5}$$

which can be interpreted as the angular velocity at the horizon of a timelike observer falling from infinity with an initially null angular momentum, usually called ZAMO (Zero Angular Momentum Observer).

2.2.2 A pedagogical example of BH superradiance

Let us introduce the process of superradiance in a straightforward way by considering a simple charged, minimally coupled scalar field on a stationary, axisymmetric background. By using the ansatz:

$$\Phi(t, r, \theta, \varphi) = \int d\omega e^{-i\omega t} Y_{lm}(\theta, \varphi)\frac{\phi(r)}{r}\,, \tag{2.6}$$

one is able to decouple the angular dependence of the field from the radial one, and rearrange the equation for the radial wavefunction as a Schroedinger-like ordinary differential equation:

$$\frac{d^2}{dr_*^2}\phi(r) - V_{\text{eff}}(r)\phi(r) = 0\,, \tag{2.7}$$

where the effective potential V_{eff} depends on the nature of the background geometry and the test field. Given that the BH horizon behaves as a one-way membrane, one can infer the following asymptotic behaviour of the problem:

$$\phi \sim \begin{cases} \mathcal{T}e^{-ik_H r_*} & \text{as} \quad r \to r_+ \\ \mathcal{R}e^{ik_\infty r_*} + \mathcal{I}e^{-ik_\infty r_*} & \text{as} \quad r \to \infty \end{cases}\,, \tag{2.8}$$

These boundary conditions allow to interpret the system as a scattering process: an ingoing wave from infinity with amplitude $\mathcal{I}$ scatters off the potential and is partially reflected and partially trasmitted, respectively with amplitudes $\mathcal{R}$ and $\mathcal{T}$. Let us now, for simplicity, assume that V_{eff} is real. Then the equations are invariant under $t \to -t$, $\omega \to -\omega$. We can therefore define another solution to eq. (2.7), $\bar{\phi}$, which satisfied complex conjugate boundary conditions. As the two solutions are independent, their Wronskian must therefore be constant. Using eq. (2.8), one can therefore easily compute the Wronskian both at horizon and infinity and equate them, to obtain:

$$|\mathcal{R}|^2 = |\mathcal{I}|^2 - \frac{k_H}{k_\infty}|\mathcal{T}|^2 \tag{2.9}$$

From this equation it is easy to see that, if k_H/k_∞ is negative, the wave is subject to an amplification $|\mathcal{R}|^2 > |\mathcal{I}|^2$. In particular, this condition is satisfied, in the Kerr case, whenever $\omega < m\Omega_H$: this is exactly the rotational superradiant condition found by Zel'dovich (2.1), provided that the angular velocity of the rotating object is now identified with the BH horizon angular velocity! As already mentioned, in order for superradiant scattering to be effective, the system must possess a dissipation mechanism. In the BH case, this friction comes from the presence of the *ergoregion*, which allows for energy extraction in a similar way to the Penrose process [64]. A common misconception is to link superradiant scattering to the presence of the horizon: actually, horizons are not related to superradiance. The latter can as well arise in horizonless objects possessing an ergoregion [65], while on the contrary it cannot, for example, in the case of non-spinning BHs, which possess an horizon but not an ergoregion. One might also wonder whether the same results can be obtained with other fundamental fields. While higher-spin bosonic fields lead to similar results, fermionic fields cannot undergo superradiant scattering, and possess a completely different phenomenology [66]. The reason for this difference lies in the very nature of fermion themselves: as these fields are described by an anti-commutative algebra, Pauli's exclusion principle limits the occupation number of a given state, and therefore an amplification.

2.2.3 The role of confinement: superradiant instabilities

From the very birth of BH superradiance, it was recognized that if superradiant scattering was to be supported by a suitable mechanism to confine modes near the BH, the system would turn unstable. Indeed, as after a scattering the amplified, reflected wave would not be able to escape at infinity, it would scatter the BH (and be amplified) again many times. This is the so-called "BH bomb" scenario. To understand why spinning BHs in confining geometries are unstable, let us introduce a toy model with a BH placed inside a confining box. Usually, the presence of a box allows for normal modes with a frequency which is inversely proportional to the box dimensions: $\omega \propto 1/L$. Nevertheless, the presence a BH inside the box translate into an intrinsic dissipation mechanism – via the BH horizon – so that instead of normal modes one can expect quasi-normal modes (QNMs) $\omega = \omega_R + i\omega_I$ with $\omega_R \propto 1/L$. In this case, by assuming an harmonic behavior of the field one has the following expression for the amplitudes of the modes:

$$A(t) \sim A_0 e^{-i\omega t} \propto A_0 e^{\omega_I t} \approx A_0(1 + \omega_I t)\,. \tag{2.10}$$

On the other hand, after a scattering off the BH, the amplitude must vary as:

$$A(t) = A_0(1 - |\mathcal{A}|^2)\,, \tag{2.11}$$

where $\mathcal{A}$ is the absorption probability the the horizon. Now consider the system at a certain time t after N interaction between the modes and the BH, such that $N = t/L$. Then, the amplitude has varied as:

$$A(t) = A_0(1 - |\mathcal{A}|^2)^N \approx A_0(1 - N|\mathcal{A}|^2) = A_0(1 - \frac{|\mathcal{A}|^2 t}{L})\,. \tag{2.12}$$

By comparing eqs. (2.10) and (2.12) one obtains:

$$\omega_I = -\frac{|\mathcal{A}|^2}{L} \tag{2.13}$$

In the non rotating limit, $|\mathcal{A}|^2 = (M/L)^{2l+2}$ [67], so that using (2.13) one obtains a *negative* ω_I. In this case, the amplitude decays in time and the system is stable.

If, on the other hand, the BH rotates, one has $|\mathcal{A}|^2 = (M/L)^{2l+1}(\omega - m\Omega_H)$ [68]. Therefore, when the superradiant condition is met, one obtains a negative $|\mathcal{A}|^2$ and therefore a *positive* value for ω_I. From eq. (2.10), it is easy to note that such a value corresponds to an exponential amplification of the amplitude, i.e. to the predicted superradiantly-induced instability.
A natural question that this toy-model prompts is the possibility to have realistic confining mechanism that could allow for the formation of superradiant instabilities around astrophysical BHs. In the years, many different mechanism were proposed for this purpose. For example, confinement can be provided by a non-asymptotically flat spacetime. This is the case of Anti-De Sitter BHs, and is relevant for the gauge-gravity duality, but less relevant from an astrophysical point of view. On the other hand, the most promising mechanisms for astrophysical BHs are most likely massive bosonic fields confinement and the presence of an astrophysical plasma.

2.2.4 Superradiant instabilities from massive fields

The most promising scenario that allows for superradiant instabilities around astrophysical BHs is represented by massive bosonic fields. Indeed, a bare mass μ can naturally confine low-frequency modes in the vicinity of the BH via a Yukawa-like suppression at large distances $\sim e^{-kr}/r$, where we defined $k = \sqrt{\mu^2 - \omega^2}$. Clearly, from this expression it is easy to see that this mechanism is efficient provided that $|\omega| < \mu$. The class of modes that satisfy this requirement are usually known as *quasi-bound states* (QBSs) and, as QNMs, are described by a discrete set of complex frequencies $\omega = \omega_R + i\omega_I$. As these modes are confined near the BH and do not radiate at infinity, they are sometimes also called non-radiative QNMs. In general, computing the spectrum of QBS and the associated superradiant instability is challenging, and requires numerical methods to solve the equations (see e.g. [69, 70, 71, 72]). Nevertheless, in particular regimes, the spectrum can be computed analitically. This is the case, for example, of the spectrum of a Klein-Gordon field under the limit $M\mu << 1$, where M is the BH mass. This case is one of the most-studied and well understood [73, 74]. The spectrum in this case reads:

$$\omega_{nlm} \sim \mu - \frac{\mu}{2}\Big(\frac{M\mu}{l+n+1}\Big)^2 + \frac{i}{\gamma_{lnm}M}\Big(\frac{am}{M} - 2\mu r_+\Big)(M\mu)^{4l+5}\,, \tag{2.14}$$

where l, m are the usual angular quantum numbers, n is the overtone number and γ_{lmn} is a coefficient that depends on the quantum numbers [1]. Notice that when the superradiant condition is satisfied, $a > 2\mu M r_+/m$, the imaginary part becomes positive and the mode is unstable. In this case, the field starts to grow exponentially because of the superradiant instability $\sim e^{\omega_I t}$ on a timescale $\tau = 1/\omega_I$. The instability timescale depends therefore on a/M, $M\mu$ and l, m, n. The strongest instability is obtained for $n = 0, l = 1, m = 1$. In the opposite limit $M\mu >> 1$, the instability is not interesting from a phenomenological point of view as even the shortest timescale obtainable in this regime is way larger than the age of the universe [56]. For the instability to be efficient on astrophysical timescales, the gravitational coupling must be of order unity $M\mu \lesssim 1$. For astrophysical BHs with a mass range

---

[1] Note that while we focus in this section for simplicity on the spin 0 case, similar relations exist also for vector [75, 76] and tensor superradiance [77, 78].

within $M_\odot - 10^9 M_\odot$, this corresponds to boson masses between $10^{-20} - 10^{-10}$eV, i.e. to ultralight bosons.
Clearly, no bosons in this mass range is known to exist in the current picture of particle physics. Nevertheless, a plethora of candidates arise from theories beyond the SM and GR. Examples are represented by QCD axions (or in general axion-like particles), dark photons or massive gravitons. If such an ultralight boson exists in this mass range, the instability can efficiently develop in a very short timescale from an astrophysical point of view. Notice, for example, that this timescale is, in the scalar case:

$$\tau_{inst}^{scalar} \approx 30 \text{ days}\Big(\frac{M}{10M_\odot}\Big)\Big(\frac{0.1}{M\mu}\Big)^9\Big(\frac{0.9}{a}\Big), \tag{2.15}$$

and even shorter for spin-1 [76, 79, 80, 81, 82, 83, 84] and spin-2 fields [77, 78, 85, 86]. During this timescale, the exponential growth of the field translates into the formation of a macroscopic, bosonic condensate – usually called "cloud"– in the vicinity of the BH. Fully non-linear numerical simulations show that the up to the 10% of the BH mass can be extracted in the process. Due to the spin-down of the BH during the process, the superradiant condition (2.1) is eventually violated: when this happens, the instability saturates. Afterwards, the cloud slowly dissipates due to the emission of nearly-monochromatic GWs [87, 88].
Superradiant instabilities represent a promising mechanism to detect ultralight bosons. In particular, with respect to standard terrestrial experiments, they possess at least two unique features: I) the interaction is purely gravitational. Even if such particles interact feebly with the SM, the equivalence principle guarantees that the interaction with gravity is universal. II) there is no need for a relic abundance: every fluctuation will be exponentially amplified by the instability. For this reason, these systems are characterized by a number of striking observable signatures based on precise GW astrophysics. Among the most promising ones, there are "gaps" in the BH mass-spin astrophysical distribution [24, 89, 83, 90, 91, 85]: the existence of a boson with a certain mass μ would imply that BHs in a certain mass range (i.e. such that $M\mu \lesssim 1$) are prone to superradiant instabilities and should therefore possess low spin. Hence, one should not observe BHs with high spin in this region of the parameter space. On the contrary, the detection of highly spinning BHs allows to place competitive constrains on the existence of such particles. A plethora of signatures arise also in binary systems with a BH endowed with a cloud: examples are dynamical friction, resonances, tidal effects [92, 93, 94, 95, 96, 97, 98]. Finally, another observable is the detection of continuous GWs emitted by the cloud, either as individual sources or as a stochastic background [24, 99, 100, 101, 102, 103, 104, 105].
Up to now, there has not been a detection of bosonic clouds around BHs. Nevertheless, this phenomenon allowed to place bounds on the existence of ultralight bosons in a previously unexplored region of the parameter space, and the forthcomings LISA and third generation detectors will allow to search in a much wider region of the parameter space. An up-to-date list of the current constrains on scalar and vector particles can be found in [30].

2.2.5 Superradiant instabilities from astrophysical plasma?

Already at the very birth of BH superradiance, Press and Teukolsky suggested that in the presence of astrophysical plasma even ordinary photons could undergo a superradiant instability [50, 106]. Indeed, it is well known that a photon propagating in a plasma is dressed with an effective mass known as the *plasma frequency*:

$$\omega_{\rm pl} = \sqrt{\frac{n_e e^2}{m_e}}\,, \tag{2.16}$$

where n_e, m_e and e are the plasma numeric density and the mass and charge of the electron, respectively. In other words, while in vacuum the photon is characterized by a *gapless* dispersion relation, in a cold plasma the dispersion relation is modified by the presence of a gap $\omega^2 = k^2 + \omega_{\rm pl}^2$, just as in the case of massive particles. Therefore, modes with $\omega < \omega_{\rm pl}$ are not able to propagate within the plasma, and are reflected back. In this case plasma is said to be *overdense.* Note that the response of a plasma depends therefore on the frequency of the photon: that is to say, plasma is a dispersive medium. Also note that, as the plasma frequency depends on the plasma density, it must be intended in general as a spatially varying effective mass. The possibility to trigger plasma-driven superradiant instabilities raised a widespread interest over the years, as it would allow for a rich phenomenology without any need to invoke ultralight bosons and BSM physics. In particular, two different scenario of potential interest were identified:

- Non-accreting BHs could suffer superradiant instabilities because of the Interstellar medium (ISM) [107, 108]. The latter is a diffuse, nearly homogeneous galactic environment with a density in a range $n_e \sim 10^{-3} - 1\text{cm}^{-3}$. Using eq. (2.16), this corresponds to $\omega_{\rm pl} \sim 10^{-12} - 10^{-10}\text{eV}$, i.e., almost miraculously, to a perfect range to trigger superradiant instabilities around stellar mass BHs. As the instability would be induced by a nearly-homogeneous and tenuous plasma – corresponding to an ultralight and nearly constant effective mass – this scenario was expected to be akin to the massive vector boson instability. Remarkably, while the current plasma frequency (i.e. at $z \approx 0$) matches the required value for the instability of stellar mass BH, a similar system was also shown to be efficient in the case of lighter primordial BHs during the radiation-dominated era, potentially affecting the cosmic microwave background (CMB) [108].
- An instability which is more akin to the original BH-bomb idea could instead arise in BHs surrounded by accretion disks. Indeed, accretion disks are way denser than the insterstellar medium, such that the effective mass would be too high for the instability to be efficient. Nevertheless, in some cases, they can be truncated at the innermost stable circular orbit (ISCO) or even further away (see e.g. [109, 110, 111, 112, 113] for some truncated disk models). In this case, one can imagine a scenario *à la BH bomb* where the disk behaves like a mirror and confine the modes in the plasma-depleted region [114, 115, 116].

Such mechanisms were advocated as a possible origin of Fast radio bursts [107], or as a way to probe the existence of primordial BHs via cosmic-distorsions in the

CMB [108]. Nevertheless, a limitation of such studies is the assumption to model the photon-plasma system using a Proca equation. The fact that the Proca equation can at most be an approximation is already clear from the counting of the degrees of freedom: a massive spin-1 field propagates three polarizations (two transverse modes and a longitudinal one), whereas photons in a cold plasma propagate only two transverse modes, since the putative longitudinal mode is electrostatic. Moreover, the phenomenology of photon-plasma interactions is dramatically more complex than a Proca toy-model also depending on the characteristics of the fluid (whether is collisional, cold/warm ecc.) and because of non-linear features. Given the interesting phenomenological implications of plasma-photon interactions around BHs, it is of utmost importance to understand the system by describing in a more realistic way photon-plasma interactions around astrophysical BHs using consistent plasma physics.

2.3 The ABC of plasma physics

Plasma is a ionized gas, made of positive ions and free, dissociated electrons. An ensemble of charged particle behaves as a plasma whenever the number of particles is high enough so that the long-rage Coulomb force determines their statistical properties, but low enough such that the force between two neighborhood particles is negligible. In other words, due to this long-range force, charged particles in a plasma exhibit *collective behaviours*. Because of its peculiar characteristics, plasma is often called *the fourth state of matter*. In general, whilst made of charged particle, a plasma is globally neutral, so that the total charge is zero. Nevertheless, the local distribution of electrons and ions inside a plasma can vary and generate electric and magnetic field at different lengthscales.

Notably, the 99% of the visible matter in the Universe (excluding DM and dark energy) is in the plasma state. Plasma fills the interplanetary, interstellar and intergalactic medium. Thus, the study of plasma is crucial to understand the details of all the structures we can see in the Universe, from stars to galaxy clusters.

2.3.1 Debye Length and collective behaviours

As already mentioned, because of long-range forces, plasmas can be characterized by a collective behaviour: the parameter that determines whether this behaviour prevails over the individual interaction between two particles is known as Debye length.

Consider a plasma in equilibrium– such that the ions and electrons are equally distributed– and assume that an external test charge is immersed in the plasma. This will generate an electric potential $\phi(r)$ inside the plasma, which will be determined by Poisson's equation:

$$\nabla^2\phi = e(n_e - n_i)\,, \tag{2.17}$$

where $n_{e,i}$ are the density of electrons and ions respectively. Now, due to their large inertia, ions can be considered a fixed background. If one assumes that electrons follow a Boltzmann distribution with temperature T, it is possible to solve eq. (2.17) to obtain:

$$\phi \sim \frac{e^{-r/\lambda_d}}{r}\,, \tag{2.18}$$

where we defined the Debye length $\lambda_d = (k_b T/e^2 n_e)$, which can be interpreted as the length scale at which the test charge is influencing the system. In other words, electrons will react to the perturbation by redistribute in order to screen the external field over a Debye length, such that on lengths greater than this quantity collective behaviour prevails over single interactions.

2.3.2 Plasma frequency

A peculariar characteristic of plasmas is they way the respond to electromagnetic perturbations by acting as a system of coupled oscillator. Consider a group of electrons in a two-species plasma that are slightly displaced from their equilibrium position x_0, while ions are fixed due to the larger inertia. Then, electrons will experience a potential that aims to take them back to their equilibrium position. However, when they reach x_0, due to energy conservation, they will posses a non-zero kinetic energy. Thus, they will continue past x_0 until they convert the kinetic energy in potential one and start over. Just like in a pendulum, this process gives rise to a harmonic behaviour. If the initial displacement δx of the electrons is small, the electric field arising from this small charge separation will be:

$$E = -en\delta x\,. \tag{2.19}$$

By applying Newton's law:

$$m_e a = m_e \frac{d^2 \delta x}{dt^2} = eE = -e^2 n \delta x\,, \tag{2.20}$$

so that one gets an harmonic differential equation $\delta\ddot{x} = \omega_{\rm pl}^2 \delta x$, where the frequency corresponds to the plasma frequency (2.16). In other words, perturbed electrons behave in plasma as a system of coupled oscillators with a typical plasma frequency $\omega_{\rm pl}$.

2.3.3 Plasma models: what are you interested in?

Plasmas are undoubtedly one of the most complex systems the nature offers us. Together with the intrinsic complexity of fluidodynamics, the action of the electromagnetic long-range force leads to a rich phenomenology at different time and length scales. For this reason, plasmas can be described with different degrees of approximation using several approaches.

A complete description of a many-particles system requires the knowledge of all positions and velocities of every single particle. This is described by the N-body distribution function $F(x_1, ..x_N, v_1, ..., v_N, t)$. Nevertheless, in most of the cases, this function cannot be computed, and is more useful to describe the system with a one-particle distribution function obtained by marginalising the remaining degrees of freedom: $f_\alpha(x_1, v_1, t) = \int F(x_1, ..x_N, v_1, ..., v_N, t) dx_2..dx_N dv_2..dv_N$, where α represent the particle species (electrons or ions). Such an approach is called kinetic theory and the relevant equation that describes the system in a statistical picture is called *Boltzmann equation.* This model is incredibly powerful, and able to describe even the shorter timescale phenomena in plasma, the already mentioned plasma oscillations $\tau_{os} = 2\pi/\omega_{\text{pl}}$. Moreover, it allows to capture effects intrinsically connected to microphysics, such as the Landau damping [117]. Nevertheless, a numerical study using kinetic theory requires particle in cell methods (PIC) [118, 119] which are prohibitively computationally expensive in the description of large-timescale phenomenology. On the other hand, a *macroscopic* description of plasmas can be obtained by building macroscopic quantities – the specie's velocity, density ecc. – as statistical moments of the one-particle distribution [120, 121, 122]. This leads to the *two-fluid formalism*, where electrons and ions are treated separately and described respectively by their own continuity (2.21) and momentum equations (2.22), coupled to the Maxwell equations, and by an equation of state (2.25):

$$\frac{\partial n_\alpha}{\partial t} + \nabla \cdot n_\alpha(x,t)\vec{V}(x,t) = 0 \tag{2.21}$$

$$n_\alpha m_\alpha \frac{\partial \vec{V}}{\partial t} + n_\alpha m_\alpha \vec{V} \cdot \nabla \vec{V} - n_\alpha q_\alpha \langle (\vec{E} + \frac{v_1 \times \vec{B}}{c}) \rangle + \nabla \cdot P = m_\alpha \int \frac{N}{V} \frac{\partial f_\alpha}{\partial t} dv \tag{2.22}$$

$$\nabla \cdot \vec{E} = 4\pi \sum_\alpha n_\alpha q_\alpha \tag{2.23}$$

$$\nabla \times \vec{B} = \frac{1}{c}\frac{\partial \vec{E}}{\partial t} + \frac{4\pi}{c} \sum_\alpha n_\alpha q_\alpha \vec{V}_\alpha \tag{2.24}$$

$$P = P(n_\alpha)\,, \tag{2.25}$$

where each species is labelled by an index α. Given that electrons and ions are treated as separate fluids, the electron oscillations at the plasma frequency are still captured by this model, which is also way computationally lighter than PIC. As this is the pivotal effect we wish to describe, in the rest of the thesis we will adopt this model. Note that another class of models that are often used in plasma astrophysics are Magnetohydrodynamics (MHD) models [123, 124]. Nevertheless, MHD models treat the electrons and ions as a single fluid and are based on the quasi-neutrality assumption, i.e. that the total charge density vanishes $n_e = Zn_i$. Clearly, this assumption is a loss of information, as this is not true in general. Nevertheless, as plasma as a whole is neutral, there is a length scale for which quasi-neutrality represents a good assumption. This scale is the already introduced Debye length. Because the fluids are treated as a whole, MHD models are unfeasible to capture the electron oscillations and therefore the photon's effective mass. They are therefore only valid at large length scales $L_{MHD} >> \lambda_d$ and timescales $\tau_{MHD} >> \omega_{\text{pl}}^{-1}$ and unsuitable for our purposes.

2.3.4 Electromagnetic waves in plasmas

The plasma frequency plays a pivotal role in the propagation of waves in plasma. As already mentioned, a photon in a plasma is dressed with an effective mass equal ω_{pl}. Nevertheless, one cannot simply interpret the system as akin to a massive vector boson. With a simple pedagogical example, we will show here how these two scenarios dramatically deviate also in the most trivial case. Consider EM plane waves in a cold, collisionless, isotropic plasma with density n_0. Let us assume the plasma is initially field free ($E_0 = B_0 = 0$), and that the perturbation has an harmonic behaviour, such that the perturbed density and velocity are also harmonic:

$$E = E_1(x)e^{-i\omega t} \quad B = B_1(x)e^{-i\omega t} \quad n = n_0 + n_1(x)e^{-i\omega t} \quad V = V_1 e^{-i\omega t} \,. \tag{2.26}$$

In the following we will adopt a two-fluid model to describe plasma and work under the assumption that ions, due to their large inertia, can be considered at rest.
The relevant field equations are therefore the Maxwell equations and the momentum equation for the electron fluid velocity, which at first order in the perturbation read:

$$\nabla \times B_1 = -i\omega E_1 + J_1 \tag{2.27}$$

$$\nabla \times E_1 = i\omega B_1 \tag{2.28}$$

$$i\omega V_1 = -\frac{e}{m_e} E_1 \tag{2.29}$$

$$J_1 = e n_0 V_1 \,. \tag{2.30}$$

The following set of equations can be easily rearranged to obtain:

$$\nabla \times (\nabla \times E_1) = \omega^2 (1 - \frac{\omega_{\rm pl}^2}{\omega^2}) E_1 \,, \tag{2.31}$$

which in the Fourier domain can be easily recasted in the tensorial form, assuming the wave number is aligned in the z direction:

$$\begin{bmatrix} \omega^2 - \omega_{\rm pl}^2 - k^2c^2 & 0 & 0 \\ 0 & \omega^2 - \omega_{\rm pl}^2 - k^2c^2 & 0 \\ 0 & 0 & \omega^2 - \omega_{\rm pl}^2 \end{bmatrix} \begin{bmatrix} E_x \\ E_y \\ E_z \end{bmatrix} = 0 \,. \tag{2.32}$$

It is trivial to see that this equation has three solutions, corresponding to the three degrees of freedom of electromagnetism in a medium: the first two are standard transverse EM waves along the x, y direction. In this case, the dispersion relation $\omega^2 = k^2 + \omega_{\rm pl}^2$ is analogous to the one of a massive field, and the plasma frequency plays the role of an effective mass. The third solution nevertheless is the longitudinal one along the z direction, characterized by an *electrostatic* dispersion relation $\omega^2 = \omega_{\rm pl}^2$ with zero group velocity $v_{gr} = \partial\omega/\partial k = 0$. This is a strong deviation from a Proca theory, where the longitudinal degree of freedom propagates and is described by the same dispersion relation as the transverse ones. Hence, even in this trivial scenario a Proca equation is unfaithful to describe the system.
In this spirit, the following chapter will be devoted to the study of photon-plasma interactions in curved spacetime in a coherent framework beyond the Proca toy model, and to a dedicated characterization of plasma-driven superradiant instabilities by taking into account the full photon-plasma dynamics.

Chapter 3

Photon-Plasma Interactions in Curved Spacetime

Summary

In this chapter, we investigate the linear and non-linear dynamics of an electromagnetic field propagating in curved spacetime in the presence of plasma. The dynamical equations are generically more involved and richer than the effective Proca equation adopted as a model in previous work. We discuss the general equations and start with the case of a cold plasma in the background of a spherically symmetric black hole, showing that the system admits plasma-driven, quasibound electromagnetic states that are prone to become superradiantly unstable when the black hole rotates. Subsequently, we extend our framework to include thermal effects and collisions and we generalize the system to the spinning case by adopting a slowly rotating approach, and unveil the presence of an efficient superradiant instability at a linear level. Finally, we discuss the impact of non-linearities on plasma-driven superradiant instabilities by adopting a flat-spacetime toy model, and show that plasma blow-out can jeopardize the efficiency of the confinement, rending superradiance ineffective.

3.1 Setup and general equations

A plasma can be classified in terms of its temperature. In a *cold plasma* the thermal velocity of the electrons is larger than that of ions, but still much smaller than the speed of an EM wave propagating in it, namely

$$v_{\text{thermal}} \equiv \sqrt{\frac{2T_e}{m_e}} \ll \frac{\omega}{k}\,, \tag{3.1}$$

where ω and k are the frequency and wave number of the EM field, and T_e is the temperature of the electrons. In this case the thermal pressure is negligible. As already shown, in a cold plasma, the longitudinal modes are plasma oscillations which do not propagate and do not transport energy. The presence of this electrostatic mode already shows that the Proca equation cannot fully describe the interaction of photons with a cold plasma.

On the other hand, in a *hot plasma*, the electron thermal velocity cannot be neglected and the electrons cannot be considered at rest with respect to propagating waves. In this case the electrostatic modes are converted into propagating, energy-transporting, longitudinal modes called Langmuir waves [121]. These modes propagate at the speed of sound in the plasma and the (nonrelativistic) equations resemble the Proca one in the case in which the electrons are ultrarelativistic [125, 126] (although this approximation is beyond the regime of validity of the original equations).

As a first step, we will limit ourselves to the study of cold plasma, since the latter provides a good description of accretion disks and ISM around BHs [127, 31]. Indeed, in the inner region of a typical accretion disk the temperature can be estimated as [128]

$$T_{\rm disk} \simeq 4\times 10^3 \alpha^{-1/4}\Big(\frac{M_\odot}{M}\Big)^{1/4}\Big(\frac{r}{M}\Big)^{-3/8}{\rm eV} \ll m_e, \tag{3.2}$$

where $\alpha \sim \mathcal{O}(1)$ is a dimensionless coefficient relating the kinematic viscosity of the fluid with the velocity of turbulent elements. Therefore, $v_{\rm thermal} \approx 0.06$ or smaller. On the other hand, for a quasibound state around a BH of mass M, $\omega \sim \omega_{\rm pl}$ and $k = 2\pi/\lambda$, where $\lambda \sim M/(M\omega_{\rm pl})^2$ is the typical length scale of the mode [89, 87]. This gives $\omega/k \sim 0.3$ or larger for the most interesting case $M\omega_{\rm pl} \lesssim 0.5$. We also stress that in this chapter we treat the plasma as spherically symmetric, and static. The first is a simplifying assumption and should be relaxed to accommodate more realistic accretion disk geometries. Once spherical symmetry is assumed, the plasma is static to very good approximation: the time scales of interest to this work are much shorter than the time scales of other important astrophysical phenomena. In particular, the BH accretion timescale can be conservatively estimated to be given by a fraction of the Eddington accretion timescale $\tau_{\rm accr} = M/\dot{M} \sim f_{\rm Edd}^{-1}\, 10^{15}\,{\rm s}$, where $f_{\rm Edd}$ is an accretion efficiency factor. For $f_{\rm Edd} \sim \mathcal{O}(1)$, which is conservative as accretion may be much less efficient, one sees that the time scale of the plasma radial motion is much longer than the time scale of the quasi-trapped long-lived perturbations studied below, $\tau_{\rm accr} \gg \omega_{\rm pl}^{-1}$.

The general study of the propagation of EM waves through a cold plasma in curved spacetime was pioneered in [129], where the authors derived the system of equations governing the plasma and the EM field in a two-fluid model. As a first study, we start from those equations and specialize to a background Schwarzschild metric, for which we study the quasibound states for different plasma configurations.

Consider a two-component plasma made of electrons and ions. Let us denote the number density and four-velocity of the electrons as n and u^μ, while J^μ stands for the ion current density. The system of differential equations for the plasma quantities reads [129]

$$\nabla_\nu F^{\mu\nu} = enu^\mu + J^\mu, \tag{3.3}$$

$$u^\mu \nabla_\mu u^\nu = e/m_e F^\nu{}_\mu u^\mu, \tag{3.4}$$

$$u^\mu u_\mu = -1, \tag{3.5}$$

$$\nabla_\mu (nu^\mu) = 0. \tag{3.6}$$

These are Maxwell's equations together with the momentum and particle conservation equations, in covariant form.

We study the propagation of a perturbation through the plasma by introducing the small perturbations $\tilde{n}, \tilde{u}^\mu, \tilde{F}_{\mu\nu}$, e.g. $F_{\mu\nu} = F_{\mu\nu}^{\rm background} + \tilde{F}_{\mu\nu}$ (and likewise for other quantities). Here we neglect second-order perturbations of the plasma and EM field, as well as any perturbation of the background metric $g_{\mu\nu}$ (since the gravitational backreactions of these fields is small). We also neglect perturbations of the ions, since they will be suppressed with respect to those of the electrons by a factor $\propto m_e/m_{\rm ion} \ll 1$. In the warm plasma case an extra term will appear, as we will see, in the momentum equation (3.4), due to the pressure of the fluid.

The presence of a plasma implies the existence of a preferred rest frame. Locally, the plasma defines surfaces of simultaneity for the observer, whose effective metric tensor is

$$h_{\mu\nu} = g_{\mu\nu} + u_\mu u_\nu . \tag{3.7}$$

The tensor $h_{\mu\nu}$ projects orthogonally onto the tangent rest plane of the (electron) plasma. Then, the kinematic of an electron fluid is described by two matrices: the rate of rotation (the vorticity) $\omega^{\mu\nu} \equiv -\omega^{\nu\mu}$, and the rate of deformation $\theta^{\mu\nu} \equiv \theta^{\nu\mu}$. This follows from the general decomposition [130]

$$\nabla_\mu u_\nu = \nabla_{(\mu} u_{\nu)} + \nabla_{[\mu} u_{\nu]} = \omega_{\nu\mu} + \theta_{\nu\mu} - u_\mu u^\alpha \nabla_\alpha u_\nu \, , \tag{3.8}$$

from which we get

$$\omega_{\mu\nu} = \frac{1}{2}(v_{\mu\nu} - v_{\nu\mu}) \, , \tag{3.9}$$

$$\theta_{\mu\nu} = \frac{1}{2}(v_{\mu\nu} + v_{\nu\mu}) \, , \tag{3.10}$$

where we defined the tensor $v^{\mu\nu} = h^{\mu\alpha} h^{\nu\beta} u_{\alpha;\beta}$. We can also define the plasma frequency as in Eq. (2.16), the electric component $E^\mu \equiv F^\mu{}_\nu u^\nu$, the magnetic component $B_{\mu\nu} \equiv h_\mu{}^\alpha h_\nu{}^\beta F_{\alpha\beta}$, and the Larmor tensor $\omega_{\rm L}{}^{\mu\nu} = -\frac{e}{m_e} B^{\mu\nu}$. With these definitions, by differentiating Maxwell's equation (3.3) and using the momentum equation (3.4), Ref. [129] obtained the perturbed equation for the vector potential perturbation $\tilde{A}^\mu$, containing both the influence of the gravitational potential and that of the moving plasma:

$$h^\alpha{}_\beta u^\delta \nabla_\delta \nabla_\gamma \tilde{F}^{\beta\gamma} - \omega_{\rm pl}^2 \tilde{F}^{\alpha\beta} u_\beta + (\omega^\alpha{}_\beta + \omega_L{}^\alpha{}_\beta + \theta^\alpha{}_\beta + \theta h^\alpha{}_\beta + \frac{e}{m_e} E^\alpha u_\beta) \nabla_\gamma \tilde{F}^{\beta\gamma} = 0, \tag{3.11}$$

where $\theta = \theta^\mu{}_\mu$. The above equation is the starting point for a rigorous analysis of the linearized photon dynamics in a cold plasma in curved spacetime. It is clearly very different from an effective Proca equation which would have the form $\nabla_\alpha \nabla^\alpha \tilde{A}_\mu = \omega_{\rm pl}^2 \tilde{A}_\mu$. In particular, note that Eq. (3.11) contains *third-order* derivatives.

In the flat spacetime limit and in the Fourier domain, the spatial part of Eq. (3.11) reads

$$\boldsymbol{k}(\boldsymbol{k} \cdot \tilde{\boldsymbol{E}}) - k^2 \tilde{\boldsymbol{E}} + \Big(1 - \frac{\omega_{\rm pl}^2}{\omega^2}\Big) \omega^2 \tilde{\boldsymbol{E}} = 0 \, , \tag{3.12}$$

which exactly coincides, in Fourier space, with equation (2.31). Therefore, this formalism correctly takes into account longitudinal electrostatic degrees of freedom:

taking $\boldsymbol{k}$ along the z direction one can write the standard dispersion tensor $\boldsymbol{D}$ and find its determinant, which reads $\det|\boldsymbol{D}| = (\omega^2\epsilon - k^2)^2\omega^2\epsilon = 0$, where we defined the plasma dielectric tensor $\epsilon = 1 - \omega_{\rm pl}^2/\omega^2$. There are two types of solutions to this dispersion relation: the first one corresponds to the longitudinal mode with $\epsilon = 0$, i.e. $\omega = \omega_{\rm pl}$; while the second one corresponds to the two transverse modes $(\omega^2\epsilon - k^2) = 0$, i.e. $\omega^2 = k^2 + \omega_{\rm pl}^2$ [11].

3.2 Quasi-bound spectrum in Schwarzschild spacetime

3.2.1 Field equations in a Schwarzschild background

We now specialize to the symmetries of the Schwarzschild background. We work in the coordinates (t, r, θ, ϕ), in which the line element reads

$$ds^2 = -f dt^2 + f^{-1} dr^2 + r^2 d\Omega_2^2 \tag{3.13}$$

with $f(r) = 1 - 2M/r$, where M is the BH mass. In this case both the vorticity and the deformation tensors are zero, as can be easily checked from Eqs. (3.9) and (3.10). The four velocity of a static plasma is $u^\alpha = (u^0, \vec{0})$, with $u^0 = f^{-1/2}$ satisfying the normalization condition $u_\mu u^\mu = -1$. From Eq. (3.4), the electric field has then only one nonvanishing radial component $E^\alpha = (0, m_e/e\,\Gamma^r_{00}(u^0)^2, 0, 0)$, where $\Gamma^\mu_{\alpha\beta}$ are the standard Christoffel's symbols. We assume an unmagnetized plasma $B_{\mu\nu} = 0$ (and therefore also ${\omega_{\rm L}}^{\mu\nu} = 0$) and work in the Landau gauge, $u_\mu \tilde{A}^\mu = 0$,.

Moreover, in any spherically symmetric spacetime it is possible to separate the angular part of the fields from the radial one by performing a multipolar expansion. Following Ref. [75], we introduce a basis of four vector spherical harmonics:

$$Z_\mu^{(1)lm} = [1, 0, 0, 0] Y^{lm}, \tag{3.14}$$

$$Z_\mu^{(2)lm} = [0, f^{-1}, 0, 0] Y^{lm}, \tag{3.15}$$

$$Z_\mu^{(3)lm} = \frac{r}{\sqrt{l(l+1)}}[0, 0, \partial_\theta, \partial_\phi] Y^{lm}, \tag{3.16}$$

$$Z_\mu^{(4)lm} = \frac{r}{\sqrt{l(l+1)}}[0, 0, \frac{\partial_\phi}{\sin\theta}, -\sin\theta\partial_\theta] Y^{lm}, \tag{3.17}$$

where $Y^{lm}(\theta, \phi)$ are the standard scalar spherical harmonics. These vector spherical harmonics satisfy the orthogonality condition

$$\int d\Omega Z_\mu^{(i)lm} \hat{\eta}^{\mu\nu} Z_\nu^{(i')l'm'} = \delta^{ii'}\delta^{ll'}\delta^{mm'}, \tag{3.18}$$

where $d\Omega = \sin\theta d\theta d\phi$ and $\hat{\eta}^{\mu\nu} = \mathrm{diag}[1, f^2, 1/r^2, 1/(r^2\sin^2\theta)]$. The perturbation of the vector potential can be decomposed in this basis as

$$\tilde{A}_\mu(r, t, \theta, \phi) = \frac{1}{r}\sum_{i=1}^{4}\sum_{l,m} c_i u_{(i)}^{lm}(t, r) Z_\mu^{(i)lm}(\theta, \phi), \tag{3.19}$$

where $c_1 = c_2 = 1$ and $c_3 = c_4 = 1/\sqrt{l(l+1)}$. Using this decomposition and a frequency-domain representation $u^{lm}_{(i)}(t,r) = u^{lm}_{(i)}(r)e^{-i\omega t}$, the field equations become

$$u_{(1)} = 0\,, \tag{3.20}$$

$$\Big(rf(l + l^2 + r^2\omega_{\rm pl}^2) - r^3\omega^2\Big)\, u_{(2)} - r^2 f^2 u'_{(3)} = 0\,, \tag{3.21}$$

$$\begin{aligned} &l(1+l)rfu_{(2)} + r^3(\omega^2 - f\omega_{\rm pl}^2)u_{(3)} \\ &-l(1+l)r^2 f u'_{(2)} + 2Mrfu'_{(3)} + r^3 f^2 u''_{(3)} = 0\,, \end{aligned} \tag{3.22}$$

$$\begin{aligned} &\Big(rf(l + l^2 + r^2\omega_{\rm pl}^2) + r^3\omega^2\Big)\, u_{(4)} \\ &-2Mrfu'_{(4)} - r^3 f^2 u''_{(4)} = 0\,, \end{aligned} \tag{3.23}$$

where $u'_{(i)} = \partial_r u_{(i)}$, we have suppressed the l superscript, and the radial dependence of $\omega_{\rm pl} = \omega_{\rm pl}(r)$. Owing to the spherical symmetry of the background, the equations do not depend on the angular number m. Note that, despite the fact that Eq. (3.11) contains third-order derivatives, the final system of equations in the frequency domain is of second differential order.

From Eqs. (3.20)–(3.23) we can immediately notice that the polar (i.e., even-parity) sector, described by the functions $u_{(1)}, u_{(2)}$ and $u_{(3)}$ is completely decoupled from the axial (i.e., odd-parity) sector, described by the function $u_{(4)}$. This resembles the case of a massive vector field discussed in Ref. [75] and is in fact a consequence of the spherical symmetry of the background. We can therefore treat the two sectors independently, as in the following.

Axial sector

Interestingly, the axial equation is identical to the axial Proca equation found in [75]. Thus, the axial sector can be easily reduced to a Schrödinger-like equation analogous to the massive vector case [75]

$$\mathcal{D}_2 u_{(4)}(r) = 0, \tag{3.24}$$

with $\mathcal{D}_2 \equiv \frac{d^2}{dr_*^2} + \omega^2 - f\left(\frac{l(l+1)}{r^2} + \omega_{\rm pl}^2\right)$, and in terms of the tortoise coordinate defined by $\frac{dr_*}{dr} = f^{-1}$. In this case the plasma frequency plays indeed the role of an effective mass for the component $u_{(4)}$. The agreement between the axial sector and the Proca axial equation lies in the symmetries of the spacetime: the axial sector is a superposition of purely *transverse* modes, and is fully decoupled from the polar one, where the longitudinal electrostatic modes reside. Given that, as shown in 2.3.4, the transverse degrees of freedom are Proca-like, the two sectors must coincide. Note that, remarkably, this argument was used in [83] to theorize the similarity between the two sectors, although the general equations of the plasma-photon system in curved spacetime were not known. Our framework is the first one to verify this assumption explicitly.

Polar sector

On the other hand, the polar sector propagates one Proca-line and one electrostatic degrees of freedom, coupled to each other. Hence, because of the "contamination" of electrostatic degrees of freedom, the polar sector is different from the Proca case.

In the monopole case ($l = 0$), only the first two spherical harmonics are defined and the field equations reduce to $u_{(1)} = 0$ and

$$(\omega^2 - \omega_{\rm pl}^2 f)u_{(2)} = 0. \tag{3.25}$$

Therefore, in the flat spacetime limit ($M \to 0$) we recover the presence of electrostatic degrees of freedom, $\omega^2 = \omega_{\rm pl}^2$, which are typical of photons propagating in cold plasma.

For $l \neq 0$, the polar equations for $u_{(2)}$ and $u_{(3)}$ can be reduced to a single Schrödinger-like equation,

$$\frac{d^2}{dr_*^2}\psi - V(r)\psi = 0, \tag{3.26}$$

where the complicated form of the effective potential $V(r)$ is given in Appendix A. As expected, $V(r \to 2M) \to -\omega^2$ and $V(r \to \infty) \to \omega_{\rm pl}^2(r \to \infty) - \omega^2$. The fact that the polar sector reduces to a single second-order differential equations implies the presence of only one dynamical degree of freedom. Note that the potential V depends on the plasma frequency $\omega_{\rm pl}(r)$ and also on its radial derivatives.

3.2.2 The hydrogenic spectrum for Proca modes

In the next section we shall compute the quasibound states of our problem by solving Eqs. (3.24) and (3.26) numerically with suitable boundary conditions. The latter select an infinite set of complex eigenfrequencies: $\omega = \omega_R + i\omega_I$. It will be useful to compare the results with the case of a Proca field with mass $\hbar\omega_{\rm pl} = \text{const}$ around a Schwarzschild BH. In the latter case, the spectrum has a clear physical interpretation in the Newtonian limit, which corresponds to the Compton wavelength of the Proca field, $\sim 1/\omega_{\rm pl}$, being much larger than the horizon size. This requires $M\omega_{\rm pl} \ll 1$. To leading order in this limit the spectrum of quasibound states has a hydrogenic form [131, 75, 79, 76, 83]

$$\omega_R \sim \omega_{\rm pl}\left(1 - \frac{(M\omega_{\rm pl})^2}{2(l+S+1+n)^2}\right), \tag{3.27}$$

$$\omega_I \sim -\frac{1}{2}C_{lS}^{(1)}(M\omega_{\rm pl})^{4l+2S+5}\omega_R\,, \tag{3.28}$$

where l is the total angular momentum[1] of the state with spin projections $S = -1$, 0, 1 (with $S = 0$ for axial modes and $S = \pm 1$ for the two polarizations of polar modes), n is the overtone number ($n = 0$ for the longest-lived, fundamental mode), and $C_{lS}^{(1)}$ are constants (given, e.g., in Ref. [30]). The most unstable mode is the polar dipole with $S = -1$, $l = 1$, which has $C_{1-1}^{(1)} = 16$ [83]. The dominant slope of the imaginary part of the mode is $\omega_I \propto (M\omega_{\rm pl})^{10}$ for the axial dipole, and $\omega_I \propto (M\omega_{\rm pl})^8$ and $\omega_I \propto (M\omega_{\rm pl})^{12}$ for the two polar dipole modes. The above analytical approximation in the Newtonian limit is in excellent agreement with the exact numerical results [73, 69, 83, 91, 132, 72, 77, 85].

In the spinning case, the imaginary part acquires a factor $\omega_I \propto (\omega_R - m\Omega)$, which depends on the BH angular velocity Ω. Therefore, in the superradiant

---

[1] This can be seen by applying the angular-momentum operator to the state [83]. Note that l was erroneously identified with the orbital angular momentum in Ref. [75]. See Ref. [30] for a discussion of different spherical bases used in the literature.

regime, $\omega_R < m\Omega$, the modes with the smallest slope in the static case (namely, the polar dipole with $S = -1$) become the ones with the shortest instability timescale, $\tau = 1/\omega_I$ [30].

In the next section we shall compare our numerical results for the full plasma-photon system with the above hydrogenic behavior of a Proca field.

3.2.3 Plasma profiles

We consider two different plasma profiles: a homogeneous density profile and a Bondi-like accretion disk model. We will examine first the case of homogeneous density, and therefore homogeneous plasma frequency, $\omega_{\rm pl} = \text{const}$. This approximation is obviously not realistic, especially close to the BH. However, it will serve as a warm-up to elucidate the structure of the equations and identify the correct limit asymptotically far from the BH.

Then, we will consider a radial dependence $\omega_{\rm pl} = \omega_{\rm pl}(r)$, as expected in the surroundings of a spherically symmetric BH. In particular, we will consider the Bondi-like accretion disk model, which describes the accretion dynamics of a non-self-interacting gas around a spherically symmetric compact object [133]. This model predicts a power-law density profile for the gas and consequently a plasma frequency of the type

$$\omega_{\rm pl}^2(r) = \omega_{\rm B}^2 \Big(\frac{2M}{r}\Big)^{\lambda} + \omega_{\infty}^2, \tag{3.29}$$

where $\sqrt{\omega_{\rm B}^2 + \omega_\infty^2}$ is the plasma frequency at the horizon (since in the relevant regime $\omega_\infty \ll \omega_{\rm B}$, with a little abuse of notation we shall refer to $\omega_{\rm B}$ as the horizon plasma density). The slope λ depends on the adiabatic index of the gas (e.g., $\lambda = 3/2$ for monoatomic species). The constant term ω_∞ is the asymptotic plasma frequency at infinity, i.e the interstellar medium plasma frequency far away from the central BH.

3.2.4 Numerical method

We compute the characteristic frequencies of our system using a direct integration shooting method [134, 76, 75]. The main idea is to integrate the system from the horizon outwards to infinity, imposing suitable boundary conditions. Close to the horizon, the solution must be a purely ingoing wave, as the horizon behaves as a one-way membrane,

$$u_{(i)} \sim e^{-i\omega r_*} \sum_n b_{(i)\,n} (r - 2M)^n, \tag{3.30}$$

where the coefficients $b_{(i)\,n}$ can be computed in terms of the arbitrary coefficient $b_{(i)\,0}$ by expanding the relevant equations near the horizon. At infinity, the solution at the leading order can be written in its most generic form as

$$u_{(i)} \sim B_{(i)} e^{-k_\infty r_*} + C_{(i)} e^{+k_\infty r_*}, \tag{3.31}$$

where $k_\infty = \sqrt{\omega_{\rm pl}^2(r \to \infty) - \omega^2}$. We are interested in strongly localized, quasibound state solutions for $\omega < \omega_{\rm pl}$, and we will therefore impose the condition $C_{(i)} = 0$, implying exponentially damped solutions at infinity, and solve the associated eigenvalue problem. This method does not rely on a specific shape of the effective potential and is thus extremely flexible. Moreover, the direct integration method works particularly well for the computation of quasibound states, while it is expected to be less precise for the computation of normal modes (corresponding to the boundary condition $B_{(i)} = 0$), especially for the highly damped modes.

Since the axial and polar sectors are decoupled and each one is described by a single second-order differential equation, for a given value of l we expect to find two families of modes (axial and polar), each one defined by an overtone number n. In the following we shall mainly focus on the fundamental ($n = 0$) modes, although tracking a fixed overtone number is difficult in the small $M\omega_{\rm pl}$ regime. As we shall see, in the same regime the imaginary part of the mode can become extremely small and sensitive to small numerical errors. The latter can be reduced by increasing the numerical accuracy and the truncation order of the series expansions at the horizon and at infinity.

This procedure is also suitable to find unstable modes, i.e. those with $\omega_I > 0$ and whose time dependence is exponentially growing as $e^{\omega_I t}$. We have searched for such modes in different configurations and found none, confirming the reasonable expectation that the system is stable in the static case.

3.2.5 Numerical Results

Constant Density plasma

Figure 3.1 shows the real part and the imaginary part of the axial eigenvalues $\omega = \omega_R + i\omega_I$, normalized to the plasma frequency. We consider $l = 1$ and two different overtone numbers, respectively $n = 0$ (orange) and $n = 1$ (blue). As expected, the imaginary part of the frequency is always negative and represents a mode which is exponentially decaying in time, while the real part is always smaller than $\omega_{\rm pl}$, a necessary condition to obtain solutions that are confined in the vicinity of the BH. Since the axial sector is the same as in the Proca case, this plot is equivalent to what found in Ref. [75] for the axial quasibound states of a Proca field around a Schwarzschild BH. The dashed curves shown in Fig. 3.1 correspond to the hydrogenic spectrum expected in the $M\omega_{\rm pl} \ll 1$ limit.

While in the axial sector the potential is simple and equivalent to that of a Proca equation, in the polar sector the situation is different. Indeed, not only are the equations more involved than in the Proca case, but the polar sector only contains a single propagating mode, in contrast with the two polar modes of a Proca field. Thus, as expected, the structure of the plasma-driven polar quasibound states is different and cannot be mapped into a hydrogenic spectrum as in the axial case. This is shown in Fig. 3.2.

In this case the numerical computation of the eigenfrequencies becomes increasingly more challenging for values of the coupling $M\omega_{\rm pl} \lesssim 0.4$ and we therefore do not show the lower part of the spectrum in Fig. 3.2. However, in order to investigate the small-mass coupling regime, $M\omega_{\rm pl} \ll 1$, we separately studied smaller intervals around $M\omega_{\rm pl} \simeq 0.15$, as shown in Fig. 3.3. Although the numerical results are noisy in this limit, we find that the scaling of ω_I is significantly different from the hydrogenic behavior predicted in the Proca case for $S = -1$. Indeed, our best fit yields $\omega_I/\omega_{\rm pl} \sim (M\omega_{\rm pl})^{10.84}$, to be compared with $\omega_I/\omega_{\rm pl} \sim (M\omega_{\rm pl})^7$ for the $S = -1$

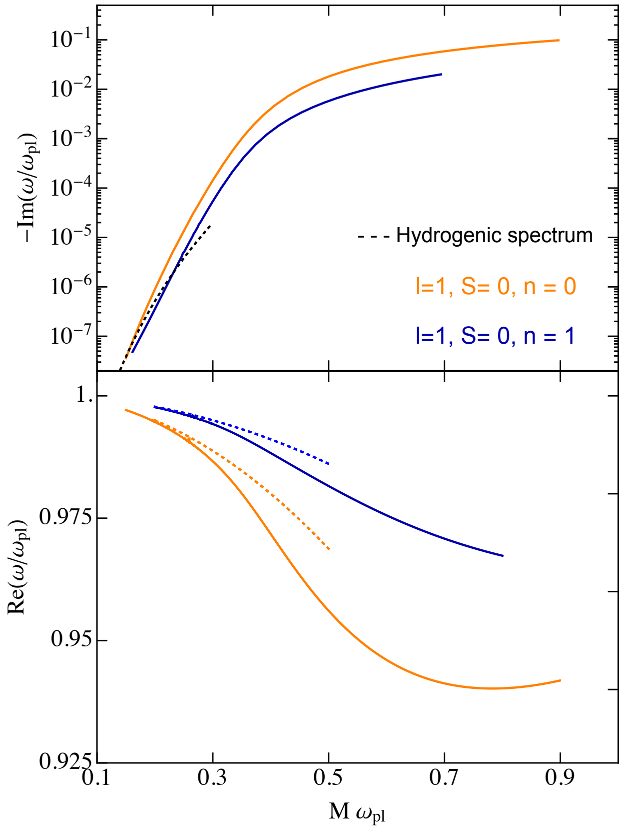

Figure 3.1. Imaginary (upper panel) and real (lower panel) part of the plasma-driven quasibound EM mode of a Schwarzschild BH in the axial sector for the case $\omega_{\rm pl} = \text{const}$. The imaginary part of the frequency is always negative, while the real part is always smaller than the plasma frequency. We show the fundamental mode ($n = 0$, orange) and the first overtone ($n = 1$, blue) for $l = 1$. The dashed curves correspond to the hydrogenic spectrum, which is recovered as expected in the limit $M\omega_{\rm pl} \ll 1$. Note that the axial sector is equivalent to that of a Proca field [75].

Proca mode. In fact, we find a scaling that is quite close to the (subleading) polar mode with polarization $S = 1$ for the massive vector case [75]. The reason why the numerical computation of the polar sector in the low-frequency regime is challenging resides on the presence of a *resonance*. This will be explained in more detail in 3.3, where a more detailed analysis is performed.

In some sense, the plasma-driven EM quasibound states are phenomenologically closer to a massive scalar field than to a Proca field. In both plasma-driven EM fields and massive scalar fields, the minimum scaling of the imaginary part (which sets the shortest, and therefore most interesting, mode lifetime) is $\omega_I/\omega_{\rm pl} \sim (M\omega_{\rm pl})^9$. This scaling is set by the axial dipole mode in the plasma-photon system. Thus, the lifetime of the fastest quasibound states in the plasma-driven case is parametrically longer than for a Proca field – for which the shortest lifetime is set by the polar modes – by a factor $(M\omega_{\rm pl})^{-2} \gg 1$.

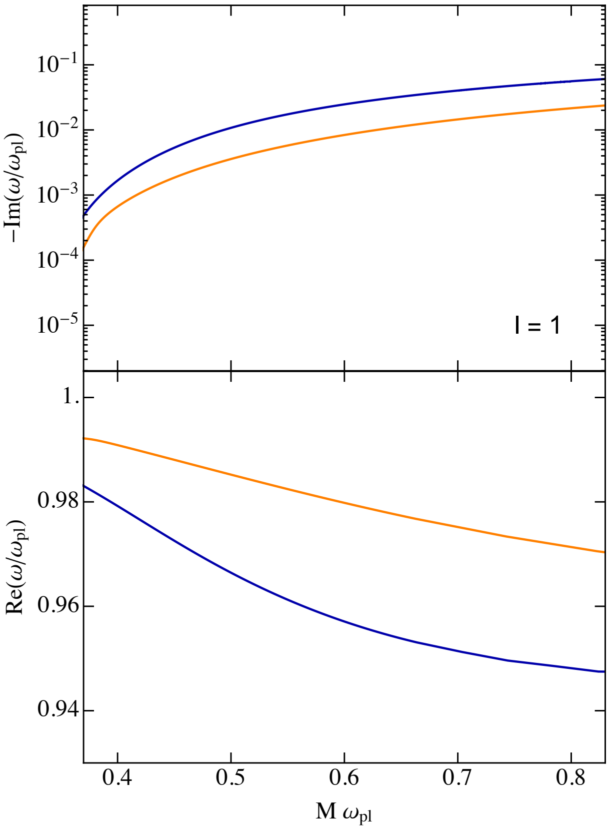

Figure 3.2. Same as in Fig. 3.1 but for the polar sector. In this case the modes do not reduce to the hydrogenic Proca spectrum in the $M\omega_{\mathrm{pl}} \ll 1$ limit.

3.2.6 Plasma profile from Bondi accretion

We now analyze the quasibound states for a more realistic plasma density profile, as predicted by Bondi accretion. In this case the axial sector is also described by Eq. (3.24), except for a radial dependence in the plasma frequency $\omega_{\mathrm{pl}} \to \omega_{\mathrm{pl}}(r) = \sqrt{\omega_{\mathrm{B}}^2(2M/r)^\lambda + \omega_\infty^2}$. The polar sector is again more involved and its potential depends nontrivially on the radial derivatives of the plasma frequency. The equations for the polar case are presented in Appendix A.

In Fig. 3.4 we show the results for the imaginary and real part of the frequency in the axial sector as a function of ω_∞, the quantity that would asymptotically corresponds to a mass term. In all cases we fix $\lambda = 3/2$ for the Bondi model (corresponding to monoatomic gas) and we show the results for different values of the horizon plasma frequency ω_{B}. We notice that, as in the homogeneous plasma case, the real (imaginary) part of the frequency decreases (increases) monotonically with $M\omega_\infty$. The effect of ω_{B} is the opposite: larger values of the density in the vicinity of the BHs lead to a smaller imaginary part and a larger real part. Indeed, for larger values of ω_{B} it is more difficult to find minima in the effective potentials, i.e. it is more difficult to support quasibound states. In fact, we were not able to find quasibound states solutions for $\omega_{\mathrm{B}} M \gtrsim 1.7$, in good agreement with the numerical

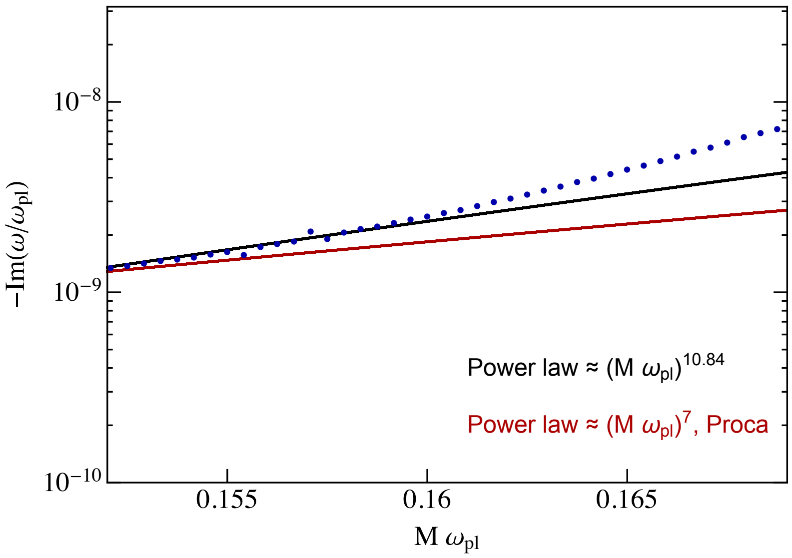

Figure 3.3. Imaginary part of the plasma-driven EM quasibound mode in the polar sector in $M\omega_{\mathrm{pl}} \ll 1$ regime. The blue dots indicate the numerical data; the black solid line is the best-fit power law, while the red line denotes the hydrogenic scaling in the Proca case.

study in Ref. [115] for a scalar toy model. Furthermore, this behavior is consistent with the $\omega_B \to 0$ limit, as in this case the spectrum shown in Fig. 3.1, with smaller values of the real part of the eigenfrequencies, must be recovered.

Note that, in general, the imaginary part of the quasibound states for a Bondi plasma profile is smaller than in the homogeneous-plasma case. This makes the numerical computation harder, especially for polar modes for which the imaginary part is even smaller than in the axial case. Although not shown, we were also able to compute the plasma-driven polar mode in the case of a Bondi profile, at least when $M\omega_\infty = \mathcal{O}(1)$. As in the homogeneous case, the axial modes are found to be the shortest lived for small values of the plasma frequency.

3.3 An extended phenomenology: Collisions, thermal corrections and superradiant instability

In this section, we include three effects that were neglected in the previous one: collisions in the plasma, thermal corrections, and the angular momentum of the background black-hole spacetime. We show that collision and thermal effects – as expected– do not affect significantly the quasibound states in the astrophysical environments of interest, so that the spectrum is robust with respect to the plasma features. Afterwards, we show that the spectrum can turn superradiantly unstable at a linear level when the BH rotates.

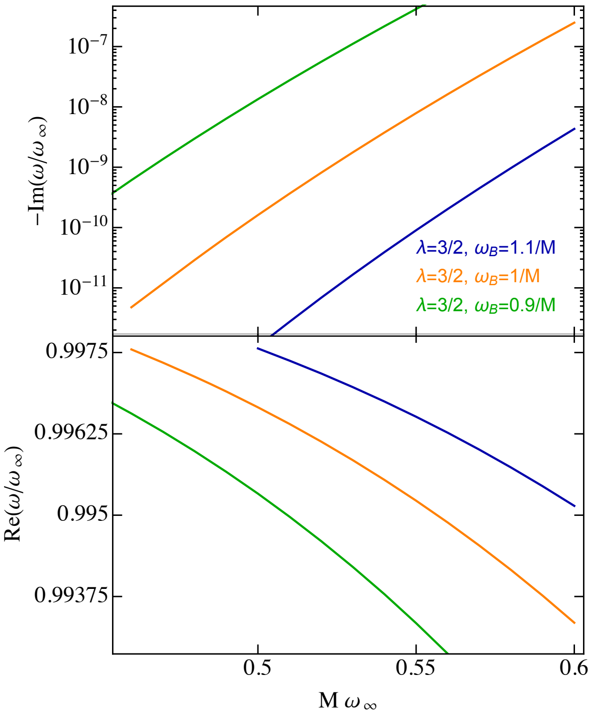

Figure 3.4. Imaginary (upper panel) and real (lower panel) part of the quasibound state frequency in the axial sector for a photon in a Bondi-accretion plasma model, see Eq. (3.29). The imaginary part is always negative, while the real part is always smaller than the plasma frequency, as expected. The imaginary part of the frequency decreases (the modes become short-lived) as the horizon plasma $\omega_{\rm B}$ density increases.

3.3.1 Collisional plasma

So far, we have ignored particle collisions in the plasma. This amounts to assume that the collision rate between electrons and ions is much smaller than the characteristic oscillation frequency of the plasma, $\omega_{\rm pl}$. In other words, it was assumed that the time τ between two electron-ion collisions is much longer than the other physical timescales in the problem. Here we show that indeed the inclusion of collision effects does not affect our results in the astrophysical environments of interest.

Let us first modify the set of Eqs. (3.3)-(3.6) in order to take into account electron-ion collisions. The electron equation of motion acquires an extra term [135]

$$u^\mu \nabla_\mu u^\nu = \frac{e}{m_e} F^\nu{}_\mu u^\mu - \frac{1}{\tau} u^\nu . \tag{3.32}$$

At the microscopic level, τ can be thought as arising from Coulomb collisions between electrons and ions around the BH [136]

$$\tau \simeq \frac{2\pi\, m_e^2 v_e^3}{n_e e^4 \log\Lambda} , \tag{3.33}$$

where v_e is the typical electron velocity and $\log\Lambda$ is the Coulomb logarithm. However, in the interest of generality, in the following we will treat the collision timescale τ as an independent parameter in the perturbed equations.

With this addition the perturbation equation (3.11) becomes

$$\begin{aligned} h^{\alpha}{}_{\beta}u^{\delta}\nabla_{\delta}\nabla_{\gamma}\tilde{F}^{\beta\gamma} - \omega_{\rm pl}^{2}\tilde{F}^{\alpha\beta}u_{\beta} + \boldsymbol{\frac{1}{\tau}h^{\alpha}{}_{\beta}\nabla_{\gamma}\tilde{F}^{\beta\gamma}} \\ +(\omega^{\alpha}{}_{\beta} + \omega_{L}{}^{\alpha}{}_{\beta} + \theta^{\alpha}{}_{\beta} + \theta h^{\alpha}{}_{\beta} + \frac{e}{m_e}E^{\alpha}u_{\beta})\nabla_{\gamma}\tilde{F}^{\beta\gamma} = 0, \end{aligned} \tag{3.34}$$

where we highlighted the new term due to collisions in bold.

In Sec. 3.3.3 we will solve this equation numerically for a nonrotating BH, and show that the effect of collisions can be safely neglected. As a back-of-the-envelope estimate, one can compare the collision timescale due to electron-proton Coulomb interactions with the other relevant timescale in the problem: $\omega_{\rm pl}^{-1}$. For densities and temperatures of astrophysical relevance, the collision timescale is much longer than the plasma oscillation time,

$$\tau\,\omega_{\rm pl} \simeq 2\times 10^{11}\left(\frac{T}{10^{7}{\rm K}}\right)^{3/2}\left(\frac{n_e}{10^{4}{\rm cm}^{-3}}\right)^{-1/2}, \tag{3.35}$$

where we estimated the typical electron velocity as their thermal velocity $v_e \simeq 0.03\sqrt{T/(10^{7}{\rm K})}$ and took $\Lambda \simeq 20$. Notice that $\tau\omega_{\rm pl} \gg 1$ even for much higher values of n_e, as those typical of accretion disks in the vicinity of the BH. Furthermore, using the background electron velocity to estimate the collision timescale is a conservative choice. In fact, when electrons are accelerated to relativistic velocities (as in the case of the superradiant instability discussed below), the collision timescale is even longer.

3.3.2 Warm plasma

Up to now, we have considered a cold plasma and ignored pressure terms in the electron equations of motion. We now turn our attention to thermal corrections arising in a warm plasma with temperature T. Thermal corrections are conceptually different from the relativistic and nonlinear corrections studied in Refs. [137, 138], arising from the acceleration of electrons to very large velocities by a strong electric field. These accelerations, however, do not imply that the plasma temperature is high. In a warm (hot) plasma the *thermal* velocity is comparable to (much higher than) the typical velocities of the propagating modes, which might not be the case even if the electrons are relativistic. Here we study what happens when thermal motion is turned on and the resulting thermal pressure gradients need to be included.

The warm plasma model adopted here is an intermediate framework between the cold plasma model (where thermal motion is completely neglected) and the hot plasma model (where thermal motion is relevant and cannot be treated within the fluid description adopted here). Since the velocities associated with the typical temperature of an accretion disk (see Eq. (3.2)) are smaller than, or at most comparable to, the phase velocity of the propagating EM mode described by a quasibound state (see 3.1 and the estimate below), an intermediate, warm-plasma approximation is well justified.

In a warm-plasma model, the momentum equation of the electrons [Eq. (3.4)] must be modified with a pressure correction [139],

$$u^\mu \nabla_\mu u^\nu = \frac{e}{m_e} F^\nu{}_\mu u^\mu - \nabla^\nu p \tag{3.36}$$

where $p = nk_BT$ is the pressure of an ideal gas. The system of equations must be closed by an equation of state $p = p(\rho)$ with $\rho = m_e n_e$ in the nonrelativistic regime. In this case the equation for the perturbed EM field (3.11) is modified to

$$\begin{aligned} & h^\alpha{}_\beta u^\delta \nabla_\delta \nabla_\sigma \tilde{F}^{\beta\sigma} - \omega_{\rm pl}^2 \tilde{F}^{\alpha\beta} u_\beta + e\, \gamma\, v_{\rm th}^2\, h^\alpha{}_\beta \nabla^\beta \tilde{n}_e \\ & + (\omega^\alpha{}_\beta + \omega_L{}^\alpha{}_\beta + \theta^\alpha{}_\beta + \theta h^\alpha{}_\beta + \frac{e}{m_e} E^\alpha u_\beta) \nabla_\sigma \tilde{F}^{\beta\sigma} = 0\,, \end{aligned} \tag{3.37}$$

where $v_{\rm th}^2 = k_BT/m_e$ is the electron thermal velocity and we assumed a polytropic equation of state with index γ, i.e., $p \propto \rho^\gamma$. This allows us to relate, at leading order, a perturbation in the temperature $\tilde{T}$ to a perturbation in the electron density: $\tilde{T} = (\gamma - 1) T\, \tilde{n}_e / n_e$.

Maxwell's equations also relate the density perturbation to the perturbation of the EM tensor. The thermal correction in Eq. (3.37) can thus be expressed in terms of the EM tensor perturbation alone,

$$\begin{aligned} & h^\alpha{}_\beta u^\delta \nabla_\delta \nabla_\sigma \tilde{F}^{\beta\sigma} - \omega_{\rm pl}^2 \tilde{F}^{\alpha\beta} u_\beta \boldsymbol{- \gamma\, v_{\rm th}^2\, h^\alpha{}_\beta \nabla^\beta u_\mu \nabla_\nu \tilde{F}^{\mu\nu}} \\ & + (\omega^\alpha{}_\beta + \omega_L{}^\alpha{}_\beta + \theta^\alpha{}_\beta + \theta h^\alpha{}_\beta + \frac{e}{m_e} E^\alpha u_\beta) \nabla_\sigma \tilde{F}^{\beta\sigma} = 0\,, \end{aligned} \tag{3.38}$$

where again the term due to thermal pressure modifying Eq. (3.11) is highlighted in bold. In the next section we shall solve this equation numerically in a Schwarzschild background and show that the effect of the plasma temperature can be safely neglected in realistic astrophysical settings, especially for the dominant quasibound states of the system. As a simple numerical estimate, Eq. (3.38) suggests that thermal effects will be negligible as long as

$$\gamma v_{\rm th}^2 \simeq \gamma 10^{-2} \sqrt{\frac{T}{10^7 \rm K}} \ll 1\,. \tag{3.39}$$

3.3.3 Quasibound states in a collisional plasma

We now solve for the EM perturbation in a collisional plasma, Eq. (3.34), around a nonspinning BH using the same numerical procedures as in the previous section. By performing the multipolar expansion (3.19), Eq. (3.34) gives

$$\begin{aligned} & f^2 u_{(4)}'' + 2fMr^{-2} u_{(4)}' \\ & + r^{-3} \left[r^3 \omega^2 - fr(l(l+1) + r^2 \omega_{\rm pl}^2) \right] u_{(4)} \\ & + \frac{f \omega_{\rm pl}^2}{1 - i\tau\omega f^{-1/2}} u_{(4)} = 0, \end{aligned} \tag{3.40}$$

for the axial sector, and

$$\begin{aligned} & f^2 u''_{(3)} + fF(r)u'_{(3)} \\ & + \left(-\frac{fl(l+1)}{r^2} + \omega^2 + \frac{i\sqrt{f}\tau\omega\omega_{\rm pl}^2}{1 - i\tau\omega f^{-1/2}}\right) u_{(3)} = 0, \end{aligned} \tag{3.41}$$

for the polar sector, where $u'_{(i)} = \partial_r u_{(i)}$ and $F(r)$ is given in Appendix A.3. As expected, when $\tau\omega \to \infty$ we recover the equations governing the collisionless case studied in 3.2. Interestingly, the standard collisional term $i\tau\omega$ appearing in flat spacetime is modified by a redshift factor, $(1 - 2M/r)^{-1/2}$.

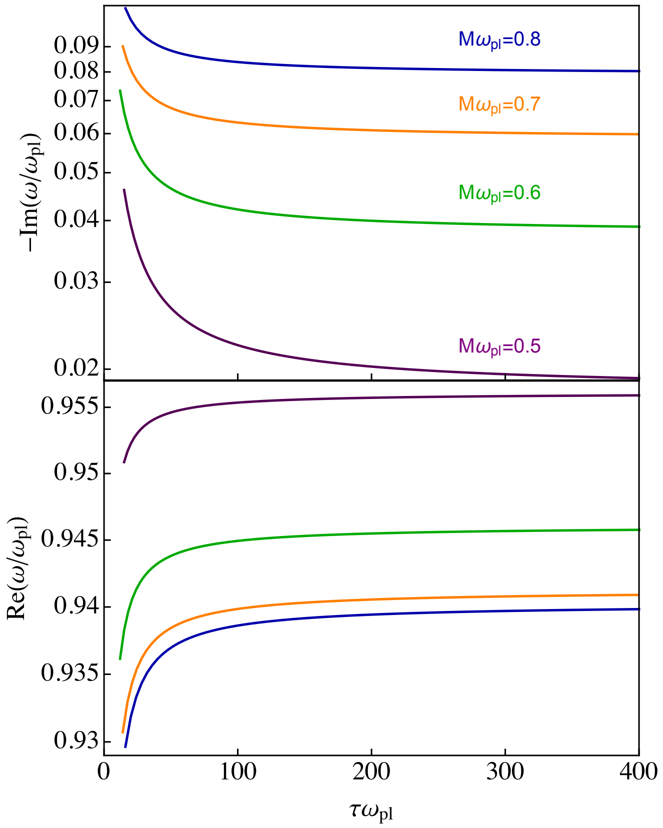

Figure 3.5. Imaginary (top) and real (bottom) part of the axial $l = 1$ mode for the quasibound states of a cold, collisional plasma in a Schwarzschild background as a function of the collision timescale τ, normalized by the plasma frequency. For large collision time $\tau \gg 1/\omega_{\rm pl}$, the results are identical to the collisionless case discussed in 3.2. When the collision time becomes very short, $\tau \ll 1/\omega_{\rm pl}$, the collisions between electrons and protons shorten the lifetime of the bound states.

In Fig. 3.5 and 3.6 we show the imaginary and real part of the fundamental axial and polar modes, respectively, as a function of the collision time, for four values of the plasma frequency. For any value of $\omega_{\rm pl}$ the dependence on τ is qualitatively the same. Namely, for very large collision timescales $\tau \gg \omega_{\rm pl}^{-1}$, the frequencies coincide with the collisionless frequencies. As expected, collisions are irrelevant when the

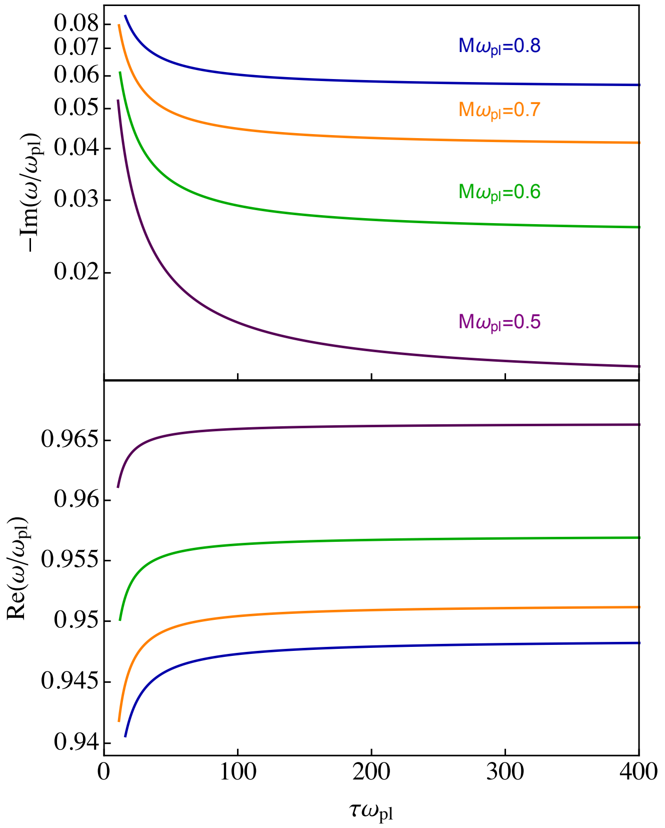

Figure 3.6. Same as in Fig. 3.5 but for the polar sector. The behaviour of the modes is the same as in the axial case, and a quenching occurs as $\tau\omega_{\rm pl} \ll 1$.

time between two collisions is much longer than the characteristic time of plasma oscillations. On the other hand, when the time between collisions is short, $\tau \ll \omega_{\rm pl}^{-1}$, the absolute value of the imaginary part starts to increase, i.e., the lifetime of the mode is shortened. Collisions between electrons and protons in this case rapidly quench the quasibound states. However, as shown in Eq. (3.35), the limit $\tau \ll 1/\omega_{\rm pl}$ is never realized in astrophysical environments, and collisions can be safely neglected. Indeed, realistic values of $\tau\omega_{\rm pl}$ are much bigger than those shown in Fig. 3.5.

This numerical result can be understood analytically as follows. Eq. (3.40) can be re-written to resemble the standard axial equation in the collisionless case, which coincides with the Proca axial equation, as

$$\mathcal{D}_2^\tau u_{(4)}(r) = 0, \tag{3.42}$$

where $\mathcal{D}_2^\tau \equiv \frac{d^2}{dr_*^2} + \omega^2 - f\left(\frac{l(l+1)}{r^2} + \mu_{\rm eff}^2\right)$ has the same differential form as in 3.2 but with the plasma frequency replaced by a collisions-dependent effective mass

$$\mu_{\rm eff}^2 = \omega_{\rm pl}^2\Big(1 - \frac{1}{1 - i\tau\omega f(r)^{-1/2}}\Big). \tag{3.43}$$

The effective mass determines the behavior of the quasibound states at infinity, $k_\infty = \sqrt{\mu_{\rm eff}^2(r\to\infty) - \omega^2}$. Clearly, in the limit $\tau \to \infty$, the effective mass tends to the plasma frequency, and the collisionless spectrum is recovered. In the opposite limit, $\tau \to 0$, the effective mass goes to zero – unable to spatially confine the modes – and consequently the quasibound spectrum is quenched. Similarly, in the polar case we found an effective mass at infinity

$$\mu_{\rm eff}^2 \sim \omega_{\rm pl}^2\Big(1 - \frac{1}{1 - i\tau\omega}\Big), \tag{3.44}$$

which asymptotically coincides with the axial one. Thus, also in the polar sector the effective mass term at infinity goes to zero as plasma becomes strongly collisional, and the polar quasibound spectrum is quenched.

3.3.4 Quasibound states in a plasma with thermal corrections

We now turn our attention to thermal corrections. Applying the multipolar decomposition to Eq. (3.36), we obtain a system of differential equations for the mode functions in frequency domain,

$$\begin{aligned}
f^2\gamma v_{\rm th}^2 r^4 u_{(2)}'' + \frac{3}{2}\gamma(f-1)fr^3 v_{\rm th}^2 u_{(2)}'& \\
-f^2r^3\left(\gamma v_{\rm th}^2 - 1\right)u_{(3)}'& \\
-r^2\big[fl(l+1) + \gamma/2\left(6f^2 + f - 3\right)v_{\rm th}^2& \\
+r^2(f\omega_{\rm pl}^2 - \omega^2)\big]u_{(2)}& \\
+\frac{1}{2}\gamma f(3f+1)r^2v_{\rm th}^2 u_{(3)} &= 0\,,
\end{aligned} \tag{3.45}$$

$$\begin{aligned}
f^2r^3u_{(3)}'' + (1-f)fr^2u_{(3)}'& \\
-f(-\gamma v_{\rm th}^2 + 1)l(l+1)r^2u_{(2)}'& \\
+r\left[-f\gamma v_{\rm th}^2 l(l+1) - f\omega_{\rm pl}^2 r^2 + r^2\omega^2\right]u_{(3)}& \\
-l(l+1)r\left[\gamma v_{\rm th}^2 - f(2\gamma v_{\rm th}^2 + 1)\right]u_{(2)} &= 0\,,
\end{aligned} \tag{3.46}$$

$$\begin{aligned}
r^2f^2u_{(4)}'' + r(1-f)fu_{(4)}'& \\
-\left[f(l + l^2 + r^2\omega_{\rm pl}^2) + r^2\omega^2\right]u_{(4)} &= 0\,.
\end{aligned} \tag{3.47}$$

In the polar sector we find the usual distinction between longitudinal $u_{(2)}$ and transverse $u_{(3)}$ modes. The former are non-dynamical in a cold plasma, but become propagating, energy-transporting modes (Langmuir waves in flat spacetime [121]) due to the thermal corrections. Indeed, from Eq. (3.45) it is easy to see that the degree of freedom $u_{(2)}$ becomes dynamical only for $v_{\rm th} \neq 0$. To show that this mode behaves as a Langmuir wave, we take the flat spacetime limit: for $r \to \infty$ and in momentum space Eq. (3.45) reads

$$\omega^2 u_{(2)} = (\omega_{\rm pl}^2 + k^2\gamma v_{\rm th}^2)u_{(2)}, \tag{3.48}$$

which is the Bohm-Gross dispersion relation describing Langmuir modes in a warm plasma [121]. In the same limit, the equation for the transverse mode (3.46) becomes

$$\omega^2 u_{(3)} = (\omega_{\rm pl}^2 + k^2)u_{(3)}. \tag{3.49}$$

Therefore, this EM wave is unaffected by thermal corrections at infinity. This is a general feature of a warm plasma model in flat spacetime: transverse waves are unaffected by pressure [122]. In curved spacetime, thermal corrections couple longitudinal and transverse polar modes and the dynamics is more involved.

On the other hand, and more importantly for our scopes, the axial sector governed by Eq. (3.47) is unaffected by first-order thermal corrections and is the same as in the cold-plasma case studied in 3.2. Indeed, being a transverse mode, $u_{(4)}$ is unaffected at infinity, and due to the spherical symmetry of the spacetime it does not couple to the polar, longitudinal, thermally-affected modes even near the BH. Given that the axial modes are the most relevant ones for the quasibound spectrum of the system, we conclude that warm-plasma corrections can be safely neglected when studying EM quasibound states and superradiance in astrophysical systems.

Thermal effects should be carefully considered for a hot plasma, where transverse modes also become affected by temperature [122]. In this case, the system must be studied using kinetic theory, solving a set of coupled Vlasov-Maxwell equations. A study of this type is beyond the scope of this work and left for future investigation.

3.3.5 Polar quasibound states in the low plasma frequency regime: reflection point in inhomogeneous plasmas

In 3.2, we computed EM quasibound states in a cold, collisionless plasma at the linear level. For the polar sector, we were unable to explore the $\omega_{\rm pl}M \ll 1$ regime with high precision, and we could only provide an estimate of the behaviour of the quasibound spectrum in this limit. In the following, we explain the physical origin of the issues encountered in the polar sector in the low-plasma-frequency limit, relating them to the behaviour of inhomogeneous plasmas in flat spacetime. Furthermore, we show that, as in flat spacetime, the inclusion of dissipative mechanisms such as collisions, thermal or nonlinear effects can “smooth out” the low-plasma-frequency regime.

The fact that, in curved spacetime, plasma behaves as an inhomogeneous medium – even when assuming a constant electronic density – can be understood by inspecting the monopole sector of the polar equation in the cold, collisionless case, given by equation (3.25). This resembles the equation describing longitudinal modes ψ_L in plasma physics: $\epsilon\psi_L = 0$, where ϵ is the dielectric tensor[2]. The solution to this equation gives the dispersion relation for longitudinal modes, $\epsilon = 0$. By analogy, we introduce an effective dielectric tensor in the BH background,

$$\epsilon_{\rm eff} = 1 - \frac{\omega_{\rm pl}^2}{\omega^2}(1 - \frac{2M}{r}). \tag{3.50}$$

Note that in the near-horizon limit $r \sim 2M$ Eq. (3.25) admits only the trivial solution $u_{(2)} = 0$. Indeed, no electrostatic modes can exist at the BH horizon. Notice that the same occurs in the case of a massive (both scalar and vector) field, making the mass contribution subdominant at the horizon [140, 75, 141]. In the flat spacetime limit, we instead recover the standard solution for electrostatic modes $\omega^2 = \omega_{\rm pl}^2$, as discussed in 3.2.

---

[2] The dielectric tensor reduces to a scalar when the plasma is isotropic (unmagnetized), as assumed here.

However, due to the BH curvature correction, the effective dielectric gains a dependence on the radius, $\epsilon_{\rm eff} = \epsilon_{\rm eff}(\omega, r)$. Therefore, plasma can be considered effectively *inhomogeneous* even when $n_e = $ const, due to the spacetime curvature [142, 143]. A peculiar characteristic of inhomogeneous plasmas is the presence of a spatial point, known as *reflection point*, where the dielectric tensor vanishes, i.e., $\epsilon(\omega, r) = 0$. At this point, the longitudinal electric field and some components of the transverse magnetic and electric field diverge [144, 145]. Clearly, this divergence is not physical: dissipation mechanisms should be added to the theory to make the field equations well-behaved at the reflection point.

Some of the most important dissipative channels are absorbtion via collisions (as discussed above) and the formation of plasma waves. When collisions are taken into account, the dielectric tensor acquires an imaginary part, the divergence is removed and a sharp (but finite) Breit-Wigner resonance appears instead[3]. Thermal corrections can also cure the divergence near the point $\epsilon = 0$ [146, 147].

Clearly, these two effects play a major role in a strongly collisional or warm plasma. If dissipative effects are not strong enough, although the divergence is removed, the maximum value of the electric field may still be very large. In this case, nonlinear effects will play the role of the dominant dissipative effect [137]. A nonlinear treatment would take into account the motion of electrons due to the strong electric field, modifying the plasma density near the resonance point. For an analysis of this nonlinear effect in flat spacetime, see [148, 145].

A similar situation arises in our system. The dielectric tensor of Eq. (3.50) makes its appearance in the denominator of the effective potential in the polar sector (see Appendix A). In the case at hand, another important dissipation channel arises: the BH horizon. In the large plasma frequency regime ($M\omega_{\rm pl} > 0.4$), dissipation through the horizon is sufficient to give rise to a complex mode frequency with a non negligible imaginary part $\omega_{\rm I} \lesssim \omega_{\rm pl}$, so that the dielectric tensor is complex and the field is well behaved. On the other hand, in the small plasma frequency regime, the BH horizon alone cannot quench the resonance and we have $\omega_{\rm I} \ll \omega_{\rm pl}$. Given that in the relevant astrophysical scenarios the plasma is cold and collisionless to very good approximation, we expect that nonlinearities will play the role of the dominant dissipative channel in this regime. Nonlinear effects are therefore crucial for the high-precision computation of the polar sector for $\omega_{\rm pl}M \ll 1$.

In the following, as a proof of principle, we characterize the role played by dissipative channels in the vicinity of the reflection point by focusing on a strongly collisional plasma as modelled in the previous sections. Although in the astrophysical systems of interest collisions can be neglected and the main dissipative effect is of nonlinear nature, we use this analysis as a jumping off point to clarify how the divergence is cured when the dielectric tensor becomes complex.

Figure 3.7 shows the absolute value squared of the complex polar wavefunction $u_{(3)}$ for different values of the collision time τ for a small plasma frequency. The position of the sharp peak corresponds to a vanishing dielectric function, $r/M = 2/(1-\omega^2/\omega_{\rm pl}^2)$ from Eq. (3.50). The peak is “smoothed out" as collisions come to dominate over

---

[3] A system in which collisions play the role of the dominant dissipative channel is the Earth's ionosphere , where the dielectric tensor depends on the altitude z [144].

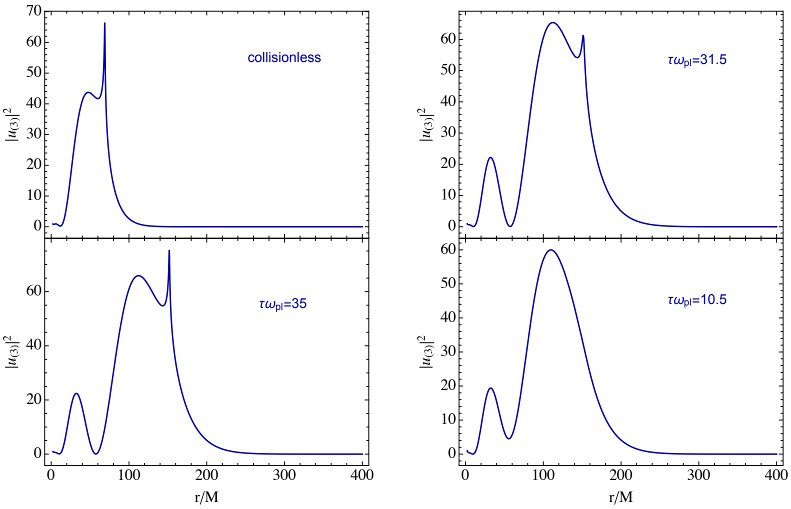

Figure 3.7. Absolute value squared of the polar $l = 1$ wavefunction $u_{(3)}$ for different values of the collision parameter τ at $M\omega_{\rm pl} = 0.35$. As plasma becomes more collisional, the resonance at the reflection point is smoothed out.

the resonance, showing that, when dissipation channels are included in the theory, the field becomes well-behaved. In flat spacetime, the effect of nonlinearity can be similarly included by adding an effective collision frequency, $\nu_{\rm eff}$, to the dielectric tensor [148, 145]. Thus, we expect that nonlinear effects should produce an effect similar to the one shown in Fig. 3.7.

3.3.6 Linearized plasma-photon dynamics in a Kerr spacetime

In previous sections we showed that collisions and thermal corrections have a small effect on quasibound states around a nonspinning BH. We are therefore justified to neglect these effects, and to focus our attention on plasma-induced superradiance in a Kerr background for a cold, collisionless plasma. In this section we derive the relevant linear perturbation equations to first order in the spin using a slow-rotation expansion [71] and numerically solve these equations to find superradiant modes.

Let us consider the Kerr metric in Boyern-Lindquist coordinates, given by (2.2)

As in the nonspinning case, since the plasma accretion timescale is much longer than the dynamical timescale of the problem, we assume a static plasma. Static observers exist outside the ergoregion of a spinning BH and their four-velocity reads $u^\alpha = (u^0, \vec{0})$, with $u^0 = g_{00}^{-1/2}$ so that Eq. (3.6) is satisfied. At $\mathcal{O}(a/M)$ the ergosphere coincides with the outer horizon, $r_+ = 2M + \mathcal{O}(a^2/M^2)$, so that, to this order, static observers exist all the way to the BH horizon.

Using the momentum equation (3.4) we obtain the background electric four-vector field giving rise to the static configuration, $E^\alpha = (0, m_e/e\,(u^0)^2\Gamma^r_{00}, m_e/e\,(u^0)^2\Gamma^\theta_{00}, 0)$, which possesses both a radial and an angular component. We also assume the plasma to be unmagnetized.

Contrary to the Schwarzschild case, where both the vorticity and deformation tensors vanish, in the Kerr spacetime the rotation of the BH induces a nontrivial vorticity in the fluid. The vorticity tensor is antisymmetric and has two nonvanishing components,

$$\omega_{r\phi} = -\frac{a\left(\Sigma - 2r^2\right)\left(a^2 - \Delta + r^2\right)}{2r\sqrt{\Sigma}\left(\Delta + \Sigma - r^2 - a^2\right)^{3/2}}\sin^2\theta, \tag{3.51}$$

$$\omega_{\theta\phi} = -\frac{a\Delta\left(a^2 - \Delta + r^2\right)}{\sqrt{\Sigma}\left(\Delta + \Sigma - r^2 - a^2\right)^{3/2}}\sin\theta\cos\theta, \tag{3.52}$$

which are nonzero already to first order in the BH spin. The deformation tensor remains zero in Kerr.

It is again convenient to separate the angular sector of the field from the radial one through a multipolar expansion. While in Schwarzschild the axial and polar sectors can be fully decoupled from each other thanks to spherical symmetry, in Kerr the axial and polar perturbations with different index l are coupled, making the field equations more challenging to solve [71]. Several methods were developed in order to solve the equations of a massive spin-1 field in a Kerr background, using a slow-rotation expansion [79, 76], analytical methods valid for ultralight Proca fields [83, 72], or numerically either without separability of the equations [91] or using a recently-discovered separability technique [82, 132].

In the following, owing to the complexity of the field equations for the problem at hand, we use the slowly-rotating approach to solve the EM perturbation equation (3.11) perturbatively. The field equations are expanded with respect to the dimensionless spin parameter $\tilde{a} = a/M \ll 1$ around the nonspinning case $\tilde{a} = 0$, and solved at different orders. This method was shown to perform well for Proca fields at second order, even for values of the spin close to extremality [76]. In our case, we are mostly interested in whether the quasibound modes discussed above and in 3.2 can turn unstable in the superradiant regime.

Using the multipolar expansion (3.19) and a frequency-domain representation, at first order in the spin the field equations assume the following form

$$u^l_{(1)} = 0\,, \tag{3.53}$$

$$\begin{aligned} A_l + Q_{l,m}[\tilde{A}_{l-1} + (l-1)B_{l-1}] \\ +Q_{l+1,m}[\tilde{A}_{l+1} - (l+2)B_{l+1}] = 0, \end{aligned} \tag{3.54}$$

$$\begin{aligned} l(l+1)\alpha_l - im\zeta_l + im\gamma_l \\ -Q_{l,m}[(l+1)(\eta_{l-1} - (l-1)\delta_{l-1})] \\ +lQ_{l+1,m}[\eta_{l+1} + (l+2)\delta_{l+1}] = 0, \end{aligned} \tag{3.55}$$

$$\begin{aligned} l(l+1)\beta_l + im\eta_l + im\delta_l - Q_{l,m}[(l+1)(\zeta_{l-1} \\ +(l-1)\gamma_{l-1})] + lQ_{l+1,m}[\zeta_{l+1} - (l+2)\gamma_{l+1}] = 0, \end{aligned} \tag{3.56}$$

where $Q_{l,m} = \sqrt{\frac{l^2-m^2}{4l^2-1}}$ while the quantities A_i, B_i, $\tilde{A}_i$, α_i, β_i, $\zeta_i, \gamma_i, \delta_i$, and η_i involve the mode functions $u^i_{(2)}$, $u^i_{(3)}$, and $u^i_{(4)}$ and their derivatives and are listed in Appendix B. This set of equations has a similar schematic form as the one obtained in the Proca case at linear order in the BH spin [76]. In particular, perturbations with a given parity and angular-momentum number l only couple with perturbations of opposite parity and index $l \pm 1$ (as shown in Appendix B, the terms A_i, α_i, ζ_i, γ_i are polar quantities, while B_i, $\tilde{A}_i$, η_i, β_i, δ_i are axial). Note that A_l, α_l, and β_l

contain corrections proportional to $m\tilde{a}$, whereas all other functions are proportional to $\tilde{a}$.

As a generic property of the set of linear perturbations, the terms multiplied by $Q_{l,m}$ do not affect the spectrum at first order in the spin and can be neglected at this order [149, 76, 79, 71]. This leads to an axial-led equation for $u^l_{(4)}$,

$$l(l+1)\beta_l + im\eta_l + im\delta_l = 0\,, \tag{3.57}$$

and a polar-led system of equations for $u^l_{(1)}$, $u^l_{(2)}$, and $u^l_{(3)}$,

$$u^l_{(1)} = 0\,, \tag{3.58}$$

$$A_l = 0, \tag{3.59}$$

$$l(l+1)\alpha_l - im\zeta_l + im\gamma_l = 0, \tag{3.60}$$

The two sectors are decoupled and do not involve couplings between different-l modes.

Axial sector at first order in the BH spin

Using the explicit form of the coefficients given in Appendix B, Eq. (3.57) can be rewritten as

$$\mathcal{D}_2 u_{(4)}(r) - \frac{4amM\omega}{r^3}u_{(4)} = \frac{4mMa\omega_{\rm pl}^2(r-2M)}{l(l+1)r^4\omega}u_{(4)}, \tag{3.61}$$

where we have suppressed the l superscript and used the differential operator $\mathcal{D}_2 \equiv \frac{d^2}{dr_*^2} + \omega^2 - f\left(\frac{l(l+1)}{r^2} + \omega_{\rm pl}^2\right)$ previously introduced (see eq. (3.24). Equation (3.61) deviates from the axial equation of a Proca field at first order in the spin [76] due to the presence of the term on the right-hand side. This correction is due to the vorticity tensor, which vanishes in the nonspinning case. Therefore, even at first order, we expect the spectrum to deviate quantitatively from that of a Proca field.

Polar sector at first order in the BH spin

The polar sector can be reduced, at first order in the spin, to a single second-order differential equation

$$\frac{d^2}{dr_*^2}\psi - V(r)\psi = 0, \tag{3.62}$$

for an appropriately defined field variable ψ (see Appendix B.2). As in the nonspinning case, although the original equations depended on two independent functions $u_{(2)}$ and $u_{(3)}$, the polar sector describes only one dynamical degree of freedom. The other degree of freedom does not propagate and remains electrostatic.

In the Schwarzschild limit ($a \to 0$) the effective potential reduces to the one obtained in 3.2. In the spinning case, the potential depends on the azimuthal number m. Moreover, the boundary condition at the horizon is modified, since $V(r \to r_+) = -(\omega^2 - 2m\omega\Omega_H)$, where Ω_H is the angular velocity at the horizon of locally nonrotating observers at first order in $\tilde{a}$. Note that this factor coincides with the expected superradiant factor, $(\omega - m\Omega_H)^2$ at first order in the BH spin.

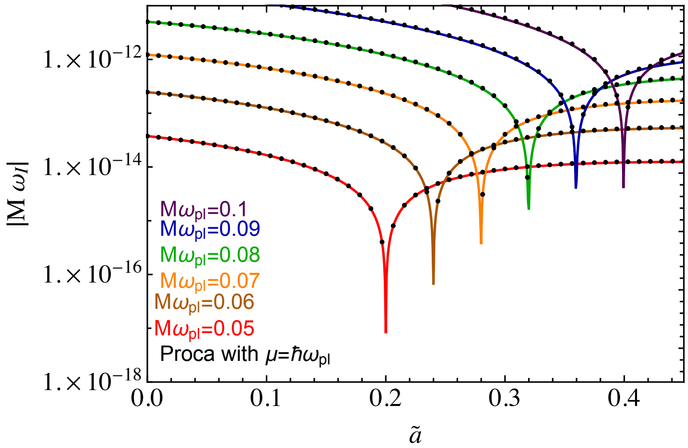

Figure 3.8. Imaginary part of the axial $l = 1 = m$ mode for different values of the plasma frequency $\omega_{\rm pl}$. The imaginary part of the mode changes sign and becomes superradiant when the superradiant condition $\omega_R < m\Omega_H$ is met. Black dots represent Proca modes with $l = 1 = m$. The difference between the two spectra is always less than 2%.

As discussed in Sec. 3.3.5, owing to the importance of nonlinear effects in the $\omega_{\rm pl}M \ll 1$ regime, a nonlinear analysis of the polar sector in a Kerr spacetime is necessary to investigate its spectrum. Therefore, in the next following we shall focus only on the superradiantly unstable axial sector.

3.3.7 Plasma-driven superradiant instability: numerical results

As in 3.2, we consider two different plasma profiles: a homogeneous density profile and the Bondi-like spherical accretion flow given by eq. (3.29).

We solve Eqs. (3.61) and (3.62) numerically with the shooting method described in 3.2. The boundary conditions are now modified according to the behavior of the effective potential at the horizon and at infinity.

Constant density plasma

In 3.2, we showed that the axial spectrum of the EM field around a nonspinning BH coincides with the axial sector of a Proca field, i.e. the real and imaginary part in the Newtonian regime coincide with Eqs. (3.27) and (3.28) with $S = 0$. On the other hand, the polar spectrum differed from Proca's and was subdominant in the large mass coupling regime $M\omega_{\rm pl} > 0.4$.

Since in the slow-rotation expansion the spin is introduced perturbatively, we expect that the axial mode should provide the shortest instability timescale in the superradiant regime, at least for values of $M\omega_{\rm pl}$ which are not too small, in order to avoid the reflection point previously discussed for the polar modes.

In Kerr, the field equations depend on the azimuthal number m. Therefore, the spectrum is characterised by a Zeeman-like splitting for different azimuthal numbers. In particular, modes with $m > 0$ can become unstable if the superradiant condition $\omega_{\rm R} < m\Omega_H$ is satisfied. Figure 3.8 shows the absolute value of the imaginary part of the axial modes with $l = 1 = m$ at first order in the BH spin, for different values of the homogeneous plasma frequency. The black dots, for comparison, represent the modes of a Proca field with mass $\hbar\omega_{\rm pl}$. Interestingly, despite the fact that Eq. (3.61) deviates from the axial Proca equation at first order, the two spectra almost coincide; the difference between an EM and a Proca mode at fixed $\omega_{\rm pl}$ is always less than 2%. When the superradiant condition $\omega_{\rm R} < m\Omega_H$ is met, the imaginary part changes sign and the modes become superradiantly unstable. Since $\omega_{\rm R} \sim \omega_{\rm pl}$ and $\Omega_H \sim a/(4M^2) + O(\tilde{a}^3)$ for a quasibound mode with $M\omega_{\rm pl} \ll 1$, the superradiant condition is met at $\tilde{a} \sim 4M\omega_{\rm pl}$, in good agreement with the crossing points in Fig. 3.8. Note that, since $\Omega_H = \mathcal{O}(\tilde{a})$, the superradiant condition requires $\omega_{\rm pl}M = \mathcal{O}(\tilde{a})$ or smaller, making it difficult to solve the equations numerically. Indeed, strictly speaking the superradiantly unstable modes require $\mathcal{O}(\tilde{a}^2)$ corrections (see Ref. [76] for a discussion), although first-order results are already sufficiently accurate [30]. When $M\omega_{\rm pl} \ll 1$, the real part of the modes depends only very weakly on the BH angular momentum and is very well approximated by the hydrogenic relation (3.27), just as for Proca fields [76].

Bondi Accretion Model

We now analyze the spectrum for a Bondi accretion model, where the plasma frequency acquires a dependence on the radius $\omega_{\rm pl} \to \omega_{\rm pl}(r)$ as described by Eq. (3.29). The modes can be obtained by solving Eq. (3.61) taking into account the radial dependence of the effective mass.

Figure 3.9 shows the (absolute value of the) imaginary part of the fundamental axial mode with $l = m = 1$ as a function of the spin parameter $\tilde{a}$ for different values of ω_B in the case $\omega_\infty = 0.05/M$. For these modes $\omega_R/\omega_\infty \sim 1$, therefore the superradiant condition $\omega_R < m\Omega_H$ becomes $4M\omega_\infty < \tilde{a}$, in agreement with the crossing points in Fig. 3.9. Consequently, for sufficiently low plasma densities at the horizon, the system admits plasma-driven superradiant modes, with much larger timescales than in the $\omega_{\rm pl} = \mathit{const.}$ case. As shown in Fig. 3.9, as ω_B increases the timescale of the mode also increases, and can become comparable to the Salpeter time. For such weakly-unstable modes, accretion must be taken into account; in particular, our formalism becomes inaccurate in this regime, as we assumed the plasma to be static.

As shown in Ref. [115] (by using a Klein-Gordon toy model) and in 3.2, if the density at the horizon grows above a critical value, the spectrum is completely quenched, making the plasma-driven instability very fragile in realistic configurations.

3.4 The nonlinear death of plasma-driven superradiant instabilities

The analysis of the last section disclosed that the photon field can be naturally confined by plasma in the vicinity of the BH via the effective mass, forming quasibound states that turn unstable if the BH spins. Nevertheless, a crucial issue was unveiled in [137], where it was argued that, during the superradiant phase, *nonlinear* modifications to the plasma frequency turn an initially opaque plasma into transparent, hence quenching the confining mechanism and the instability itself. In

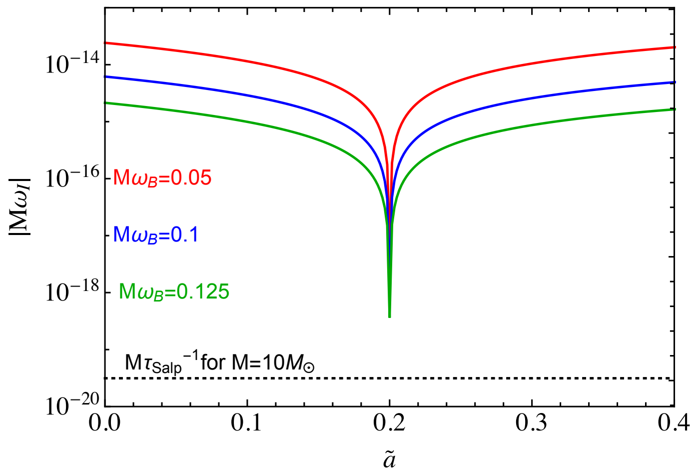

Figure 3.9. Superradiant axial modes with $l = 1 = m$ in a Bondi accretion model [see Eq. (3.29)] with plasma asymptotic frequency $\omega_\infty = 0.05/M$, for different values of the plasma frequency at the horizon, $\omega_{\rm pl} \approx \omega_{\rm B}$. The imaginary part of the modes is some orders of magnitude smaller than in the $\omega_{\rm pl} = const.$ case, and can become comparable to the Salpeter time (marked as a dashed line for the case of $M = 10M_\odot$).

the nonlinear regime, a transverse, circularly polarized electromagnetic (EM) wave with frequency ω and amplitude E modifies the plasma frequency of a homogeneous plasma as [150]

$$\omega_{\rm pl} = \sqrt{\frac{n_e e^2}{m\sqrt{1+\frac{e^2E^2}{m^2\omega^2}}}}\,, \tag{3.63}$$

where the extra term is the Lorentz factor of the electrons. In other words, as the field grows, the electrons turn relativistic and their relativistic mass growth quenches the plasma frequency. As argued in Ref. [137], the threshold of this modification lies in the very early stages of the exponential growth, before the field can extract a significant amount of energy from the BH.

While in this specific configuration the quenching of the instability is evident, this argument suffers for a number of limitations. In particular, circularly polarized plane waves in a homogeneous plasma are the only solutions that are purely transverse, as the nonlinear $\vec{v} \times \vec{B}$ Lorentz force vanishes (here $\vec{v}$ is the velocity of the electron, while $\vec{B}$ is the magnetic field). In this case, the plasma density is not modified by the travelling wave and even a low-frequency wave with large amplitude can simply propagate in the plasma, without inducing a nonlinear backreaction. In every other configuration instead (including an inhomogeneous plasma, different polarization, or breaking of the planar symmetry, all expected for setups around BHs), longitudinal and transverse modes are coupled, and therefore the plasma density can be dramatically modified by the propagating field. This backreaction effect leads to a richer phenomenology as high-amplitude waves can push away electrons from some regions of the plasma, thus creating both a strong pile-up of the electron density in some regions and a plasma depletion in other regions. For example, in the case of a circularly polarized wave scattered off an inhomogeneous plasma, the backreaction on the density increases the threshold for relativistic transparency, as electrons are piled up in a narrow region, thus increasing the local density and making nonlinear transparency harder [151]. However, in the case of a coherent long-timescale phenomenon such as superradiant instability, one might expect that, if the plasma is significantly pushed away by a strong EM field, the instability is quenched a priori, regardless of the transparency. Overall, the idealized configuration of Ref. [150] never applies in the superradiant system, and the nonlinear plasma-photon interaction is much more involved.

The goal of this section is to introduce a more complete description of the relevant plasma physics needed to understand plasma-photon interactions in superradiant instabilities. To this purpose, we shall perform $3+1$ nonlinear numerical simulations of the full Maxwell's equations.

3.4.1 $3+1$ decomposition of the field equations

Generic spacetime

In the following, we will decompose the set of equations (3.3)-(3.6) at a fully nonlinear level by adopting a 3+1 formalism. Let us introduce a foliation of the spacetime into spacelike hypersurfaces Σ_t, orthogonal to the 4-velocity of the Eulerian observer n^μ. We then express the line element as

$$ds^2 = -(\alpha^2 - \beta_i\beta^i)\, dt^2 + 2\,\beta_i\, dx^i\, dt + \gamma_{ij}\, dx^i\, dx^j, \tag{3.64}$$

where α is the lapse, β^i is the shift vector, and γ_{ij} is the spatial 3-metric. We can define the electric and the magnetic fields as [152]

$$E^\mu = -n_\nu F^{\nu\mu}, \qquad B^\mu = -n_\nu F^{*\nu\mu}, \tag{3.65}$$

where $F^{*\mu\nu} = -\frac{1}{2}\epsilon^{\mu\nu\lambda\sigma}F_{\lambda\sigma}$ is the dual of $F^{\mu\nu}$. The EM tensor can be decomposed as

$$F^{\mu\nu} = n^\mu E^\nu - n^\nu E^\mu + {}^{(3)}\epsilon^{\mu\nu\sigma}B_\sigma, \tag{3.66}$$

where ${}^{(3)}\epsilon^{\mu\nu\sigma} = n_\lambda \epsilon^{\lambda\mu\nu\sigma}$ is the Levi-Civita tensor of the spacelike hypersurface Σ_t. Note that E^μ and B^μ are orthogonal to n^μ and are spacelike vectors on the 3-surfaces Σ_t.

We can define the charge density as $\rho = n_\mu J^\mu$, and the 3-current as ${}^{(3)}J^\mu = h^\mu{}_\nu J^\nu$, where $h^\mu{}_\nu$ is the projection operator onto Σ_t. Finally, we can write the Maxwell equations as [152]

$$D_i E^i = \rho, \tag{3.67}$$

$$D_i B^i = 0, \tag{3.68}$$

$$\partial_t E^i = \mathcal{L}_\beta E^i + \alpha K E^i + [\vec{D} \times (\alpha\vec{B})]^i + \alpha\, {}^{(3)}J^i, \tag{3.69}$$

$$\partial_t B^i = \mathcal{L}_\beta B^i + \alpha K B^i - [\vec{D} \times (\alpha\vec{E})]^i, \tag{3.70}$$

where D_i is the covariant derivative with respect to the 3-metric γ_{ij}, and K_{ij} is the extrinsic curvature. Here the first equation is the Gauss' law, the second equation is equivalent to the absence of magnetic monopoles, and the last two are the evolution equations for the electric and magnetic fields, respectively. The EM 4-current is given by ions and electrons $J^\mu = J^\mu_{\rm (ions)} + J^\mu_{(e)}$. We assume ions to be at rest, due to the fact that $m \ll m_{\rm (ions)}$, so that $J^\mu_{\rm (ions)} = \rho_{\rm (ions)} n^\mu$. For electrons instead we have $J^\mu_{(e)} = -e n_e u^\mu$. Let us decompose u^μ into a component along n^μ, $\Gamma = -n^\mu u_\mu$, and a component on the spatial hypersurfaces, ${}^{(3)}u^\mu = h^\mu{}_\nu u^\nu$. The 4-velocity of the fluid can be written as

$$u^\mu = \Gamma n^\mu + {}^{(3)}u^\mu = \Gamma(n^\mu + \mathcal{U}^\mu)\,, \tag{3.71}$$

where we defined ${}^{(3)}u^\mu = \Gamma \mathcal{U}^\mu$. The above expression allows us to write $\rho = n_\mu J^\mu = \rho_{\rm (ions)} + \rho_{(e)} = \rho_{\rm (ions)} + e n_{EL}$, where $n_{EL} = \Gamma n_e$ is the electron density as seen by the Eulerian observer. The density of ions is constant in time, and will be fixed when constructing the initial data[4]. As $J^\mu_{\rm (ions)}$ is orthogonal to Σ_t, the 3-current ${}^{(3)}J^\mu$ receives only contributions from electrons, and we have ${}^{(3)}J^\mu = -e n_e \Gamma \mathcal{U}^\mu = -e n_{EL} \mathcal{U}^\mu$. Thus, the source terms that appear in Eqs. (3.67)-(3.69) are

$$\rho = \rho_{\rm (ions)} + e n_{EL}, \qquad {}^{(3)}J^\mu = -e n_{EL} \mathcal{U}^\mu. \tag{3.72}$$

Let us now move to Eq. (3.4). Projecting it on n^μ and Σ_t we obtain respectively (see Appendix C for the explicit computation):

$$\begin{aligned}
\partial_t \Gamma &= \beta^i \partial_i \Gamma - \alpha \mathcal{U}^i \partial_i \Gamma + \alpha \Gamma K_{ij} \mathcal{U}^i \mathcal{U}^j \\
&\quad - \Gamma \mathcal{U}^i \partial_i \alpha + \frac{e}{m} \alpha E^i \mathcal{U}_i\,, \qquad (3.73)\\
\partial_t \mathcal{U}^i &= \beta^j \partial_j \mathcal{U}^i - \mathcal{U}^j \partial_j \beta^i - \alpha a^i - \alpha \mathcal{U}^i K_{jl} \mathcal{U}^j \mathcal{U}^l \\
&\quad + \frac{\alpha}{\Gamma} \frac{e}{m} \left(-\mathcal{U}^i E^j \mathcal{U}_j + E^i + {}^{(3)}\epsilon^{ijl} B_l \mathcal{U}_j \right) \\
&\quad + 2\alpha K^i{}_j \mathcal{U}^j + \mathcal{U}^i \mathcal{U}^j \partial_j \alpha - \alpha \mathcal{U}^j D_j \mathcal{U}^i \qquad (3.74)
\end{aligned}$$

Finally, we can write the continuity equation (3.6) as

$$\partial_t n_{EL} = \beta^i \partial_i n_{EL} + \alpha K n_{EL} - \alpha \mathcal{U}^i \partial_i n_{EL} - \alpha n_{EL} \nabla_\mu \mathcal{U}^\mu. \tag{3.75}$$

While the above decomposition is valid for a generic background metric, from now on we will focus on a flat spacetime.

Flat spacetime

We use Cartesian coordinates, so that $g_{\mu\nu} = \eta_{\mu\nu} = \mathrm{diag}\{-1, 1, 1, 1\}$. As a consequence, we have that for any 3-vector ${}^{(3)}V^i = {}^{(3)}V_i$, and

$$\alpha = 1, \qquad \beta^i = 0, \qquad K_{ij} = 0. \tag{3.76}$$

In these coordinates we can write the equations for the EM field as

$$\begin{aligned}
\partial_i E^i &= \rho_{\rm (ions)} + e n_{EL}, \qquad (3.77)\\
\partial_i B^i &= 0, \qquad (3.78)\\
\partial_t E^i &= [\vec{\partial} \times \vec{B}]^i - e n_{EL} \mathcal{U}^i, \qquad (3.79)\\
\partial_t B^i &= -[\vec{\partial} \times \vec{E}]^i, \qquad (3.80)
\end{aligned}$$

---

[4] Note that with the conventions we used, electrons carry *positive* charge, while ions carry *negative* charge.

the evolution equations for Γ and $\mathcal{U}^i$ as

$$\partial_t\Gamma = -\mathcal{U}^i\partial_i\Gamma + \frac{e}{m}E^i\mathcal{U}_i, \tag{3.81}$$

$$\partial_t\mathcal{U}^i = -\mathcal{U}^j\partial_j\mathcal{U}^i + \frac{1}{\Gamma}\frac{e}{m}\Big[-\mathcal{U}^iE^j\mathcal{U}_j + E^i + (\vec{\mathcal{U}}\times\vec{B})^i\Big], \tag{3.82}$$

and the continuity equation as

$$\partial_t n_{EL} = -\mathcal{U}^i\partial_i n_{EL} - n_{EL}\partial_i\mathcal{U}^i. \tag{3.83}$$

Moreover, from the normalization condition that $u^\mu u_\mu = -1$ we can obtain a constraint for Γ and $\mathcal{U}^i$:

$$\Gamma^2(1-\mathcal{U}^i\mathcal{U}_i) = 1. \tag{3.84}$$

3.4.2 Numerical Setup

In this section we discuss our numerical setup, describing the integration scheme and the initialization procedure.

Integration scheme

We evolve $\vec{E}$, $\vec{B}$, Γ, $\vec{\mathcal{U}}$, and n_{EL} with Eqs. (3.79)-(3.83), using the constraints (3.77) and (3.84) to evaluate the convergence of the code. The profile of $\rho_{(\text{ions})}$ is kept constant, consistently with the approximation that ions are at rest. For the numerical integration we used the fourth-order accurate Runge-Kutta algorithm, computing the spatial derivatives with the fourth-order accurate centered finite differences scheme. For simplicity we shall simulate the propagation of *plane* EM wave packets along the z direction, and therefore we will obtain field configurations that are homogeneous along the x and y directions. This feature allows us to impose periodic boundary conditions in the x and y directions, as they preserve the homogeneity of the solution without introducing numerical instabilities. We impose periodic boundary conditions also on the z axis and, in order to avoid the spurious interference of the EM wave packet with itself, we choose grids with extension along z large enough to avoid interaction with spurious reflected waves during the simulations.

Initialization procedure

When constructing the initial data for the simulations we first set the profile of the plasma. We start by setting $\Gamma(t=0,\vec{x}) = 1$ and $\vec{\mathcal{U}}(t=0,\vec{x}) = 0$, so that the plasma is initially at rest. Then, we initialize the profile of n_{EL} with barrier-like shape of the following form:

$$\begin{aligned} n_{EL}(t=0,\vec{x}) &= 2n_{\text{bkg}} - n_{\text{max}} \\ &+ (n_{\text{max}} - n_{\text{bkg}}) \\ &\times \Big[\sigma(z;W_1,z_1) + \sigma(z;-W_2,z_2)\Big], \end{aligned} \tag{3.85}$$

Where $\sigma(z;W,z_0) = (1+e^{-W(z-z_0)})^{-1}$ is a sigmoid function. The qualitative behavior of Eq. (3.85) is shown in Fig. 3.10, where we can see that n_{bkg} is the

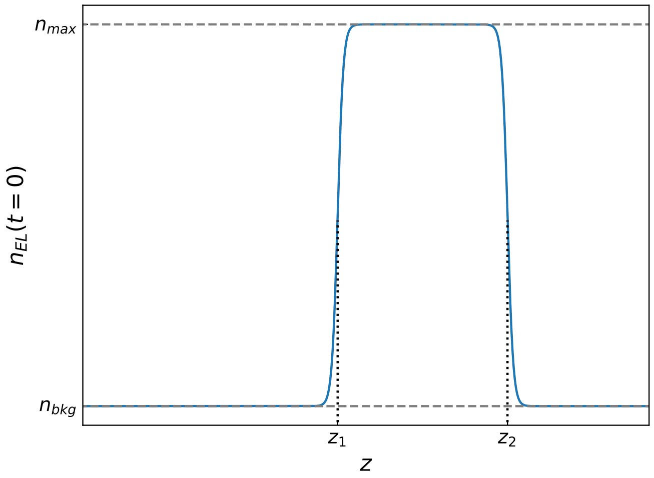

Figure 3.10. Qualitative behavior of the barrier-shaped initial profile for the plasma, Eq. (3.85). $n_{\rm max}$ and $n_{\rm bkg}$ are the values of the plasma density inside the barrier and on the background, while the parameters $z_{1,2}$ and $W_{1,2}$ determine the position and the steepness of the boundaries of the barrier, respectively.

background value of the plasma density and $n_{\rm max}$ is the plasma density at the top of the barrier. The parameters $z_{1,2}$ determine the location and width of the barrier, while the parameters $W_{1,2}$ control its steepness. Note that this profile was chosen to reproduce a very crude toy model of a matter-density profile around a BH [153], where the accretion flow peaks near the innermost stable circular orbit and is depleted between the latter and the BH horizon. In our context this configuration is particularly relevant because EM waves can be superradiantly amplified near the BH and plasma confinement can trigger an instability [108, 114, 115, 116]. Finally, the constant profile of $\rho_{\rm (ions)}$ is determined by imposing that the plasma is initially neutral, so that $\rho_{\rm (ions)}(t=0,\vec{x}) = -en_{EL}(t=0,\vec{x})$. Once the profile of the plasma has been assigned we proceed to initialize the EM field. We consider a circularly polarized wave packet moving forward in the z-direction:

$$\vec{E} = A_E \begin{pmatrix} \cos[k_z(z-z_0)] \\ \sin[k_z(z-z_0)] \\ 0 \end{pmatrix} e^{-\frac{(z-z_0)^2}{2\sigma^2}}, \tag{3.86}$$

$$\vec{B} = A_E \frac{k_z}{\omega} \begin{pmatrix} -\sin[k_z(z-z_0)] \\ \cos[k_z(z-z_0)] \\ 0 \end{pmatrix} e^{-\frac{(z-z_0)^2}{2\sigma^2}}, \tag{3.87}$$

where A_E is the amplitude of the wave packet, σ is its width, z_0 its central position, ω is the frequency, and $k_z = \sqrt{\omega^2 - \omega_{\rm pl}^2}$, where $\omega_{\rm pl} = \sqrt{\frac{e^2\, n_{\rm bkg}}{m}}$ is the plasma frequency computed using $n_{\rm bkg}$, as the wave packet is initially located outside the barrier (i.e., $\sigma \ll z_1 - z_0$).

3.4.3 Results

Here we present the results of our numerical simulations of nonlinear plasma-photon interactions in different configurations. We shall consider a low-frequency, circularly polarized wave packet propagating along the z direction and scattering off the plasma barrier with the initial density profile given by Eq. (3.85).

Linear regime

As a consistency check of our code, we tested that for sufficiently low amplitude waves our simulations are in agreement with the predictions of linear theory. We set units such that $e = m = 1$ and consider an initial wave packet of the electric field centered at $z_0 = 0$, with a characteristic width $\sigma = 5$. We also set $\omega = 0.5$ and $A_E = 10^{-6}$, so that the evolution can be described by the linear theory. The plasma barrier was situated between $z_1 = 40$ and $z_2 = 100$, and we set $W_1 = W_2 = 1$. The background density of the plasma was $n_{\rm bkg} = 0.01$ so that $\omega_{\rm pl}^{(\rm bkg)} = 0.1$ and all the frequency content of the EM wave is above the plasma frequency of the background. We run 6 simulations with $n_{\rm max} = \{n_{\rm bkg}, 0.25, 0.5, 0.75, 1, 1.25\}$, that correspond to plasma frequencies at the top of the barrier $\omega_{\rm pl}^{(\rm max)} = \{0.1, 0.5, 0.707, 0.866, 1, 1.12\}$, respectively, and fall in different parts of the frequency spectrum of the EM wave packet. In the linear regime, we expect that the frequency components above $\omega_{\rm pl}^{(\rm max)}$ will propagate through the plasma barrier, while the others will be reflected, and this setup allows us to clearly appreciate how this mechanism takes place. In all these simulations we used a grid that extends in $[-1, 1] \times [-1, 1] \times [-450, 450]$, with a grid step $\Delta x = \Delta y = \Delta z = 0.2$ and a time step $\Delta t = 0.1$, so that the Courant-Friedrichs-Lewy factor is CFL $= 0.5$ The final time of integration was set to $T = 400$. Figure 3.11 shows some snapshots of the numerical results at different times for different values of $\omega_{\rm pl}^{(\rm max)}$. It is evident that the analytical predictions of linear theory are confirmed: as the plasma frequency of the barrier increases, less and less components are able to propagate through it and reach the other side. In particular, when $\omega_{\rm pl}^{(\rm max)} \gtrsim 0.9$ the wave is almost entirely reflected, and the transmitted component becomes negligible. Furthermore, in the linear regime the backreaction on the density is effectively negligible, as the barrier remains constant over the entire simulation (in fact, we observed a maximum variation of n_{EL} of the order of 10^{-11}, which is clearly not appreciable on the scale of Fig. 3.11).

To better quantify the frequency components that are propagated and the agreement between the simulations and the analytic expectation in the linear regime, we computed the (discrete) Fourier transform of the time evolution of E^x in two points along the z axis: $z = -50$ and $z = 150$, which are located before and after the plasma barrier, respectively. Figure 3.12 shows the absolute value of the Fourier transform for the different values of the plasma frequency in the barrier, which are represented as vertical dotted lines. As we can see from the Fourier transform at $z = 150$, the transmitted waves have only components with frequency $\omega > \omega_{\rm pl}^{(\rm max)}$, in agreement with the fact that only modes above this threshold can propagate. Hence, the barrier perfectly acts as a high-pass filter, with a critical threshold given by the plasma frequency.

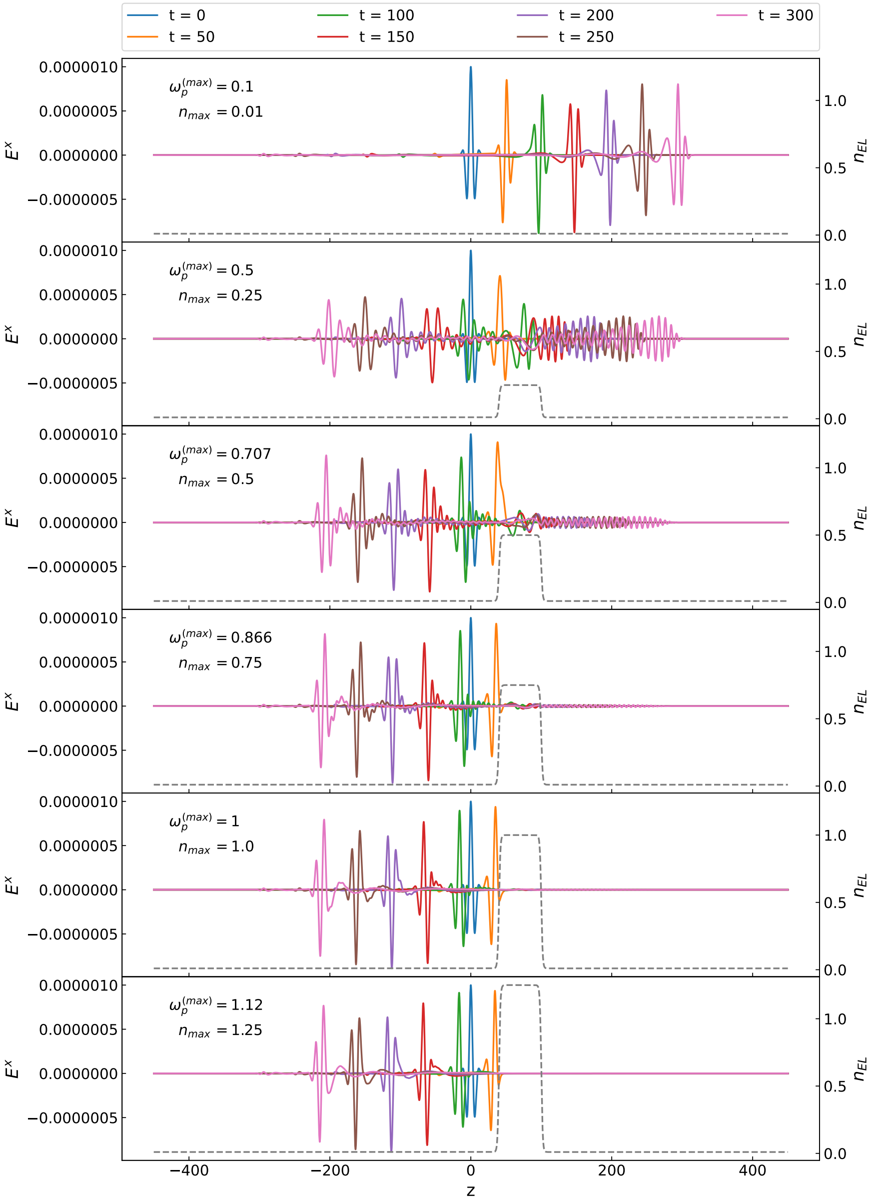

Figure 3.11. Propagation of an EM wave packet on a barrier of plasma in the linear regime. Here we show some snapshots of the evolution of E^x for different values of the plasma density in the barrier, $n_{\rm max}$, and we represent the initial profile of n_{EL} with a gray dashed line. When the plasma frequency in the barrier $\omega_{\rm pl}^{(\rm max)}$ becomes larger than ω, the wave packet is mostly reflected by the barrier, while the transmitted component is suppressed. The corresponding animations are available online [154].

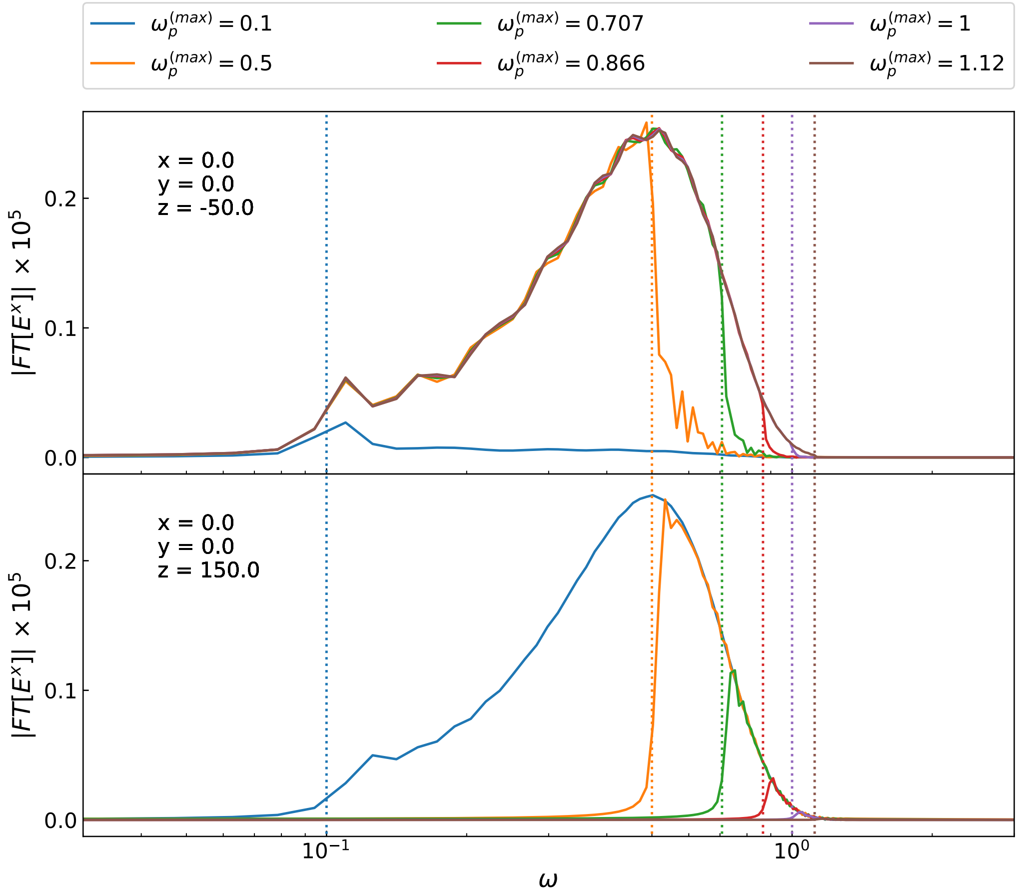

Figure 3.12. Absolute value of the discrete Fourier transform of E^x extracted before (upper panel) and after (lower panel) the plasma barrier. The different colors refer to the different values of the plasma density inside the barrier, and hence to different values of the plasma frequency $\omega_{\rm pl}^{(\rm max)}$, indicated with vertical dotted lines. We can clearly see that the barrier reflects the frequency components below $\omega_{\rm pl}^{(\rm max)}$, and transmits the components above it.

Nonlinear regime

We can now proceed to increase the amplitude of the field until linear theory breaks down and the interaction becomes fully nonlinear. As anticipated, we shall show that the evolution is more involved than in the idealized model described in [150]. Indeed, even from a first qualitative analysis, it is evident from the z-component of the momentum equation (3.82) that in the nonlinear regime electrons will experience an acceleration along the z axis due to the nonlinear Lorentz term $(\vec{\mathcal{U}} \times \vec{B})^z$. The formation of a current along the z directions implies a modification of the density profile because of the continuity equation, and also the formation of a longitudinal electric field that tries to balance and preserve charge neutrality. In the following, we will support this qualitative analysis with the results of the numerical simulations and show that nonlinear effects can have a dramatic impact on the system dynamics.

In this set of simulations, we set units[5] such that $e = 1$ and $m = 1000$, and we consider an initial wave packet of the electric field centered at $z_0 = -150$, with a width[6] $\sigma = 100$ and $\omega = 0.001$. We vary the amplitude of the EM in a range $0.1 \leq A_E \leq 1000$. As for the plasma profile, we adopt a similar geometric model to the linear case, with the barrier placed between $z_1 = 100$ and $z_2 = 650$, with $W_1 = W_2 = 0.1$. We consider a background density $n_{\rm bkg} = 5 \times 10^{-6}$, and a maximum barrier density $n_{\rm max} = 0.5$, that corresponds to a plasma frequency of $\omega_{\rm pl}^{(\rm max)} = 0.022$. We use a numerical grid that extends in $[-2, 2] \times [-2, 2] \times [-750, 850]$, with a grid spacing $\Delta x = \Delta y = \Delta z = 0.2$, and a time step $\Delta t = 0.1$, so that CFL $= 0.5$. The final time of integration was set to $T = 500$.

The parameters are chosen such that the frequency of the wave packet is always much larger than $\omega_{\rm pl}^{(\rm bkg)}$, but a significant component of the spectrum, namely $\approx 97.5\%$, is below the plasma frequency of the barrier, and should therefore be reflected if one assumes linear theory. First of all, we quantify the value of the electric field which gives rise to nonlinearities. A crucial parameter that characterizes the threshold of nonlinearities in laser-plasma interactions is the peak amplitude of the normalized vector potential, defined as $a_0 = e\mathbf{A}/m$ (see e.g. [155, 156]). Specifically, when $a_0 \gtrsim 1$, electrons acquire a relativistic transverse velocity, and therefore the interactions become nonlinear. Given our units, and estimating $A \approx E/\omega$, we obtain a critical electric field $E_{\rm crit} \gtrsim m\omega/e \approx 1$.

We performed a set of simulations choosing different values of the initial amplitude of the EM wave packet in the range $0.1 \leq A_E \leq 1000$. Figure 3.13 shows snapshots of the numerical simulations for some selected choices of A_E. It is possible to observe that in the case $A_E = 1$ (top panel) the density profile of plasma is not altered throghout all the simulation, as in the linear case discussed in the previous section. Moreover, at sufficiently long times, the wavepacket is reflected by the barrier, in agreement with linear theory predictions. From the second panel on (i.e.

---

[5] Note that, in rationalized Heaviside units, changing m (and hence the classical electron radius) simply accounts for rescaling lengths, times, and masses in the simulations. Lengths and times are rescaled by $[m]^{-1}$, while the electric field amplitude scales as $[m]^2$. Hence, the results of this section can be obtained in the case $m = 1$ by rescaling the other quantities accordingly.

[6] While formally the initial profile of the EM field, Eq. (3.87), represents a circularly polarized wave packet, the chosen value of the parameter σ reduces the y component of the electric field, making the polarization effectively elliptic.

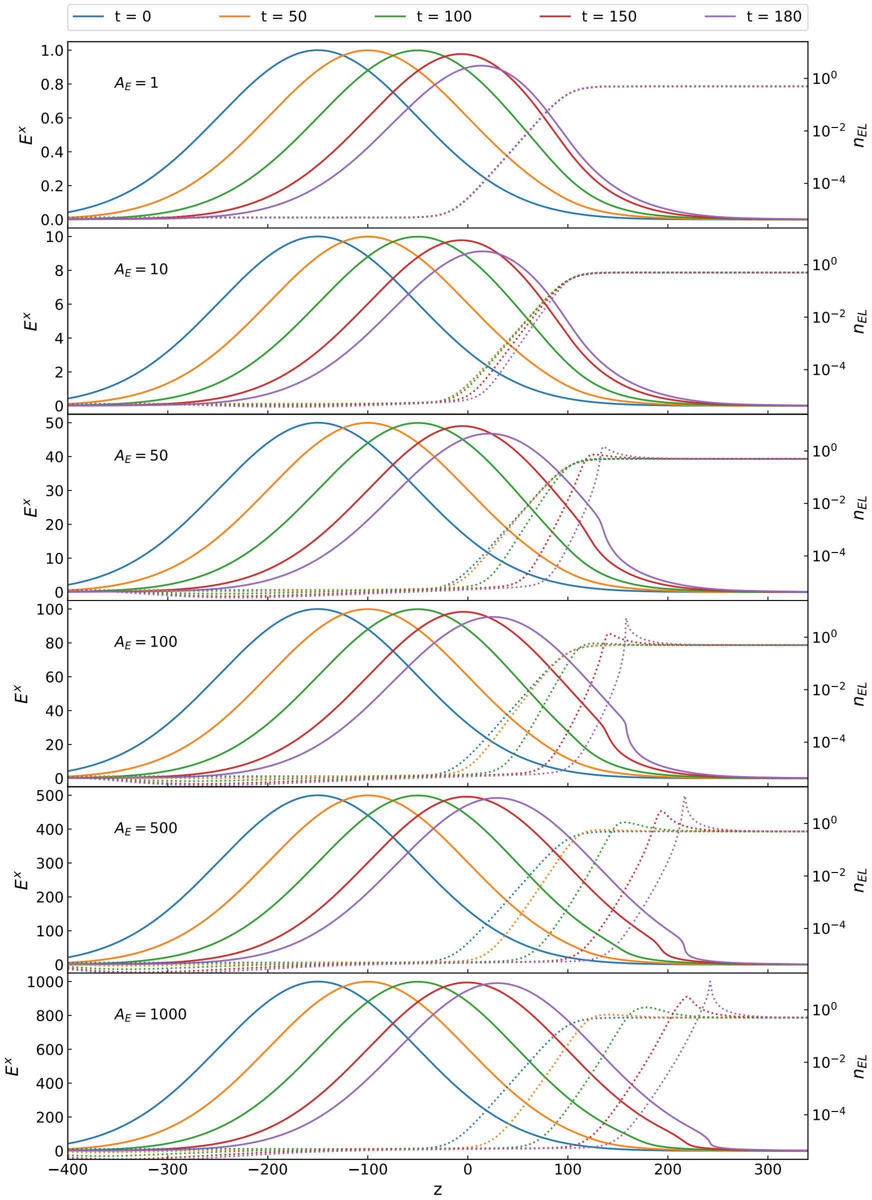

Figure 3.13. Snapshots of the evolution of E^x (solid line) and n_{EL} (dashed lines) for the simulations of the propagation of an EM wave packet inside a plasma barrier in the nonlinear regime. The initial profile of n_{EL} is not varied across the simulations, and the different panels refer to different choices of the initial amplitude of the wave packet. The backreaction effects of the EM field onto the plasma density increase with A_E, and for $A_E \gtrsim 50$ wave packet "transports" electrons along the z axis, eventually creating a plasma-depleted region (*blowout regime*). The corresponding animations are available online [154].

as $A_E \gtrsim 10$), instead, the wavepacket induces a nonnegligible backreaction on the plasma density. This effect increases significantly for higher amplitudes, and it is due to the nonlinear couplings between transverse and longitudinal polarizations: the nonlinear Lorentz term $(\vec{\mathcal{U}} \times \vec{B})^z$ in the longitudinal component of the momentum equation (3.82) induces a radiation pressure on the plasma, and hence a longitudinal velocity $\vec{\mathcal{U}}^z$; as electrons travel along the z direction and ions remain at rest, a large longitudinal field due to charge separation is created, which tries to balance the effect of the Lorentz force and restore charge neutrality. This phenomenology resembles the one of plasma-based accelerators, where super-intense laser pulses are used to create large longitudinal fields that can be used to accelerate electrons [157].

To quantify the collective motion induced by nonlinearities we computed the velocity dispersion of electrons as

$$\sqrt{\langle \mathcal{U}^2 \rangle} = \sqrt{\frac{\int_V d^3x \, n_{EL} \, \mathcal{U}_i \mathcal{U}^i}{\int_V \, d^3x \, n_{EL}}}. \tag{3.88}$$

Since the field are constant along the transverse directions[7], then $n_{EL}(x, y, z) = n_{EL}(z)$ and $\mathcal{U}^i(x, y, z) = \mathcal{U}^i(z)$. This allows us to evaluate the above integral as

$$\sqrt{\langle \mathcal{U}^2 \rangle} = \sqrt{\frac{\int_{z_{-\infty}}^{z_{+\infty}} dz \, n_{EL}(z) \, \mathcal{U}_i(z) \mathcal{U}^i(z)}{\int_{z_{-\infty}}^{z_{+\infty}} \, dz \, n_{EL}(z)}}, \tag{3.89}$$

where $z_{\pm\infty}$ are the boundaries of the z domain and we compute the integral using the trapezoidal rule. In the upper panel of Fig. 3.14 we plot the behavior of the velocity dispersion with respect to the initial amplitude A_E for different times. As we can see the nonlinearities start becoming relevant in the range $1 \lesssim A_E \lesssim 10$, where electrons start to acquire a collective motion. This is also confirmed by the middle panel, where the solid and dashed lines denote the maximum of $|\vec{\mathcal{U}}|$ and $\mathcal{U}^z$, respectively. While these quantities do not represent the collective behavior of the system, they have the advantage of not containing the contribution given by the portion of the plasma barrier that has not been reached yet by the EM wave. From this plot we can observe that in the range $1 \lesssim A_E \lesssim 10$, the electrons start acquiring a relativistic velocity with a large component on the transverse plane.

As already mentioned, the longitudinal motion of electrons generate a longitudinal field. Nevertheless, plasmas can sustain longitudinal fields only up to a certain threshold, usually called *wave-breaking (WB) limit*, above which plasma is not able to shield and sustain anymore electric fields, and the fluid description breaks down. This phenomenon was pioneered in [158] for the case of nonlinear, nonrelativistic cold plasmas, where the critical longitudinal field for WB was found to be $E^z_{\rm WB} = m\omega_{\rm pl}/e$, and later generalized for pulses with relativistic phase velocities [159]. This threshold field represents the limit after which the plasma response loses coherence as neighbouring electrons start crossing each other within one plasma frequency period. Therefore, above this critical electric field the plasma is not anymore able to coherently act as a system of coupled oscillators, and the fluid model based on collective effects breaks down. This leads to the formation of a spike in n_{EL}, which

---

[7] In Appendix D.2 we show how the homogeneity of the fields along the transverse plane is preserved during the evolution.

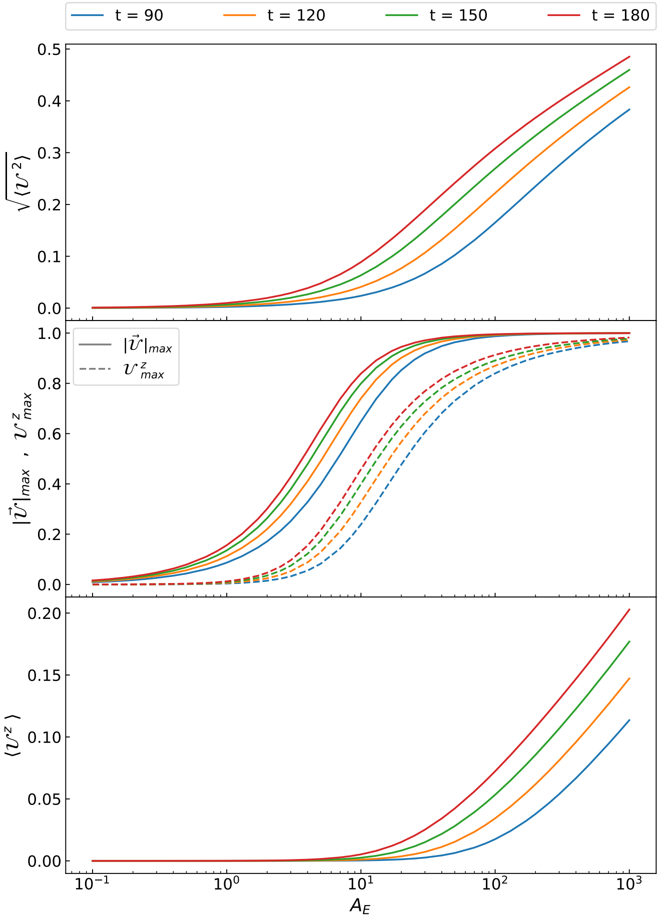

Figure 3.14. Collective behavior of plasma in the nonlinear regime as a function of the initial amplitude A_E of the EM wavepacket. The upper panel shows the velocity dispersion $\sqrt{\langle \mathcal{U}^2 \rangle}$, the middle panel shows the maximum value of $|\vec{\mathcal{U}}|$ (solid lines) and of the longitudinal velocity $\mathcal{U}^z$ (dashed lines), while the lower panel shows the collective longitudinal velocity $\langle \mathcal{U}^z \rangle$. The nonlinearities start becoming relevant in the range $1 \lesssim A_E \lesssim 10$, where the velocity dispersion increases and the motion of electrons has a large component on the transverse plane. For $A_E \gtrsim 10$ the plasma enters in the blowout regime, where electrons are "transported" by the EM field, and acquire a positive collective longitudinal velocity.

eventually diverges, and to a steepening of the longitudinal component of the electric field. Full particle-in-cell numerical simulations are required after the breakdown (see, e.g., [160, 161]). In our simulations, we observe the WB phenomenon at late time for large values of the electric field, in which cases we can only extract information before the breakdown of the model.

In order to better appreciate how the WB takes place, we repeated the simulation with $A_E = 1$ for a longer integration time and a larger grid. In the upper panel of Fig. 3.15 we show the evolution of E^x (solid lines) throughout all the simulation, where we can clearly see that the incoming wave packet is reflected by the plasma barrier. However, for $t \approx 700$, the longitudinal component of $\vec{\mathcal{U}}$ leads to an evolution of the plasma density. In this stage the plasma loses coherence and n_{EL} develops local spikes that increase in height and becomes sharper with time. When one of these spikes becomes excessively narrow, the fluid description of the system breaks down and the simulation crashes. This can be observed from the bottom panel of Fig. 3.15, where we show the longitudinal component of $\vec{E}$ together with the plasma density profile. Note that WB occurs as soon as the nonlinearities come into play (we observed it already for $A_E = 1$), and the fluid description in the nonlinear regime cannot be used for long-term numerical simulations. However the good convergence of the code even slightly before WB takes place (see Appendix D.1) ensures the reliability of the results up to this point.

Overall, Figs. 3.13 and 3.15 show that for $A_E \sim 1$ the system becomes weakly nonlinear, in agreement with the previously mentioned analytical estimates.

Going back to the snapshots of the evolutions in Fig. 3.13, we now wish to analyze the behavior of the system for larger electric fields, where the backreaction is macroscopic. We can see that in this case, i.e. for $A_E \gtrsim 50$, all the electrons in the plasma barrier are "transported" in the z direction and piled up within a plasma wake whose density grows over time. This corresponds to a *blowout regime* induced by radiation pressure. In order to better describe how the system reaches this phase, we can compute the longitudinal component of the collective electron velocity as

$$\langle \mathcal{U}^z \rangle = \frac{\int_V d^3x \, n_{EL} \, \mathcal{U}^z}{\int_V d^3x \, n_{EL}} = \frac{\int_{z-\infty}^{z+\infty} dz \, n_{EL}(z) \, \mathcal{U}^z(z)}{\int_{z-\infty}^{z+\infty} dz \, n_{EL}(z)}, \tag{3.90}$$

where, again, we took advantage of the homogeneity of the system along the transverse direction to reduce the dimensionality of the domain of integration. The results are shown in the lower panel of Fig. 3.14, where we can see that for $A_E \lesssim 10$, the longitudinal momentum remains low and is not influenced by the wavepacket. For $A_E \gtrsim 10$ instead, $\langle \mathcal{U}^z \rangle$ starts to increase in time, indicating that the system is in the blowout regime, as electrons are collectively moving forward in the z direction.

Overall, the above analysis shows that when the idealized situation studied in [150] cannot be applied and the nonlinear Lorentz term does not vanish, the general physical picture is drastically different and that penetration occurs in this setup due to radiation-pressure acceleration rather than transparency.

3.4.4 Implication for the instability and conclusions

Motivated by exploring the plasma-driven superradiant instability of accreting BHs at the full nonlinear level, we have performed $3+1$ numerical simulations of a plane

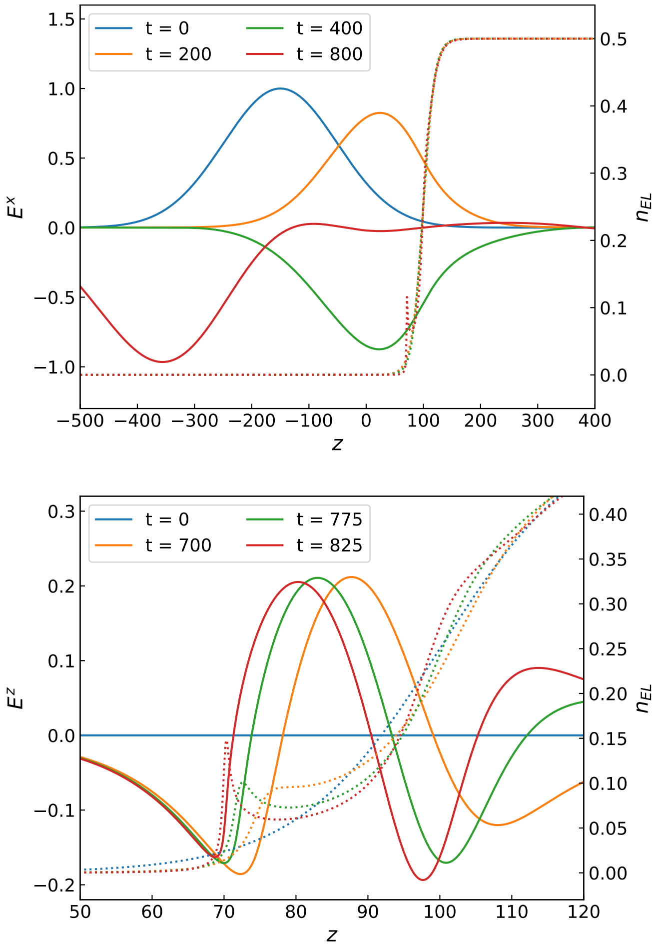

Figure 3.15. Evolution of the electric field and plasma density in the case of $A_E = 1$. Upper panel: snapshots of E^x (solid lines) and n_{EL} (dotted lines) of the full evolution, where we can see that the wave packet is mostly reflected by the plasma barrier. Lower panel: snapshots of the longitudinal component E^z (solid lines) and n_{EL} (dotted lines) focusing on the last stages of evolution. Here we can clearly see the WB phenomenon taking place, with the plasma density developing spikes in regions where the longitudinal component of the electric field increases steeply.

wave of very large amplitude but small frequency scattered off an inhomogeneous plasma barrier. Although nonlinear plasma-photon interactions are well studied in plasma-physics applications, to the best of our knowledge this is the first analysis aimed at exploring numerically this interesting setup in generic settings.

One of our main findings is the absence of the relativistic transparency effect in our simulations. As already mentioned, the analysis performed in [150] showed that, above a critical electric field, plasma turns from opaque to transparent, thus enabling the propagation of EM waves with frequency below the plasma one. From Eq. (3.63), such critical electric field for transparency is $E_{\rm crit}^{\rm transp} = \frac{m}{e}\sqrt{\omega_{\rm pl}^2 - \omega^2}$. In our simulations, we considered electric fields well above this threshold, yet we were not able to observe this effect. On the contrary, in the nonlinear regime the plasma strongly interacts with the EM field in a complex way. The role of relativistic transparency in more realistic situations than the one described in [150] was rarely considered in the literature and is still an open problem [162]. Nevertheless, some subsequent analysis found a number of interesting features, and revealed that its phenomenology in realistic setups is more complex.

In Ref. [151] an analytical investigation of a similar setup was performed by considering the scattering between a laser wavepacket and a sharp boundary plasma. The conclusion of the analysis is that, when plasma is inhomogeneous, nonlinearities tend to create a strong peaking of the plasma electron density (and hence of the effective plasma frequency), suppressing the laser penetration and enhancing the critical threshold needed for transparency. Subsequently, Refs. [163, 164] confirmed this prediction numerically, and showed that in a more realistic scenario transparency can occur but the phenomenology is drastically different from the one predicted in [150]. For nearly-critical plasmas, transparency arises due to the propagation of solitons, while for higher densities the penetration effect holds only for finite length scales. Nevertheless, these simulations were performed by considering a simplified momentum equation due to the assumption of a null-vorticity plasma, which is typically suitable for unidimensional problems, but likely fails to describe complex-geometry problems as the one of superradiant fields. Using particle-in-cell simulations, it was then realized that radiation-pressure can push and accelerate the fluid to relativistic regimes, similarly to our results, and produce interesting effects such as hole-boring, ion acceleration, and light-sail [165, 166].

While the complicated interplay between relativistic transparency and radiation-pressure acceleration is still an open problem [162, 167], we argue that the latter, which arises in generic situations with very overdense plasmas and high amplitude electric fields, is sufficient to dramatically quench the plasma-driven superradiant instability. To enforce this conclusion, we provide a rough estimate of the total energy extracted from the BH before nonlinear effects take place [137]. In order for the instability to be efficient on astrophysical timescales, $\omega \lesssim \omega_{\rm pl} \approx O(1/(GM))$, where G is Newton's constant and M is the BH mass [115]. This gives a critical electric field

$$E_{\rm crit} = \frac{m\omega}{e} \approx 4 \times 10^5 \frac{\rm V}{\rm cm}\Big(\frac{M_\odot}{M}\Big) \tag{3.91}$$

The associated total energy can be estimated as $U = E_{\rm crit}^2 L^3$, where L is the size of the condensate formed by the superradiant instability, and corresponds to the location of the plasma barrier. This gives

$$U \approx 10^7 \mathrm{J}\Big(\frac{M}{M_\odot}\Big)\Big(\frac{L}{6M}\Big)^3 \tag{3.92}$$

where we assumed that the peak of the plasma barrier roughly corresponds to the location of the peak density of an accretion disk, $L \approx 6M$. On the other hand, the total rotational energy of the BH is given by $K = MR^2\Omega^2$, where R and Ω are the radius and the angular velocity of the horizon, respectively. To efficiently satisfy the superradiant condition, $\Omega \gtrsim \omega_{\rm pl} \approx \mathcal{O}(1/(GM))$, so that

$$K \approx 10^{43} \mathrm{J}\Big(\frac{M}{M_\odot}\Big)\,. \tag{3.93}$$

Therefore, when the electric field reaches the threshold for nonlinearities, the total energy extracted from the BH is tiny, $U/K \approx 10^{-36}$.

Another argument supporting this conclusion is that, for the superradiant instability to be sustainable, the maximum energy leakage of the confining mechanism cannot exceed the superradiant amplification factor of the BH. For EM waves, the maximum amplification factor (for nearly extremal BHs and fine-tuned frequency) does not exceed $\approx 4\%$ and is typically much smaller [30]. Therefore, the instability is not quenched only if the plasma is able to confine more than 96% of the EM field energy. Our simulations shows that in the nonlinear regime the situation is quite the opposite: almost the entirety of the EM field is not confined by the plasma, thus destroying its capability to ignite the instability. We expect this argument to be valid also when $\omega_{\rm pl} \gg \omega$, in which case plasma depletion through blowout is negligible, but the EM field can still transfer energy into longitudinal plasma motion.

Note that the arguments above are extremely conservative, since are based on a number of optimistic assumptions that would maximize the instability. First of all, realistic accretion flows around BHs are not spherical nor stationary, especially around spinning BHs. This would generically introduce mode-mixing and decoherence, rendering the instability less efficient. More importantly, even in the linear regime a disk-shape accretion geometry can (partially) confine modes that are mostly distributed along the equatorial plane, but would naturally provide energy leakage along off-equatorial directions [168, 116]. Finally, a sufficiently high plasma density in the corona could quench photon propagation in the first place [115], at least at the linear level during the early stages of the instability.

Chapter 4

Dark Photon Superradiance quenched by dark matter

Summary

Black-hole superradiance has been used to place very strong bounds on a variety of models of ultralight bosons such as axions, new light scalars, and dark photons. It is common lore to believe that superradiance bounds are broadly model independent and therefore pretty robust. In this section we show however that superradiance bounds on dark photons can be challenged by simple, compelling extensions of the minimal model. In particular, if the dark photon populates a larger dark sector and couples to dark fermions playing the role of dark matter, then superradiance bounds can easily be circumvented, depending on the mass and (dark) charge of the dark matter.

4.1 Dark photon superradiance in an extended dark sector

Until recently, studies of the superradiant instability assumed that the superradiant field was free from interactions, as expected for a field only minimally coupled to gravity. However, as number densities can reach extreme values in the process, the effect of interactions can be crucial, even for very weakly interacting fields. Recent studies have considered the effect of self-interactions, both for scalar and vector fields [169, 170], axion-photon couplings [171, 172], interactions with astrophysical plasmas [108, 107, 138, 115, 173, 174, 116], and models of DPs kinetically mixed with Standard Model photons [175, 176].

In this section, we consider the interaction of a (vector) superradiant field with other (fermionic) fields in the dark sector, which constitute the entirety or just a fraction of the dark matter (DM). In other words, we consider an extended dark sector, populated not only by a massive DP, but also by dark fermions.

The new dark fermions constitute a dark plasma, which can alter the dispersion relation of the DP and possibly affect its superradiant instability. Intuitively, in analogy to the already discussed SM case (see chapter 3), the presence of a dark fermion should generate a gap in the dispersion relation of the DPs, effectively endowing it with a plasma mass

$$\omega_{\rm pl}^{\chi} = \left(\frac{4\pi\alpha_\chi\rho_\chi}{m_\chi^2}\right)^{1/2} , \tag{4.1}$$

where ρ_χ is the energy density of the dark fermions, m_χ its mass, and $\alpha_\chi = q_\chi^2/(4\pi)$ the fine structure constant within the dark sector.

We assess the effect of an extended dark sector on the superradiant instability by studying quasibound states around nonspinning BHs. We solve numerically for the (linear) quasibound states of a DP in the presence of a dark plasma and we find – as expected – that the interaction with a (sufficiently dense) dark plasma can significantly alter the lifetime of quasibound states. Extrapolated to spinning BHs, our results indicate that superradiant bounds on DPs can be completely invalidated in motivated models granting a DM candidate. In the following, we will show that simple models of $\sim$ TeV self-interacting DM (SIDM) [26], can generate $\omega_{\rm pl}^{\chi} \simeq 10^{-13} - 10^{-14}\,$eV around the BH and make the superradiance timescale much longer than other astrophysical timescales, such as the accretion one, thus invalidating some of the current DP bounds. Note that, because the superradiance instability is quenched by the presence of the dark plasma, backreaction due to the cloud can be safely neglected, justifying our linear analysis.

4.2 Setup

In the following, we will consider a massive spin-1 field coupled to a dark fermion current. The dark sector is then described by the Lagrangian

$$\mathcal{L} = -\frac{1}{4}F_{\mu\nu}F^{\mu\nu} - \frac{1}{2}\mu^2 V_\mu V^\mu - J_\mu V^\mu , \tag{4.2}$$

where V^ν is the DP field, $F^{\mu\nu} = \nabla^\mu V^\nu - \nabla^\nu V^\mu$ is the field strength, μ is the DP mass and J^μ is the dark sector current. We assume that the dark sector is secluded from the Standard Model. For instance, we assume that the kinetic mixing between dark and ordinary photons is sufficiently small that we can neglect it.

Varying the action leads to a Proca equation sourced by the dark current:

$$\nabla_\mu F^{\nu\mu} + \mu^2 V^\nu = q_\chi n u^\nu + J_2^\nu , \tag{4.3}$$

where n is the density of the fermions, q_χ is their dark charge, u^μ is their four-velocity, and J_2^ν is the current of a second species which we assume to be present to neutralize the plasma. Note that deriving Eq. (4.3) and using the conservation of the currents leads to the Lorenz condition $\nabla_\mu V^\mu = 0$. The Proca equation must be solved jointly with the momentum equation describing the motion of the dark fermions

$$u^\mu \nabla_\mu u^\nu = \frac{q_\chi}{m_\chi} F^{\nu\mu} u_\mu , \tag{4.4}$$

where m_χ is the fermion mass. The conservation of the current also implies the continuity equation

$$\nabla_\mu (n u^\mu) = 0 . \tag{4.5}$$

We will solve the system perturbatively by considering small perturbations for the DP field, the density and four velocity of the dark plasma (i.e. $F_{\mu\nu} = F_{\mu\nu}^{\rm background} + \tilde{F}_{\mu\nu}$ and the same for n and u^μ). In order to simplify the problem, we neglect the perturbations in the second, oppositely charged species, $\tilde{J_2}^\mu = 0$, in analogy to the standard case of an electron-ion plasma. The presence of a second fermion would only shift the (dark) plasma frequency, with the exact amount depending on its mass and background density. Given the uncertainties in other parameters, we can re-absorb this shift in the following definition of the plasma frequency for one species.[1] We will also neglect higher order perturbations and the backreaction of the field on the metric, as they are negligible, at least during the first stages of the superradiant instability. The perturbed equations of motion are

$$\nabla_\mu \tilde{F}^{\nu\mu} + \mu^2 \tilde{V}^\nu = q_\chi \tilde{n} u^\nu + q_\chi n \tilde{u}^\nu \,, \tag{4.6}$$

$$\tilde{u}^\mu \nabla_\mu u^\nu + u^\mu \nabla_\mu \tilde{u}^\nu = \frac{q_\chi}{m_\chi} \tilde{F}^{\nu\mu} u_\mu + \frac{q_\chi}{m_\chi} F^{\nu\mu} \tilde{u}_\mu \,, \tag{4.7}$$

$$\tilde{u}^\mu u_\mu = 0 \,, \tag{4.8}$$

$$\nabla_\mu \tilde{V}^\mu = 0 \,. \tag{4.9}$$

As in the SM case, following the procedure outlined in Refs. [129], this set of equations can be reassembled into a third-order, differential master equation. We report the details of this procedure applied to our system in Appendix E. The master equation for the linear perturbations of the DP field in the presence of a moving, magnetised (or not) plasma reads

$$\begin{aligned} & h^\xi{}_\alpha u^\mu \nabla_\mu (\nabla_\sigma \tilde{F}^{\alpha\sigma} + \mu^2 \tilde{V}^\alpha) \\ & + (\theta^\xi{}_\alpha + \omega^\xi{}_\alpha + \theta h^\xi{}_\alpha + \omega_L{}^\xi{}_\alpha)(\nabla_\sigma \tilde{F}^{\alpha\sigma} + \mu^2 \tilde{V}^\alpha) \\ & + \frac{q_\chi}{m_\chi} E^\xi u_\alpha (\nabla_\sigma \tilde{F}^{\alpha\sigma} + \mu^2 \tilde{V}^\alpha) = {\omega_{\rm pl}^\chi}^2 \tilde{F}^{\xi\mu} u_\mu \,, \end{aligned} \tag{4.10}$$

where $\omega_{\rm pl}^\chi$ is the dark plasma frequency defined in Eq. (4.1), while $E^\alpha, \omega_L^{\alpha\beta}, \omega^{\alpha\beta}$ and $\theta^{\alpha\beta}$ are the background electric field, Larmor tensor, vorticity and deformation defined in analogy to the previous section. As anticipated, both the bare DP mass and the “effective" plasma mass (4.1) appear in this equation. It is straightforward but important to verify that

- in the $\omega_{\rm pl}^\chi \to 0$ limit, Eq. (4.10) reduces to the vacuum Proca equation,

$$\nabla_\sigma \tilde{F}^{\sigma\alpha} = \mu^2 \tilde{V}^\alpha \,; \tag{4.11}$$

- in the $\mu \to 0$ limit, Eq. (4.10) matches the one for the Standard Model photon in a cold plasmic medium on an arbitrary spacetime background [129] and introduced in the previous section (3.11), once we identify the field and the plasma with the Standard Model ones.

---

[1] For the vanilla DM model we will discuss in Section 4.5, the situation is actually very similar to that of an electron-positron plasma, with the two species of opposite charges having the same mass [26]. In this case the change in the dark plasma frequency should roughly be a factor $\sim \sqrt{2}$ [177].

Also, it is important to notice that Eq. (4.10) is a third-order differential equation, at variance with the vacuum Proca case, and that it depends on the background plasma configuration.

4.3 Equations a in Schwarzschild spacetime

We now specialize to the Schwarzschild background. As in the previous chapter, assuming that the background plasma is also spherically symmetric, it is convenient perform a multipolar expansion of the dark EM field as

$$\tilde{V}_\mu(r,t,\theta,\phi) = \frac{1}{r}\sum_{i=1}^{4}\sum_{l,m} c_i u^{lm}_{(i)}(t,r) Z^{(i)lm}_\mu(\theta,\phi), \tag{4.12}$$

where $Z^{(i)lm}_\mu$ are the vector spherical harmonics (3.14)-(3.17).

The behavior of the DP perturbations depends on the plasma profile through the dark plasma frequency $\omega^\chi_{\rm pl}$. In the following, we consider two different configurations: a static plasma, and a plasma in free fall. A static plasma is not a realistic configuration, especially in the vicinity of the BH horizon, but its perturbation equations take a simple form, allowing us to understand the interplay between bare and effective masses analytically. Studying two plasma configurations will also allow us to explore the dependence of the quasibound states on the background plasma four-velocity.

Static plasma

Using the decomposition (4.12) and working in the frequency domain, $u^{lm}_{(i)}(t,r) = u^{lm}_{(i)}(r)e^{-i\omega t}$, we obtain a set of three equations from the radial and angular components of Eq. (4.10). Using the Lorenz condition, it is possible to close the system and rewrite the field equations in a more straightforward way. We give here the final form of the perturbation equations, and a detailed derivation in Appendix F.1. By analogy with the previous section, we can introduce the differential operator $\mathcal{D} \equiv \frac{d^2}{dr_*^2} + \omega^2 - f\left(\frac{l(l+1)}{r^2} + \mu^2\right)$[2], so that the equations read

$$\begin{aligned}
\mathcal{D}\ u_{(2)} =& \frac{1}{r^3(\omega^2 - f{\omega^\chi_{\rm pl}}^2)} f((2(-3M+r)\omega^2 \\
&+ f(6M + r(-2 + l(l+1) + r^2\mu^2)){\omega^\chi_{\rm pl}}^2)u_{(2)} \\
&+ 2(3M - r)(\omega^2 - f{\omega^\chi_{\rm pl}}^2)u_{(3)} - f^2 r^2 {\omega^\chi_{\rm pl}}^2 u'_{(3)}\,,
\end{aligned} \tag{4.13}$$

$$\begin{aligned}
\mathcal{D}\ u_{(3)} =& \frac{f}{r^2\omega^2}(-l(l+1)(2\omega^2 - f{\omega^\chi_{\rm pl}}^2)u_{(2)} \\
&+ {\omega^\chi_{\rm pl}}^2((r^2\omega^2 - fl(l+1))u_{(3)} + fl(l+1)ru'_{(2)}),
\end{aligned} \tag{4.14}$$

$$\mathcal{D}\ u_{(4)} = f{\omega^\chi_{\rm pl}}^2 u_{(4)}\,. \tag{4.15}$$

---

[2] Note that here the operator $\mathcal{D}$ contains the bare DP mass and not the plasma frequency, unlike in the previous section.

As in the SM photon case, owing to the spherical symmetry of the background, the axial sector ($u_{(4)}$) is decoupled from the polar sector ($u_{(2)}$, $u_{(3)}$), the equations do not depend on the azimuthal number m, and there is no mixing between modes with different quantum number l. In the limit $\omega_{\rm pl}^{\chi} \to 0$, Eqs. (4.13)-(4.15) reduce to the standard equations for a noninteracting Proca field in a Schwarzschild spacetime [75].

From Eqs. (4.13)-(4.15), it is immediate to see that the interplay between the bare mass and the plasma frequency is nontrivial. Naively, one might expect the perturbations to depends on a total mass (squared) given by the squared sum of the bare and effective masses, at least for transverse modes. However, this is true only for the axial sector, see Eq. (4.15). For the polar sector, the interplay is less straightforward.

In the limit of flat spacetime, Eqs. (4.14)-(4.15) read

$$\Big(\frac{d^2}{dr_*^2} + \omega^2 - \mu^2\Big) u_{(3,4)} = {\omega_{\rm pl}^{\chi}}^2 u_{(3,4)} \,, \tag{4.16}$$

leading, in momentum space, to the dispersion relation

$$\omega^2 = k^2 + (\mu^2 + {\omega_{\rm pl}^{\chi}}^2) \tag{4.17}$$

of transverse massive modes in a plasma, where the bare and effective masses are squared-summed. For the radial component of the field we instead obtain

$$\epsilon_{\rm pl}\Big(\frac{d^2}{dr_*^2} + \omega^2 - \mu^2\Big) u_{(2)} = \frac{{\omega_{\rm pl}^{\chi}}^2}{\omega^2} \mu^2 u_{(2)} \,, \tag{4.18}$$

where we introduced the plasma dielectric tensor $\epsilon_{\rm pl} = 1 - {\omega_{\rm pl}^{\chi}}^2/\omega^2$. From this equation we can verify that our formalism recovers the expected phenomenology in two important limits:

- if $\mu \to 0$, the right-hand side vanishes and the only solution is $\epsilon_{\rm pl} = 0$, i.e. $\omega^2 = {\omega_{\rm pl}^{\chi}}^2$. In the absence of a mass, this degree of freedom does therefore become electrostatic. In fact, a massless spin-1 particle in a cold plasmic medium only propagates two degrees of freedom, while the third one is electrostatic [11].
- if $\omega_{\rm pl}^{\chi} \to 0$, $\epsilon_{\rm pl} \to 1$ we recover the dispersion relation of a propagating Proca degree of freedom in vacuum $\omega^2 = k^2 + \mu^2$. For realistic plasma density profiles that vanish at spatial infinity – as the one we will consider in this work (see Sec. 4.3) – this degree of freedom behaves as a propagating Proca degree of freedom at large r.

Free-fall plasma

Up to now we have modelled the plasma surrounding the BH as static. We now want to relax this approximation, by considering a more realistic free-falling plasma. A freely-falling massive particle follows the geodesics of the Schwarzschild spacetime, and its four velocity reads

$$u^{\mu} = ((1 - 2M/r)^{-1}, -\sqrt{2M/r}, 0, 0) \,. \tag{4.19}$$

As its motion is purely radial, this plasma configuration does not break the spherical symmetry and therefore, when the field is decomposed in spherical harmonics, it does not generate couplings between different l, m modes and the axial and polar sectors decouple as in the static-plasma case. Moreover, as the plasma four-velocity does not depend on time, the system is still stationary (at least at the linearized level when backreaction is neglected). Therefore, even in the case of a free-falling plasma, we can work in the frequency domain and perform the same multipolar expansion as in Eq. (4.12) with the assumption of a harmonic time dependence $\sim e^{-i\omega t}$. The corresponding field equations are much more involved than in the static plasma case, and are reported in Appendix F.2.

In the case of a static plasma, the field equations reduce to second order differential equations. In the case of free-fall, the perturbation equations remain instead of third order, and thus require three boundary conditions, as we will see. In the following, owing to the complexity of the equations, we will focus on the axial sector to explore the impact of the background plasma velocity field.

Schematically, the third-order equation governing the axial sector in the case of free-fall plasma reads

$$A_1 u_{(4)}(r) + A_2 u'_{(4)}(r) + A_3 u''_{(4)}(r) + A_4 u'''_{(4)}(r) = 0 \tag{4.20}$$

where the coefficients A_i are given in Appendix F.2. It is interesting to study the above equation in the limit of vanishing plasma frequency,

$$4M\mathcal{D}u_{(4)} + \Big(2M\mathcal{D}u_{(4)} - r(\mathcal{D}u_{(4)})' u'_{(4)}\Big) = 0\,, \tag{4.21}$$

where the $\mathcal{D}$ operator was introduced in the previous section. From Eq. (4.10), we know that in this limit we must recover the vacuum Proca equation, $\mathcal{D}u_{(4)}(r) = 0$ [75], which is indeed a solution to Eq. (4.21). As we shall discuss in the next section, this is also the only solution compatible with the boundary conditions of the problem.

Finally, as the free-fall velocity vanishes at large distances, the field equations have the same asymptotic behavior at spatial infinity as in the case of an everywhere static plasma.

Plasma density profile and plasma frequency

The density of a plasma in free-fall can be obtained by solving the continuity equation (4.5) with four-velocity (4.19). This leads to a density profile of the form [178]

$$\rho(r) = \frac{\dot{M}}{4\pi\sqrt{2M}}\frac{1}{r^{3/2}}\,, \tag{4.22}$$

where $\dot{M}$ is a constant mass flux. This profile features an increasing density at the horizon, and vanishes at spatial infinity. We can then express the plasma frequency as

$$\omega_{\rm pl}^{\chi\,2} = \omega_H^2\Big(\frac{2M}{r}\Big)^{3/2}\,, \tag{4.23}$$

where ω_H is the plasma frequency at the horizon, which in the following we will treat as a free parameter.

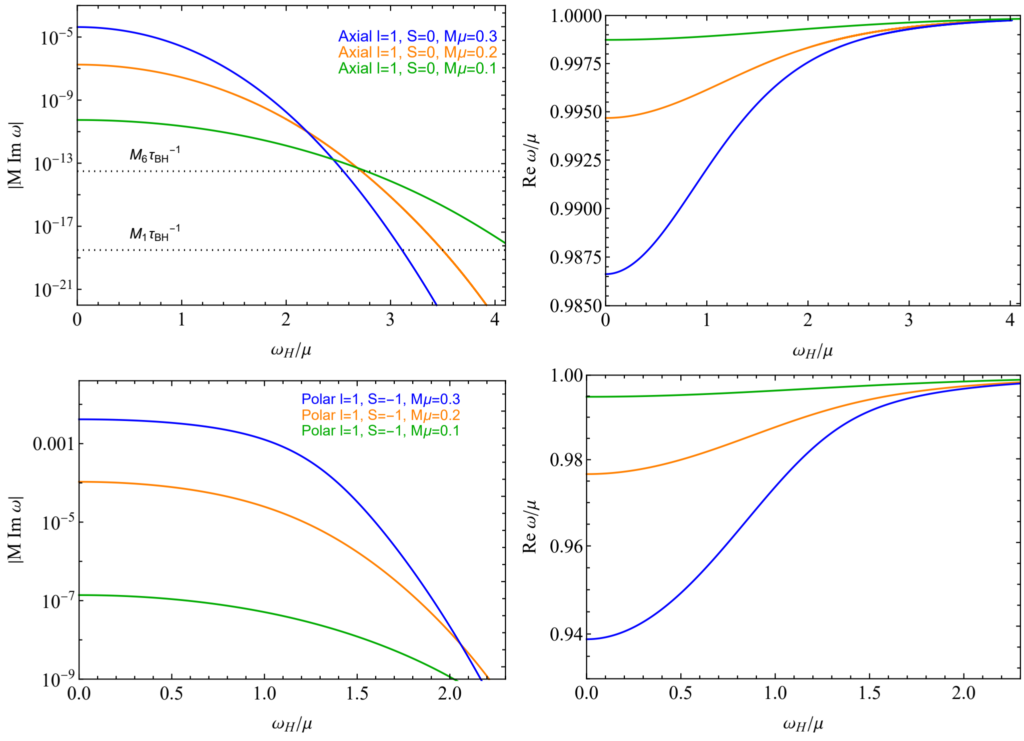

Figure 4.1. (Upper panels) Imaginary (left) and real (right) part of the axial $l = 1, S = 0$ mode as a function of ω_H/μ for different values of μ and for a static plasma. As the dark plasma frequency at the horizon increases, it effectively unbounds the modes: the binding energy $\omega_\mathrm{R}/\mu - 1$ and the imaginary part ω_I both go to zero, leading to larger timescales. (Lower panels) Same as in the upper panels but for the $l = 1, S = -1$ dominant polar mode. Here and in the following $S = (-1, 0, 1)$ denotes the spin projection of the mode [75], with $S = 0$ for axial modes and $S = \pm 1$ for the two polarizations of polar modes.

To better compare perturbations in static and free-falling plasmas, we shall assume that the plasma frequency takes the form (4.23) also in the static case (where the continuity equation is satisfied for any time-independent ρ).

Note that the radial infall of the dark particles is not affected by dark interactions. This is because the plasma is neutral [26], so the net force acting on the particles is zero.

4.4 Quasibound spectrum of a Proca field in a plasma

4.4.1 Numerical method and boundary conditions

In the following, we will solve the perturbation equations numerically using the direct integration shooting method, as in the previous chapter (see 3.2.4). Nevertheless, while in the static case the system is composed of second-order differential equations, in the free-fall case the field equations are of third differential order. Hence, while in the former we can apply the standard boundary conditions (3.30) and (3.31), in the latter we will need an extra one.

At infinity, we can impose the same asymptotic conditions as in the static case. This is because the two configurations coincide in this limit, where the free-fall radial velocity vanishes. On the other hand, by expanding the axial field equation at leading order at the horizon, we obtain

$$\frac{d^2}{dr_*^2}u_{(4)} + b\frac{d}{dr_*}\Big(\omega^2 u_{(4)} + \frac{d^2}{dr_*^2}u_{(4)}\Big) + \omega^2 u_{(4)} = 0\,, \tag{4.24}$$

where b is a constant. We can still impose that, at the leading order, the near-horizon solution is an ingoing wave, $u_{(4)}(r) \sim b_{(4)\,0}e^{-i\omega r_*}$, where again $b_{(4)\,0}$ is an arbitrary coefficient (see eq. (3.30)). However, in this case it is not possible to compute all the next-to-leading-order coefficients $b_{(i)\,n}$ solely in terms of $b_{(i)\,0}$ by solving the field equations recursively as in the static-plasma case, since one coefficient is left unconstrained. To obtain the full solution near the horizon, we need a third, physically motivated, boundary condition. In particular, we must impose that the velocity perturbation of the fermions vanishes asymptotically at the horizon,

$$\tilde{u}_\phi = \mathcal{O}(r - 2M)\,. \tag{4.25}$$

Indeed, in a free-fall plasma massive particles reach a background radial velocity equal to the speed of light at the horizon (as can be seen from Eq. (4.19)), so any nonvanishing perturbation at the horizon would violate causality. This condition is automatically satisfied in the static case, where even in the vicinity of the BH horizon the plasma is static. As can be seen from Eq. (E.1.5) in Appendix E, the extra boundary condition (4.25) translates into a requirement on the component of the field orthogonal to the background four-velocity at the horizon. This third boundary condition provides the missing relation to obtain the asymptotic solution (3.30) in terms of a single arbitrary coefficient $b_{(i)\,0}$.

4.4.2 Spectrum of quasibound modes

Figure 4.1 shows the dependence of the axial (upper panels) and polar (lower panels) spectrum on the ratio ω_H/μ between the dark plasma frequency at the horizon and the bare DP mass for different values of μ in a *static* plasma[3]. The two sectors show the same behavior: as $\omega_H \to 0$, the plasma density goes to zero and we recover the results of Ref. [75] describing the quasibound states of a noninteracting Proca field in a Schwarzschild spacetime. As ω_H becomes larger, the real part of the mode frequency increases rapidly toward the value of the bare mass, and therefore the binding energy of the modes, $\omega_{\rm R}/\mu - 1$, vanishes. Meanwhile, the imaginary part decreases dramatically, leading to much larger timescales. Hence, the modes become more and more unbound. This behavior is due to the fact that as the effective mass increases at the horizon, the minimum in the effective potential flattens and therefore the formation of quasibound states is strongly hampered. The same phenomenology was recovered in a similar system in [115].

When the effective mass is sufficiently large (which roughly occurs when $\sqrt{\omega_H^2 + \mu^2}M \gg 0.1$), we find an exponential decay of the imaginary part, as in the case of large

---

[3] For the axial sector, we are able to solve for the dominant mode for larger values of ω_H/μ and with higher precision, owing to the simplicity of the axial equation.

bare mass [56]. In this case the modes become extremely long lived and of less astrophysical interest. Importantly, this would also affect the superradiant timescale over which the BH spin is dissipated, which is typically comparable to that of the quasibound states in the (stable) nonspinning limit [30].

In the upper left panel of Fig. 4.1 we show the values (dashed horizontal lines) of the (inverse) timescale $\tau_{\rm BH} \equiv 0.1\,\tau_{\rm Salpeter}$, where $\tau_{\rm Salpeter} \simeq 4.5 \times 10^7$ years is the Salpeter timescale. This is the characteristic timescale of accretion of an astrophysical BH, and is the relevant one to compare with the superradiant timescale when deriving bounds from the superradiant instability [30, 79, 76, 83, 91, 179] (see Sec. 4.6 for more details on experimental limits). In particular, if the superradiant timescale $1/|\omega_{\rm I}|$ is much longer than $\tau_{\rm BH}$ the superradiant instability is ineffective.

As a rule of thumb, when $1/|\omega_{\rm I}| \gg \tau_{\rm BH}$, plasma effects are likely to completely invalidate superradiant bounds, since they destroy the quasibound states in the first place. In Fig. 4.1 we show two examples, for $M = 10^6 M_\odot \equiv M_6$ and $M = 10 M_\odot \equiv M_1$; in both cases if $\omega_H \gtrsim 2-4\,\mu$ the mode lifetimes are longer than the BH accretion timescale. The same happens for the polar mode (lower panels of Fig. 4.1), although in this case it is numerically more challenging to push the modes towards large values of ω_H/μ, and therefore we do not show $\tau_{\rm BH}$ in that plot. Nevertheless, it is clear that also in the polar case the imaginary part of the modes becomes extremely small when $\omega_H \gtrsim 2-4\,\mu$, as in the axial case.

We conclude that the presence of a dark plasma, if sufficiently dense, can completely quench the quasibound spectrum of a DP and cause a dramatic increase of the mode lifetime. This would correspond to a severe weakening of the superradiant instability around a spinning BH.

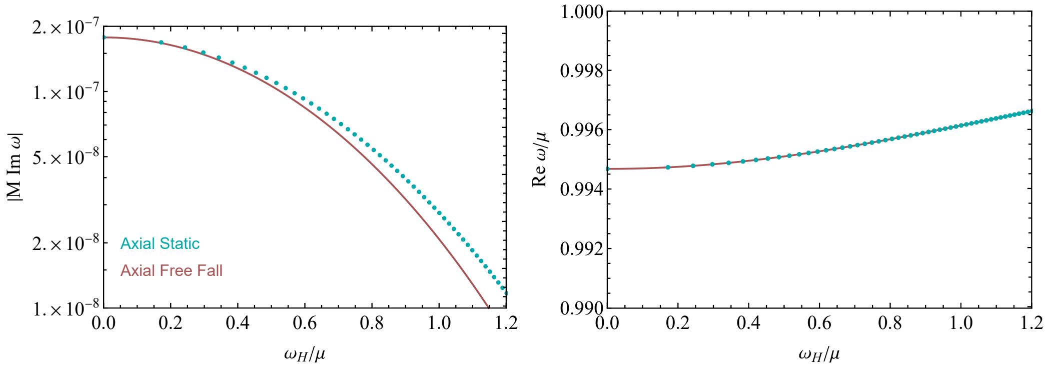

Figure 4.2. Imaginary and real part of the axial $l = 1, S = 0$ mode as functions of the ratio ω_H/μ with mass $M\mu = 0.2$ for the static (dotted blue) and free-fall (red) case. For $M\omega_H = 0$, i.e. in the absence of plasma, the two configurations coincide to the vacuum Proca axial mode. As ω_H/μ increases, the real part of the mode is very similar for the two configurations, while the imaginary part of the mode decreases faster in the free-fall case. Overall, the two configurations exhibit a similar behavior.

Figure 4.2 shows a comparison between the dominant axial mode in the static and free-fall configurations for $M\mu = 0.2$. For $\omega_H/\mu = 0$, i.e. in the absence of plasma, the two modes coincide with the vacuum Proca axial mode. This is because, in the absence of plasma (when the dark plasma frequency goes to zero) the solution is trivially given by a vacuum Proca equation, see Eq. (4.10). Interestingly, as ω_H/μ

increases, the real part of the mode is essentially unaffected by the plasma motion, while the imaginary part decreases faster in the free-fall configuration. Overall, the free-fall configuration has the same phenomenology as the static one: as the dark plasma frequency increases, the binding energy goes to zero and the timescales are severely stretched. In the free-fall case, the drop in the imaginary part is slightly more severe. One can thus expect the superradiant instability to be even more severely weakened in this case.

In principle, one might wonder about backreaction effects of the dark electromagnetic field onto the plasma. These might include breaking of the spherical symmetry of the plasma, effects on the motion of the plasma particles, or relativistic transparency effects [137]. However, these effects can only become relevant for sufficiently large DP field amplitudes. As we have argued, the presence of a sufficiently dense dark plasma prevents the superradiant instability from growing the DP field efficiently. As the quenching mechanism arises already at the linear level, the field remains at all times as small as the initial perturbation, and its backreaction effects are thus negligible.

4.5 DM models

In the previous sections we have shown that a dark plasma frequency comparable to, or larger than, the bare DP mass can greatly alter the quasibound states, possibly suppressing the DP superradiant growth. Here we sketch a simple DM model that can generate a sizable plasma frequency around a BH. The numerical conclusions of the previous sections are of course independent of the mechanism generating the fermionic relic abundance, and we could simply *assume* the existence of a UV model generating the correct density at low redshift. Nevertheless, we find it useful to write down an illustrative model, which is not intended to be exhaustive of all possibilities. We hope our work motivates research into other alternatives in this direction.

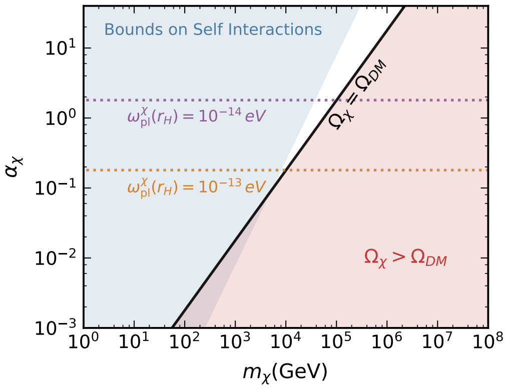

Figure 4.3. Parameter space of interest for a simple secluded DM model. The blue shaded region is excluded because of the self-interactions bound from dwarf galaxies [180], while the solid black line indicates the parameters for which the correct relic abundance is obtained via freeze-out. The horizontal dotted lines indicates the value of α_χ corresponding to two different plasma frequencies, assuming Bondi-Hoyle accretion around the BH horizon and the full DM density at "infinite" distance from it.

Let us consider a fermion χ with mass m_χ coupled to our DPs with fine structure constant α_χ. We consider χ to be a DM candidate and set its abundance via freeze-out. For simplicity, we study a “secluded" scenario, so that couplings to the Standard Model thermal bath are not important for thermal freezeout [181, 26] and the relic abundance is set by the process $\bar{\chi}\chi \leftrightarrow VV$ (where V schematically denotes the DP), which in the limit $\mu \ll m_\chi$ has a cross section

$$\langle \sigma v \rangle_{\bar{\chi}\chi \leftrightarrow VV} \simeq \frac{\pi \alpha_\chi^2}{m_\chi^2}. \tag{4.26}$$

The DM relic abundance is obtained when the annihilation cross section is of the order

$$\langle \sigma v \rangle_{\bar{\chi}\chi \leftrightarrow VV} \simeq \frac{1}{10^9 \mathrm{GeV}^2}, \tag{4.27}$$

where we took $T_{\mathrm{fo}} \simeq m_\chi/10$ for the freezeout temperature and assumed typical values for the relativistic degrees of freedom in the early universe [182].

The dark fermions in this model will exhibit self-interactions due to the exchange of a DP. Self-interactions are especially enhanced in the limit of small DP mass, as the cross section presents a forward scattering enhancement. In fact, in the Born limit the transfer cross section for a DM particle of velocity v_χ reads

$$\sigma_{\mathrm{self}} \simeq \frac{8\pi \alpha_\chi^2}{m_\chi^2 v_\chi^4} \ln\Big(\frac{m_\chi^2 v_\chi^2}{\mu^2}\Big). \tag{4.28}$$

Limits on DM self-interactions (SIDM) from observations of galaxy clusters, galaxies, and dwarf-galaxy halos [180, 180, 183, 26] restrict this cross section to be roughly $\sigma_{\mathrm{self}}/m_\chi \lessapprox 0.1 - 100\,\mathrm{cm}^2/\mathrm{g}$.

Comparing the couplings needed to set the relic abundance, one can see easily that the SIDM constraint excludes thermal freezeout for DM masses smaller than $m_\chi \sim$ TeV. This is shown in Fig. 4.3. The blue shaded area indicates the region excluded by measurements of dwarf galaxies [180], which limit the cross section to be $\sigma_{\mathrm{self}}/m_\chi \lesssim 10 - 100\,\mathrm{cm}^2/\mathrm{g}$ for DM velocities $v_\chi \sim 10^{-4}$ (here we also fixed $\mu = 10^{-14}$eV, but the dependence on the DP mass is very weak). The solid black line indicates the parameters for which the correct relic abundance is obtained via freeze-out. The horizontal dotted lines indicates the value of α_χ corresponding to two different plasma frequencies, defined as usual as

$$\omega_{\mathrm{pl}}^\chi = \Big(\frac{4\pi \rho_\chi \alpha_\chi}{m_\chi^2}\Big)^{1/2} \simeq 1.8 \times 10^{-13} \mathrm{eV} \Big(\frac{\rho_\chi}{10^5\,\mathrm{GeV/cm}^3}\Big)^{1/2} \Big(\frac{0.1}{\alpha_\chi}\Big)^{1/2}, \tag{4.29}$$

where in the last step we used Eqs. (4.26) and (4.27) to relate m_χ to α_χ[4]. The normalization of ρ_χ is estimated by assuming Bondi-Hoyle accretion, which gives the following density close to the BH horizon

$$\rho_\chi(r_{\mathrm{H}}) \simeq 2.4 \times 10^5 \rho_\chi^\infty \Big(\frac{0.01}{v_{\mathrm{rel}}}\Big)^3, \tag{4.30}$$

---

[4] Notice that the second line of Eq. (4.29) is valid *only* if the freeze-out happens via Eq. (4.26). If other interactions, independent of α_χ, set the relic abundance, then the full expression of the plasma frequency (with no a priori relation between α_χ and m_χ) should be used.

where $v_{\rm rel}$ is the relative BH-DM velocity far from the BH and $\rho_\chi^\infty \approx 0.4{\rm GeV/cm}^3$ is the DM ambient density far away from the horizon.

From Fig. 4.3 we see that, within this minimal model, dark fermions can naturally dress the DP with a plasma mass, but the available parameter space is small and confined to generate a plasma frequency of roughly $\sim 10^{-13}\,$eV, if we require the dark fermion to be in the perturbative regime ($\alpha_\chi \lesssim 1$), have the correct relic abundance, and avoid SIDM bounds. However, as already mentioned, this simple, minimal model is easily extendable to widen the allowed parameter space. This can be achieve by: i) relaxing self-interaction bounds, or/and ii) producing the DM relic abundance through a different interaction. One possibility to relax SIDM bounds is to have a large splitting for the Dirac fermion, which kinematically suppresses self-interactions [184, 185]. A simple extension to evade the relic abundance requirement is described in Ref. [26], where the DM fermion is also charged under $SU(2)_{\rm L}$. In this case, the relic abundance can be set at early times by freeze-out via the weak interaction. At late times, the weak cross section remains small, while the long-range cross section mediated by the DP comes to dominate as the DM cools and slows, reducing to the vanilla model described here. In this way, it can be possible to extend to lower DM masses, increasing the allowed plasma frequency.

Another possibility occurs if the DP is produced gravitationally during inflation and DM thermalizes through interactions in the dark sector and not with standard-model particles [186]. In this respect it would be interesting to extend the analysis of [186] to smaller DP masses which are relevant for plasma-triggered BH superradiant instabilities.

Finally, the DM density around the BH may be much larger than the value set by Bondi-Hoyle accretion, possibly leading to even larger plasma frequencies. This would be the case, for example, if DM spikes are present around the BH [187, 188].

4.6 Impact of DP-DM coupling on current DP bounds from BH superradiance

Probing ultralight DPs is an extremely challenging task, as lab-based experiments become impractical for very long wavelengths [189]. Most of the constraints on DP masses smaller than $\mu \sim 10^{-10}$ eV then come from astrophysics and cosmology, typically assuming a kinetic mixing between the DP and the ordinary photon [190, 191, 192]. In this regard, superradiance represents a unique possibility to probe very light DPs even without assuming a kinetic mixing to the SM photon.

In the past years, many authors have put tight constraints on DPs using the BH mass-spin distribution (see, e.g., Refs. [89, 79, 76, 83, 100, 90, 91, 193, 194, 179] and [30] for a recent summary of the constraints). The basic physics in all these cases is the same: if a DP with the correct mass is present in the spectrum of the theory, a superradiant growth can be triggered on short-enough timescales and extract angular momentum and energy from astrophysical BHs, making the measured spins inconsistent with the DP itself, and also leading to peculiar gravitational-wave signatures [30]. In particular, current stellar-origin BH mass-spin measurements in X-ray binaries[5] exclude DP masses between $\mu \sim 5\times10^{-14}$–$2\times10^{-11}\,$eV, while

---

[5] Note that constraints from X-ray binaries might be affected by systematic errors in the

supermassive BH spin measurements exclude lighter masses, $\mu \sim 6 \times 10^{-20}$–$2 \times 10^{-17}$eV [79, 76, 83, 91, 179] and $\mu \sim 8.5 \times 10^{-22}$–$4.6 \times 10^{-21}$eV [196]. These bounds are reported in Fig. 4.4, where the red bands refer to highly-spinning supermassive BHs, while the blue ones to stellar-mass BHs (see Ref. [83] for a similar plot).

In order for these bounds to apply, the superradiant rate should be fast enough to grow a maximally-filled cloud within the relevant BH timescale, $\tau_{\rm BH}$. Our present analysis shows that, in motivated DM models, it may be very easy to make the superradiant timescale larger than $\tau_{\rm BH}$. In particular, within the simple class of DM models described in the previous section, we have shown that it is possible to obtain plasma frequencies of the order $\omega_{\rm pl}^{\chi} \sim 10^{-13}$ eV, or greater. Our numerical results from Sec. 4.4 indicate that the dark plasma can quench the superradiance instability any time $\omega_{\rm pl}^{\chi} \gtrsim \mu$ (see, *e.g.*, the upper left panel of Fig. 4.1). This means that DPs a factor of few lighter than $\mu = 10^{-13}$ eV are easily rescued thanks to plasma effects, in a minimal SIDM model. This corresponds to the gray region in Fig. 4.4, where the vertical line is drawn using the reference value in Eq. (4.29), divided by a factor of 2 to account for the onset of the effect observed in Fig. 4.1.

As outlined in Sec. 4.5, it seems also likely that simple extensions of this model could rescue even larger DP masses, corresponding to the green region in Fig. 4.4.

Finally, we stress that our argument can invalidate superradiance bounds while leaving unchanged constrains of different nature in the same mass range. For example, cosmological constrains typically rely on resonant effects on large scales [190], where the dark plasma density is several orders of magnitude smaller than around a BH. Such constrains are reported, e.g. in [189]. Another relevant example in this mass range are recent constrains on the couplings of dark photons with baryons, imposed using LIGO/VIRGO data [197].

---

determination of the BH spin, see discussion in Ref. [195].

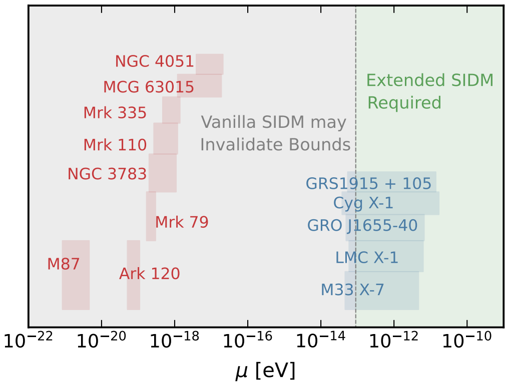

Figure 4.4. Constraints on DP masses derived from highly-spinning supermassive (red bands) and stellar-mass (blue bands) BHs as computed in Ref. [83]. The gray region indicates the masses for which the simple SIDM model of Sec. 4.5 can introduce strong plasma effects which invalidate the bounds. The green region indicates masses for which extensions of the simplest model are required in order to generate a sizable enough $\omega_{\rm pl}^{\chi}$ without overproducing DM and without violating SIDM bounds.

4.7 Conclusions

In this work, we have studied for the first time the quasibound states of a DP field in the presence of a (dark) plasma. The latter dresses the DP with an additional density-dependent mass, which can significantly alter the quasibound spectrum. In particular, we showed that if the generated plasma frequency is $\gtrsim 2-4$ times the DP bare mass, then the state lifetime increases dramatically and (extrapolating to spinning BHs) the superradiant instability is effectively quenched, similarly to the case of bosons with a large bare mass ($M\mu \gg 1$ [56]) which is of limited astrophysical interest. This has important implications for observational bounds on DPs. We outlined a simple, motivated particle physics model that naturally provides a sizable plasma frequency, possibly bearing a way out from current superradiance bounds from BH mass-spin measurements.

Interestingly, our analysis also shows that if current or future detectors will discover gravitational-wave signatures of a new light vector particle through BH superradiance [79, 76, 83, 91, 105, 104] this could be used to set relevant constraints on the DP scenario in various motivated DM models.

Chapter 5

Axionic Superradiance and Plasma Effects

Summary

Superradiant fields around BHs can couple naturally –although very feebly– with SM particles. Couplings between superradiant fields and the SM are pivotal to describe properly the evolution of the system. In this chapter, we study these couplings using numerical relativity. We first focus on the coupled axion-Maxwell system evolving on a black hole background. By taking into account the effect of the coupling concurrently with the growth of the axionic cloud, we observe for the first time that a new stage emerges: that of a stationary state where a constant flux of electromagnetic waves is fed by superradiance, for which we find accurate analytical estimates. Moreover, we show that the existence of electromagnetic instabilities in the presence of plasma is entirely controlled by the axionic coupling; even for dense plasmas, an instability is triggered for high enough couplings.

5.1 Bursts of light from axions?

The QCD axion is one of the most promising DM candidate that could potentially be probed via BH superradiance. As already discussed, the precise development of the instability is well understood in vacuum and in the absence of couplings to the Standard Model [24, 89, 87, 30, 88]. Nevertheless, axions admit a number of possible couplings: among them, notable examples are self-interacting theories and couplings to the SM photon. In the following, we are going to consider the latter scenario in the contest of BH superradiance. In previous works, it was argued analytically and with numerical simulations, that such couplings to the Maxwell sector might trigger *parametric instabilities*, whereby the scalar cloud transfers energy to electromagnetic (EM) radiation [198, 199, 172, 171]. In other words, any EM fluctuation in the axionic condensate might be parametrically amplified, giving rise to powerful bursts of EM radiation, sometimes called BLASTs (*Black hole Lasers powered by Axionic SuperradianT Instabilities*). This process is based on the decay of the axions into a pair of photons with opposite helicity $a \to \gamma\gamma$. Nevertheless, it was suggested that the presence of a surrounding plasma may quench the parametric

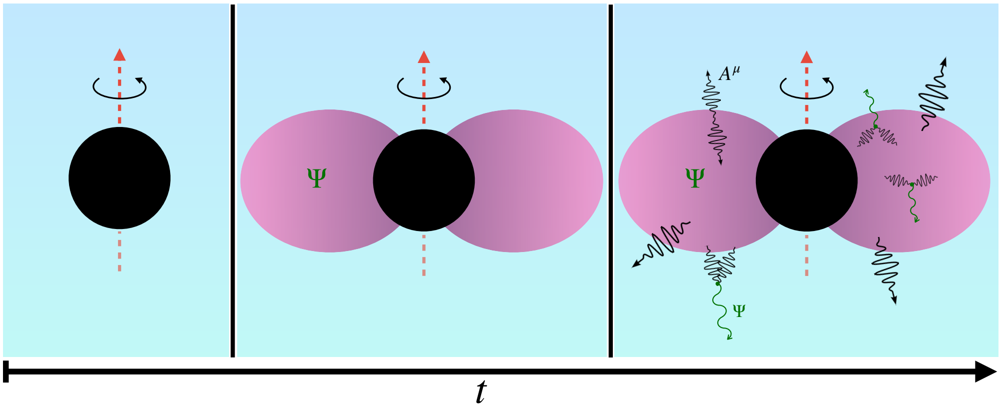

Figure 5.1. Schematic illustration of our setup. Starting from a spinning BH of mass M (*left*), a SR cloud of mass M_c is formed in the dominant (dipolar) growing mode (*center*). For sufficiently large couplings to the Maxwell sector, the configuration is unstable: any small EM fluctuation will trigger emission of EM radiation (black lines, *right* panel). Some of these waves recombine to create axion waves (green lines). The blue background indicates the presence of a plasma.

instability due to the high energy (large "effective mass") of typical astrophysical environments [137, 174, 138]: that is to say, as photons in a plasma are dressed with an effective mass, the decay of the axion may be prohibited by kinematic reasons if the photons are too heavy.

The previous works left important gaps: (i) the parametric instability was shown to give rise to periodic bursts of light, but its period and amplitude were not studied. In fact, the effect of a SR growing cloud was also not understood properly.[1] (ii) The role of plasmas in the development of EM instabilities is known poorly, but could have a drastic effect (see e.g. recent works on dark photon SR [175, 176]), since the plasma frequency is rather large in most astrophysical circumstances.

5.2 The theory and general framework

We consider a real, massive (pseudo)scalar field Ψ with axionic couplings to the EM field. In addition, the EM field is coupled to a cold, collisionless electron-ion plasma. In this setup, the Lagrangian takes on the following form:

$$\begin{aligned}\mathcal{L} = \frac{R}{16\pi} - \frac{1}{4}F_{\mu\nu}F^{\mu\nu} - \frac{1}{2}\nabla_\mu\Psi\nabla^\mu\Psi - \frac{\mu^2}{2}\Psi^2 \\ - \frac{k_\mathrm{a}}{2}\Psi\, {}^*F^{\mu\nu}F_{\mu\nu} + A^\mu j_\mu + \mathcal{L}_\mathrm{m}\,.\end{aligned} \tag{5.1}$$

The mass of the scalar field Ψ is given by $m_\mathrm{a} = \mu\hbar$, A_μ is the vector potential, $F_{\mu\nu} \equiv \nabla_\mu A_\nu - \nabla_\nu A_\mu$ is the Maxwell tensor and ${}^*F^{\mu\nu} \equiv \frac{1}{2}\epsilon^{\mu\nu\rho\sigma}F_{\rho\sigma}$ is its dual. We use the definition $\epsilon^{\mu\nu\rho\sigma} \equiv \frac{1}{\sqrt{-g}}E^{\mu\nu\rho\sigma}$, where $E^{\mu\nu\rho\sigma}$ is the totally anti-symmetric Levi-Civita symbol with $E^{0123} = 1$. We define the Lagrangian for the plasma as $\mathcal{L}_\mathrm{m}$, while k_a quantifies the axionic coupling which we take to be constant. There exists

---

[1] As we show here, bursts will in general not occur, but give way to a stationary emission of light.

a wide variety of theories predicting axions and axion-like particles, and generically $k_{\rm a}$ is independent of the boson mass. Therefore, we take $k_{\rm a}$ to be an additional free parameter of the theory. Notice that we do not consider self-interactions, which could appear as an expansion of the axion's periodic potential. This corresponds to a region $k_{\rm a} f_{\rm a} \geq \mathcal{O}(1)$ predicted in models such as clockwork axions [200, 201] and magnetic monopoles in the anomaly loop [202, 203], where f_a is the decay constant of the axion.[2] In principle, a similar analysis could be performed for scalar couplings ($\mathcal{L} \supset k_{\rm s} \Psi F^{\mu\nu} F_{\mu\nu}$), at least when the coupling strength is weak [172].

Finally, j_μ is the plasma current, and captures both the contributions of the electrons and the much heavier ions. In this work, we adopt a two-fluid formalism model for the plasma, where electrons and ions are treated as two different fluids, coupled through the Maxwell equations. Hence, the plasma current is given by $j^\mu = \sum_s q_s n_s u_s^\mu$, where the index s represents the sum over the two different species, electrons and ions, and q_s, n_s, u_s^μ are the charge, number density and four velocity of the fluids, respectively.

An axion cloud produced from SR can grow to be $\lesssim 10\%$ of the BH mass [81, 207, 87]. We will consider the cloud's backreaction on the geometry to be small and thus evolve the system on a fixed background. The gravitational coupling μM determines the strength of the interaction between the BH and the axion and is a crucial quantity. In order for SR to be efficient on astrophysical timescales, the gravitational coupling must be $\mathcal{O}(1)$. For $\mu M \ll 0.1$, the exponential growth is too slow, while the instability is exponentially suppressed for $\mu M \gg 1$ [56, 208]. Consequently, we will perform simulations in the range $\mu M \sim 0.1 - 0.3$.

From the Lagrangian of our theory (5.1), we obtain the equations of motion for the scalar and EM field. In order to close the system, we also need to consider the continuity and momentum equation of the fluids, which come from the conservation of the energy-momentum tensor for the Maxwell-plasma sector. Ignoring the backreaction of the fields in the spacetime, we obtain:

$$\begin{aligned} \left(\nabla^\mu \nabla_\mu - \mu^2\right) \Psi &= \frac{k_{\rm a}}{2} \, {}^*F^{\mu\nu} F_{\mu\nu} \,, \\ \nabla_\nu F^{\mu\nu} &= j^\mu - 2 k_{\rm a} {}^*F^{\mu\nu} \nabla_\nu \Psi \,, \\ u_s^\nu \nabla_\nu u_s^\mu &= \frac{q_s}{m_s} F^\mu_{\ \nu} u_s^\nu \,, \\ \nabla_\mu (n_s u_s^\mu) &= 0 \,, \end{aligned} \tag{5.2}$$

where the index s denotes again the particular fluid species. Finally, we impose the Lorenz condition on the vector field

$$\nabla_\mu A^\mu = 0 \,, \tag{5.3}$$

thereby fixing our gauge freedom.

5.2.1 Modeling superradiance

Even though we are interested in an axion cloud that grows through SR, and thus requires a spinning BH described by the Kerr metric, we will instead mimic SR growth

---

[2] The strong self-interaction regime was discussed in e.g. [204, 169, 205, 206], where transitions to various cloud modes and distortion of bound state wavefunctions are expected.

without the need of a spinning BH. The reason is of a practical nature: timescales to superradiantly grow an axion cloud are larger than $\sim 10^6 M$ [209, 69, 208], a prohibitively large timescale for our purposes. Therefore, we mimic SR growth following Zel'dovich [47, 48, 210], by adding a simple Lorentz-invariance violating term to the Klein-Gordon equation,

$$\left(\nabla^\mu \nabla_\mu - \mu^2\right) \Psi = C \frac{\partial \Psi}{\partial t} + \frac{k_\mathrm{a}}{2} {}^*F^{\mu\nu} F_{\mu\nu} \,. \tag{5.4}$$

Here, C is a constant, which in the absence of the axionic coupling gives rise to a linear instability on a timescale of the order $1/C$, where we can tune C to be within our numerical limits. For further details, we refer to Appendix G.2.

5.2.2 Modeling plasma

As already discussed in previous chapters, the plasma frequency acts as an effective mass for the transverse polarizations of the photons. This effect is crucial to take into account when studying parametric instabilities as the axion decay into photons could be suppressed in a dense plasma, i.e., when $\omega_\mathrm{pl} \gg \mu$. Throughout this work, we work under the following assumptions regarding the plasma.

1. We drop non-linear terms in the axion-photon-plasma system. That is to say, as long as the EM field is small, it is sufficient to consider only the linear response of the medium. Consequently, the backreaction of the EM field onto the axion field is not included.

2. We ignore the oscillations of the ions due to the EM field. Whenever the plasma is non-relativistic, this assumption is justified due to the larger inertia of the ions compared to the electrons and we can treat them as a neutralizing background. In the relativistic regime however, there is a critical threshold for which this approximation is no longer valid, defined as $\Gamma_\mathrm{e} \gg m_\mathrm{ion}/m_\mathrm{e}$ [120], where Γ_e is the Lorentz factor of the electrons.

3. For simplicity, we consider as initial data a locally quasi-neutral plasma, i.e., $Z n_\mathrm{ion} \approx n_\mathrm{e}$, where Z is the atomic number, such that we have a vanishing charge density. As plasma is globally neutral, this approximation is valid at large enough length-scales for our setup. In particular, it holds in systems where typical length-scales are much larger than the Debye length (see 2.3.1).

4. We assume a cold and collisionless plasma. In principle, our formalism can be extended straightforwardly to include both thermal and collisional effects by adding a few terms in the momentum equation, as already shown in Sec. 3.3. In particular, thermal effects can be included by considering a non-negligible pressure for the fluid and an equation of state, while electron-ion collisions can be modeled using a term proportional to the relative velocity of the two fluid species.

5. We neglect the evolution of the fluid's four velocity with respect to an *Eulerian observer* due to gravity. The 3+1 decomposition of the momentum equation (I.6.25), shows how after linearization the evolution is dictated both by a

gravitational term a_i and an EM term E_i. In a Schwarzschild BH background, the only non-vanishing component of the gravitational term is $a^r = M/r^2$, which assumes the well known form of gravitational acceleration by a spherical object.[3] Since we are interested in the effect of plasma in a localized region of spacetime, i.e., the axion cloud, which is situated around the Bohr radius, an easy estimate shows that the effect of gravity is sufficiently small in the timescales of interest. For example, let us consider a cloud with $\mu M = 0.1$, located around $r = 200M$. In this case, we have that $a^r = 2.5 \times 10^{-5} M^{-1}$. Thus for an initially zero velocity fluid, this term only gives significant modifications on a timescale $t \sim 10^5 M$, which is much longer than the growth timescales of the EM field. Furthermore, note that the gravitational term is suppressed with respect to the EM term by a factor of $m_{\rm e}/q_{\rm e} \sim 10^{-22}$. Neglecting the evolution of the velocity due to gravity has two consequences for our system of evolution equations.

First of all, while the momentum equation for the electrons still has the EM term, we neglect this term for the ions according to assumption (ii). Therefore, the ionic momentum equation becomes trivial. In fact, it means that ions with initially zero velocity, do not evolve. Consequently, we can consider them as a stationary, neutralizing background without evolving the fluid.

Secondly, by neglecting the gravitational term, the constraint of the electron momentum equation (C.1.7) reduces at the linear level to $u^\nu \partial_\nu \Gamma = 0$. Since $\Gamma = 1$ linearly due to its quadratic dependence on the velocity, the constraint equation is trivially satisfied. Hence, dropping the gravitational term allows for a great simplification of our evolution scheme.

5.2.3 Numerical procedure

To evolve the system, we solve numerically the equations of motion (5.2) around a Schwarzschild BH with mass M. We denote the spatial part of the Maxwell field $\mathcal{A}_i$, the electric field E^i, the magnetic field B^i, an auxiliary field $\mathcal{Z}$, and finally the conjugate momentum Π of the scalar field. Using these variables and applying the 3+1 decomposition to the equations of motion, we obtain the evolution equations for the scalar field, EM field, and the plasma. A detailed account of the formulation of our system as a Cauchy problem can be found in Appendix I.

Besides the evolution equations, the 3+1 decomposition also provides us with a set of constraint equations, which are shown explicitly in (I.1.10). The initial data we construct should satisfy these equations. For the electric field, we assume the following profile:

$$\begin{aligned} E^r &= E^\theta = \mathcal{A}_i = 0\,, \\ E^\varphi &= E_0 e^{-\left(\frac{r-r_0}{\sigma}\right)^2} M\,, \end{aligned} \tag{5.5}$$

where $E^i = F^{i\mu} n_\mu$ $(i = r, \theta, \varphi)$, with n_μ defined as the normal vector of the spacetime foliation. Here, E^φ can be an arbitrary function of r and θ. We choose a Gaussian profile with E_0, r_0, and σ the typical amplitude, radius and width of the Gaussian, respectively. The EM pulse is initialized in *all* our simulations at $r_0 = 40M$ with

---

[3] In fact, this term corresponds to the surface gravity when evaluated at the horizon.

Run	$k_{\rm a}\Psi_0$	μM	$10^3 CM$	$10^4 E_0 M/\Psi_0$
$\mathcal{I}_1$	0.0	0.3	0.0	8.1
$\mathcal{I}_2$	0.0295	0.3	0.0	8.1
$\mathcal{I}_3$	0.147	0.3	0.0	8.1
$\mathcal{J}_1$	0.0737	0.2	4.0	100.0
$\mathcal{J}_2$	0.0737	0.2	4.0	1.0
$\mathcal{J}_3$	0.0737	0.2	4.0	0.01
$\mathcal{J}_4$	0.0737	0.2	4.0	0.0001
$\mathcal{J}_5$	0.0737	0.2	4.0	8.1
$\mathcal{J}_6$	0.0563	0.2	4.0	8.1
$\mathcal{J}_7$	0.0328	0.2	4.0	8.1
$\mathcal{J}_8$	0.00737	0.2	4.0	8.1
$\mathcal{J}_9$	0.0737	0.2	0.08	8.1
$\mathcal{J}_{10}$	0.0737	0.2	0.2	8.1
$\mathcal{J}_{11}$	0.0737	0.2	0.8	8.1
$\mathcal{J}_{12}$	0.0737	0.2	1.0	8.1
$\mathcal{J}_{13}$	0.0737	0.2	2.0	8.1
$\mathcal{J}_{14}$	0.0737	0.2	8.0	8.1
				$\omega_{\rm pl}M$
$\mathcal{K}_1$	0.147	0.3	0.0	0.01
$\mathcal{K}_2$	0.147	0.3	0.0	0.1
$\mathcal{K}_3$	0.147	0.3	0.0	0.15
$\mathcal{K}_4$	0.147	0.3	0.0	0.2
$\mathcal{K}_5$	0.147	0.3	0.0	0.3
$\mathcal{K}_6$	0.147	0.3	0.0	0.4
$\mathcal{K}_7$	0.295	0.3	0.0	0.2
$\mathcal{K}_8$	0.590	0.3	0.0	0.2
$\mathcal{K}_9$	0.0737	0.1	2.0	0.02
$\mathcal{K}_{10}$	0.0737	0.1	2.0	0.07

Table 5.1. Summary of the simulations discussed in the main text. $\mathcal{I}_i$ simulations do not include plasma nor SR growth. $\mathcal{J}_i$ simulations do include SR growth yet are still without plasma, while $\mathcal{K}_i$ simulations do include the plasma. We denote the axionic coupling $k_{\rm a}\Psi_0$, the mass coupling μM, the artificial SR parameter C, and the ratio between the initial amplitude of the electric field E_0 (5.5) and the scalar field Ψ_0 (G.1.5). In the simulations that include the plasma ($\mathcal{K}_i$), we report the plasma frequency $\omega_{\rm pl}$ as well, while the initial EM amplitude is $10^4 E_0 M/\Psi_0 = 8.1$, which is not shown in the table due to space limitations. In *all* our simulations, we initialize the EM pulse at $r_0 = 40M$ with $\sigma = 5M$.

$\sigma = 5M$. Moreover, we have tested that our results do not depend on these factors, thus confirming their generality. For the initial data of the scalar field, we use a quasi-bound state which is constructed through Leaver's method (see Appendix G.1). We consider the cloud to occupy the dominant (dipolar) growing mode with an amplitude Ψ_0, whose normalization is defined in (G.1.5). Finally, the constraint equation for the plasma is trivially satisfied as we explain in Appendix I.4, and for simplicity we take a constant density plasma as initial data.

To keep track of the scalar and EM field during the time evolution, we perform a multipolar decomposition. In the scalar case, we directly project the field Ψ onto spheres of constant coordinate radius using the spherical harmonics with spin weight $s_{\mathrm{w}} = 0$ to obtain $\Psi_{\ell m}$ (H.0.1). In the EM case, we track the evolution of the field using the Newman-Penrose scalar Φ_2, which captures the outgoing EM radiation at infinity (see Appendix H). Analogous to the scalar case, we project these using spherical harmonics, yet now using spin weight $s_{\mathrm{w}} = -1$ to obtain $(\Phi_2)_{\ell m}$ (H.0.5). In our figures, we show $|(\Phi_2)_{\ell m}| = \sqrt{(\Phi_2)^*_{\ell m}(\Phi_2)_{\ell m}}$. Since this captures massless waves, $|(\Phi_2)_{\ell m}| \propto 1/r$ at large spatial distances.

Throughout this work, we will discuss various simulations. In Table 5.1, the specific parameters of these simulations are listed. Furthermore, a schematic illustration of our setup can be seen in Fig. 5.1.

5.3 Superradiance turned off

An axion cloud coupled to the Maxwell sector can give rise to a burst of EM radiation. The initial explanation of this phenomenon was outlined in [198], while the full numerical exercise followed in [172, 171]. In this section, our goal is to carefully perform a further analysis and, as we will see, find some new features of the system. Throughout this section, we assume SR growth to be absent, as in [172, 171]. Even though this is clearly an artificial assumption, as it means that the cloud was allowed to grow without being coupled to the Maxwell sector, it allows us to isolate and understand better some of the phenomena. The full case will be dealt with afterwards.

As shown analytically on a flat spacetime, but also numerically in a Kerr background [172, 171], upon growing the cloud to some predetermined value, an EM instability is triggered depending on the quantity $k_{\mathrm{a}}\Psi_0$. In particular, there exist two regimes, a *subcritical* regime and a *supercritical* regime. In the former, no instability is triggered and some initial EM fluctuation does not experience exponential growth. Conversely, in the supercritical regime, an instability is triggered and the axion field "feeds" the EM field, which grows exponentially, resulting in a burst of radiation. The boundary between these regimes is set by two competing effects; the parametric production rate of the photon, $\propto \mu k_{\mathrm{a}}\Psi_0$, and their escape rate from the cloud, $\propto \mu^2 M$. The latter is approximated by the inverse of the cloud size. Similarly to previous works, we find the boundary to be on the order $k_{\mathrm{a}}\Psi_0 \sim 0.1 - 0.4$ for $\mu M \sim 0.2 - 0.3$.

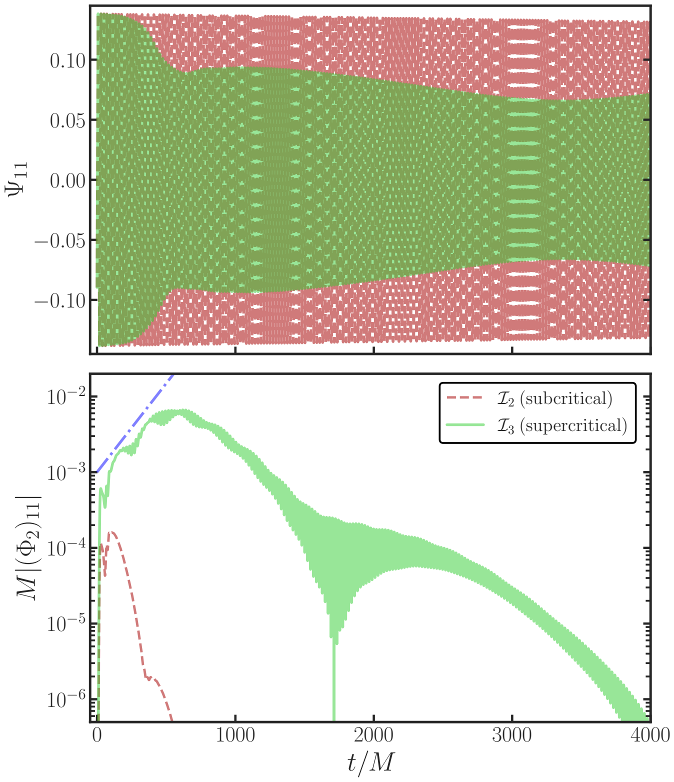

Figure 5.2. Top Panel: The time evolution of the (real part of the) dipolar, $\ell = m = 1$, bound state component of an axion cloud around a Schwarzschild BH in two scenarios: coupling is subcritical (dashed red, $\mathcal{I}_2$) or supercritical (green, $\mathcal{I}_3$). As a consistency check, we also evolve with a vanishing coupling to the Maxwell sector ($\mathcal{I}_1$), which we find to be almost indistinguishable from the subcritical case. **Bottom Panel:** The time evolution of the absolute value of the $\ell = m = 1$ component of the Newman-Penrose scalar Φ_2 for a subcritical and supercritical coupling. The blue dashdotted line shows the growth rate, $\lambda = 0.0054$, as estimated from equation (77) of [172]. In both panels, the field is extracted at $r_{\rm ex} = 20M$ and $\mu M = 0.3$.

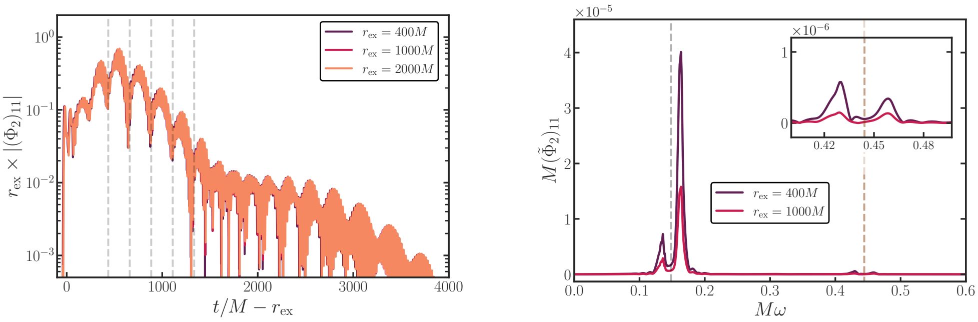

Figure 5.3. Top Panel: The dipolar component $|(\Phi_2)_{11}|$ of the EM field in the supercritical regime with $\mu M = 0.3$, for simulation $\mathcal{I}_3$. The alignment of the waveforms shows that we are dealing with EM radiation. High-frequency oscillations are set by the mass scale μ, whereas "beatings" (circumscribed by vertical dashed lines) are controlled by $1/\mu^2$. **Bottom Panel:** Fourier transform of the signal, taken on the entire time domain, showing the dominant frequencies in the problem. The gray and brown dashed lines show $N(\omega_0/2)$ for $N = 1, 3$, respectively, where $\omega_0 \approx \mu$ is the frequency of the fundamental mode.

5.3.1 The process at large

In the following, we explore these two regimes by evolving the coupled system describing a SR cloud of axions coupled to the Maxwell sector, while we initialize it with a small vector fluctuation E_0.

Figure 5.2 summarizes well the possible outcomes, which depend on the strength of the coupling $k_{\rm a}\Psi_0$. For small enough couplings to the Maxwell sector, the axion field is left unaffected, and remains in a bound state of (near) constant amplitude around the BH. For large couplings however, in what we term the *supercritical* regime, the amplitude of the axion field decreases. This transition signals a parametric instability whereby axions are quickly converted into photons.

The bottom panel of Fig. 5.2 shows the behavior of the EM radiation during this process (we show only the dipolar component $\ell = m = 1$ of the Newman-Penrose scalar, but we find that higher modes are also excited to important amplitudes, see Appendix J.2). In the subcritical regime, any initial EM fluctuation decays on short timescales. However, in the supercritical regime a burst is initiated; these are the photons that are created by the axion cloud. Furthermore, we find the growth rate to follow estimates from earlier work [172]. Specifically, it is approximated by taking the production rate of the photons and subtracting the rate at which photons leave the cloud: $\lambda \sim \lambda_* - \lambda_{\rm esc}$, where $\lambda_* \sim \frac{1}{2}\mu k_{\rm a}\Psi_0$ and $\lambda_{\rm esc} \sim 1/d$, where d is the size of the cloud. This estimate is indicated by the blue dashdotted line in Fig. 5.2.

At late times, the system settles to a final, stationary state. In the subcritical regime, this final state is almost the same as its initial state since the axion cloud is barely affected by the EM perturbation. Conversely, in the supercritical regime, the parametric instability has driven the axion field to decrease to a subcritical value. Therefore, in the absence of SR growth, no further instability can be triggered and the axion cloud settles on a final state with a lower amplitude than its initial value while the created photons travel outwards.

5.3.2 Axion and photon emission

Although the axion is massive, EM waves are massless and allowed to travel freely once outside the cloud. To study EM wave propagation, we monitor the system at large radii. The top panel of Fig. 5.3 summarizes our findings for EM radiation, where we align waveforms in time. Some features are worth noting: (i) we find that Φ_2 decays like the inverse of the distance to the BH, as might be expected for EM waves; (ii) the pattern of the waveform is not changing as it propagates, typical of massless fields. The radiation travels at the speed of light, as it should.

Additionally, we observe an interesting morphology in the EM burst. It has a high-frequency component slowly modulated by a beating pattern. While the high-frequency component is set by the boson mass μ, with oscillation period $\sim 2\pi/(\mu/2)$, the beating frequency scales with $1/\mu^2$ as its origin lies with the presence of the cloud. Specifically, when the photons are produced inside the cloud, they travel through it allowing for further interactions. These photon “echoes” exhibit a symmetric frequency distribution with respect to the primary photons, lying around $\mu/2$. This can be seen in the Fourier transform in the bottom panel of Fig. 5.3. The frequency difference between these peaks, $\Delta\omega$, corresponds to the observed beating timescale, $\sim 2\pi/\Delta\omega$, indicated by the dashed lines in the top panel of Fig. 5.3. In addition to the bulk of photon frequencies near half the axion mass, there are other peaks in the frequency domain, namely two around $M\omega \sim 0.45$. We believe these higher order peaks do not originate from a parametric resonance, as one would expect peaks for each integer N at $N\mu/2$, while we find the peaks at *even* N to be absent. Furthermore, the bandwidth of higher order parametric resonances is extremely small, making it hard to trigger those. We rather believe these additional peaks to be a result from photon “echoes” as well, generated at later times, i.e., photons produced by the parametric mechanism that are up-scattered by the axion cloud. These results are different from a homogeneous axion background, where only echoes with the same frequency are produced. The discrepancy is due to the large momentum tail of the axion cloud.

Besides the expected EM radiation, the reverse process – two photons combining to create an axion – may also provide a non-negligible contribution. In fact, this process has been explored in the context of axion clusters [211], where energetic axions are created that can not be stimulated anymore, hence they escape the cluster (so-called “sterile axions”). Projecting this scenario in the context of SR instabilities translates into the creation of unbound axion states, with frequencies $\omega > \mu$, that are thus able to escape to infinity. Such axion waves are indeed produced in our setup, as can be seen in Fig. 5.4. The large scalar field contribution far away from the cloud is *only* present the supercritical regime. Since these are massive waves, the dependence with time and distance from the source is less simple due to dispersion. As components with different frequencies travel with different velocities, the wave changes morphology when traveling to infinity, which is apparent in the top panel of Fig. 5.4.

The Fourier transform of the axion waves is shown in the bottom panel of Fig. 5.4. It indeed contains components with frequency $\omega > \mu$, showing that the field is energetic enough to travel away from the source. The frequencies of the peaks correspond to a group velocity $v = \sqrt{1 - \mu^2/\omega^2} = 0.036$ and $v = 0.18$ for

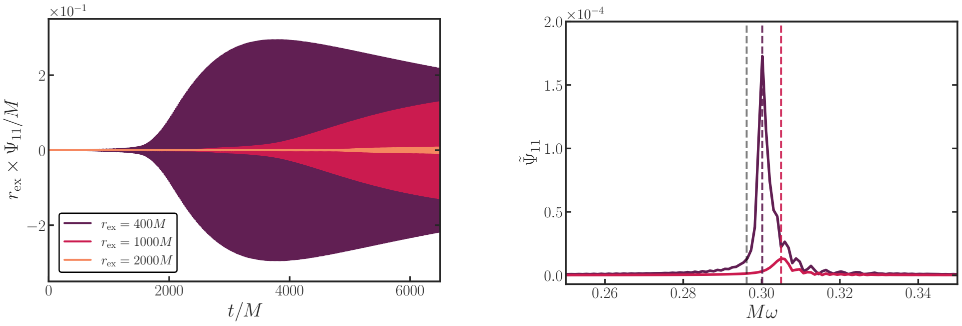

Figure 5.4. **Top Panel:** The dipolar component of the axion field in the supercritical regime (simulation $\mathcal{I}_3$). When extracted at large radii, the non-zero value of Ψ_{11} is only present in the supercritical regime and explained by the production of axion waves. Due to dispersion, the morphology of the wave changes while traveling outwards. **Bottom Panel:** The Fourier transform of the dipolar component, taken on the entire time domain shown in the top panel. The gray dashed line shows the frequency of the fundamental mode of the bound state, while the coloured dashed lines indicate the frequency of the peak of each curve situated at $\omega > \mu$, confirming these are axion waves.

$r_{\rm ex} = 400M$ and $r_{\rm ex} = 1000M$, respectively. Note that this Fourier transform is taken over the full time domain and thus dominated by the late signal of the axion waves, consisting of larger amplitude, non-relativistic waves. This also explains why the peak for the $r_{\rm ex} = 1000M$ curve is at higher frequency; the slower waves did not have time to arrive yet at this larger radius. If we instead calculate the Fourier transform on only the first part of the signal, we capture the (more) relativistic components. These emitted axion waves can in principle be detected by terrestrial axion detectors if the BH is close enough to Earth.

Besides the dipole component, also higher order scalar multipoles are created by the photons. In fact, from our initial data, only scalar multipoles with odd ℓ can be produced. This selection rule is detailed in Appendix L. The higher multipoles for both the axion and photon radiation are shown in Appendix J.2, where it can also be seen that excited photons can recombine to create axion waves with twice the axion mass.

5.4 Superradiance turned on

The formation of an EM burst is determined by whether the photon production from the parametric instability is dominant over the escape rate from the cloud or vice versa. The initialization of the system in a supercritical state however, is artificial. Instead, it starts in the subcritical regime and potentially grows supercritical through SR. Previous works claimed that this process developed through a burst-quiet sequence: a burst of EM and axion waves would deplete the cloud, which would then grow on a SR timescale before another burst occurred [171]. We argue that in fact bursts do not occur, and that the process is smoother than thought. As we will show, the presence of SR introduces two important differences: (i) the growth rate of the EM field is modified and (ii) the system is forced into a stationary phase.

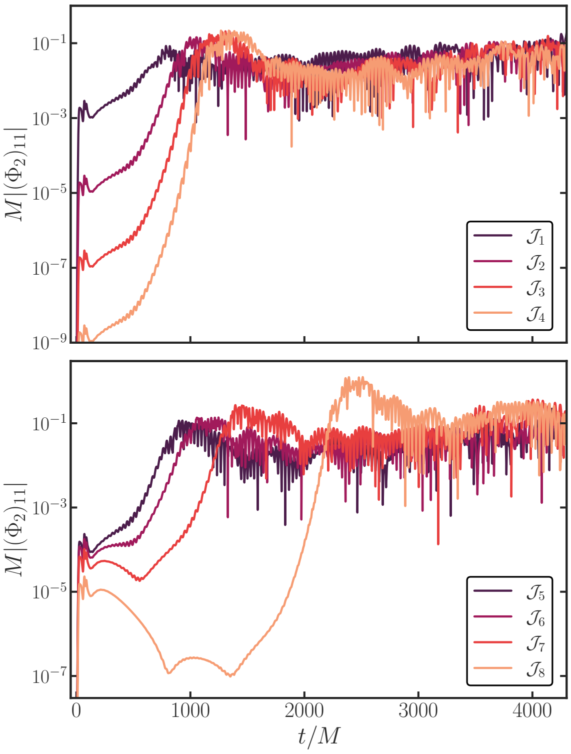

Figure 5.5. Top Panel: The time evolution of the dipolar component of the EM field including SR growth for different strengths of the initial EM pulse (see Table 5.1). The field is extracted at $r_{\text{ex}} = 20M$ and $\mu M = 0.2$. **Bottom Panel:** Same as above, but while varying the initial coupling strength $k_{\text{a}}\Psi_0$. Notice how a stationary state is reached instead of a burst of EM waves. Moreover, the final EM value is independent of initial conditions, even though the timescale required to reach saturation does depend on how the fields were initialized.

5.4.1 Numerical results

We numerically evolve the coupled axion-photon system under the influence of a SR growing cloud. In these simulations, we start the system in the subcritical regime, and let it evolve to supercriticality via (artificial) SR, since now $C \neq 0$.

Figure 5.5 illustrates the behaviour of the system. We evolve different initial conditions, corresponding to different seed EM fields E_0/Ψ_0 and different couplings $k_{\text{a}}\Psi_0$, and we see a *saturation* of the EM field, to a value which is independent on the initial conditions.[4] This stability is simply achieved by turning on SR growth like in equation (5.4). In contrast to the previous section where the bound state solely loses energy, the supplement to the axion cloud is dominant at first, resulting in exponential growth. As the cloud approaches the critical value, parametric decay to the EM field begins to compensate for the energy gain from the BH, ultimately reaching a phase where energy gain and loss are balanced. As a result, the entire system consisting of the axion cloud and the EM field is constantly pumped by SR

---

[4] As could be anticipated, the timescale to reach saturation does depend on initial conditions: lower field values or lower couplings require larger timescales.

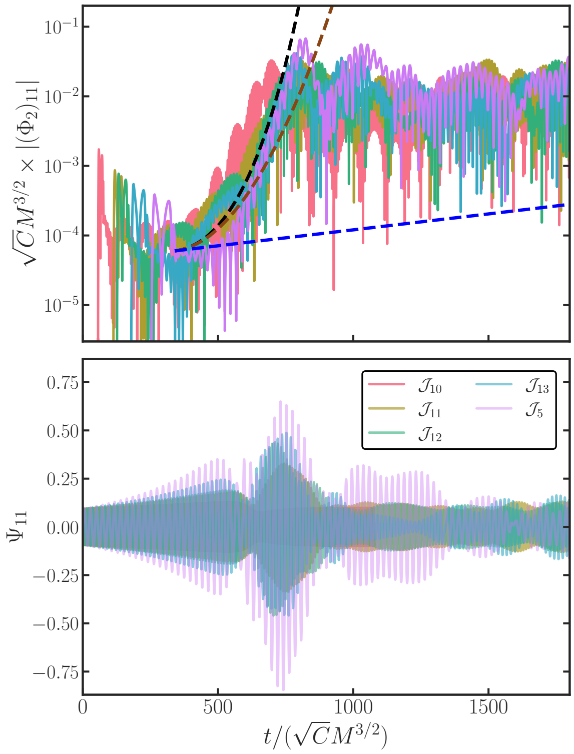

Figure 5.6. Top Panel: The dipolar component of EM radiation with SR turned on. The field is extracted at $r_{\rm ex} = 400M$ and $\mu M = 0.2$. The blue, black and brown dashed lines show the growth rate predicted by the standard Mathieu equation, the SR Mathieu equation (5.9) and its first order expansion (5.10), respectively. The value of C is varied for simulations $\mathcal{J}_i$, see Table 5.1. Note the rescaling on both the horizontal and vertical axis with $\sqrt{C}$, where we scale all simulations onto $\mathcal{J}_{14}$. Thus, our results indicate a clear, simple dependence on the SR rate, which we investigate analytically below in Section 5.4.2 and 5.4.3. **Bottom Panel:** Same as above, but for the scalar dipolar component extracted at $r_{\rm ex} = 20M$.

growth, with a steady emission of EM waves traveling outwards.

The saturation value of the EM field does depend on the SR parameter C. This is simply due to the fact that the more axions that are created by SR, the more photons that can be produced through the parametric mechanism. We find the saturation value to be proportional to $\sqrt{C}$, shown in the top panel of Fig. 5.6. This result is also supported by analytical estimates in Section 5.4.3, in particular equation (5.15). Additionally, our results demonstrate that the timescale required to reach saturation (at fixed initial field values), scales with $\sqrt{C}$ as well. This behaviour is explained in the following section.

These simulations provide us with robust evidence that the saturation phase is (i) independent of the initial data, and (ii) occurring for all tested values of C which span 2 orders of magnitude, allowing for universal predictions. In the following, we discuss various features related to the saturation phase.

Evolution of the cloud's morphology – When the system has just reached the critical boundary, the EM field starts growing (super-)exponentially until it reaches

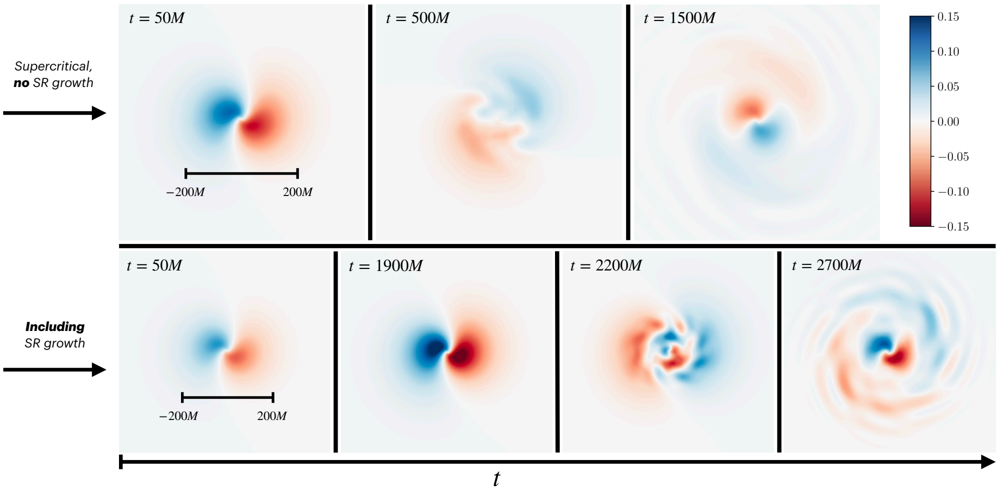

Figure 5.7. Snapshots of the axion profile during the evolution of the axion-photon system. Upper row shows the system in the supercritical regime (simulation $\mathcal{I}_3$), but *without* SR growth. The cloud starts in its initial dipole state, and gets disrupted by the parametric instability. Afterwards the configuration settles down while axion waves propagate to infinity. On the bottom row, we show an initially subcritical cloud, yet *with* SR growth turned on, $C = 10^{-3}M^{-1}$ (simulation $\mathcal{J}_{12}$). Again, the cloud starts in its dipole mode, yet now it grows in amplitude due to SR. Afterwards, the cloud is disrupted due to the EM instability, eventually settling down to a saturation phase wherein axion waves are continuously produced.

the saturation value. When this happens, the non-linear backreaction in the Klein-Gordon equation becomes important. In absence of SR, the EM field quickly decays in time after reaching its maximum and with that its backreaction onto the axion field, allowing the cloud to settle back to a stable configuration at late times (see Fig. 5.2). Conversely, in presence of SR, the EM field settles to a large and constant value that continuously backreacts onto the axion field. Consequently, it starts to exhibit strong deviations from the initial pure bound state configuration as overtones are triggered, i.e., it acquires a beating-like pattern. This can be seen in Fig. 5.6, where around $t \sim 700\sqrt{C}M^{3/2}$ the saturation phase ensues and there is no relaxation to the pure quasi-bound state. We show a series of snapshots from the cloud's evolution in the two distinct scenarios in Fig. 5.7.

Angular structure of outgoing EM waves – During the saturation phase, there is a nearly constant emission of EM waves. For observational purposes, we probe the angular structure of the outgoing radiation. We do this through the multipole components of Φ_2, while up to now only the dipole was considered. A subset of these multipoles is shown Fig. 5.8. From the differences in amplitude between different modes, we conclude that the radiation is not isotropic. In fact, we find that the dominant radiation is on the equatorial plane (see inset of Fig. 5.8), where the density of the axion cloud is highest. To strengthen this result, we also compute analytically the excitation coefficients of these multipoles given our initial data. We report them in Appendix L.

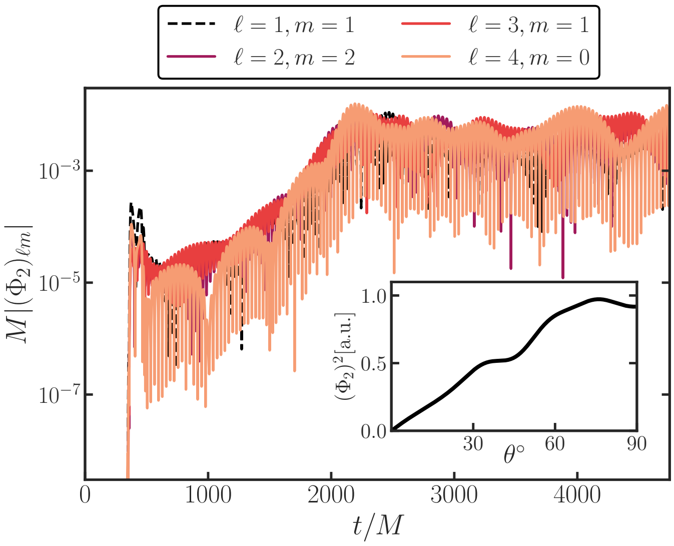

Figure 5.8. A subset of the multipoles of the EM field for simulation $\mathcal{J}_{12}$, extracted at $r_{\rm ex} = 400M$. Every multipole up to $\ell \leq 6$ has approximately a similar contribution. The inset shows the angular structure of the outgoing EM waves in the saturation phase (where all multipoles up to $\ell \leq 8$ are taken into account). The y axis is reported in arbitrary units (a.u.). The dominant production of the photons is on the equatorial plane where the cloud's density is highest.

5.4.2 Growth rate

In previous work [172], it was shown that in absence of SR, the growth rate of the EM field can be approximated by a simple, analytical expression. This is a consequence of the fact that when the background spacetime is Minkowski and the background axion field is a coherently oscillating, homogeneous condensate, the Maxwell equations can be rearranged in the form of a Mathieu equation [172, 212]. The growth rate is then found by taking the production rate of the photons ($\sim$ the Floquet exponent of the dominant, unstable mode of the Mathieu equation) and subtracting the escape rate of the photons from the cloud ($\sim$ inverse of the cloud size). However, while this approach yields accurate predictions in absence of SR (see Fig. 5.2), it does not in presence of SR (blue dashed line in Fig. 5.6). Remarkably, as we will show, a simple adjustment to the Minkowski toy model restores its validity. Additional details are provided in Appendix K.1.

Let us consider the Maxwell equations in flat spacetime. We adopt Cartesian coordinates and assume the following ansatz for the EM field,

$$A_\mu(t, \vec{x}) = \alpha_\mu(t, \vec{p}) e^{i(\vec{p}\cdot\vec{x} - \omega t)}\,, \tag{5.6}$$

where $\vec{p}$ is the wave vector which we assume to be aligned in the $\hat{z}$ direction without loss of generality, i.e., $\vec{p} = (0, 0, p_z)$. To mimic the amplification of the axion field via

SR, we consider a homogeneous condensate which exponentially grows in time as[5]

$$\Psi = \frac{1}{2}(\psi_0 e^{-i\mu t} + \psi_0^* e^{i\mu t})e^{Ct}\,. \tag{5.7}$$

Adopting the field redefinition $y_k = e^{i\omega t}\alpha_k$, rescaling the time as $T = \mu t$ and projecting along a circular polarization basis $e_\pm$ such that $y = y_\omega e_\pm$, we obtain a "superradiant" Mathieu-like (SM) equation:

$$\partial_T^2 y_\omega + \frac{1}{\mu^2}\Big(p_z^2 + 2p_z e^{\frac{CT}{\mu}}\psi_0 k_{\mathrm{a}}(C\cos T - \mu\sin T)\Big)y_\omega = 0\,. \tag{5.8}$$

Unsurprisingly, for $C = 0$, this equation reduces to the original Mathieu equation.[6] From (5.8), we find two new features; an extra oscillating term $\sim C\cos T$, and, most importantly, an exponentially growing factor $\sim e^{\frac{CT}{\mu}}$. By solving (5.8) numerically, we find that, similar to the standard Mathieu equation, this equation admits instability bands, albeit with a larger growth rate. Fitting the exponent of the numerical solution, we conclude that the solution to the superradiant Mathieu equation is well described by a super-exponential expression $y_\omega \sim e^{\lambda_{\mathrm{SM}} t}$, with

$$\lambda_{\mathrm{SM}} = \frac{\mu}{2} k_{\mathrm{a}}\psi_0 e^{Ct/2}\,. \tag{5.9}$$

In Appendix K.1, we show the comparison between this expression and the numerical solutions as well as an analytic derivation of (5.9) using a multiple-scale method.

We confront the growth rate of the EM field when considering the full axion-photon system in a Schwarzschild background with the growth rate from our toy model (5.9) in Fig. 5.6. Here, the standard Mathieu growth rate (blue dashed line), the full solution and first order expansion in C (black and brown dashed lines, respectively) can be seen, where the latter is defined by

$$\lambda_{\mathrm{SM}} t \approx \frac{\mu}{2} k_{\mathrm{a}}\psi_0 (t + \frac{Ct^2}{2})\,. \tag{5.10}$$

In all of the curves, the time it takes for photons to leave the cloud has been taken into account. Furthermore, we use the critical value for the coupling $k_{\mathrm{a}}\Psi_0$. Remarkably, the SM growth rate matches the numerical results closely. Moreover, the Ct^2 term from (5.10) that appears at first order naturally explains why the timescale to reach saturation scales as $\sqrt{C}$.

Hence, when considering the axion-photon system under the influence of SR, a simple extension to Mathieu equation allows for elegant, analytic predictions of our numerical results. Note that the true value for SR is many orders of magnitude lower than the one considered in this work and thus we expect the correction to be subdominant (unlike here). Finally, this prediction neglected the backreaction onto the axion cloud. Hence, it naturally breaks down when the rate of energy loss due to conversion to photons becomes comparable the SR growth, i.e., when the saturation phase ensues.

---

[5] We adopt a different notation to distinguish the amplitude of the homogeneous axion field in this toy model, ψ_0, with the one of the axion cloud around the BH, Ψ_0.

[6] Our result includes a sine instead of the cosine found in [172], which originates from a small sign mistake in their derivation, see equation (19). This has no consequences for the physics, as it only induces a $\pi/2$ phase shift.

5.4.3 Saturation phase

As can be seen in Figs. 5.5 and 5.6, turning on SR growth forces the system into a stationary configuration. Here, the energy loss of the cloud due to the parametric instability balances the SR pump sourced by the rotational energy of the BH. A description of this phase is remarkably simple as we will show below. A similar conclusion was found in [198].

For the photons to reach an equilibrium phase, it is required that the parametric decay rate, $\lambda_{\rm pd}$, equals the escape rate of the photon, $\lambda_{\rm esc}$. Assuming that the former can be approximated by the decay rate in the homogeneous condensate case [172, 212], we have

$$\lambda_{\rm pd} \approx \frac{k_{\rm a}\Psi_{\rm sat}\mu}{2} \approx \frac{1}{d} \approx \lambda_{\rm esc}\,, \tag{5.11}$$

where $\Psi_{\rm sat}$ is the average amplitude of the scalar field *within the cloud* at saturation. In the non-relativistic regime, we can approximate the size of the cloud by the standard deviation of the radius $d = \langle r\rangle \approx 2\sqrt{3}r_{\rm c} = 4\sqrt{3}/(\mu^2 M)$. This yields a relation for which the cloud reaches saturation, namely

$$k_{\rm a}\Psi_{\rm sat} \approx \frac{\mu M}{2\sqrt{3}}\,. \tag{5.12}$$

This is indeed what we find in the bottom panel of Fig. 5.6, since $k_{\rm a}\Psi_{\rm sat} \approx 0.2/(2\sqrt{3}) \approx 0.06$.

Additionally, we consider the equilibrium condition of the axion cloud. It is sourced by the SR rate $\Gamma_{\rm SR}$, yet loses energy due to the parametric instability, $\Gamma_{\rm PI}$. In our setup, these two rates are

$$\Gamma_{\rm SR} = \frac{C}{2} \quad \text{and} \quad \Gamma_{\rm PI} \approx 2\Gamma_{\Psi\to\gamma\gamma} f_\gamma\,, \tag{5.13}$$

where $\Gamma_{\Psi\,\to\,\gamma\gamma} = \hbar k_{\rm a}^2\mu^3/(16\pi)$ is the perturbative decay width of the axion-to-photon conversion and f_γ is the photon occupation number. When the dominant production is in a narrow band around $p_\gamma = \mu/2$, we have [213]

$$f_\gamma(p_\gamma = \mu/2) = \frac{8\pi^3 n_\gamma}{4\pi p_\gamma^2 \Delta p_\gamma} \approx \frac{2\pi^2 A_\gamma^2}{\hbar k_{\rm a}\Psi_{\rm sat}\mu^2}\,, \tag{5.14}$$

where $\Delta p_\gamma \approx 2k_{\rm a}\Psi_{\rm sat}\mu$ is the photon dispersion bandwidth, approximated to be the resonant bandwidth at $p_\gamma = \mu/2$. Moreover, A_γ is the photon amplitude, which relates to our measure of the EM field Φ_2 as $A_\gamma \sim 2\Phi_2/\omega$, where $\omega \sim \mu$ is the frequency of the axion field. Finally, $n_\gamma = 2\rho/(\hbar\omega)$ is the photon number density, with $\rho = A_\gamma^2\omega^2/2$ the energy density. Substituting these relations into (5.13), we find that inside the cloud

$$\frac{A_\gamma^2}{\Psi_{\rm sat}^2} \approx \frac{2C}{\pi\mu k_{\rm a}\Psi_{\rm sat}} \approx \frac{C}{\pi\lambda_{\rm esc}}\,, \tag{5.15}$$

were we used again (5.11). Hence, this simple analytical estimate shows that the EM field stabilizes to a value proportional to $\sqrt{C}$. This result is in excellent agreement with our simulations (see Fig. 5.6) and it allows us to consider a case in which C coincides with the SR growth timescale.

The total energy flux of the photons with frequency $\mu/2$ is defined as [198]

$$\frac{\mathrm{d}E}{\mathrm{d}t} = \frac{\hbar\mu}{2} n_\gamma \lambda_{\mathrm{esc}}\, \chi r_{\mathrm{c}}^3 \,, \tag{5.16}$$

where χr_{c}^3 is the volume of the cloud. Here, χ is a numerical factor where in the non-relativistic regime, $\chi \approx \mathcal{O}(10^2)$.[7] Assuming the SR rate Γ_{SR} to be equal to the decay rate Γ_{PI} in the saturation phase (5.13), we get that

$$\begin{aligned}\frac{\mathrm{d}E}{\mathrm{d}t} \approx 7.6 \times 10^{45} &\left(\frac{\chi}{100}\right)\left(\frac{2.5\times 10^2 M}{\tau_s}\right) \\ \times &\left(\frac{0.2}{\mu M}\right)^2 \left(\frac{10^{-13}\mathrm{GeV}^{-1}}{k_{\mathrm{a}}}\right)^2 \mathrm{erg/s}\,,\end{aligned} \tag{5.17}$$

where $\tau_s = C^{-1}$. To probe the SR regime, we tune C to match the well-known SR growth rate in the dominant growing mode [73]

$$\Gamma_{\mathrm{SR}} \approx \frac{a_{\mathrm{J}}\,(\mu M)^9}{24M} \quad \text{when} \quad \mu M \ll 1\,, \tag{5.18}$$

where a_{J} is the spin of the BH. Using this in (5.17), we obtain

$$\begin{aligned}\frac{\mathrm{d}E}{\mathrm{d}t} \approx 8.1 \times 10^{40} &\left(\frac{\chi}{100}\right)\frac{a_{\mathrm{J}}}{M} \\ \times &\left(\frac{\mu M}{0.2}\right)^7 \left(\frac{10^{-13}\mathrm{GeV}^{-1}}{k_{\mathrm{a}}}\right)^2 \mathrm{erg/s}\,.\end{aligned} \tag{5.19}$$

Note how lower couplings lead to higher fluxes. Although this may sound counterintuitive, it is explained by the fact that for lower couplings, the axion field saturates at higher values. As the EM flux is proportional to the axion field value, this leads to a higher flux. [8] As a consequence, the saturation phase opens a channel to constrain axionic couplings “from below”. Finally, the divergence of (5.17) and (5.19) at small couplings indicates when our model breaks down. In particular, the equilibrium condition (5.12) suggests a minimum value for the coupling for which the cloud's mass becomes larger than its maximum of $M_{\mathrm{c}} = 0.1M$. For example, for $\mu M = 0.2$, the minimum coupling for which our description holds is $k_{\mathrm{a}} > 3.8 \times 10^{-18}$ GeV^{-1}. Lower couplings then this yield an unphysical situation and thus a breakdown of our description.

---

[7] To obtain χ, we introduce a threshold value ϵ for the absolute value of the scalar field, and define

$$\chi = \int_0^\infty \mathrm{d}r\, r^2 \int \mathrm{d}\Omega\, \Theta\left(|\Psi| - \epsilon\right)\,,$$

where Θ is the Heaviside step function and $\epsilon \sim 0.5 \max(\Psi)$. We checked that the order of χ does not strongly depend on ϵ.

[8] A similar behaviour was found in the context of dark photons with kinetic mixings to the Standard Model photon [175].

5.4.4 Implications for superradiance

Using the scaling relation (5.15), we can probe the system in the regime of SR and thereby test the validity of (5.19) with our numerical simulations. Before doing so, however, we must argue why we are able to extend our results beyond the probed regime for C.

Either end of the tested parameter space for C is accompanied by numerically challenges. For high C, there is an extreme growth on short timescales which makes the code diverge. For low C, the evolution timescale of the system becomes prohibitively large. Besides the simulations shown in Fig. 5.6, we did two additional simulations, $\mathcal{J}_9$ (low C) and $\mathcal{J}_{14}$ (high C), on each end of the spectrum. Regarding the latter, we find indications that the saturation phase is ruined as the EM field starts to grow from its saturation value after spending some time in the saturation phase. Physically, this is to be expected. In the case of extreme SR growth, the balance between the production and escape rate of the photons is distorted; the photons simply do not have time to escape the cloud while plenty of axions are produced. In this scenario, a more burst-like radiation pattern could be possible.[9] Since we are interested in SR in this work, we do not probe this regime further.

The regime of low C is of interest as the SR rate is at significantly lower values than what we can probe numerically (5.18). From the lowest C we probe, $\mathcal{J}_9$, we find that even though there is an apparent decrease after the super-exponential growth, the $\sqrt{C}$ scaling is respected at late times. Physically, the perseverance of the saturation phase makes sense. When the growth rate is small, the system becomes adiabatic; as the axions are slowly produced, the system steadily approaches the critical value at which the system is in equilibrium and a saturation phase ensues.

To extract the energy flux from our simulations, we exploit the properties of the Newman-Penrose scalar. In particular, we can define

$$\frac{\mathrm{d}^2 E}{\mathrm{d}t\mathrm{d}\Omega} = \lim_{r\to\infty} \frac{r^2}{2\pi} |\Phi_2|^2 \,, \tag{5.20}$$

where $\mathrm{d}\Omega \equiv \sin\theta \mathrm{d}\theta \mathrm{d}\varphi$. Decomposing (5.20) in terms of spin-weighted spherical harmonics, we obtain

$$\frac{\mathrm{d}E}{\mathrm{d}t} = \sum_{\ell m} \int \mathrm{d}\Omega \, \frac{1}{2\pi} |(\Phi_2^\circ)_{\ell m} \; {}_{-1}Y_{\ell m}|^2 \,, \tag{5.21}$$

where $\Phi_2 = \Phi_2^\circ / r$. From our simulations, we extract $(\Phi_2)_{\ell m,\mathrm{sim}}$ for a certain C_sim at large radii ($r = r_\mathrm{ex}$) by averaging over a sufficient period in the saturation phase. Then, we scale these multipoles to match their saturation value in the case of SR according to

$$(\Phi_2)_{\ell m,\mathrm{SR}} \approx \frac{(\Phi_2)_{\ell m,\mathrm{sim}}}{\sqrt{C_\mathrm{sim}/(2\Gamma_\mathrm{SR})}} \,, \tag{5.22}$$

where Γ_SR is defined in (5.18). We do this for each multipole and sum them according to (5.21) to obtain the total flux. As the contribution to the energy flux becomes smaller for higher multipoles, we sum each multipole until the increment is less

---

[9] Such a scenario could be realized in the case of a Bosenova [204], where the axion density sharply rises on short timescales.

than 5%. In practice, this means summing the first ~ 8 values of ℓ. Following this procedure, we find the following estimate from our simulations for the total, nearly constant, energy flux in the saturation phase:

$$\frac{\mathrm{d}E}{\mathrm{d}t} = 9.10 \times 10^{40} \left(\frac{10^{-13}\ \mathrm{GeV}^{-1}}{k_{\mathrm{a}}}\right)^2 \mathrm{erg/s}\,, \tag{5.23}$$

where we assumed $\mu M = 0.2$ and the BH to be maximally spinning. This matches closely the theoretical prediction from (5.19).

Besides the photon production, the parametric instability also affects the axion cloud. As we showed in equation (5.12), the axion amplitude at saturation is independent of C. By translating the amplitude of the axion field to the mass of the cloud, the impact of coupling axions to photons becomes much more apparent [87]. It is well-established that, in the purely gravitational case, the cloud is able to obtain a maximum mass of $M_{\mathrm{c}} \lesssim 0.1M$. As can be seen in Fig. 5.9, through the coupling to the Maxwell sector, the cloud's mass can saturate significantly below this maximum. Note that in this estimate, we assume the profile of the cloud to be hydrogen-like which is only strictly true in the no-coupling case. Consequently, when the cloud is disrupted due to the strong backreaction onto the axion field in the saturation phase, this approximation is not expected to hold. Nevertheless, for the (much) lower SR growth rate, the EM flux is less strong and thus the cloud less disrupted.

Figure 5.9 has severe implications for current constraints on the mass of ultralight bosons that are set through either GW searches [214, 101, 215, 216, 217] or spin measurements of BHs [89, 218, 87, 90, 91, 219, 220, 193, 196, 221, 194]. Due to the reduced cloud mass, the backreaction to the spin down of the BH could be negligible, which means current constraints no longer apply, as they assume no interactions for the axion. Furthermore, the environmental effect of the SR cloud on the gravitational waveform in BH binaries becomes less relevant [92, 93, 94, 222, 95, 223, 224, 225, 97].

5.5 Surrounding plasma

The presence of plasma affects the axion-to-photon conversion in the parametric instability mechanism, as the transverse polarizations of the photon are dressed with an effective mass, i.e., the plasma frequency ω_{pl}. Therefore, when $\omega_{\mathrm{pl}} > \mu/2$, the process $\Psi \to \gamma + \gamma$ becomes kinematically forbidden. Even though it is common lore to approximate the photon-plasma system with a Proca toy model, the full physics is more involved: as already shown in sec. 2.3.4, already in the simplest case of a cold, collisionless plasma, the longitudinal degrees of freedom are electrostatic, unlike the Proca case (for details see [173, 174]). In curved space, these transverse and longitudinal modes are coupled and thus the Proca model cannot assumed to be correct a priori. Moreover, non-linearities provide additional couplings between the modes, and also the inclusion of collisions or thermal corrections create strong deviations from a Proca theory. Hence, a consistent approach from first principles is imperative. In this section, we take a first step in that direction by studying a linearized axion-photon-plasma system.

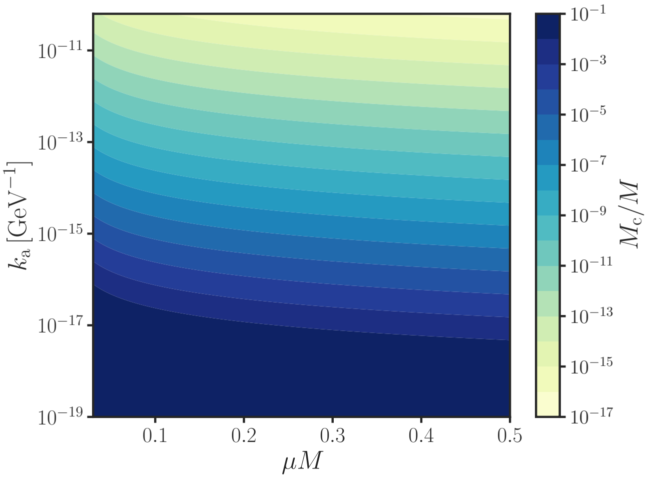

Figure 5.9. Contour plot of the mass of the cloud (M_c) *at saturation* depending on the axionic and mass coupling, $k_a\Psi_{sat}$ and μM, respectively. The dark blue area at the bottom denotes the maximum mass of 10% that the cloud can achieve in the purely gravitational case.

5.5.1 Without superradiance

We start by studying the axion-photon-plasma system in absence of SR, and initialize the axion cloud in a supercritical state with $k_a\Psi_0 \ll 1$. We evolve the system on a BH background for different values of the plasma frequency (see Table 5.1). Note that there is no backreaction onto the axion field in our linearized setup.

Figure 5.10 summarizes the main results. When $\omega_{pl} < \mu/2$, the plasma has little impact on the system and the parametric instability ensues. When $\omega_{pl} \geq \mu/2$ instead, a suppression of the photon production is seen. We find the growth rate estimated in equation (19) of [199] to fit our simulations well, when taking into account the finite-size effect of the cloud as $\lambda_{esc} \sim 1/d$, i.e.,

$$\lambda \approx \frac{\mu^2\sqrt{\mu^2 - 4\omega_{pl}^2}}{2\mu^2 - 4\omega_{pl}^2} k_a\Psi_0 - \lambda_{esc}\,. \tag{5.24}$$

Finally, the beating pattern in the EM radiation at larger radii (see bottom panel of Fig. 5.10) is explained by the photons having to travel through the cloud, thereby scattering of the axions.

Additionally, we show the Fourier decomposition of the signal in Fig. 5.11. As we concluded from Fig. 5.10, for low ω_{pl}, the parametric instability is barely hindered and a clear peak arises at half the boson mass. However, when $\omega_{pl} > \mu/2$, we observe the presence of modes with a frequency very close to ω_{pl}. We find good agreement between these peaks and the plasma-driven quasi-bound states computed in a similar setup [173]. Note however, that these bound states are extremely fragile and geometry dependent, and may disappear if more realistic plasma models are considered [115]. We conjecture the origin of the two additional peaks at $\omega_{pl} \pm \mu$ to be up and down-scattering from the quasi-bound state photons with the axion cloud.

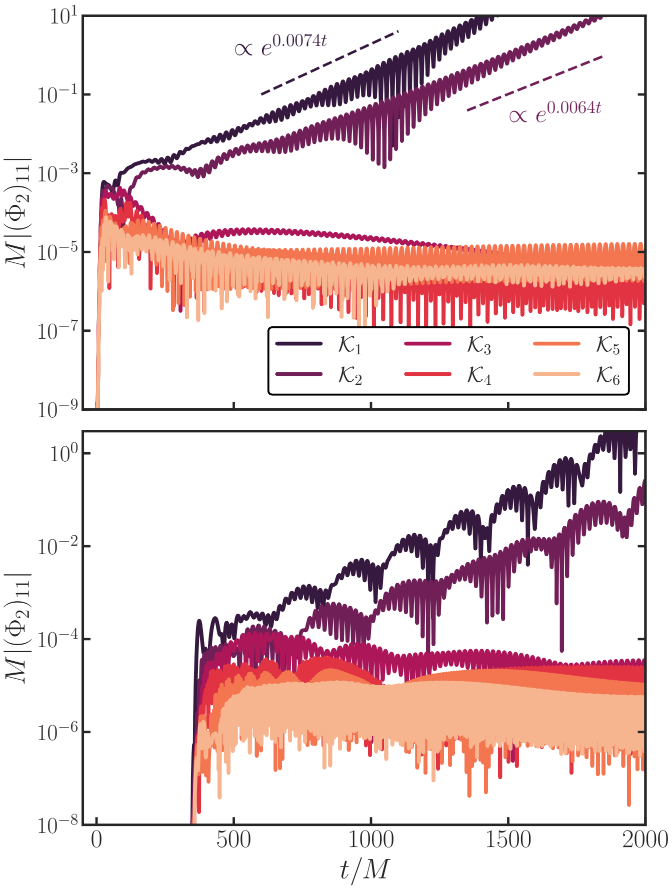

Figure 5.10. Top Panel: Time evolution of the dipolar component $|(\Phi_2)_{11}|$ of the EM field, extracted at $r_{\rm ex} = 20M$ for $\mu M = 0.3$, in the presence of plasma. The plasma frequency $\omega_{\rm pl}$ is progressively larger for simulations $\mathcal{K}_1$–$\mathcal{K}_6$, see Table 5.1. The exponential growth rate (dashed lines) is determined from (5.24). **Bottom Panel:** Same as above but now the field is extracted at $r_{\rm ex} = 400M$. The modulations arise from scattering of photons with the axion cloud, similar to Fig. 5.3.

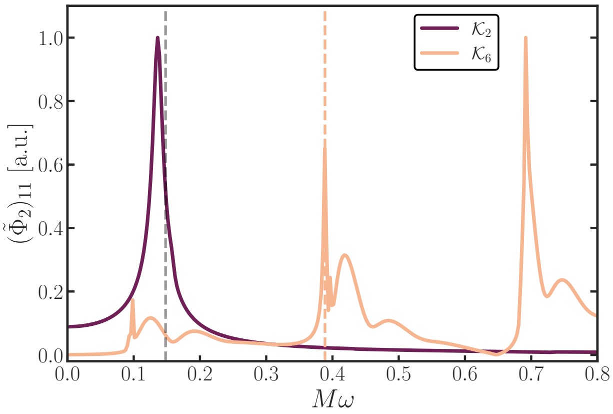

Figure 5.11. Fourier transform of $(\Phi_2)_{11}$ extracted at $r_{\rm ex} = 20M$ for simulations $\mathcal{K}_2$ ($\omega_{\rm pl} < \mu/2$) and $\mathcal{K}_6$ ($\omega_{\rm pl} > \mu/2$) with $\mu M = 0.3$. The y axis is shown in arbitrary units such that both are visible on the same figure. The gray dashed line denotes half the boson mass, while the other dashed line shows the plasma-driven quasi-bound state frequency for $\omega_{\rm pl} = 0.4$, located at $M\omega = 0.3887 - 0.0016i$.

Due to the fact that modes with frequency $\omega_{\rm pl} - \mu$ are decaying, their amplitude is highly suppressed compared to the up-converted ones.

We now focus on the high axionic coupling regime. In the toy model considered in [199], it was shown that even when $\omega_{\rm pl} \geq \mu/2$, an EM instability could be triggered for high enough $k_{\rm a}\Psi_0$. In Fig. 5.12, we confirm this prediction numerically and show, for the first time, the presence of an instability in dense plasmas. This might seem in tension with the kinematic argument that for $\omega_{\rm pl} > \mu/2$ the axion decay into two photons is forbidden. However, as we show in the inset of Fig. 5.12, the frequency centers at $\omega = \mu$ instead of the usual $\omega = \mu/2$. This suggests the photon production to be dominated by a different process, namely $\Psi + \Psi \to \gamma + \gamma$.

To support this hypothesis, we study again the connection with the Mathieu equation (see e.g. [226]). As we detail in Appendix K.1, in flat spacetime, the Maxwell equations in presence of a plasma can indeed be recast into a Mathieu equation which admits instability bands whenever $\omega^2 = p_z^2 + \omega_{\rm pl}^2 = n^2\,\mu^2/4$, with $n \in \mathbb{N}$. Therefore, when $\omega_{\rm pl} > \mu/2$, the first instability band ($n = 1$) at $\omega = \mu/2$ can indeed not be triggered, yet it is still possible to trigger the second band at $n = 2$, where $\omega = \mu$. This matches exactly the phenomenology observed in Fig. 5.12 and thus we conclude the EM instability to correspond to the second instability band of the Mathieu equation, which indeed is triggered by the process $\Psi + \Psi \to \gamma + \gamma$ (and kinematically viable even for $\omega_{\rm pl} > \mu/2$) [212]. This analysis can be continued for even higher branches. However, since these get progressively narrower, (extremely) high values of the axionic coupling could be necessary to trigger instabilities in higher bands.

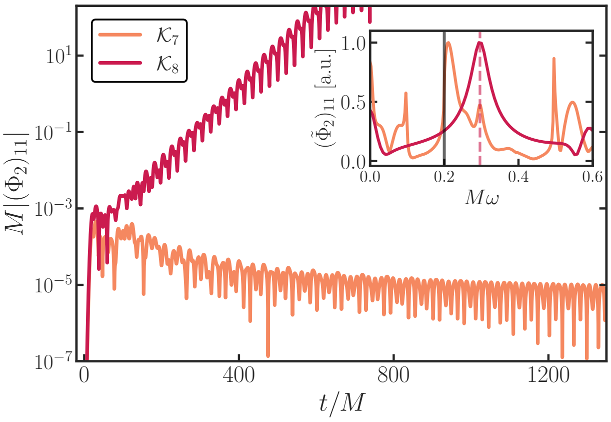

Figure 5.12. Time evolution of $|(\Phi_2)_{11}|$ extracted at $r_{\mathrm{ex}} = 20M$ for simulations $\mathcal{K}_7$ and $\mathcal{K}_8$ with $\mu M = 0.3$. Even though in both simulations $\omega_{\mathrm{pl}} = 0.2 > 0.15 = \mu/2$, the instability can be restored when $k_{\mathrm{a}}\Psi_0$ is high enough. The inset shows the Fourier transform of both curves, with the gray line indicating the plasma frequency. The red dashed line shows the frequency of the peak for $\mathcal{K}_8$, which is at $M\omega = 0.3$, indicating that the second instability band of the Mathieu solution is triggered.

5.5.2 With superradiance

We now probe the axion-photon-plasma system starting from a subcritical regime, yet letting it evolve to supercritical values via SR. Based on the previous section, we expect the system to turn unstable at some point, as the axionic coupling $k_{\mathrm{a}}\Psi_0$ grows indefinitely. Due the longer timescales associated with this process, we anticipate assumption (v), regarding the neglecting of the gravitational term, to be violated for the same parameter choices as before. Therefore, we evolve the system with $\mu M = 0.1$, such that all the assumptions are still justified.

In Fig. 5.13, we show two simulations, $\mathcal{K}_9$ ($\omega_{\mathrm{pl}} < \mu/2$) and $\mathcal{K}_{10}$ ($\omega_{\mathrm{pl}} > \mu/2$), which capture well the two distinct outcomes. In the former, the usual instability with $\omega = \mu/2$ ensues when the system has reached the supercritical threshold, yet in the latter, the time to reach this threshold is longer as the axionic coupling must grow sufficiently to trigger the second instability band. Note that, similar to the previous section, there is no backreaction onto the axion field, which therefore merely acts as a big reservoir for the EM field. This naturally explains the absence of a saturation phase. Should the backreaction be included however, there is no physical reason to expect that the saturation phase is ruined by the presence of plasma as it does not interfere with the balance between the energy inflow from the BH and energy outflow from the emitted photons. We therefore expect that the general outcome from the analysis in Section 5.4.3 still holds, aside from minor modifications.[10]

By allowing the axionic coupling to take on arbitrarily high values, an instability is thus always triggered, regardless of the plasma frequency. In practice however, it is bounded by constraints on the coupling constant k_{a} and the mass of the cloud

---

[10] For example, the presence of a plasma affects the escape rate, as photons will travel more slowly through it, i.e., $v_\gamma < c$.

(which relates to Ψ_0) when SR growth is saturated. We can estimate this maximum axionic coupling, and therefore the maximum plasma frequency (= electron density) for which an instability occurs. We do this using the flat space toy model detailed in Appendix K.2. From (K.2.9), it is immediate to see that the critical value to trigger an instability in the presence of an overdense plasma (when $\omega_{\rm pl} \gtrsim p_z$) is given by

$$k_{\rm a}\psi_0 \gtrsim \frac{\omega_{\rm pl}^2 + p_z^2}{2\mu p_z} \approx \frac{\omega_{\rm pl}^2}{\mu^2}\,. \tag{5.25}$$

This condition corresponds to the requirement that the harmonic term in the Mathieu-like equation dominates over the non-oscillatory one (cf. (K.2.9)). We have confirmed that this flat spacetime model closely matches the simulations in curved spacetime. Therefore, we can safely use the (flat spacetime) relation between the axion amplitude and the mass of the cloud [30] to obtain

$$k_{\rm a} \gtrsim 8\times 10^2 \left(\frac{\omega_{\rm pl}^2}{\mu^2}\right)\left(\frac{0.1}{M_{\rm c}/M}\right)^{1/2}\left(\frac{0.2}{\mu M}\right)^2 . \tag{5.26}$$

Note that when $\omega_{\rm pl} \approx \mu$, this condition reduces to the one derived in [171], while in the case $\omega_{\rm pl} \gg \mu$, stronger constrains on the coupling are imposed. We can translate this into the following condition for when an instability is triggered

$$\begin{aligned}\frac{10^{-13}\ {\rm GeV}^{-1}}{k_{\rm a}} \lesssim{}& 8\times 10^5 \left(\frac{10^{-3}\ {\rm cm}^{-3}}{n_{\rm e}}\right)\left(\frac{M_{\rm c}/M}{0.1}\right)^{1/2} \\ &\times \left(\frac{1M_\odot}{M}\right)^2\left(\frac{\mu M}{0.2}\right)^4 .\end{aligned} \tag{5.27}$$

Since current constraints on the coupling constant are around 10^{-13} GeV^{-1} [227], this means a plasmic environment can at least be a few orders of magnitude higher than the interstellar medium ($n_{\rm e} \in (10^{-3}, 1)$ cm^{-3}) and still an EM instability would be triggered.

5.6 Observational prospects

Based on the previous section, there are two distinct outcomes for parametric photon production in presence of plasma; (i) the dominant instability for $\omega_{\rm pl} < \mu/2$, and (ii) higher band instabilities in the regime of large axionic couplings, for $\omega_{\rm pl} > \mu/2$. In situation (i), the plasma frequency establishes a threshold for the frequency of the emitted photons. In the case of the interstellar medium, characterized by an electron density of approximately 1 cm^{-3} [228], the value of $\omega_{\rm pl}$ is estimated to be around 10^{-11} eV$/\hbar$ (2.16), corresponding to a frequency of 7.6 kHz. This should be compared to e.g. a BH with mass $5M_\odot$, which can effectively ($\mu M = 0.4$) accumulate an axion cloud with the same frequency, i.e., $\mu \approx 10^{-11}$ eV. In this case, the axion cloud would decay into pairs of photons with a frequency of approximately 3.8 kHz, which is close to the threshold value required for observation. For higher μ, the mass of the plasma can be considered negligible, and we anticipate that the primary photon flux will exhibit a nearly monochromatic energy of $\mu/2$ within the radio-frequency band.

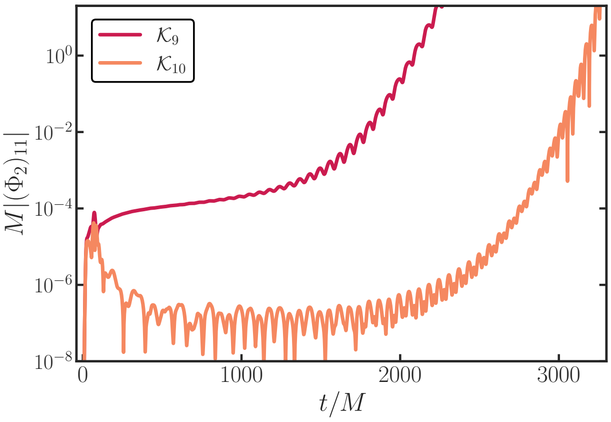

Figure 5.13. The dipolar component of EM radiation extracted at $r_{\rm ex} = 20M$ for simulations $\mathcal{K}_9$ ($\omega_{\rm pl} = 0.02$) and $\mathcal{K}_{10}$ ($\omega_{\rm pl} = 0.07$) with $\mu M = 0.1$. Although initially subcritical, SR drives the axionic coupling high enough such that an instability can occur, even when $\omega_{\rm pl} = 0.07 > 0.05 = \mu/2$.

Note however, that for higher μ, we need to invoke subsolar-mass BHs to grow the cloud on astrophysically relevant timescales. Besides the total photon flux derived analytically (5.19) and extracted from our simulations (5.23), we also demonstrate, for the first time, the anisotropic emission morphology in the frame of the BH, see Fig. 5.8. Consequently, one expects varying observer inclination angles to result in quantitatively distinct signals.

Situation (ii) presents an opportunity to observe photons produced by axion clouds beyond stellar-mass BHs. Still, the typical frequency of these photons fall below the MHz band, and thus poses a challenge for current Earth-based radio observations. However, the forthcoming moon-based radio observatories can potentially detect these signals [229]. Moreover, in the case of a rapidly spinning BHs resulting from binary mergers, one can anticipate that the radio signals will follow strong gravitational wave emissions with a delay determined by the SR timescale. Consequently, by employing multi-messenger observations between gravitational wave detectors and lunar radio telescopes, constraints can be imposed on the axion-photon coupling.

Finally, the projected saturated value of $k_{\rm a}\Psi_{\rm sat}$ can induce a rotation in the linear polarization emitted in the vicinity of BHs [230, 231]. This phenomenon has been investigated in the context of supermassive BHs [232, 233, 234]. It should be noted however that due to the significant hierarchy between the ultra-low SR mass window and the plasma mass generated by a dense environment, higher-order instabilities are not expected to occur in supermassive BHs. Consequently, the axion cloud outside an supermassive BH remains robust against axion-photon couplings.

5.7 Conclusions

In this chapter, we performed a detailed numerical study of the dynamics of boson clouds around BHs with axionic couplings to the Maxwell sector. We demonstrate the existence of an EM instability, thereby confirming previous studies. However, while those works assumed that the cloud is allowed to grow before turning on the coupling, we relax this assumption and study the axionic coupling simultaneously with the growth of the cloud, conform to the SR mechanism. We find that, in this setup, a stationary state emerges, wherein every produced axion by SR is converted into photons that escape the cloud at a steady rate. This leads to strong observational signatures, as the nearly monochromatic and constant EM signal could have a luminosity comparable with some of the bright- est sources in our universe. Moreover, the depletion of the axion cloud impacts current constraints on the boson mass. Additionally, we study the influence of a surrounding plasma on the EM instability. In the regime of small axionic couplings, we find the expected suppression of the instability when the plasma frequency exceeds half the boson mass. Surprisingly however, the instability can be restored for high enough couplings. We show how the Maxwell equations in presence of plasma reduce to a Mathieu equation, which naturally explains how the restoring of the instability is associated with higher-order instability bands. With this interpretation in mind, we conclude that (very) dense plasmas do not necessarily quench the parametric instability; it solely depends on the value of the axionic coupling.

Chapter 6

Superradiant Instabilities by accretion disks in Scalar-Tensor Theories

Summary

We study the superradiant instability in scalar-tensor theories of gravitation, where matter outside a black hole provides an effective mass to the scalar degree of freedom of the gravitational sector. We discuss this effect for arbitrarily spinning black holes and for realistic models of truncated thin and thick accretion disks (where the perturbation equations are nonseparable), paying particular attention to the role of hot coronal flows in the vicinity of the black hole. The system qualitatively resembles the phenomenology of plasma-driven superradiant instabilities in General Relativity. Nevertheless, we show that the obstacles hampering the efficiency of plasma-driven superradiant instabilities in General Relativity can be circumvented in scalar-tensor theories. We find a wide range of parameter space where superradiant instabilities can be triggered in realistic scenarios, and discuss the constraints on scalar-tensor theories imposed by this effect. In particular, we argue that the existence of highly spinning accreting black holes is in tension with some scalar-tensor alternatives to the dark energy, e.g. symmetron models with screening.

6.1 Superradiant instabilities triggered by accretion disks

Scalar-tensor theories are among the most interesting and well-studied extensions of General Relativity (GR). In this class of theories, the gravitational sector includes one or more scalar fields which are nonminimally coupled to the standard metric. A quite general action of scalar-tensor theories with one scalar field reads [36]:

$$S = \frac{1}{16\pi G}\int d^4x\sqrt{-g}[\mathcal{F}(\phi)R - Z(\phi)g^{\mu\nu}\partial_\mu\phi\partial_\nu\phi - -U(\phi)] + S_m(\psi_m, g_{\mu\nu})\,, \quad (6.1)$$

where R is the Ricci scalar, $g_{\mu\nu}$ is the metric, ϕ is a scalar field, and the last term denotes the action of matter fields minimally coupled to the metric. Depending on the expressions of the functions $\mathcal{F}$, Z, and U, it is possible to recover different theories. For example, for $\mathcal{F} = \phi$, $Z \propto \phi^{-1}$, and $U = 0$, Eq. (6.1) represents Brans-Dicke theory. Actions with scalar fields nonminimally coupled to gravity also arise from string theory, Kaluza-Klein-like theories, and braneworld scenarios. These theories have been intensively investigated in cosmology [37, 235]. Likewise, astrophysical implications of scalar-tensor theories for compact objects have been explored in detail [17].

A crucial requirement for these theories is that their weak-field limit, i.e. length scales between the micrometer and the astronomical unit, must be consistent with GR, which in this regime has been tested with extreme precision [34, 17]. Typically, scalar-tensor theories with interesting cosmological phenomenology must feature some screening mechanism, hiding the scalar field on local scales [9, 10]. It is thus relevant to study the phenomenology of these theories in the strong gravity regime, where deviations from GR might be more dramatic. In this section, we perform a detailed analysis of matter-triggered superradiant instabilities for spinning black holes (BHs) in scalar-tensor theories (see [30] for an overview on BH superradiance). This effect was unveiled in [236, 114], where it was shown that the presence of matter outside BHs can trigger either spontaneous scalarization or a superradiant instability in the system, due to the scalar field acquiring an effective mass squared proportional to the trace of the stress-energy tensor of the surrounding matter. The scope of this work is to investigate whether this superradiant instabilities can arise if one considers realistic models of accreting BHs. A similar analysis was recently performed in [115] in the context of plasma-driven [108, 107] superradiant instabilities of photons in GR for BHs accreting a tenuous plasma, using a spin-0 toy model (see also [116] for an extension to the Proca case, and [173, 174] for a recent analysis of photon-plasma interactions in curved spacetime). It was shown in [115] that the complex geometry of accretion disks and the high values of plasma density near the BH can significantly quench the instability.

Nevertheless, we show that this problem can be circumvented in scalar-tensor theories for realistic accretion-disk configurations, because the effective mass depends also on the scalar-tensor coupling. For a cold, collisionless plasma the effective photon mass corresponds to the plasma frequency [108, 107, 173, 174] (2.16). As already discussed, the plasma effective mass lies in a range able to trigger superradiant instabilities if $n_e \sim 10^{-3} - 10^{-2}\,\mathrm{cm}^{-3}$, i.e. for plasma densities typical of the interstellar medium [107]. The plasma density near an accreting BH is several orders of magnitude bigger [115]. In this case, the effective mass is too large to induce an instability on a sufficiently short time scale.

However, as we shall later discuss, in scalar-tensor theories the effective mass squared is [236, 114]

$$\mu_{\text{eff}}^2 = -2\alpha T \sim 2\alpha\rho \,, \tag{6.2}$$

where T is the trace of the stress-energy tensor, $\rho = m_N n_e$ is the matter-energy density of the gas (with nucleon mass m_N), α is a free parameter related to the nonminimal coupling of the scalar field, and the last step above is valid for a nonrelativistic disk (see details below). Thus, in the scalar-tensor case the effective mass depends on $n_e^{1/2}$ as in the standard photon-plasma case but, crucially, also on a free effective coupling α. As we shall discuss, depending on the value of α, the effective mass can be in the optimal range to trigger a superradiant instabilities for realistic plasma configurations around BHs.

Another effect that can drastically quench plasma-driven BH superradiant instabilities are nonlinearities [137] (see 3.4). Nevertheless, as we shall later discuss, the situation is radically different in the case of scalar-tensor theory, at least for the case of relativistic transparency. Indeed, while also in this case the backreaction induces a change in the plasma four-velocity, because the effective mass depends only on the trace of the stress-energy tensor, it is not suppressed by a Lorentz factor.

6.2 General equations and framework

The action in Eq. (6.1) is in the so-called Jordan frame, where the scalar field is nonminimally coupled to the metric. By performing a conformal transformation of the metric and a field redefinition for the scalar field,

$$\begin{aligned} g^E_{\mu\nu} &= \mathcal{F}(\phi) g_{\mu\nu}\,, \\ \Phi(\phi) &= \frac{1}{4\pi}\int d\phi \left[\frac{3}{4}\frac{\mathcal{F}'(\phi)^2}{\mathcal{F}(\phi)^2} + \frac{1}{2}\frac{Z(\phi)}{\mathcal{F}(\phi)}\right]^{1/2}\,, \\ \mathcal{A}(\Phi) &= \mathcal{F}^{-1/2}(\phi)\,, \\ V(\Phi) &= \frac{U(\phi)}{\mathcal{F}^2(\phi)}\,, \end{aligned} \tag{6.3}$$

it is possible to describe the system in the so-called Einstein frame, where the action takes the form:

$$S = \int d^4x \sqrt{-g^E}\left(\frac{R^E}{16\pi} - \frac{1}{2} g^E_{\mu\nu}\partial^\mu\Phi\partial^\nu\Phi - \frac{V(\Phi)}{16\pi}\right) + S(\psi_m, \mathcal{A}(\Phi)^2 g^E_{\mu\nu})\,. \tag{6.4}$$

In the Einstein frame, the scalar field is minimally coupled to the gravity sector, but matter fields are coupled to the effective metric $\mathcal{A}(\Phi)^2 g^E_{\mu\nu}$, so that the weak equivalence principle is preserved while its strong version is violated. In this frame, we assume a generic analytic behavior for the potentials around a GR solution with a constant value $\Phi^{(0)}$ of the scalar field[1],

$$V = \sum_{n=0} V_n (\Phi - \Phi^{(0)})^n\,, \tag{6.5}$$

$$\mathcal{A} = \sum_{n=0} A_n (\Phi - \Phi^{(0)})^n\,. \tag{6.6}$$

Then, by expanding the field equations for $\varphi \equiv \Phi - \Phi^{(0)} \ll 1$, it is possible to rearrange the field equation for the scalar field in a GR background as (see [236, 114] for details)

$$[\Box^E - \mu^2_{\text{eff}}(r,\theta)]\varphi = 0\,, \tag{6.7}$$

---

[1] We consider the field equations in the Einstein frame but laboratory clocks and rods refer to the Jordan-field metric $g_{\mu\nu} = \mathcal{A}^2 g^E_{\mu\nu}$. Physical asymptotic quantities related to the metric (e.g., masses and angular momementa) are obtained from their Einstein-frame counterpart by rescaling the latter with suitable powers of $A(\Phi^{(0)})$. In practice, recovering GR in the weak-field regime requires $A(\Phi^{(0)}) \approx 1$ so the distinction between Einstein- and Jordan-frame asymptotic quantities is negligible for our purposes.

with an *effective* mass squared term

$$\mu_{\text{eff}}^2(r,\theta) = \frac{V_2}{8\pi} - 2\alpha T^E(r,\theta)\,, \tag{6.8}$$

where $\alpha = A_2/A_0$ Following [114] we focus on asymptotically-flat spacetimes (which requires $V_0 = V_1 = 0$) and on theories admitting GR vacuum solutions (which requires $A_1 = 0$). For the rest of this analysis we will also assume $V_2 = 0$. This term is related to a standard bare mass, and neglecting it corresponds to assuming a massless field.

We are therefore left with a Klein-Gordon equation with an effective mass squared proportional to the trace of the stress-energy tensor of the surrounding matter. Since the matter backreaction on the metric is typically negligible, and owing to BH no-hair theorems in this class of theories [237], the background is described by the Kerr solution. The sign of the parameter α has a crucial impact on the phenomenology of the system [236, 114]. If $\alpha < 0$ the effective mass squared in Eq. (6.7) is negative, and leads to a possible tachyonic instability and to a scalarization of the BH. If instead $\alpha > 0$, the effective mass squared is positive and the system can undergo a superradiant instability. In this chapter, we will focus on the latter case. In particular, from eq. (6.8), it is immediate to notice a strong similarity with the previously discussed plasma-driven superradiant instability 3, as also in this case the dynamics is governed by a spatially-varying effective mass. Therefore, one can imagine also in this case (at least at a linear level) a superradiant instability "a là BH-bomb" (see 2.2.5).

6.2.1 Effective mass

Stress-energy tensor of accretion disks

As previously discussed the effective mass-squared term depends on the trace of the stress-energy tensor of the matter fields surrounding the BH. In this section we characterize this term for realistic accretion disk profiles.

We consider different types of effective mass. In general, the stress energy-tensor of an accretion disk can be fully described by four different components [32]:

$$T^\mu_\nu = (T^\mu_\nu)_{\text{FLU}} + (T^\mu_\nu)_{\text{VIS}} + (T^\mu_\nu)_{\text{MAX}} + (T^\mu_\nu)_{\text{RAD}}\,, \tag{6.9}$$

which are, respectively, the fluid component, the viscosity component, the electromagnetic component, and the radiation one. Most models of accretion disks assume a particular form of the stress energy-tensor. For example, thick accretion disk models rely on a perfect fluid approximation, which states that $(T^\mu_\nu)_{\text{VIS}} = (T^\mu_\nu)_{\text{MAX}} = (T^\mu_\nu)_{\text{RAD}} = 0$. Throughout this work, we will consider this assumption, in which the stress energy-tensor reads

$$(T^\mu_\nu)_{\text{FLU}} = (\rho u^\mu)(W u_\nu) + \delta^\mu_\nu P\,, \tag{6.10}$$

where ρ, W, P are respectively the mass-energy density, enthalpy, and pressure. By neglecting the internal energy density of the fluid, the stress-energy tensor trace reads $T = -\rho + 3P$. Note that while the perfect fluid approximation holds for thick disks, in our case we can use the same approximation also for thin disks. Thin disks have a nonvanishing stress part, which for example in the Shakura-Sunyev model can be described using a nearly-linear viscosity approximation [31]. However, the stress part can be written as $(T^{\mu}_{\nu})_{\rm VIS} \propto \sigma^{\mu}_{\nu}$, where $\sigma^{\mu\nu}$ is the shear tensor of the four-velocity of the fluid. Since the shear tensor is by definition *traceless*, the effective mass is independent of the viscosity.

In what follows we will also neglect the effect of pressure, as it is subdominant. Indeed, if one for example assumes the equation of state of an ideal gas, then $P = c_s^2\rho$, where c_s is the speed of sound of the fluid. Since for accretion disks c_s is at least two orders of magnitude smaller than the speed of light, we are in the nonrelativistic regime, $P \ll \rho$, and we can safely neglect pressure corrections to the effective mass. Thus, the trace of the stress-energy tensor in our models is simply $T \approx -\rho$.

Accretion disks features: truncation, typical densities, and coronae

In the following, we will be interested in accretion environments that exhibit a sharp cut-off sufficiently far away from the BH horizon. In these models the disk creates a cavity that can potentially trap scalar modes leading to an instability. A system that satisfies this requirement is the truncated disk accretion model. Truncated disk models are commonly used in BH accretion physics and, depending on the accretion rate, the location of the truncation can be close to the Innermost Stable Circular Orbit (ISCO) (high/soft state) or very far from it, even at $200 - 400M$ or more (low/hard state). Whenever this happens, in the region within the truncation radius and down to the vicinity of the BH, only a hot coronal flow can exist (see e.g. [109, 110, 111, 112, 113]). The Comptonization of hot electrons in the coronal medium is believed to explain the hard, X-ray tail that follows the black-body like emission spectrum of the disk. For this reason, the truncated disk + corona model succeeds in explaining features in the emission spectrum [110].

Another ideal configuration producing sufficiently wide cavities in the density profile near the BH are counter-rotating disks that extend all the way to the ISCO. In this case, the ISCO is sufficiently far away from the horizon ($6 \leq r_{\rm ISCO}/M \leq 9$ depending on the BH spin) so that the cavity is able to trap modes. Finally, another interesting possibility are magnetically-arrested disks, where a strong poloidal magnetic field disrupts the disk at a relatively large radius, creating a cavity. Also this model supports the presence, inside the cavity, of a hot, low-density coronal flow [238]. In general, these flows are always very tenuous and quasispherical, and their density is lower than the disk's one by some orders of magnitude (see [239] for an estimate or, e.g., [240, 241] for GR magneto-hydrodynamics simulations). In what follows, we shall therefore describe truncated thin and thick disks by taking into account an additional coronal structure.

Plasma profiles

We consider different models of density profiles, discussed below. In all models, since the time scales of interest are much shorter than the typical BH accretion time scales [174], we shall neglect the time dependence of the matter fields. Moreover, we shall restrict to axisymmetric configurations in which $\rho = \rho(r, \theta)$ (that of course

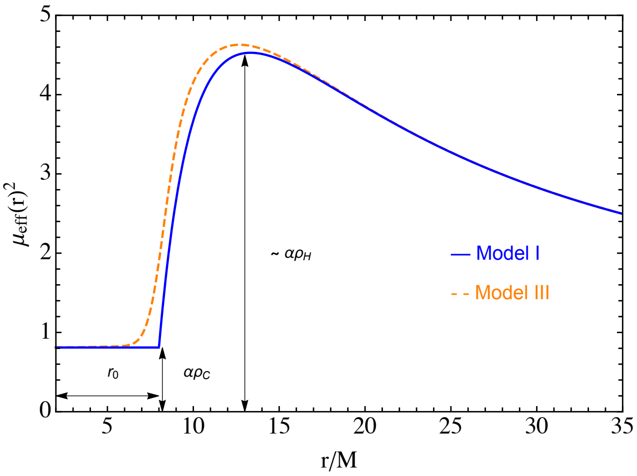

Figure 6.1. Radial profile of the effective mass in Model I with $\alpha\rho_C M^2 = 0.9$, $\alpha\rho_H M^2 = 20$ and $r_0 = 8M$ (solid blue) and Model III with $\beta = 500$ (dashed orange). The profiles are similar, but in Model III the sharp cutoff is smoothed out. For convenience, we have chosen unrealistic values to better highlight the three fundamental parameters $(r_0, \alpha\rho_C, \alpha\rho_H)$ that govern the salient features of the geometry.

reduce to spherical configurations for purely radial profiles).

Model I describes a thick disk+corona system where the corona is described by a constant asymptotic term. The full profile reads

$$\mu^2_{\rm eff,I}(r,\theta) = \alpha\left[\rho_H\Theta(r-r_0)\left(1-\frac{r_0}{r}\right)\left(\frac{r_0}{r}\right)^{\frac{3}{2}} + \rho_C\right], \tag{6.11}$$

where $\Theta(x)$ is the Heaviside step function. When the scalar coupling $\alpha = 1$, this model coincides with the one studied in [115] with a suitable choice of the parameters ρ_H, ρ_C, and r_0. In order to investigate the role of the mass at spatial infinity, in Model II we truncate the corona at r_0:

$$\mu^2_{\rm eff,II}(r,\theta) = \alpha\left[\rho_H\Theta(r-r_0)\left(1-\frac{r_0}{r}\right)\left(\frac{r_0}{r}\right)^{\frac{3}{2}} + \rho_C\Theta(r_0-r)\right]. \tag{6.12}$$

In Model III we investigate the effects of the sharp cut-off produced by the Heaviside function in Models I and II by replacing it with a sigmoid-like function:

$$\mu^2_{\rm eff,III}(r,\theta) = \frac{\alpha\rho_H}{1+e^{-2(r-r_0)}}\left[1-\frac{r_0}{r\left(1+\frac{\beta}{r^4}\right)}\right]\left(\frac{r_0}{r}\right)^{\frac{3}{2}}. \tag{6.13}$$

Figure 6.1 shows that, with a suitable choice of β, Model III is very similar to Model I, except that the effective mass does not display a sharp cutoff.

Model IV describes a realistic scenario for a standard, truncated thin disk with an additional structure made by an ADAF-type corona which extends in the inner zones where the disk evaporates [242, 243]. We therefore model the disk using the Shakura-Sunyev solution and the corona by the self-consistent solution described in [244]. In our analysis, we vary the coronal density by several orders of magnitude to investigate its effect on the instability. Furthermore, in thin disks the thickness is $H/R \ll 1$. To try to capture this effect we multiply the radial Shakura-Sunyev profile by a $\sin^2\theta$ [115]. As a matter of fact, even more thinner profiles can be considered, but they would require higher angular resolution when computing the spectrum (see Sec. 6.3). As for the ADAF-type corona, the geometry is quasispherical so we can safely neglect deviations from spherical symmetry. Therefore, in Model IV we consider the following effective mass:

$$\mu^2_{\mathrm{eff,IV}}(r,\theta) = \alpha\left[\rho_H \Theta(r-r_0)\left(1-\sqrt{\frac{r_0}{r}}\right)^{\frac{11}{20}}\left(\frac{r_0}{r}\right)^{\frac{15}{8}} \times \sin^2\theta + \rho_C\left(\frac{1}{r}\right)^{\frac{3}{2}}\right]. \quad (6.14)$$

Finally, to explore the difference between the radial geometry of a thin and a thick disk, in Model V we also consider a radial profile typical of a thick-disk axisymmetric model with the same corona as in Model IV:

$$\mu^2_{\mathrm{eff,V}}(r,\theta) \quad = \quad \alpha\left[\rho_H \Theta(r-r_0)\left(1-\frac{r_0}{r}\right)\left(\frac{r_0}{r}\right)^{\frac{3}{2}} \sin^2\theta \ + \ \rho_C\left(\frac{1}{r}\right)^{\frac{3}{2}}\right]. \quad (6.15)$$

Note that the salient features of these models can be qualitatively captured by three parameters, which, on physical grounds, should produce the following effects (see also Fig. 6.1):

- Parameter ρ_H represents the height of the barrier. If this value is high enough, it can naturally confine the scalar modes into a cavity. The higher the ρ_H the more efficient the confinement. As ρ_H represents a potential barrier rather than a bare mass (at variance with the standard superradiant instability from massive bosons), increasing ρ_H should not stabilize the modes, but only confine them better.

- Parameter r_0 is the width of the cavity. If it is large enough, the barrier can efficiently confine the modes. In particular, a necessary requirement is that the width of the cavity must be greater than (or at least comparable to) the Compton wavelength of the modes [245]. In the following we consider two representative truncation values: $r_0 = 8M$ and $r_0 = 14M$.

- Parameter ρ_C, instead, represents an offset that introduces an effective asymptotic mass to the scalar field, thus contributing to stabilizing the modes. Note also that, if the barrier is high enough and the modes are strongly confined in it, ρ_C should be relevant only inside the cavity, because the part of the scalar field transmitted outside should be negligible. This effect will be explored by comparing Model I with Model II.

In particular, as we shall later discuss, in the disk $\mu_{\mathrm{eff}}M \sim \sqrt{\alpha\rho_H}M$ should be sufficiently large for the barrier to confine the mode efficiently, whereas in the corona $\mu_{\mathrm{eff}}M \sim \sqrt{\alpha\rho_C}M$ corresponds to the gravitational coupling that governs the effective mass of the field inside the cavity. As such, $\sqrt{\alpha\rho_C}M \ll \mathcal{O}(0.1)$ for the instability not to be quenched.

6.3 Numerical Methods for Non-Separable Equations in Arbitrarily Spinning Spacetime

In this section we present the numerical methods used to compute the spectrum of accreting spinning BHs in scalar-tensor theories. We assume a stationary background and a $e^{-i\omega t}$ time dependence for the perturbation, where $\omega = \omega_R + i\omega_I$ is the (complex) eigenfrequency. Unstable modes correspond to solutions having $\omega_I > 0$, which exponentially grow in time. In the specific case of superradiant instabilities, this exponential growth is triggered if the mode satisfies the superradiant condition [30], i.e. $0 < \omega_R < m\Omega_H = \frac{ma}{r_+^2 + a^2}$, where aM is the BH angular momentum, r_+ is the radius of its event horizon, and m is the azimuthal number of the mode.

We use a procedure consisting in two different numerical methods, both in the frequency domain. We first use a direct shooting method 3.2.4 for finding solutions of Eq. (6.7) in the case of spherical symmetry, i.e. for nonspinning BHs and when the effective mass profile depends only on the radial coordinate. Imposing suitable boundary conditions at the horizon and at infinity, the shooting method allows us to solve the eigenvalue problem. Then, the wavefunctions and eigenfrequencies are used as starting guess solutions for computing the spinning case, by applying a numerical method suitable for nonseparable differential equations. In particular, following [72], we express Eq. (6.7) as a nonlinear eigenvalue problem which we solve with the nonlinear inverse iteration algorithm [246] (see below for details). Starting with the spherical symmetric case, we can iteratively solve the problem by gradually increasing the spin until we obtain the desired spinning configuration. With this method we can study also quasiextremal BHs and generic nonseparable equations.

For the case of effective mass profiles having a θ-dependence through $\sin^2\theta$, the field equations are nonseparable even for a nonspinning BH. In this case we introduce an extra iterative cycle in the procedure. We express the generic effective mass of any of the previous models as

$$\mu_{\text{eff}}^2(r,\theta) = \mu_r^2(r)(1 - k\cos^2\theta) + \mu_0^2(r)\,, \tag{6.16}$$

where $\lim_{r\to\infty}\mu_r(r) = 0$, we introduced the fictitious parameter k connecting purely radial profiles ($k = 0$) with θ-depending profiles ($k = 1$), whereas $\mu_0^2(r)$ comes from the BH corona. The extra cycle consists in applying the nonlinear inverse iteration to finding the mode of a nonspinning BH with a nonspherical density profile ($k = 1$), using solutions with $k = 0$ as starting guess: at each iteration we gradually increase k and use the previous result as a guess, until we obtain the desired configuration with $k = 1$ and zero BH spin. Finally, we use the latter solution as a starting guess to find the modes of a spinning BHs with $k = 1$, as previously explained. Details of the latter numerical method outlined above are given in the next subsection.

Nonseparable perturbations: Čebyšëv interpolation and nonlinear eigenvalue problem

Let us consider the case of nonseparable perturbations, which is relevant for both spinning BHs and even for nonspinning BHs if the effective mass depends on the angular coordinate θ.

We assume an axisymmetric (Kerr) background so that perturbations have a definite azimuthal number m. We rewrite Eq. 6.7 in the following form:

$$\begin{aligned}&\left\{\frac{1}{\Delta(r)}[\boldsymbol{\mathcal{L}}^2 + a^2\cos^2\theta(\mu_{\text{eff}}^2(r,\theta) - \omega^2)] - \frac{1}{\Delta(r)}\frac{\partial}{\partial r}\left[\Delta(r)\frac{\partial}{\partial r}\right]\right.\\ &-\omega^2 - \frac{P_+^2}{(r-r_+)^2} - \frac{P_-^2}{(r-r_-)^2} + \frac{A_+}{r-r_+} - \frac{A_-}{r-r_-}\\ &\left.+\,\mu_{\text{eff}}^2(r,\theta)\left(1 + \frac{B_+}{r-r_+} - \frac{B_-}{r-r_-}\right)\right\}\varphi(t,r,\theta,\phi) = 0\,,\end{aligned} \tag{6.17}$$

where $A_\pm = \mp 2\omega^2 M + \frac{P_+^2 + P_-^2 - (8M^2 - a^2)\omega^2}{r_+ - r_-}$, $B_\pm = \frac{2M^2 - a^2}{r_+ - r_-} \pm M$, $r_\pm = M \pm \sqrt{M^2 - a^2}$, $P_\pm = \frac{ma - 2\omega M r_\pm}{r_+ - r_-}$, $\boldsymbol{\mathcal{L}}^2 = -\frac{1}{\sin\theta}\frac{\partial}{\partial\theta}\left(\sin\theta\frac{\partial}{\partial\theta}\right) - \frac{1}{\sin^2\theta}\frac{\partial^2}{\partial\phi^2}$, and $\Delta(r) = (r - r_+)(r - r_-)$. Note that the dependence on k is contained inside $\mu_{\text{eff}}^2(r,\theta)$ in the above equation.

At the horizon we must have ingoing waves,

$$\varphi \sim (r - r_+)^{iP_+}\,, \tag{6.18}$$

whereas, as previously discussed, we impose that there are no waves coming from infinity,

$$\varphi \sim r^{-1-\frac{M\left(2\omega^2 - \mu_\infty^2\right)}{k_\infty}} e^{k_\infty r}\,. \tag{6.19}$$

We apply the following ansatz for the scalar field [72]:

$$\varphi(t,r,\theta,\phi) = F(r)\sum_{l,m} B_{lm}(\zeta(r))Y_{lm}(\theta,\phi)e^{-i\omega t}\,, \tag{6.20}$$

where

$$F(r) = \left(\frac{r - r_+}{r - r_-}\right)^{iP_+}(r - r_-)^{-1-\frac{M\left(2\omega^2 - \mu_\infty^2\right)}{k_\infty}} e^{k_\infty(r - r_+)} \tag{6.21}$$

captures the asymptotic behaviors of the solution. Henceforth for simplicity we drop the index m from B_{lm}. In the numerical results presented in the next section we will always consider the case $m = 1$. In the above ansatz $B_l(\zeta(r))$ are radial functions depending on the auxiliary radial coordinate $\zeta \in (-1, 1)$, defined by the following mapping

$$\zeta(r) = \frac{r - \sqrt{4r_+(r - r_-) + r_-^2}}{r - r_-}\,, \tag{6.22}$$

$$r(\zeta) = \frac{4r_+ + r_-(\zeta^2 - 1)}{(\zeta - 1)^2}\,. \tag{6.23}$$

By performing a spherical harmonics decomposition of Eq. 6.17, we obtain an infinite cascade of coupled radial equations:

$$\left[\frac{\partial^2}{\partial\zeta^2} + C_l^{(1)}(\zeta)\frac{\partial}{\partial\zeta} + C_l^{(2)}(\zeta)\right]B_l(\zeta) + \sum_{j=-4}^{4} C_{l,j}^{(3)}(\zeta)B_j(\zeta) = 0\,, \tag{6.24}$$

where we have the following expressions for the couplings

$$C^{(3)}_{l,j}(\zeta) = -\frac{c^{(1)}_{l,j}}{\zeta'^2(r(\zeta))}\left\{\frac{a^2[\mu_r^2(r(\zeta))+\mu_0^2(r(\zeta))-\omega^2]}{\Delta(r(\zeta))} - k\mu_r^2(r(\zeta))\left[1+\frac{B_+}{r(\zeta)-r_+}-\frac{B_-}{r(\zeta)-r_-}\right]\right\} + \frac{kc^{(2)}_{l,j}a^2\mu_r^2(r(\zeta))}{\zeta'^2(r(\zeta))\Delta(r(\zeta))}\,, \quad (6.25)$$

with the Clebsch-Gordan coefficients:

$$c^{(1)}_{l,j} = \langle l,m|\cos^2\theta\,|j,m\rangle = \frac{1}{3}\delta_{lj} + \frac{2}{3}\sqrt{\frac{2j+1}{2l+1}}\,\langle j,2,m,0|\,l,m\rangle\,\langle j,2,0,0|\,l,0\rangle\ , \quad (6.26)$$

$$c^{(2)}_{l,j} = \langle l,m|\cos^4\theta\,|j,m\rangle = \frac{1}{5}\delta_{lj} + \frac{4}{7}\sqrt{\frac{2j+1}{2l+1}}\,\langle j,2,m,0|\,l,m\rangle\,\langle j,2,0,0|\,l,0\rangle + \frac{8}{35}\sqrt{\frac{2j+1}{2l+1}}\,\langle j,4,m,0|\,l,m\rangle\,\langle j,4,0,0|\,l,0\rangle\ , \quad (6.27)$$

and the following expressions for the remaining functions

$$C^{(1)}_l(\zeta) = \left(\frac{1}{r(\zeta)-r_+}+\frac{1}{r(\zeta)-r_-}\right)\frac{1}{\zeta'(r(\zeta))} + \frac{1}{\zeta'(r(\zeta))}\frac{2F'(r(\zeta))}{F(r(\zeta))} + \frac{\zeta''(r(\zeta))}{\zeta'^2(r(\zeta))}\,, \quad (6.28)$$

$$C^{(2)}_l(\zeta) = \frac{1}{\zeta'^2(r(\zeta))}\left\{\frac{F''(r(\zeta))}{F(r(\zeta))} + \left[\frac{1}{r(\zeta)-r_+}+\frac{1}{r(\zeta)-r_-}\right]\frac{F'(r(\zeta))}{F(r(\zeta))} + \frac{P_+^2}{[r(\zeta)-r_+]^2} + \frac{P_-^2}{[r(\zeta)-r_-]^2} - \left[\mu_r^2(r(\zeta))+\mu_0^2(r(\zeta))\right]\left[1+\frac{B_+}{r(\zeta)-r_+}-\frac{B_-}{r(\zeta)-r_-}\right] - \frac{A_+}{r(\zeta)-r_+} + \frac{A_-}{r(\zeta)-r_-} + \omega^2 - \frac{l(l+1)}{\Delta(r(\zeta))}\right\}\,. \quad (6.29)$$

The couplings $c^{(1)}_{l,j}$ are nonzero for $j\in\{l,l\pm2\}$, while $c^{(2)}_{l,j}$ are nonzero for $j\in\{l,l\pm2,l\pm4\}$, thus each l-mode is coupled with 4 other differing ones. In order to find solutions we truncate the infinite tower to some L (i.e. we neglect perturbations with $l>L$) and transform the remaining (finite) set of radial equations into a matrix form. The radial coordinate is then discretized through a Čebyšëv interpolation, which is defined by the following polynomials

$$p_n(\zeta) = \frac{\prod_{q\neq n}(\zeta-\zeta_q)}{\prod_{q\neq n}(\zeta_n-\zeta_q)} = \frac{p(\zeta)w_n}{\zeta-\zeta_n}\,, \quad (6.30)$$

$$p(\zeta) = \prod_{q=0}^{N}(\zeta-\zeta_q)\,, \quad (6.31)$$

with Čebyšëv nodes

$$\zeta_n = \cos\left(\frac{\pi(2n+1)}{2(N+1)}\right), \tag{6.32}$$

and corresponding weights [72, 247, 248]

$$w_n = \frac{1}{p'(\zeta_n)} = (-1)^n \sin\left(\frac{\pi(2n+1)}{2(N+1)}\right). \tag{6.33}$$

where $N+1$ is the number of interpolation points and $n \in [0, N]$. The radial functions B_l are hence described by a set of $(L+1)(N+1)$ coefficients $B_l(\zeta_k)$, that define a $(L+1)(N+1)$-dimensional array $\underline{B}$, while the radial equations take the form

$$\begin{aligned}&\sum_{q=0}^{N}\left[p''_q(\zeta_n)B_l(\zeta_q) + C^{(1)}_l(\zeta_n)p'_q(\zeta_n)B_l(\zeta_q)\right] + C^{(2)}_l(\zeta_n)B_l(\zeta_n) + \\ &\sum_{j=-4}^{4} C^{(3)}_{l,j}(\zeta_n)B_j(\zeta_n) = 0\end{aligned} \tag{6.34}$$

By exploiting the second barycentric form of the Lagrange polynomials, we can get numerically robust differentiation matrices [72, 247, 248]:

$$p'_q(\zeta_n) = \begin{cases} \frac{w_q/w_n}{\zeta_n-\zeta_q} & n \neq q \\ -\sum\limits_{b,b\neq n}^{N} p'_b(\zeta_n) & n = q \end{cases} \tag{6.35}$$

$$p''_q(\zeta_n) = \begin{cases} 2p'_q(\zeta_n)\left(p'_n(\zeta_n) - \frac{1}{\zeta_n-\zeta_q}\right) & n \neq q \\ 2p'_q(\zeta_n)p'_n(\zeta_n) + \sum\limits_{b,b\neq n}^{N} \frac{2p'_b(\zeta_n)}{\zeta_n-\zeta_b} & n = q \end{cases} \tag{6.36}$$

At the end of this procedure we obtain a nonlinear eigenvalue problem in ω and $\underline{B}$,

$$\mathbf{A}(\omega)\underline{B} = 0\,, \tag{6.37}$$

to be solved through nonlinear inverse iteration [246].

6.4 Results

6.4.1 Models I: key ingredients for the instability

We start by studying the first three models with the same density profiles considered in [115], to show that the obstacles existing in plasma-driven superradiant instabilities can be circumvented in scalar-tensor theories. Figure 6.2 shows the modes of Model I with $\rho_H = 4/M^2, \rho_C = 0.09/M^2$, $r_0 = 8M$, and different values of α. For $\alpha = 1$ we recover the results obtained in [115]. In this case, superradiance does not appear before $a/M = 0.99$. However, if we consider lower values of α the effective mass

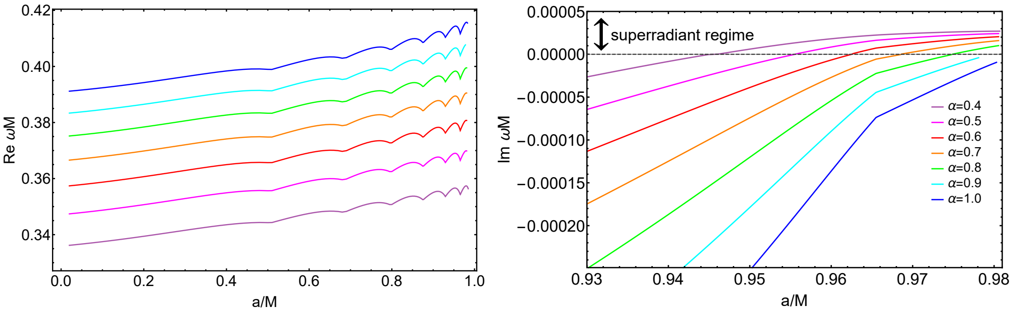

Figure 6.2. Real (left panel) and imaginary (right panel) part of the modes in Model I as a function of the BH spin for different values of the coupling α. For lower values of this parameter, ω_R decreases and the modes become superradiantly unstable for smaller values of the BH spin.

of the scalar field (and hence the superradiant mode frequency) decreases and the superradiant condition is fulfilled for smaller values of the spin. This is evident by looking at the real part of the mode frequency in the left panel of Fig. 6.2. As the coupling α decreases, the real part becomes smaller, eventually entering the superradiance condition. Therefore, while in plasma-driven superradiant instabilities in GR a small increase of the coronal mass is sufficient to quench the instability [115], in scalar-tensor theories decreasing α is sufficient to circumvent this obstacle and recover an efficient superradiant regime, as also discussed more in detail below.

Nevertheless, by decreasing α too much, the potential barrier becomes too low and is not able to confine the modes. For the case of Model I, we numerically find that when $\alpha < 0.15$ the eigenfunctions start having a nonnegligible amplitude even after the potential barrier, suggesting that the confinement starts becoming inefficient.

Assuming a high spinning BH, the superradiant instability can therefore be quenched in the following cases:

- If the density of the corona is high enough to stabilize the system. In Model I and for the chosen parameters, this happens when $\sqrt{\alpha\rho_C}M > 0.42$.
- If the barrier is not high enough to confine modes. This starts happening when $\sqrt{\alpha\rho_H}M < 0.76$.
- If the width of the cavity is not sufficiently large as to support quasibound states inside it. Indeed, when the effective mass within the cavity is negligible (i.e., $\sqrt{\alpha\rho_C}M \ll 0.1$), this system resembles the original BH bomb, where the frequencies scale as the inverse of the width of the cavity, $\omega_R \sim 1/r_0$ [245]. In Fig. 6.3 we show that we recover the same scaling in our system.

Reversing the argument, if the barrier is high enough and the cavity wide enough, modes can be confined efficiently. If in addition the coronal density is tenuous enough not to provide modes in the cavity with a too large effective mass, then an efficient superradiant instability can develop around an accreting spinning BH. We shall come back to this point in Sec. 6.5.

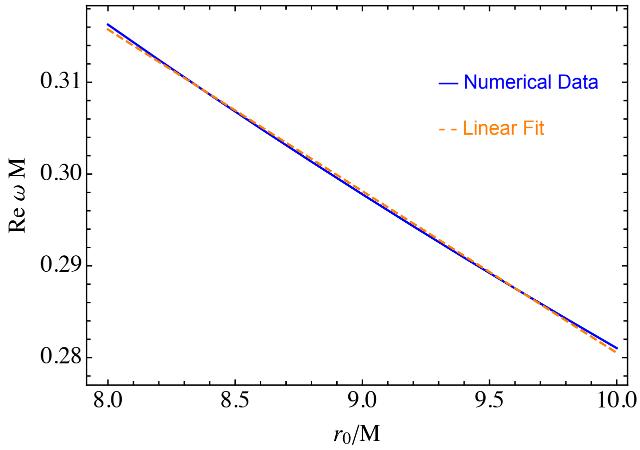

Figure 6.3. Real part of the mode frequencies in Model I as a function of r_0 for $\alpha\rho_H M^2 = 4$, $\alpha\rho_C M^2 = 0$, and $a = 0$. The real part decreases linearly with $1/r_0$, as can be observed by comparing the numerical result with a linear fit.

For the time being we wish to stress that the main difference with respect to [115] is the free parameter α appearing in scalar-tensor theories. In [115], it was shown that, even though the disk can create a cavity where superradiant modes can develop, an extremely tenuous plasma inside this cavity (of the order of $n_e \sim 10^{-2}\text{cm}^{-3}$ for $M = 10M_\odot$) is sufficient to quench the instability. Given that realistic coronal densities are orders of magnitude higher, the instability is strongly suppressed. On the other hand, as discussed in detail in Sec. 6.5 below, in our system there are large unconstrained ranges of α in which the effective mass due to the corona is negligible and, *yet*, the disk barrier is sufficiently high.

6.4.2 Models II and III: truncation of the corona and smoothness of the profiles

Model II aims to quantitatively verify that only the coronal density *inside* the cavity is relevant for providing an additional effective mass. For this reason, we truncate the corona at r_0, where the disk begins. We obtain numerical results which almost coincide with those of Model I, confirming that what is really relevant to increase the effective mass – and hence to possibly quench the instability – is only the density inside the cavity.

Finally, in Model III we replace the step function of the inner edge by a sigmoid, in order to show that the corners in both the real and imaginary parts shown in Fig. 6.2 are an artifact of the Heaviside function used in modelling the density profile. In Fig. 6.4 we show that when the barrier is instead described by a smooth sigmoid, the corners disappear, and the resulting modes are also smooth functions of the model parameters.

6.4.3 Models IV and V: role of the corona density

In these models, we study the impact of different coronal density by parametrizing $\rho_C = \gamma\rho_H$ and varying the parameter γ in the realistic range $10^{-6} - 10^{-1}$ (see

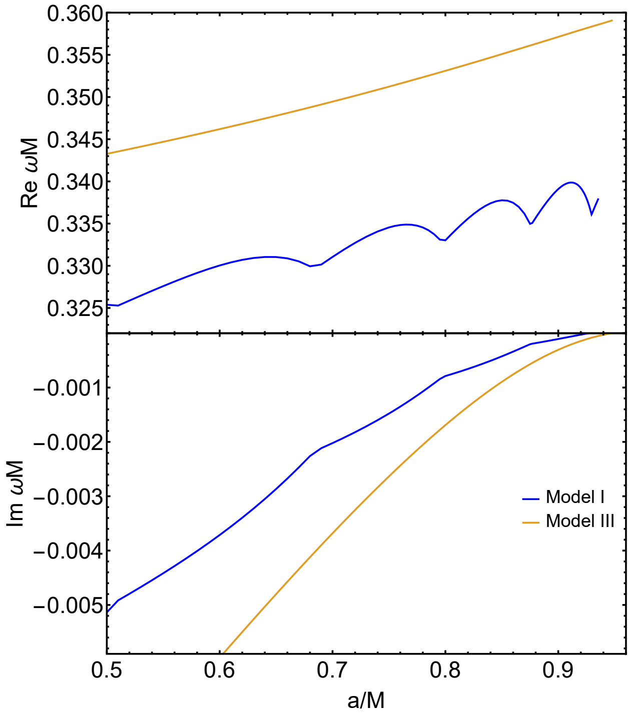

Figure 6.4. Real and imaginary parts of modes respectively from Model I (blue) and Model III (orange). By replacing the step function with a sigmoid, the profile becomes more regular and the corners disappear.

e.g. [239, 240, 242]). Figure 6.5 show the imaginary part of the solutions for $\gamma = 10^{-6}$, $r_0 = 14M$, $\rho_H = 4/M^2$ obtained by varying the parameter α in Model IV and Model V. By varying α across two orders of magnitude the instability is preserved with qualitatively similar features: this is because the coronal density is so low that it remains negligible, while the disk density is sufficiently high to confine the modes in this range of α. Thus, if the coronal density is strongly suppressed with respect to the disk one, it is possible to have an instability in a wide range of the coupling α. Also note that assuming a larger truncation radius yields a smaller spin threshold for the instability. This is because, akin to the original BH bomb phenomenon, the real part of the frequency decreases with the truncation radius $\omega_R \sim 1/r_0$ [245] (see Fig. 6.3).

Finally, Fig. 6.6 shows the imaginary part of the modes as a function of α for different density ratios γ in Model V with $\rho_H = 4/M^2$ and $r_0 = 8M$. Note that, for certain values of α (e.g. $\alpha \approx 1$ for the parameters chosen in Fig. 6.6) the modes are independent of γ in the $\gamma \ll 1$ limit. This is because the coronal density in this regime is subdominant and does not affect the mode. On the other hand, as the α parameter grows, the coronal effective mass eventually becomes relevant and quenches the instability. In particular, for the chosen parameters the instability is suppressed when $\alpha\gamma \gtrsim O(10^{-1})$.

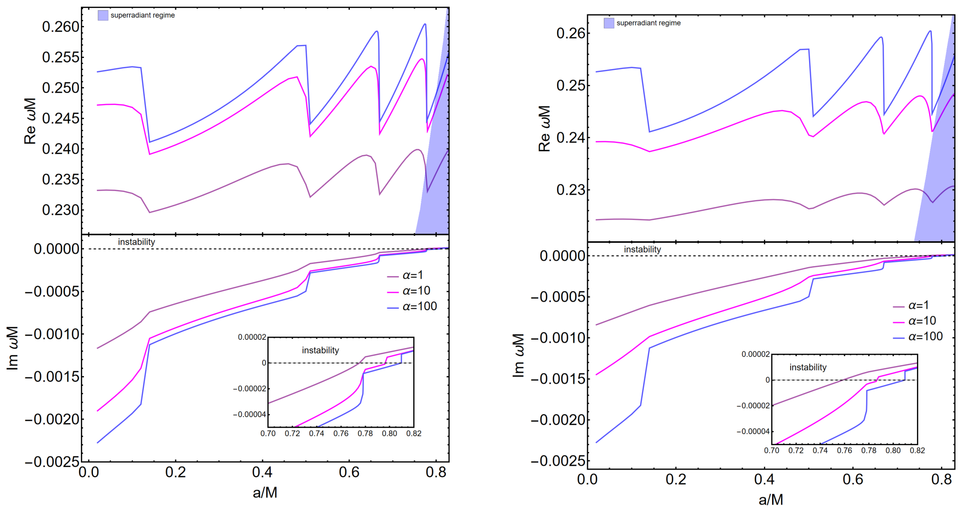

Figure 6.5. Superradiant modes of Model IV (left) and Model V (right) for $r_0 = 14M$ and $\gamma = 10^{-6}$ as functions of the dimensionless spin parameter for different values of α. Even by varying α across two orders of magnitude, the instability is preserved.

6.5 Constraints on scalar-tensor theories from spinning BH observations

After having explored the parameter space of our models and having identified the key features of the plasma-triggered superradiant instability in scalar-tensor theories, we are now in a position to draw a general picture and use it to identify the parameter space of scalar-tensor theories in which the instability is effective.

The first key ingredient is a sufficiently dense disk that extends down to the BH up to some truncation radius $r_0 > \mathcal{O}(\text{few})M$, as predicted in various models. The requirement that the disk can effectively confine scalar modes implies

$$\sqrt{\alpha \rho_H} M \gtrsim 1 \, . \tag{6.38}$$

For a standard thin disk the typical outer density is [31, 33]:

$$\rho \approx 169 \frac{f_{\rm Edd}^{\frac{11}{20}}}{(r/M)^{\frac{15}{8}}} \left(1 - \sqrt{\frac{r_0}{r}}\right)^{\frac{11}{20}} \left(\frac{0.1}{\beta}\right)^{\frac{7}{10}} M_6^{-\frac{7}{10}} \mathrm{kg/m}^3 \, , \tag{6.39}$$

where r_0 is the truncation radius, β is the viscosity parameter, $f_{\rm Edd} = \dot{M}/\dot{M}_{\rm Edd}$ is the mass accretion Eddington ratio, and we defined $M_6 = M/(10^6 M_\odot)$. Using the above normalization, Eq. (6.38) yields a *lower* bound on the scalar coupling,

$$\alpha \gtrsim \alpha_c = \frac{1}{\rho_H M^2} \approx 3 \times 10^6 M_6^{-13/10} \, , \tag{6.40}$$

so that supermassive BHs would yield a smaller lower bound.

The above condition is necessary but not sufficient. In the presence of a corona with characteristic density $\rho_C = \gamma \rho_H$, one should also require that the effective mass inside the cavity be not too large, namely,

$$\sqrt{\alpha \rho_C} M \lesssim 1 \, . \tag{6.41}$$

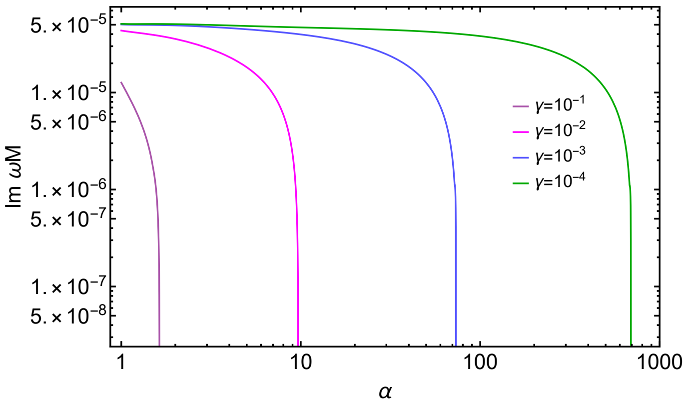

Figure 6.6. Imaginary part as a function of α in Model V for different values of the density ratio γ between the corona and the disk for a spinning BH with $a = 0.97M$. When $\alpha\gamma \gtrsim O(10^{-1})$, the instability is suppressed. Hence, the lower γ, the more efficient the instability is across several orders of magnitudes in α.

This condition can be written as a *upper* bound on the scalar coupling,

$$\alpha \lesssim \frac{\alpha_c}{\gamma} \approx \frac{3}{\gamma} \times 10^6 M_6^{-13/10} \,. \tag{6.42}$$

Since the corona is much less dense than the disk, $\gamma \ll 1$ and condition 6.38 has always some overlap with condition 6.41. In particular, provided the disk truncation is not too close to the BH horizon, the superradiant instability can occur when

$$3 \times 10^6 \lesssim \alpha M_6^{13/10} \lesssim 3 \left(\frac{10^{-4}}{\gamma}\right) 10^{10} \,, \tag{6.43}$$

where we have normalized the typical coronal density such that $\gamma = \rho_C/\rho_H = 10^{-4}$.

Remarkably, different classes of BHs could constrain different ranges of α, extending roughly from $\alpha \sim \mathcal{O}(100)$ for $M \sim 10^9 M_\odot$ up to $\alpha \sim \mathcal{O}(10^{17})$ for $M \sim 5M_\odot$. Furthermore, as shown in the previous section the instability time scale, $\tau = 1/\omega_I$, is typically very short compared to astrophysical time scales. The instability can therefore be effective to change the dynamics of the system (see [87, 30] for the phenomenology of the BH superradiant instability in various systems).

This implies that, providing the accretion flow can be accurately modelled, constraints on scalar-tensor theories coming from the observation of highly-spinning accreting BHs can rule out scalar-tensor theories with positive couplings in a very wide range. Interestingly, while there exists stringent constraints on $\alpha < 0$ coming from spontaneous scalarization and the absence of dipolar radiation in binary pulsars [236, 114, 249], the regime where $\alpha > 0$ is essentially unconstrained and is relevant for cosmology.

The $\alpha \gg 1$ regime is particularly interesting for certain scalar-tensor theories. For example, in the symmetron model [9] the conformal factor reads[2] $A(\phi) = 1 + \alpha\phi^2/2$ and requiring the Milky Way to be screened imposes $\alpha \gtrsim 10^6 - 10^8$ [252, 251, 253],

---

[2] The bare mass term and scalar self-interactions of this cosmological model are negligible for astrophysical BHs [250, 251], so the approximations assumed in Sec. 9.2 apply.

which perfectly lies in the range that can be potentially excluded by accretion-driven BH superradiance.

6.6 On the role of nonlinearities for plasma-driven superradiant instability in scalar-tensor theories

As previously discussed, we find a wide range of parameter space prone to trigger matter-driven BH superradiant instabilities in scalar-tensor theories. Since during the instability the amplitude of the scalar field grows exponentially in a short timescale, linear theory eventually breaks down. It is therefore crucial to understand the modifications that nonlinearities will introduce in the system. This can be done by analysing the backreaction of the superradiantly growing scalar field on to the plasma. In the Jordan frame, plasma particles follow geodesics, as it can be easily seen by the conservation of the matter stress energy tensor:

$$\nabla_\nu T^{\mu\nu} = 0 \rightarrow \frac{Du^\mu}{D\tau} = u^\nu \nabla_\nu u^\mu = 0, \tag{6.44}$$

where u^μ is the plasma four velocity in the Jordan frame. Switching to the Einstein frame, this equation can be rewritten as (see e.g. [36]):

$$\frac{Du_E^\mu}{D\tau_E} = f_\nu u_E^\nu u_E^\mu - f_E^\mu (u_{E\,\mu} u_E{}^\mu), \tag{6.45}$$

where $u_E^\mu = dx^\mu/d\tau_E$ and τ_E are the four velocity and proper time in the Einstein frame, respectively, whereas $f_\nu = -\partial_\nu \ln A(\Phi)$ and $f_E^\mu = g_E^{\mu\nu} f_\nu$. By expanding the conformal factor around $\Phi \sim \Phi^{(0)}$ as before, this equation can be rewritten to the leading order as

$$\frac{Du_E^\mu}{D\tau_E} = -\alpha\Big(\varphi\partial_\nu\varphi u_E^\mu u_E^\mu - g_E^{\mu\alpha}\varphi\partial_\alpha\varphi(u_E{}^\nu u_{E\,\nu})\Big). \tag{6.46}$$

From this equation it is possible to observe that the acceleration of the plasma particles in the Einstein frame depends on nonlinear terms in the scalar field φ, with coupling constant α. By solving this equation it is then possible to relate the backreaction on the four velocity with the backreaction on the density via the continuity equation of the fluid. Hence, as in the previously studied photon-plasma case 3.4, nonlinear effects can modify the density of the fluid, which evolves dynamically. The details on the evolution depend on the specific models and on higher-order scalar interactions in the scalar-tensor theories. In principle, one could expect that in some models a plasma blow-up scenario akin to the photon-plasma case may be possible.

Nevertheless, and most crucially, this system is safe from another nonlinear effect, the relativistic transparency, which severely hampers plasma-driven superradiant instabilities in GR [137]. Due to this nonlinear correction, the effective photon mass in a plasma is modified in the relativistic regime as in (3.63) [150, 254, 137]. As already discussed, this effect can be interpreted as a relativistic increase of the relativistic electron mass-energy, and it is therefore a completely different effect from the field backreaction on the density distribution. We will now show that in scalar-tensor theories the effective mass does not suffer from a similar suppression. Indeed, in this system the effective mass is the trace of the stress-energy tensor, $T^{\mu\nu} = \rho u^\mu u^\nu$. The crucial point is that, no matter what the fluid four-velocity is, the trace of this tensor is always the rest-mass density, given that $u_\mu u^\mu = -1$ is a relativistic invariant. Therefore, even if the plasma is accelerated to relativistic velocities, the expression of the effective mass does not change (although the density becomes a dynamical quantity as discussed before). This follows from the fact that the trace of a tensor is a scalar quantity, which is invariant under Lorentz boosts. Hence, no Lorentz boost factor enters in the effective scalar mass in the relativistic nonlinear regime, at variance with the standard case of plasma-photon interactions, so that the system does not suffer from relativistic transparency effects. Nevertheless, one could still expect a plasma blow-up scenario as in 3.4: thus, further non-linear studies are imperative to understand the non-linear behavior of the system.

6.7 Conclusions

We have studied in detail the phenomenon of matter-driven BH superradiant instabilities in scalar-tensor theories. We have considered arbitrarily spinning BHs and realistic models of truncated thin and thick accretion disks. In general the linearized scalar equation is nonseparable, and we have discussed in detail an efficient numerical method to find the unstable modes for this system.

We found two interesting results: i) although the qualitative features of the instability are akin to the case of plasma-driven electromagnetic superradiant instabilities within GR, the obstacles preventing the latter (namely suppression due to the corona [115] and nonlinearities [137]) can be circumvented in scalar-tensor theories; ii) Remarkably, there exists a very wide range of (positive and large) scalar couplings where BH superradiant instabilities can be triggered in realistic scenarios. This range is unconstrained by observations and it actually includes the regime where certain scalar-tensor alternatives to the dark energy, e.g. symmetron models with screening, can evade solar system constraints while remaining cosmologically viable. Our results suggest that such theories could be ruled out as dark-energy alternatives by the observation of highly spinning BHs, using the same technique adopted to constrain ultralight bosons from BH mass-spin observations [24, 89, 30]. However, at variance with the ultralight boson case, here an accurate modelling of the accretion flow around the BH is needed in order to quantitatively characterize the instability.

Furthermore, the possibility of circumventing nonlinear damping effects suggests that the models proposed for ordinary plasma-driven instabilities (e.g. as a possible explanation for fast radio bursts [107] or for constraints on primordial BHs [108]) could actually work in the context of scalar-tensor theories.

Although the quantitative features of the instability depend on the geometry of the accretion flow near a BH, the key ingredients are naturally predicted in various models: i) a sufficiently dense disk with a sharp transition from a low-density to a high-density region in the vicinity of the ISCO; ii) A sufficiently tenuous corona in the low-density region, such that its density is much smaller than the one of the disk; iii) a BH spinning sufficiently fast to make the quasibound modes unstable against the superradiant instability.

The numerical method implemented to compute the unstable modes in the absence of separable equations is general and robust, and could find applications in other contexts.

Another interesting finding is the fact that the unstable modes of this system resemble a quasibound state in the vicinity of the BH but are in fact propagating waves far from it. Therefore, one could imagine situations in which (perhaps during the superradiant growth) the quasibound states are not efficiently trapped and could propagate to infinity, possibly after several reflections within the cavity. The scalar modes in the Einstein frame correspond to a (breathing) scalar polarization of the gravitational waves in the Jordan frame. Therefore, the phenomenology of this effect would be similar to the gravitational-wave echoes predicted for matter fields [255], near-horizon structures [256], and exotic compact objects [257]. A more detailed study of this interesting phenomenon, that we leave to the future, will probably require a time-domain analysis.

Finally, an important follow-up of our work is to study backreaction effects on the plasma and the full dynamics of the system at the nonlinear level.

Chapter 7

Relativistic perturbation theory for black-hole boson clouds

Summary

Linear perturbations around black hole spacetimes can be quasinormal, quasibound, or even superradiantly unstable, the latter leading to the formation of macroscopic boson clouds. In this chapter, we develop a relativistic perturbation theory for boson clouds around rotating black holes that supersedes the non-relativistic "gravitational atom" approximation and brings close agreement with numerical relativity. We first introduce a relativistic product and corresponding orthogonality relation between (massive) scalar modes, which extends a recent result for gravitational perturbations, and forms the basis for our framework. We then derive the analog of time-dependent perturbation theory in quantum mechanics. As a demonstration, we apply these techniques to calculate the self-gravitational frequency shift of a Kerr superradiant mode, improving the error by a factor of four (from 28% to 7%) for the largest masses considered. We thereby provide a conceptually new approach to calculate black-hole mode dynamics, with practical application for precision gravitational-wave astronomy.

7.1 Motivations

In black hole (BH) physics, the analysis of mode solutions of bosonic fields was initiated by Regge and Wheeler [258], Zerilli [259], and Teukolsky [260, 261]. It is now well known that the response of a BH to the perturbation of a massless field consists of a series of damped sinusoids called quasi-normal modes (QNMs) [208, 262]. Unlike normal modes, which exist for conservative systems and have purely real spectrum, QNMs appear in dissipative systems and have complex frequencies $\omega = \omega_{\rm R} + i\omega_{\rm I}$, with the imaginary part setting their decay time. For BHs, dissipation arises due to radiation of the field through the horizon and away to infinity.

As discussed in the previous chapters, *massive* fields around BHs admit an additional class of solutions known as quasi-bound states (QBSs). Whereas QNMs are radiative solutions, with frequency $|\omega| > \mu$, where μ is the field mass, QBSs are spatially confined by the Yukawa suppression and have $|\omega| < \mu$. Thus, QBSs do not radiate at infinity, although they still dissipate through the horizon. Via the superradiant instability, the formation of a macroscopic boson cloud and the spin-down of the BH translates into potentially observable signatures, such as gaps in the BH spin-mass (Regge) plane, gravitational wave emission from the condensate, or signatures in binary systems [83, 96, 102, 90, 100, 104, 85, 79, 92, 93, 95, 223, 105, 103, 222]. Superradiant instabilities, therefore, represent a powerful probe of ultralight bosons beyond the Standard Model, such as axions or dark photons.

Given these (and other) prospects for deviations from linear mode evolution, there is considerable interest in calculating nonlinear perturbative effects involving QBSs or QNMs [96, 263, 264, 265, 266]. However, due to the non-Hermiticity of the system, the spectral theorem does not guarantee the orthogonality or completeness of these modes—which moreover often diverge at the BH horizon or infinity—so it is not clear *a priori* how to incorporate them into a perturbative framework.

For QBSs, the problem can be simplified using the "gravitational atom" or "hydrogenic" approximation. Indeed, at leading order in the gravitational coupling $\alpha = \mu M$, where M is the BH mass, and beyond the field's Compton length, $r \gg \mu^{-1}$, QBSs reduce to eigenfunctions of the hydrogen atom Hamiltonian. In this limit, the ingoing condition at the BH horizon is replaced by a regularity condition at the origin [73, 74, 76, 92]. Thus, a hydrogenic inner product $\langle \cdot | \cdot \rangle_H$ can be defined, in analogy to quantum mechanics, and mode orthogonality is guaranteed by the spectral theorem in the absence of dissipative boundaries.[1]

The hydrogenic approximation (and its relativistic corrections [92]) has been widely used to compute various perturbative corrections to the linear problem [92, 169, 94, 222, 267, 263]. For instance, to leading order, a potential term δV arising from, e.g., a binary companion, or a quartic self-interaction, gives rise to level mixing through the matrix element $\langle n\ell m | \delta V | n'\ell' m' \rangle_H$ [92]. The self-gravity of the state also gives rise to a shift in the mode frequency, proportional to the matrix element $\langle n\ell m | \delta V | n\ell m \rangle_H$ [83, 169]. However, this approximation has two drawbacks: it breaks down for higher values of α, and it does not take into account the dissipative nature of the problem. To accurately model the phenomenology of massive fields around black holes, we require a *relativistic* perturbative framework, based on an appropriate notion of orthogonality between the modes.

In this chapter, we introduce a bilinear form for massive scalar fields in Kerr to take the place of the hydrogenic inner product in fully relativistic calculations. Under this bilinear form, which is a natural extension of the gravitational bilinear form of Ref. [268], Kerr QNMs and QBSs are truly orthogonal—for all values of α. The product reduces to the hydrogenic inner product in the limit $\alpha \to 0$, but it is also applicable in the relativistic regime, and forms the basis for a relativistic perturbation theory in terms of modes.

Using the relativistic product, we derive the anolog of time-dependent perturbation theory in quantum mechanics for the scalar field. As an application, we calculate the leading relativistic frequency shift due to the self-gravity of a superradiant mode, and we find a significant improvement over the hydrogenic approximation when comparing to previously-published numerical-relativity results [104], improving the agreement by a factor of 4 even at $\alpha = 0.4$. Our product therefore opens a new path

---

[1] The same is not true for QNMs, which still radiate to infinity.

to accurate nonlinear mode calculations.

7.2 Bilinear form for massive scalars

We first extend the bilinear form of [268] to scalar *massive* perturbations of Kerr and prove the orthogonality of scalar modes with both quasinormal and quasibound asymptotic conditions.

The Kerr line element for a black hole of mass M and spin parameter a is given by

$$\mathrm{d}s^2 = -\left(1-\frac{2Mr}{\Sigma}\right)\mathrm{d}t^2 - \frac{4Mar\sin^2\theta}{\Sigma}\mathrm{d}t\mathrm{d}\phi + \frac{\Sigma}{\Delta}\mathrm{d}r^2 + \Sigma\mathrm{d}\theta^2 + \frac{\Lambda}{\Sigma}\sin^2\theta\mathrm{d}\phi^2, \quad (7.1)$$

in Boyer-Lindquist coordinates, where $\Delta = r^2 + a^2 - 2Mr$, $\Sigma = r^2 + a^2\cos^2\theta$, $\Lambda = (r^2+a^2)^2 - \Delta a^2\sin^2\theta$. We denote the event horizon (the greater root $r_\pm$ of Δ) by r_+ and define the tortoise coordinate, $dr/dr_* = \Delta/\Sigma$.

The Klein-Gordon equation on a Kerr background (which coincides with the Teukolsky equation for a spin $s = 0$ massive field [261]) reads

$$\mathcal{O}\Phi \equiv (\Box - \mu^2)\Phi = 0, \quad (7.2)$$

where μ is the mass of the scalar field Φ. A product between two solutions of the Klein-Gordon equation can be built as follows. Start from a “base” product (related to the symplectic form),

$$\Pi_\Sigma[\Phi_1,\Phi_2] = \int_\Sigma d\Sigma_a(\Phi_1\nabla^a\Phi_2 - \Phi_2\nabla^a\Phi_1), \quad (7.3)$$

where Σ is a co-dimension 1 sub-manifold. One can easily verify that, if Φ_1, Φ_2 are solutions, the product is conserved (i.e., independent of Σ) and that it is $\mathbb{C}$-linear in both entries, or bilinear.

Reference [268] showed that one can build, from this base product, an infinite number of conserved quantities by inserting symmetry operators of the equation of motion. In Kerr, one can make use of the symmetry operators associated with the time-translation and ϕ rotation isometries, L_t and L_ϕ, as well as with the Killing tensor of the spacetime. One can also use the symmetry operator associated with the t–ϕ spacetime symmetry, $\mathcal{J}$, whose action on a scalar field simply takes $t \to -t$ and $\phi \to -\phi$. Note that the Teukolsky operator and the t–ϕ reflection operator commute on $s = 0$ Weyl scalars, $\mathcal{O}\mathcal{J} = \mathcal{J}\mathcal{O}$.

The product relevant for the orthogonality relation can be built from the t–ϕ reflection operator [268]. For scalar massive (or massless) perturbations *with compact support* it is given by

$$\langle\langle\Phi_1,\Phi_2\rangle\rangle = \Pi_\Sigma[\mathcal{J}\Phi_1,\Phi_2]\,. \quad (7.4)$$

In Boyer-Lindquist coordinates, the bilinear form reads

$$\langle\langle\Phi_1,\Phi_2\rangle\rangle = \int_{r_+}^{\infty} dr \int d\Omega\Big[\frac{2Mra}{\Delta}\left(\mathcal{J}\Phi_1\partial_\phi\Phi_2 - \Phi_2\partial_\phi\mathcal{J}\Phi_1\right) + \frac{\Sigma}{\Delta}\left(r^2+a^2+\frac{2Mra^2}{\Sigma}\sin^2\theta\right)$$
$$\times\left(\mathcal{J}\Phi_1\partial_t\Phi_2 - \Phi_2\partial_t\mathcal{J}\Phi_1\right)\Big], \quad (7.5)$$

where $d\Omega = \sin\theta d\theta d\phi$. In addition to being bilinear and conserved, one can easily prove, in analogy to Ref. [268], that

1. the bilinear form is symmetric, $\langle\langle\Phi_1, \Phi_2\rangle\rangle = \langle\langle\Phi_2, \Phi_1\rangle\rangle$; and
2. the time-translation symmetry operator is symmetric with respect to the bilinear form, $\langle\langle L_t\Phi_1, \Phi_2\rangle\rangle = \langle\langle\Phi_1, L_t\Phi_2\rangle\rangle$.

7.3 Extension to mode solutions

Quasinormal and quasibound states are mode solutions of the Teukolsky equation, $\Phi_{\ell m\omega} = e^{-i\omega t+im\phi}R_{\ell m\omega}(r)S_{\ell m\omega}(\theta)$, where $S_{\ell m\omega}$ are the $s = 0$ spin-weighted spheroidal harmonics with angular numbers ℓ, m [261] and the radial solution can be defined in terms of an asymptotic series involving a three-term recursion relation [269, 270]. The modes are required to be regular at the horizon, $\Phi \sim e^{-ik_H r_*}$ as $r_* \to -\infty$, where $k_H = \omega - m\Omega_H$ and Ω_H is the angular frequency of the outer horizon $\Omega_H = a/(2Mr_+)$. At infinity, the two families satisfy

$$\Phi \sim r^{-1}e^{ikr_*}, \qquad r_* \to \infty \quad \text{(QNMs)}, \tag{7.6}$$

$$\Phi \sim r^{-1}e^{-ikr_*}, \qquad r_* \to \infty \quad \text{(QBSs)}, \tag{7.7}$$

where $k = \sqrt{\omega^2 - \mu^2}$.

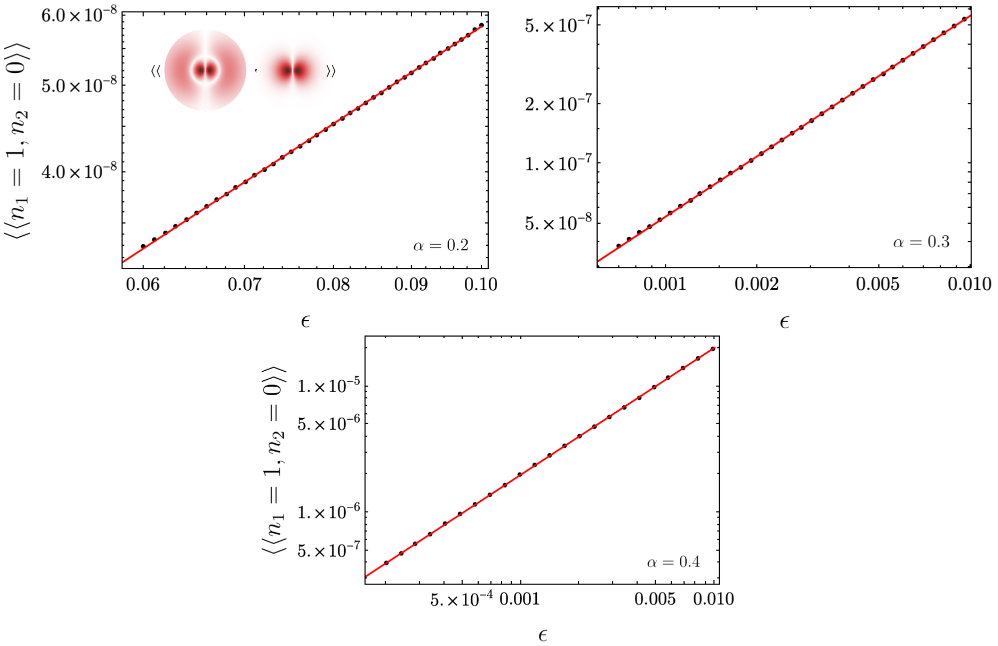

Figure 7.1. The relativistic product between two $\ell = m = 1$ QBSs in Schwarzschild, as a function of the counter-term regularization point $\epsilon = \bar{r}/r_+ - 1$, for different scalar field masses. The red curve is a power-law fit, showing convergence to zero. In the top-left corner, we show the absolute value of the radial mode-functions around the BH. Modes are normalized to have $\langle\langle n, n\rangle\rangle = 1$ in the regularization limit.

Because the radial solutions have non-compact support, and for $\omega_{\rm I} < 0$ actually diverge as $r_* \to -\infty$ (QNMs and QBSs) and as $r_* \to +\infty$ (QNMs), we must find a suitable, finite extension of the bilinear form (7.4). In analogy with Ref. [268], we extend the definition of the bilinear form to a complex radial integration contour $\mathcal{C}$, such that the radial integral is absolutely convergent. We define the bilinear form over a pair of QNMs or QBSs with complex frequencies ω_1, ω_2 by integrating over a complex r_* contour such that

$$\arg r_* + \arg(\omega_1 + \omega_2) = -\pi/2, \quad r_* \to -\infty\,, \tag{7.8}$$

and running along the real axis elsewhere. If the product is over one or two QNMs, we also take

$$\arg r_* + \arg(\pm k_1 \pm k_2) = \pi/2, \quad r_* \to \infty\,, \tag{7.9}$$

where the plus (minus) sign holds for QNMs (QBSs).

Explicitly, the bilinear form on modes reads

$$\langle\langle \Phi_1, \Phi_2 \rangle\rangle_{\text{modes}} = i\delta_{m_1 m_2} e^{-i(\omega_1-\omega_2)t} \int_{\mathcal{C}} dr \frac{1}{\Delta} K(r) R_1 R_2, \tag{7.10}$$

where

$$K(r) = \alpha_{12}(r^2+a^2)^2(\omega_2+\omega_1) - 2Mra\alpha_{12}(m_1+m_2) - \gamma_{12}(\omega_2+\omega_1)a^2\Delta, \tag{7.11}$$

$$\alpha_{12} = 2\pi \int_0^\pi d\theta \sin\theta S_1 S_2, \tag{7.12}$$

$$\gamma_{12} = 2\pi \int_0^\pi d\theta \sin^3\theta S_1 S_2. \tag{7.13}$$

Note that, as demonstrated for Kerr QNMs in Ref. [268], this product can be used to project initial data onto modes, resulting in the known mode excitation coefficients [271, 272, 273]. In the hydrogenic limit, this reduces to the familiar inner product on the (real) hydrogenic mode functions,

$$\langle\langle \Phi_1, \Phi_2 \rangle\rangle \to \delta_{m_1 m_2} \int_0^\infty dr \int_0^\pi d\theta\, r^2 \sin\theta R_1 R_2 S_1 S_2 = \langle \Phi_1 | \Phi_2 \rangle_H, \tag{7.14}$$

up to an overall factor. In this limit, no regularization is required.

7.3.1 The counter-term subtraction method

For QBSs in Schwarzschild, it is convenient to adopt an alternative regularization involving counter-term subtraction [274]. This is particularly useful when mode solutions are only known numerically. Consider for simplicity the bilinear form (7.4) in Schwarzschild. It is immediate to see that in this case the integrals in r and θ factorize, with the latter reducing to the orthogonality condition for spherical harmonics,

$$\langle\langle \Phi_1, \Phi_2 \rangle\rangle = i\delta_{m_1 m_2}\delta_{l_1 l_2}(\omega_1+\omega_2) \int_{r_+}^\infty dr \frac{r^2}{f} R_1 R_2, \tag{7.15}$$

where $f = 1 - 2M/r$. It is convenient to define the scalar function $R(r) = X(r)/r$, so that the radial integral becomes simply

$$\langle\langle \Phi_1, \Phi_2 \rangle\rangle \sim \int dr f^{-1} X_1 X_2 = \int dr_* X_1 X_2. \tag{7.16}$$

In the near-horizon limit, the solution X can be described by the series expansion

$$X(r) \sim \sum_{n=0}^{+\infty} X_{r_+}^n \sim \sum_{n=0}^{+\infty} e^{-i\omega r_*}(r-r_+)^n b_n(\omega). \tag{7.17}$$

At leading order, the mode behaves as

$$X_{r_+}^0(r) \sim e^{-i\omega r_*} \sim (r-r_+)^{r_+\omega_I}. \tag{7.18}$$

When the mode is stable ($\omega_I < 0$) this term diverges at the horizon. To regularize this divergence, we simply subtract the near-horizon integral of the leading order term,

$$\begin{aligned}\langle\langle \Phi_1, \Phi_2 \rangle\rangle_{\text{Schwarzschild QBS}} = i\delta_{m_1 m_2}\delta_{l_1 l_2}\,(\omega_1+\omega_2) \lim_{\bar{r}_*\to-\infty} \Bigg[\int_{\bar{r}_*}^{\infty} dr_* X_1(r'_*)X_2(r'_*) \\ + \frac{i}{\omega_1+\omega_2} X_1(\bar{r}_*)X_2(\bar{r}_*) + (\text{higher orders})\Bigg].\end{aligned} \tag{7.19}$$

Note that this method is suitable to regularize the horizon divergence of both (massless or massive) QNMs and QBSs, as their leading-order behavior in the near-horizon expansion coincides.

This method can be extended to regularize the divergence of any order $N = n_1+n_2$ in the horizon expansion (7.17),

$$X_{r_+}^{n_1} X_{r_+}^{n_2} \sim (r-r_+)^N (r-r_+)^{r_+(\omega_{I1}+\omega_{I2})}. \tag{7.20}$$

The N-th term in the expansion is regular if $r_+\omega_{I1} + r_+\omega_{I2} + N \geq 0$. However, QBSs with interesting (i.e., potentially detectable) phenomenology are long lived modes, $M|\omega_I| \ll 1$. In this limit, all terms beyond the leading order are regular, and the subtraction of the leading order divergence (7.19) is sufficient.

The complex contour and the counter-term subtraction method give equivalent definitions of the mode product. To see this, we separate the integral into

$$\langle\langle \Phi_1, \Phi_2 \rangle\rangle \sim \int_{\mathcal{C}} dr_* X_1 X_2 = \int_{\mathcal{C}_+} dr_* X_1 X_2 + \int_{\bar{r}_*}^{+\infty} dr_* X_1 X_2. \tag{7.21}$$

where $C_+ : r_* = \bar{r}_* + \rho e^{i\beta}$ and β is an angle in the complex plane chosen to satisfy condition (7.8). Assuming the modes are very bound $M|\omega_I| \ll 1$ and in the limit of $\bar{r}_* \to -\infty$, we find that the first integral is equal to

$$\begin{aligned} e^{-i(\omega_1+\omega_2)\bar{r}_*} e^{i\beta} \int_{\infty}^{0} d\rho\; e^{-i(\omega_1+\omega_2)\rho e^{i\beta}} \left[1+\mathcal{O}(\rho^{-1})\right] = \frac{i}{\omega_1+\omega_2} e^{-i(\omega_1+\omega_2)\bar{r}_*} \left[1+\mathcal{O}(\rho^{-1})\right] \\ = +\frac{i}{\omega_1+\omega_2} X_1(\bar{r}_*)X_2(\bar{r}_*) \left[1+\mathcal{O}(\bar{r}_*^{-1})\right]. \end{aligned} \tag{7.22}$$

This is precisely the counter term defined in (7.19).

7.4 Mode orthogonality

With the finite bilinear form in hand, from property 2 we obtain

$$(\omega_1 - \omega_2)\langle\langle \Phi_1, \Phi_2 \rangle\rangle = 0 \tag{7.23}$$

for a pair of QNMs or QBSs with frequencies ω_1, ω_2. Then, either $\langle\langle \Phi_1, \Phi_2 \rangle\rangle = 0$ or $\omega_1 = \omega_2$, proving that QNMs and QBSs are orthogonal. In particular, modes of the two families are also mutually orthogonal.

We now numerically compute the product (7.19) between two QBSs in Schwarzschild with different radial numbers[2] n. We do so in the hydrogenic ($\alpha = M\mu \ll 1$) and relativistic ($\alpha \simeq 1$) regimes. To compute the QB frequencies and radial solutions, we use the Leaver continued fraction method [269]. We perform product integrals (7.19) numerically using MATHEMATICA.

Figure 7.1 shows the product between the $\ell = m = 1$ fundamental mode and the first overtone as a function of the integral regulator $\epsilon = \bar{r}/r_+ - 1$. Different panels span the hydrogenic regime and the relativistic regime. The product between the two modes goes to zero as a power-law as $\epsilon \to 0$ in all cases, confirming numerically the orthogonality to a precision of order 10^{-7}. For higher values of α, we are able to probe the integral for smaller r due to better convergence resulting from milder divergences at the horizon. We obtain similar results also for higher radial overtones.

7.5 Relativistic perturbation theory

We now describe our relativistic approach to compute transitions between modes in the presence of a potential δV,

$$\mathcal{O}\Phi + \delta V \Phi = 0\,. \tag{7.24}$$

We begin with an ansatz for the scalar field in terms of a superposition of modes with time-dependent amplitudes,

$$\Phi = \sum_q c_q(t)\Phi_q, \tag{7.25}$$

where the usual time dependence of Φ_q is left implicit. This ansatz does not fully capture the solution because QB and QN modes, while being orthogonal, do not form a complete basis [271]. However, it should be valid at intermediate times, after the prompt emission from the initial perturbation and before the effect of scattering off the BH potential becomes dominant. The duration of this intermediate regime is set by the amplitudes and decay rates of the modes, and is therefore longer for long-lived modes, which are most relevant for observations.

Substituting the mode decomposition in (7.24) and using the bilinear form to project onto a mode n, we obtain

$$\sum_q \langle\langle \Phi_n, \mathcal{O} c_q(t)\Phi_q \rangle\rangle + \langle\langle \Phi_n, c_q(t)\delta V \Phi_q \rangle\rangle = 0. \tag{7.26}$$

---

[2] The product between states with different ℓ, m numbers is trivial, as their orthogonality in Schwarzschild follows from the orthogonality of the spherical harmonics. The orthogonality between different ℓ modes becomes non trivial in Kerr [268], due to the spin-weighted spheroidal harmonics.

We now use the fact that the Teukolsky operator vanishes on mode solutions, and that modes are orthogonal and have frequency ω_q. Because the bilinear form (7.5) contains derivatives with respect to the Boyer-Lindquist time, we need to take care in taking the excitation coefficients out of the product. We assume derivatives of the excitation coefficients to be of the same order as the external potential, $\dot{c} \sim \delta V$, $\ddot{c} \sim \delta V^2$, etc., so we drop all derivatives above the first to keep only the leading order in δV.

Our equation for the coefficients c_n then reads,

$$2i\omega_n \dot{c}_n \langle\langle \Phi_n, \Phi_n \rangle\rangle + \mathcal{O}(\delta V^2) = \sum_q c_q \langle\langle \Phi_n, \delta V \Phi_q \rangle\rangle. \tag{7.27}$$

Therefore, just like in quantum mechanics,[3] we find that perturbations can induce mode mixing through the matrix element $\langle\langle \Phi_n, \delta V \Phi_q \rangle\rangle$, where $\langle\langle \cdot, \cdot \rangle\rangle$ now stands for the bilinear form (7.5), augmented with suitable regularization.

7.6 Frequency shift

We apply our relativistic perturbative framework to calculate the frequency shift of a superradiant mode in Kerr due to its self-gravity. For simplicity, and following [263], we take a semi-Newtonian approximation for the gravitational potential of a mode,

$$\delta V(r) = -2\mu^2 \left[\frac{1}{r} \int_{r_+}^{r} d^3 r' T^t_t + \int_r^\infty d^3 r' \frac{T^t_t}{r'} \right], \tag{7.28}$$

where T is the (relativistic) stress-energy tensor of the (unperturbed) scalar field and the integration is carried out over flat space.[4]

To estimate the correction $\delta\omega_n$ to the mode frequency, we restrict the ansatz (7.25) to a single mode, and take the coefficient $c_n(t) \propto e^{-i\delta\omega_n t}$. Rearranging (7.27), we find

$$\delta\omega_n = -\frac{\langle\langle \Phi_n, \delta V \Phi_n \rangle\rangle}{2\omega_n \langle\langle \Phi_n, \Phi_n \rangle\rangle}. \tag{7.29}$$

This approach is similar in spirit to that outlined in Refs. [276, 277, 278, 266]. In the nonrelativistic limit, this formula reduces to that found in Refs. [169, 263]. Note that superradiantly unstable QBSs, which have $\omega_I > 0$ and decay at infinity, have no divergence at the horizon and therefore require no regularization.

We now calculate numerically the frequency shift (7.29) for superradiant modes with $\ell = m = 1$. For a given coupling α, we set the BH spin to be close to the superradiant bound $m\Omega_H \gtrsim \omega_R$, the same setup as [263]. For this application, we use the `Black Hole Perturbation Toolkit` to compute the modes' spin-weighted spheroidal harmonics [279].

---

[3] In the nonrelativistic limit, our equation reduces to the standard formula in quantum mechanics (including the quantum mechanics inner product), modulo a factor of $2\omega_n \sim 2\mu$ due to our definition of the potential (see, e.g., [275]).

[4] We note that simply introducing the relativistic volume element in this integration leads to additional divergences. However, a fully relativistic calculation of the self-gravity for this example is beyond the scope of this work. As we show numerically, such corrections are subleading compared to those that come from the bilinear form.

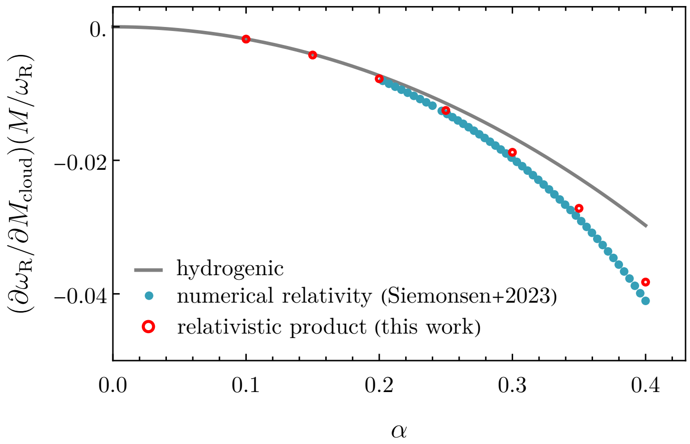

Figure 7.2. Frequency shift due to the self-gravity of a superradiant mode in Kerr ($\ell = m = 1$, $n = 0$). We compare our result based on the relativistic product with the hydrogenic approximation, and with the fully relativistic (numerical) frequency shift from Ref. [263]. For the analytic results, we plot $\delta\omega/M_{\rm cloud}$, which should be a good approximation of the derivative for small cloud masses.

In Fig. 7.2, we compare for several α our perturbative calculation of $\delta\omega/M_{\rm cloud}$ against the numerical relativity estimate of $\partial\omega/\partial M_{\rm cloud}$ from [263]. We find excellent agreement, including significant improvement over the hydrogenic approximation, which begins to fail around $\alpha \simeq 0.3$. For $\alpha = 0.4$, the error is reduced from 28% to 7%. The remaining disagreement is likely due to the approximation that $\delta\omega$ is linear in the cloud mass ($\partial\omega/\partial M_{\rm cloud} \simeq \delta\omega/M_{\rm cloud}$) and to our semi-Newtonian approximation for the potential.

7.7 Application to tidal potential

As another example, we consider the tidal, Newtonian potential arising from a non-spinning binary companion to a (Schwarzschild) black hole endowed with a QB state. In the hydrogenic approximation, this was shown to give rise to transitions between modes of the QB spectrum [92, 267].

A binary companion induces a perturbation in the background metric $g^{\mu\nu} = g_0^{\mu\nu} + \delta g^{\mu\nu}$. This leads to a shift in the potential of the scalar field (at leading order) $\delta V \sim \delta g_{tt} \sim \sum_{\ell_p m_p} r^{\ell_p} Y_{\ell_p m_p}$, where the subscript distinguishes the angular numbers of the perturbation [92].[5] We neglect the time dependence of the potential due to the companion's motion. This could be introduced after the calculation of the matrix element in an adiabatic approximation [92], or taken fully into account in the relativistic matrix element.

We compute the level mixing due to this external potential between modes with $\ell = 1$, $m = 1, -1$, and $n = 0, 1$ (or $|211\rangle$ and $|31\,{-1}\rangle$ in the hydrogenic notation[6]). Note that this transition is allowed in the case of tidal quadrupolar

---

[5] In our formalism, it is possible to consistently include relativistic corrections to the tidal potential. However, a full description of the binary system is beyond the scope of this work.

[6] In this notation, states are labelled by the three quantum numbers $|\tilde{n}\ell m\rangle$, where $\tilde{n} = \ell + n + 1$

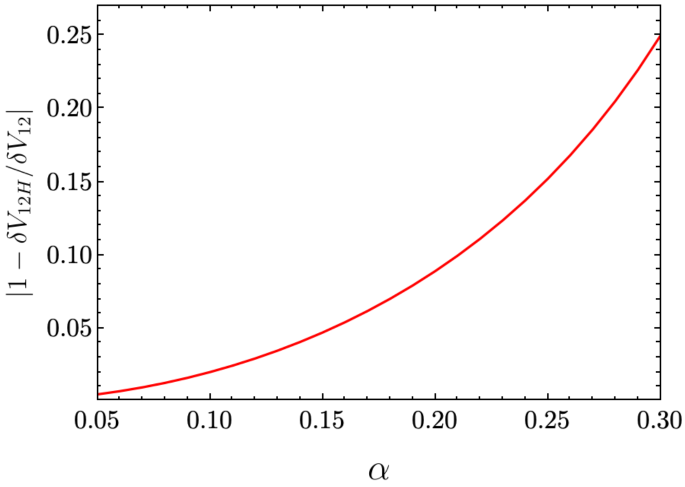

Figure 7.3. Relative difference in the matrix element of the companion's tidal potential, computed with our bilinear form and in the hydrogenic approximation. The discrepancy increases with α, as the hydrogenic approximation breaks down.

perturbations $\ell_p = 2$ by the angular selection rules due to the angular dependence of the perturbed potential [92]. These selection rules survive in the relativistic limit (at least in Schwarzschild) as the bilinear form reduces to the standard inner product for spherical harmonics. We will therefore focus on the radial part of the matrix element.

In the hydrogenic approximation, the matrix elements of δV read

$$\langle \tilde{n}_1 \ell_1 m_1 | \delta V | \tilde{n}_2 \ell_2 m_2 \rangle_H \sim \int_0^\infty dr\, r^4 R^H_{\tilde{n}_1 \ell_1 m_1} R^H_{\tilde{n}_2 \ell_2 m_2}, \tag{7.30}$$

where $R^H_{n\ell m}$ are the hydrogenic wavefunctions,

$$R^H_{\tilde{n}\ell m}(r) = \sqrt{\left(\frac{2\mu\alpha}{\tilde{n}}\right)^3 \frac{(\tilde{n}-\ell-1)!}{2\tilde{n}(\tilde{n}+\ell)!}} \left(\frac{2\alpha\mu r}{\tilde{n}}\right)^\ell e^{-\frac{\mu\alpha r}{\tilde{n}}} L^{2\ell+1}_{\tilde{n}-\ell-1}\left(\frac{2\mu\alpha r}{\tilde{n}}\right). \tag{7.31}$$

Notice that the hydrogenic wavefunctions are everywhere regular and are integrated from the origin, as already discussed.

The matrix element appearing in the fully relativistic perturbative expansion (7.27), on the other hand, reads

$$\langle\langle n_1 \ell_1 m_1, \delta V n_2 \ell_2 m_2 \rangle\rangle \sim \int_{r_+(1+\epsilon)}^\infty dr\, r^2 f(r) X_1(r') X_2(r') + \frac{i r_+^2}{\omega_1 + \omega_2} X_1(R) X_2(R)\,, \tag{7.32}$$

Notice that the potential modifies the boundary regularization term at the horizon. In the nonrelativistic limit, the full radial solutions X become real and tend to the hydrogenic approximation: $R^H_{n\ell m}(r) \approx \mathrm{Re}(X_{n\ell m}(r))/r$.

We evaluate the relativistic matrix element (7.32) on numerical Klein-Gordon solutions. We find that this converges to a finite nonzero value as we take the

---

is the principal quantum number.

integral regulator $\epsilon \to 0$, confirming that the tidal potential gives rise to level-mixing between the two modes under consideration.

In Fig. 7.3 we show the relative difference between the hydrogenic matrix element appearing in Ref. [92] and our fully relativistic treatment (7.32), for a range of scalar masses α. While the matrix elements obtained with the two methods are overall comparable, the relative error clearly increases for higher α, as the hydrogenic approximation starts to loose accuracy.

Interestingly, whilst the relative error is below 1% for $\alpha \approx 0.05$, it can be as high as 10% already for values of $\alpha \simeq 0.2$, where the radial solutions are still relatively accurate (within at most 5%). This suggests that relativistic corrections to the mode product itself—included in our fully relativistic bilinear form, but not in the quantum-mechanics inner product—contribute significantly to the matrix element. Previous work on mode mixing focused on relativistic corrections to the decay width of the modes [97], or resorted to fully numerical methods [96].

7.8 Conclusions

In this chapter, we introduced a bilinear form for massive scalar-field perturbations of Kerr and showed that modes are orthogonal with respect to this product. Our bilinear form replaces the standard quantum mechanics inner product—often employed in a hydrogenic approximation—making no assumption on the strength of the gravitational coupling α. We also introduced an approach to compute perturbative corrections to mode evolution due to an applied potential, and applied this to recover frequency shifts due to the self-gravity of a superradiant state. For large values of α, accurate results were previously only obtainable using numerical relativity.

Our bilinear form and perturbative framework have both conceptual and practical importance.

Other applications could be to compute corrections due to self-interaction terms such as quartic potentials [169], or in the sine-Klein-Gordon equation for the QCD axion [204]. In future work, we also hope to explore transitions between QN and QB modes, and to rigorously derive angular selection rules for massive perturbations in Kerr using the bilinear form.

Another natural extension would be to generalize our product to massive spin-1 fields. This scenario presents a number of difficulties as the Proca equation is not separable using the standard Teukolsky formalism. Nevertheless, an ansatz yielding separability of the Proca equation in Kerr spacetime was recently discovered [280, 82], and could allow for a generalization of the bilinear form.

Finally, in the context of BH binaries, the gravitational product [268] could be used with the second-order Teukolsky equation [281, 282] to estimate nonlinear corrections to the BH ringdown. This could be used to inform waveform development and address recent questions on nonlinear effects during the ringdown [283, 284, 285, 264, 265].

Part II
Tests of General Relativity using gravitational waves

Chapter 8

Testing GR: an introduction

In 1916, after linearizing the field equations in the weak-field limit, Einstein showed that a natural prediction of GR was the existence of transverse GWs travelling at the speed of light. A century after, on September 2015, the LIGO-VIRGO collaboration reported for the first time a direct detection of a GW signal produced by a binary BH system [13]. This historical event marked the birth of GW astronomy, and provided for the first time access to the strong-field, highly-relativistic regime. Nowadays, the collaboration released three catalogue of events [286, 287, 288], corresponding to nearly 100 coalescences composed of BHs and NSs binaries. These events already allowed to perform sensitive tests of GR in the strong field regime (see e.g. [14, 15, 16, 17, 18]). Up to now, none of the tests showed clear evidence in support of physics beyond GR. Nevertheless, the new generation detectors Einstein Telescope [289, 290] and Cosmic Explorer [291], together with the future space-based Laser Interferometer Space Antenna (LISA) [292], will allow to reach unprecedented sensitivities, and therefore to test even extremely more feeble deviations [293, 294, 295, 296, 297].

Moreover, just a few months ago in June 2023, several Pulsar Timing Array collaborations– NANOGrav, EPTA, PPTA, CPTA – released observational data showing clear evidence of a stochastic GW background at nHz frequencies, most likely originating from supermassive BH binaries [298, 299, 300, 301, 302, 303, 304, 305, 306].

Therefore, the plethora of present and future GW observations offer a unique opportunity to probe the nature of gravity in different highly dynamical systems– ranging from stellar mass binaries to EMRIs and supermassive BH binaries– with an unrivalled precision. Most crucially, while previous tests were based on weak-gravity and quasi-stationary assumptions [34, 35], where the relevant velocities are non-relativistic and the gravitational field is weak with respect to the energy of the system, GWs allow to probe the *strong* gravity regime, where deviations from GR may be more prominent.

The evolution of a BH binary can be divided into three stages. During the *inspiral* phase, the two BHs evolve adiabatically, and get closer to each other due to the continuous emission of GWs. During this phase, the orbital velocities of the two bodies are only mildly relativistic, and the evolution can be therefore described by adopting a post-Newtonian (PN) approach. Afterwards, during the *merger* phase a common horizon is formed. In this regime, the system turns highly dynamical and non-linear, and the PN formalism breaks down. Hence, fully numerical simulations are necessary to describe this stage. After the merger, the system is composed of a highly perturbed remnant, that afterwards relaxes to a Kerr BH during the final stage, known as *ringdown*.

When considering modifications to GR, depending on the details of the underlying theory, deviations might be more easily detectable in particular types of systems. For example, systems at high redshift may be way more suitable with respect to low-redshift ones to probe theories that modify the propagation features of GWs . The former are ideal targets of future space-based interferometers and future third-generation ground-based detectors [1] Another notable example comes from quadratic gravity theories [308, 309], where higher order curvature terms in the action are naturally suppressed by the inverse of the curvature radius (see e.g. [310, 311]). Hence, stellar-mass objects may be more suitable to detect deviations rather then supermassive BHs, where the curvature radius is much larger.

Moreover, different detectors are sensible to different stages of the GW waveform. In particular, while ground-base detectors are extremely sensible to the late-inspiral and merger, space-based interferometers are unique to probe thousands of cycles in the sensitivity band during an extreme mass-ratio inspiral. Because of this, even the smallest deviation to the rate of change of the binding energy during the inspiral – e.g. because of the presence of an extra channel of emission besides GWs – could be more feasibly detected using EMRIs (see e.g. [312, 313, 314]). Finally, PTAs are sensible to extremely low frequency waves obtainable only during the *early* inspiral of supermassive BHs, but cannot probe the late inspiral or the merger phase. Consequently, they are able to probe GR at large separation and low frequencies, but cannot probe theories that deviate from GR only in the latest stages. For these reasons, different detectors and sources offer *complementary* ways to test GR in different ways [315, 17].

As a final remark, in order to perform competitive tests of GR using binary black holes, a detailed understanding of the binary parameters (e.g. eccentricity and precession) and the impact of the surrounding environment is imperative. Indeed, these effects may mimic or mask modifications to GR, jeopardizing possible tests. In particular, unlike in the NS binaries case, BHs in binaries are likely to possess a high spin and strongly precess. While this entails a richer phenomenology, it also makes it more difficult to perform GR test. Hence, accurate waveform models accounting for these effects are crucial [316, 317, 318, 319, 320]. Together with intrinsic parameters, also environmental effects can potentially jeopardize the robustness of GR test. For example, the presence of accretion disks around BHs can induce dynamical friction, accretion or planetary migration during the inspiral phase. While these effects are not expected to be relevant for most EMRIs detectable with LISA [33], they are instead expected to play a crucial role in supermassive BH binaries detectable with PTAs [321, 322, 323, 324, 325, 326, 327, 328, 329]. A more detailed discussion of this aspect will follow in chapter 10.

---

[1] *Notably, the latter can potentially reach* $z \sim 100$ *for binaries with total mass* $M \approx 10 - 30 M_\odot$ *at a signal-to-noise ratio* ≈ 8 *[307]. Conversely, current ground-based detectors are limited to* $z \sim 1$.

In this thesis, we will focus on tests of GR during the inspiral phase, both in the case of EMRIs and supermassive BH binaries. Moreover, we will focus on *null* tests of GR, by adopting a model-agnostic approach and search for generic deviations, without assuming specific beyond GR theories. In the following, we begin with a brief description of the typical features of the systems of interest.

8.1 Extreme mass-ratio inspirals

In EMRIs, a stellar mass compact object $(1 - 10M_\odot)$ spirals around a supermassive BH $(10^5 - 10^9 M_\odot)$, such that the mass ratio q is extremely small $q \approx 10^{-4} - 10^{-8}$. Such supermassive BHs are expected to reside at the center of most large galaxies. Indeed, from a precise observation of stellar kinematics, we know that most neighboring galaxies host one. Also in our very own galaxy, stellar dynamics provide evidence for a BH with a mass $\sim 4 \times 10^6 M_\odot$, called Sgr A* [330]. Therefore, EMRIs are expected to form whenever stellar-mass objects are captured from the nuclear star cluster surrounding the massive BH. After the capture, the dynamics is expected to initially be described by very eccentric orbits accompanied by the emission of bursts of GWs (when the small object is near the pericenter), and then into the evolution to a more circular inspiral [331]. In this latter phase, the system emits continuously GWs in the mHz range, making EMRIs ideal targets for LISA. Moreover, EMRIs represent probably the most promising systems to test with exquisite precision the nature of spacetime in a strong gravity regime. Indeed, due to the extreme mass-ratio, *GW emission in the early inspiral phase* affect the orbit in a much longer timescale than the orbital one, i.e. $T_{inspiral} \propto q^{-1} >> T_{orbital}$. Hence, the evolution of the system is remarkably adiabatic, and the secondary object is expected to perform an incredible number of orbits (*proportional to* q^{-1}) while emitting GWs in the LISA band. In particular, even at the very end of the inspiral, the secondary spends two years in the vicinity of the Innermost Stabel Circular Orbit (ISCO), emitting $\sim 10^5$ GW cycles [332]. Thus, the signal encodes an extremely detailed map of the spacetime features, and will allow to probe the mass and spin of the primary (and therefore its "Kerrness") with unrivalled accuracy [333, 334, 331]. Remarkably, while EMRIs can probe deviations from GR with extreme accuracy by probing the primary objects, they can also potentially unveil these modifications from the motion of the secondary. This feature is extremely important because, as already mentioned, some theories such as quadratic gravity ones induce a more prominent deviation on stellar mass objects rather than supermassive ones.

As a notable example, in a recent series of paper it was shown how, if the secondary carries a scalar charge, the extra emission of scalar radiation in addition to GWs cause a dephasing in the orbit which leaves a clear imprint in the waveform observable by LISA [335, 312, 311, 313, 314, 336, 337]. These studies were performed both for specific beyond GR theories and in a model-agnostic approach, by encapsulating a large class of theories. Such works have subsequently been generalized to the vector case [338, 339]. In the following chapter, we will extend this analysis to the case of a dipole setup rather than a monopole charge, and highlights the main differences in the phenomenology.

Last but not least, if the primary is endowed with a specific environment, EMRIs can test its features with accuracy. For example, in the case of a superradiant cloud, the emitted signal is characterized by specific features which are observable by LISA [92, 93, 222, 97, 96, 95, 266] (see also chapter 7 for related work). Another notable (and less exotic) example comes from LISA-based probes of accretion physics, up to now only accessible with EM observations [340, 341, 33, 342].

EMRIs are therefore ideal target to test both physics beyond GR and the SM [297, 292].

8.2 Supermassive BH binaries and pulsar timing arrays

A neutron star is the spinning remnant of a massive star. After a supernova process, the remnant consist of a structure of stellar mass dense material consisting mostly of neutrons. Neutron stars are highly spinning, as during the collapse the angular momentum ωr^2 is conserved, and since the radius decreases dramatically, the rotation period can become as small as $\sim O(1)$ms. Similarly, during the collapse the magnetic flux is conserved, and therefore the remnant is characterized by extreme magnetic fields $\sim 10^{12}G$ or higher. Because of this, high-energy particles in the neutron star magnetosphere emit powerful radiation in the radio band, moving on open magnetic field lines over the magnetic poles. If moreover the magnetic field is not aligned with the axis of rotation, which is typically the case, the radio beam sweeps a circle with the rotation orbital period. Hence, an observer receives periodic short radio signals along the line of sight, much like a lighthouse effect. Remarkably, due to their large inertia, pulsars are extremely stable rotators, and therefore the timing of the signals is precise enough to allow to consider them "natural clocks" (see e.g. [343]). Nevertheless, a number of effects can induce small modifications or modulations in the time of arrival (TOA) of the pulses: the motion of the earth, the effect of the gravitational field of the solar system, the presence of a binary companion and the dispersion effects induced by the interstellar plasma, that alters the group velocity of the pulses [344, 345]. Hence, one can define a "time residual" as the difference between the expected TOA and the measured one. Most notably, also GWs can produce a residual in the signals by inducing a redshift. Hence, if one take into account a correct modelling of all the other effects inducing residuals, one can actually use signals from a system of well-timed pulsars (a "pulsar timing array") as GW detectors [346, 347]. The residual can be simply computed as the integral of the redshift $R(t) \equiv \int_0^t z(t')dt'$. For a GW, one obtains [315]:

$$R \sim h/f \,, \tag{8.1}$$

such that for residuals of ≈ 100ns, GWs with frequencies $f \approx 10^{-9} - 10^{-8}$Hz and strain $h \approx 10^{-15}$ would induce an observable effect. Therefore, as PTAs are sensible to ≈ 10nHz frequencies, they can be used to probe GWs emitted from the early inspiral phase of supermassive ($> 10^8 M_\odot$) BH binaries. These binaries would emit GWs continuously as they slowly inspiral, and the signals could be detected either individually or as a stochastic background.

A natural question would nevertheless be how to disentangle GWs as a source of residuals from other possible effects. Remarkably, Hellings and Downs (HD) [348] were able to compute the correlations between the residuals of a pair of pulsars

caused by the stochastic GW background as a function of the angle between the pair. Hence, the HD correlation curve is a smoking gun of GW-induced residuals and can be used to disentangle other possible origins.
The total energy emitted in GWs by a population of supermassive BH binaries in the universe was first computed by Phinney under the assumption *of circular orbits in the Newtonian limit at leading order* [349]:

$$\frac{dE_{\rm GW}}{df} = \frac{\pi}{3}\frac{(G\mathcal{M})^{5/3}}{G(\pi f)^{1/3}}\,, \tag{8.2}$$

where f is the frequency of the signal and $\mathcal{M}$ is the chirp mass of the binary. In terms of a different observable, this corresponds to a scaling of the GW spectrum $\Omega_{\rm GW} \propto f dE_{\rm GW}/df \propto f^{2/3}$. Nevertheless, it was soon realized that the scaling obtained by Phinney in the vanilla model would actually be extremely modified by the effects of the environments surrounding the binary [321, 322, 323, 324, 325, 326, 327, 328, 329]. Indeed, such environment can introduce dissipative effects at negative PN orders, which are therefore pivotal in the early inspiral. Examples include, e.g., dynamical friction (-5.5 PN) and stellar scattering (-5 PN). In particular, these effects would modify the spectrum by leading to a steeper scaling. Most crucially, even the presence of eccentricity leads to a similar effect [350, 351]. Hence, a deep knowledge of the binaries features and the environment is required to deduce solid predictions from measurements.

In recent years, some PTA collaborations provided for the first time evidence for a common spectrum of stochastic nature.

In 2020 the NANOGrav collaboration reported evidence for a stochastic spectrum [352], which nevertheless did not exhibit clear evidence of an HD angular correlation.
Nevertheless, in June 2023, several PTA collaborations– NANOGrav [298, 299], EPTA (in combination with InPTA) [300, 301, 302], PPTA [303, 304, 305] and CPTA [306]– found clear evidence for a stochastic background characterized by an HD angular correlation, thereby confirming its quadrupolar nature. The scaling of the reported spectrum, $\Omega_{\rm GW} \propto f^{(1.6,2.3)}$ at 1σ, is in tension with the vanilla SMBH binary scaling by 2σ. Nevertheless, as already mentioned environmental effects are expected to alleviate such tension. Hence, even though different explanations of cosmological origins for the spectrum could also faithfully reproduce the observed data (examples are first-order phase transitions [353, 354, 355, 356, 357, 358, 359, 360, 361, 362, 363, 364, 365], cosmic strings and domain walls [366, 367, 368, 369, 370, 371, 372, 373, 374, 375, 376, 377, 378, 379, 380, 381, 382, 383], or scalar-induced GWs generated from primordial fluctuations [384, 385, 386, 387, 388, 389, 390, 391, 392, 393, 394, 395, 396, 397, 398, 399, 400, 401, 402, 403, 404, 405, 406]), the SMBH scenario remains the leading explanation.
In principle, many beyond GR theories also introduce dissipative effects at negative PN order, thereby acting on the spectrum similarly to some environmental effects. Example include dipole radiation (-1 PN), extra-dimentions or a varying Newton's constant (both at -4 PN) (see e.g. [17, 18, 407]). Therefore, given that BHs in the PTA band have extremely large orbital separations in the early-inspiral, one can expect such corrections to play a major role in such systems. Since negative PN

deviations may be prominent in these systems, and also lead to a steeper scaling, PTAs measurements can potentially be used to develop novel tests of GR. In chapter 10 we develop a framework to map different beyond GR theories into a modified SGWB spectrum in a model-agnostic way, and show that current data already allow to place competitive constrains on specific theories.

Chapter 9

EMRIs and fundamental dipoles

Summary

Even if globally neutral, in various scenarios compact objects can have a nonvanishing dipole moment. Examples include neutron stars with magnetic dipoles, black-hole microstates in the string-theory fuzzball scenario, and classical black holes in modified theories of gravity with spin-induced scalarization or Lorentz-violating terms. A fundamental dipole moment would give rise to rich phenomenology, for example to intrinsic precession and extra emission channels in binary systems. We show that extreme mass-ratio inspirals (EMRIs) detectable by future gravitational-wave interferometers allow us to study a fundamental dipole on the secondary object in a model-agnostic fashion. By developing a general model for a fundamental scalar dipole, we compute the extra flux associated with it. This effect is suppressed by the square of the mass ratio relative to the case of fundamental charges, making its detection with EMRIs very challenging for the typical dipole moments predicted in various models. On the other hand, for the same reason the impact of an extra dipole for constraints on extra fundamental charges is likely negligible, making the latter constraints more robust.

9.1 Compact objects and fundamental dipoles

The famous no-hair theorems predict that, in a large class of theories, black holes (BHs) are described by the Kerr-Newman solution and do not have any extra charge other than the electromagnetic one. Circumventing these no-go theorems has motivated both theoretical work – aimed at finding theories in which BHs can have hair – and phenomenological work – aimed at finding the consequences of this extra hair (see, e.g., [17, 408]). The most natural and best studied case is when BHs are endowed with extra fundamental charges, which give rise to dipolar radiation in binary systems and can be probed with binary pulsar timing and gravitational-wave (GW) inspirals (see [17] for a review).

The absence of dipolar emission in binary pulsars [249] and in GW events [407, 16] already puts stringent constraints on the existence of fundamental charges in various contexts.

In the future, extreme mass-ratio inspirals (EMRIs) – one of the main targets of future space detectors such as LISA [409] – will provide a unique probe to search for extra fundamental charges [297, 410], either in the context of specific modified theories of gravity [335, 312, 311] or in a model-agnostic fashion, as recently shown [313, 314, 336, 337] for scalar fields (see Refs. [338, 339] for extensions to the vector case).

In addition to new fundamental charges, there is strong theoretical and phenomenological motivation for models in which compact objects are *globally neutral* (hence evading standard dipole-emission constraints) but can nevertheless have higher multipole moments. The most natural example are magnetars, which are endowed with strong magnetic dipole moments (see [411] for a review). Furthermore, in the context of modified gravity theories, BHs could have a fundamental dipole moment in Lorentz-violating theories [412], in dynamical Chern-Simons gravity [309, 413], and in theories featuring spin-induced spontaneous scalarization [414, 415, 416, 417] (see [418] for a recent review). Finally, in the context of BH microstates emerging in the string-theory fuzzball scenario [419, 420, 421], a long-lasting problem is to find consistent solutions which are globally neutral. Remarkably, this was recently achieved with topological solitons [422, 423], which are globally neutral but have an intrinsic dipole moment.

Motivated by the above scenarios in various contexts, in this chapter we wish to study the impact of fundamental dipoles for GW tests of fundamental physics with EMRIs.

9.2 Setup

9.2.1 Theoretical framework

Let us consider the following generic action [313]

$$S[\mathbf{g},\Phi,\psi]=S_0[\mathbf{g},\Phi]+\alpha S_c[\mathbf{g},\Phi]+S_m[\mathbf{g},\Phi,\psi], \tag{9.1}$$

where Φ is a massless scalar field,

$$S_0[\mathbf{g},\Phi]=\int \mathrm{d}^4x\frac{\sqrt{-\mathbf{g}}}{16\pi}(R-\frac{1}{2}\partial_\mu\Phi\partial^\mu\Phi), \tag{9.2}$$

S_m is the action of the matter fields ψ, while the action S_c describes a generic non-minimal coupling between gravity and the scalar field, whose coupling constant is α. As in Refs. [313, 314, 336, 337], we will assume that the theory is continuously connected to GR in the $\alpha\to 0$ limit and that either α has dimensions $[\alpha]=(\text{mass})^n$ with $n\geq 1$ or that the theory is such that no-hair theorems hold. *Note that this assumption encapsulates a large number of theories: while in most scalar-tensor theories of gravity the no-hair theorem holds (e.g. Brans-Dicke, see [424, 237]), a notable example of a theory that evades this constrain but is still described by this framework is scalar Gauss-Bonnet gravity, where n=2.*

An EMRI is a binary system in which a small compact object with mass $m_{SCO}=2\mu$ is spiraling around a supermassive BH with mass $M\gg\mu$. Owing to the small mass ratio, $q=\mu/M\ll 1$, one can model the secondary using the "skeletonized approach" [425, 426, 427], in which the secondary object is treated as a point particle.

Nevertheless, as we want to describe an object endowed with a dipolar field, we will use the skeletonized approach to model the secondary as an elementary dipole made by two point particles with mass μ displaced by a constant separation δy^μ, which we assume to be small with respect to the length scale of the exterior spacetime, $\sim M$. Therefore, the action of the matter fields reduces to

$$S_m[\mathbf{g},\Phi] = -\sum_{i=1,2} \int \mathrm{d}\lambda m_i(\Phi)\sqrt{\mathbf{g}_{\mu\nu}\frac{\mathrm{d}y_i^\mu}{\mathrm{d}\lambda}\frac{\mathrm{d}y_i^\nu}{\mathrm{d}\lambda}}, \tag{9.3}$$

where the two worldlines of the particles are given by $y^\mu_{1,2}(\lambda) = y^\mu(\lambda) \pm \frac{1}{2}\delta y^\mu$ with $y^\mu(\lambda)$ world-line of the center of mass of the dipole.

From the action, we can now derive the field equations and solve them by perturbatively expanding the fields at the leading order in the mass ratio. The Einstein equations for the gravitational field read

$$G_{\mu\nu} = R_{\mu\nu} - \frac{1}{2}\mathbf{g}_{\mu\nu}R = T^{(s)}_{\mu\nu} + \alpha T^{(c)}_{\mu\nu} + T^p_{\mu\nu}, \tag{9.4}$$

where $T^{(s)}_{\mu\nu}$ is the stress energy tensor of the scalar field, $T^{(c)}_{\mu\nu}$ is the term arising from the variation of the non-minimal coupling term S_c, while $T^p_{\mu\nu}$ is the stress-energy tensor of the two-particle dipole,

$$T^{p\ \mu\nu} = 8\pi \sum_{i=1,2} \int \mathrm{d}\lambda m_i(\Phi)\frac{\delta^{(4)}(x^\alpha - y_i^\alpha(\lambda))}{\sqrt{-\mathbf{g}}}\frac{\mathrm{d}y_i^\mu}{\mathrm{d}\lambda}\frac{\mathrm{d}y_i^\nu}{\mathrm{d}\lambda}. \tag{9.5}$$

Varying the action with respect to the scalar field yields

$$\Box\Phi + \frac{8\pi\alpha}{\sqrt{-\mathbf{g}}}\frac{\delta S_c}{\delta\Phi} = 16\pi \sum_{i=1,2} \int \mathrm{d}\lambda m_i'(\Phi)\frac{\delta^{(4)}(x^\mu - y_i^\mu(\lambda))}{\sqrt{-\mathbf{g}}}, \tag{9.6}$$

where the prime denotes derivative of a function with respect to its argument.

As discussed in [313, 314], due to the mass dimensions of the coupling α, GR modifications to the background are suppressed by the mass ratio of the binary (or absent if the no-hair theorems are satisfied). Hence, the exterior spacetime of the primary can be approximated as (or is exactly) the Kerr metric. In these settings, one can neglect the terms proportional to α in Eqs. (9.4) and (9.6), since they are suppressed by the mass ratio. In absence of the secondary, the resulting set of equations coincide with those of general relativity with a free scalar field, for which the no-hair theorem applies. Therefore, the background scalar field is just a constant Φ_0.

By expanding (9.6) at linear order $\Phi = \Phi_0 + \varphi$, we obtain the following equation for the perturbation φ:

$$\Box\varphi = 16\pi \sum_{i=1,2} \int \mathrm{d}\lambda m_i'(\Phi_0)\frac{\delta^{(4)}(x^\mu - y_i^\mu(\lambda))}{\sqrt{-\mathbf{g}}}, \tag{9.7}$$

where the operator $\Box$ is evaluated on the background Kerr metric $\mathbf{g}^0_{\mu\nu}$. The same expansion leads $m_i(\Phi)$ in Eq. (9.5) to be evaluated at $\Phi = \Phi_0$. Thus, at the leading order the gravitational equations (9.4) coincide with the standard ones for two infinitely close point masses in general relativity.

Let us now discuss the physical meaning of the terms $m_i(\Phi_0)$ and $m_i'(\Phi_0)$ by generalizing the argument of Ref. [314] to the case of our two-particle system. These functions can be evaluated in a region which is sufficiently close to the particles (relatively to the length scale of the exterior spacetime, $\sim M$), but sufficiently far away from them with respect to length scale of the particle themselves, *given by their Schwarzschild radius* $\sim \mu$, so that we can evaluate the equations in the weak-field limit. We therefore choose a reference frame $\{\tilde{x}^\mu\}$ centered at the center of mass of the compact object and consider Eqs. (9.5) and (9.7) in an intermediate region, $\mu \ll \tilde{r} \ll M$, where $\tilde{r}^2 = \tilde{x}^i \tilde{x}_i$. Let us first consider Eq. (9.5) evaluated at $\Phi = \Phi_0$. As in this region we are in the weak-field limit, the stress-energy tensor of a particle reduces to its matter density and thus it follows that $m_1(\Phi_0) = m_2(\Phi_0) = \mu$.

We can now turn to the study of Eq. (9.7). Expanding the latter to leading order in the infinitesimal displacement $\delta y^\mu \ll x^\mu$ in these coordinates yields

$$\nabla^2 \varphi = 16\pi A(\Phi_0)\delta^{(3)}(\tilde{x}^i) + 16\pi B(\Phi_0)\delta\tilde{y}^i \partial_i \delta^{(3)}(\tilde{x}^j), \tag{9.8}$$

where $A(\Phi_0) = \frac{1}{2}(m_1'(\Phi_0)+m_2'(\Phi_0))$ and $B(\Phi_0) = \frac{1}{2}(m_1'(\Phi_0)-m_2'(\Phi_0))$. If $B(\Phi_0) = 0$, then the solution φ has exactly the same form as in [314], and therefore $A(\Phi_0)$ can be associated with the monopolar scalar charge per unit of mass of the object (we shall denote this quantity by d). As we instead wish to describe an intrinsically dipolar field configuration, for the moment we ignore this term. Setting $A(\Phi_0) = 0$ we recognize the equation for the potential of a dipole, which is solved by

$$\varphi = \frac{4B(\Phi_0)\delta\tilde{y}^i \tilde{x}_i}{\tilde{r}^3}. \tag{9.9}$$

By direct comparison with the potential of a dipole with dipole vector $P^i = \mu d \delta\tilde{y}^i$, which is

$$\varphi = \frac{P^i \tilde{x}_i}{\tilde{r}^3}, \tag{9.10}$$

it is clear that we can interpret $4B(\Phi_0)\delta\tilde{y}^i$ as a dipole vector and therefore $B(\Phi_0) = \frac{1}{4}\mu d$, $m_1'(\Phi_0) = -m_2'(\Phi_0) = \frac{1}{4}\mu d$ where, as mentioned, d is the scalar charge per unit of mass of the secondary. Finally, the equation for the scalar field reads

$$\Box\varphi = 4\pi T\,, \tag{9.11}$$

where

$$T = \mu d \left[\int \mathrm{d}\lambda \frac{\delta^{(4)}(x^\mu - y^\mu(\lambda) + \frac{\delta y^\mu}{2})}{\sqrt{-\mathrm{g}}} - \int \mathrm{d}\lambda \frac{\delta^{(4)}(x^\mu - y^\mu(\lambda) - \frac{\delta y^\mu}{2})}{\sqrt{-\mathrm{g}}} \right]. \tag{9.12}$$

The above discussion shows that our system can indeed be understood as a scalar dipole made of two particles with the same mass but opposite scalar charge, whose center of mass inspirals onto a standard supermassive (Kerr) BH. This suggests to introduce the dipole moment tri-vector per unit of mass-squared:

$$p^i = \frac{d}{\mu}\delta y^i. \tag{9.13}$$

Notice that this is a dimensionless quantity, in analogy with the dimensionless charge d.

In the case in which $A(\Phi_0) \neq 0$, then the secondary has a nonvanishing net charge as well as a dipole moment. While we are mostly interested in the case of zero net charge, later on we will also consider this scenario, as our formalism allows to analyse deviations from scalar emission from a fundamental charge due to the presence of an extra dipole component.

9.2.2 Scalar equation via Teukolsky formalism

The inhomogeneous Klein-Gordon equation (9.7) can be solved via Teukolsky formalism [261]. First of all, we must characterize the wordlines of the two particles, $y_i^\mu(\lambda)$, that appear on the right-hand side of Eq. (9.7). Since for an EMRI the inspiral timescale is much longer than the orbital time scale, $T_{\text{inspiral}} \gg T_{\text{orbital}}$, we can adopt an adiabatic approximation, which allows us to consider the center of mass of the dipole as being in nearly geodesic motion. This approximation facilitates the evaluation of the emitted energy flux $\dot{E}$ from the inspiral at each time. For simplicity, we will consider equatorial, circular orbits of the Kerr metric and use Boyer-Lindquist coordinates $\{t, r, \theta, \phi\}$. The geodesic of the centre of mass in this setting is described by the following constants of motion, which describe the energy, angular momentum, and angular velocity of the center of mass, respectively,

$$E_c = \frac{a\sqrt{M} + \sqrt{r_0}(r_0 - 2M)}{r_0^{3/4}\sqrt{2a\sqrt{M} + \sqrt{r_0}(r_0 - 3M)}}, \tag{9.14}$$

$$L_c = \frac{\sqrt{M}(r_0^2 - 2a\sqrt{Mr_0} + a^2)}{r_0^{3/4}\sqrt{2a\sqrt{M} + \sqrt{r_0}(r_0 - 3M)}}, \tag{9.15}$$

$$\Omega_c = \frac{\sqrt{M}}{a\sqrt{M} + r_0^{3/2}}, \tag{9.16}$$

where r_0 is the radial coordinate of the geodesic and Ma is the angular momentum of the Kerr BH. Hence, the wordline of the center of mass is $y^\mu(\lambda) = (t_p(\lambda), r_0, \pi/2, \Omega_c t_p(\lambda))$. We will assume that the displacement δy^μ is constant, i.e. it does not depend on the affine parameter λ. Note that in general, if the displacement is not aligned with the spin of the primary, the interaction between the latter and the scalar dipole will induce precession even in the case of initially circular and equatorial orbits. Hence, for generic orientations of the dipole moment, our assumption of a constant displacement is only valid on timescales that are much shorter than the precession timescale, such that this effect can be neglected. The precession timescale is shorter than, or at most comparable (for relativistic orbits) to the inspiral timescale, but much larger than the orbital one, i.e. $T_{\text{inspiral}} \gg T_{\text{precession}} \gg T_{\text{orbital}}$, see e.g. [428] [1]. Hence, while our formalism does not allow us to consistently evolve

---

[1] *More quantitatively, one can infer the orbital timescale from the angular velocity* $T_{orb} \sim (r^3/M)^{1/2}$. *The precession and inspiral timescales on the other hand, are inversely proportional to the mass ratio:* $T_{precession} \sim r^{5/2}/\mu M^{1/2}$, $T_{inspiral} \sim r^4/\mu M^2$, *so that in the extreme mass-ratio limit they are way larger than the orbital one. Furthermore, the precession timescale become comparable to the inspiral one only for relativistic orbits around the ISCO* $r \sim O(M)$, *while for most of the evolution* $T_{inspiral} >> T_{precession}$.

the binary through the entire inspiral (for generic displacements), it safely allows us to evaluate the scalar fluxes throughout the orbital motion. Of course this limitation is absent if the displacement δy^μ is orthogonal to the equatorial plane, since there is not precession in that case.

With this in mind, we can simplify the field equation (9.11) by expanding the trace of the stress energy tensor with respect to the constant displacement between the two particles, $\delta y^\mu = (\delta t, \delta r, \delta\theta, \delta\phi)$. This yields

$$T \simeq \frac{1}{\sqrt{-\mathbf{g}}}(\delta t\partial_t + \delta r\partial_r + \delta\theta\partial_\theta + \delta\phi\partial_\phi)(\sqrt{-\mathbf{g}}T_p)\,, \tag{9.17}$$

where T_p has the same expression of the source of the scalar field in the setting in which the secondary is endowed with a scalar monopolar charge:

$$T_p = \frac{\mu d}{\Sigma\sin\theta|\dot{t_p}|}\delta(r-r_0)\delta(\theta-\frac{\pi}{2})\delta(\phi-\Omega_c t)\,, \tag{9.18}$$

with $\Sigma = r^2 + a^2\cos^2\theta$ and $\dot{t}_p = dt_p(\lambda)/d\lambda$. Finally, we can perform a Fourier transform and expand both the scalar field and the source in spin-weighted spheroidal harmonics

$$\varphi(t,r,\Omega) = \int \mathrm{d}\omega \sum_{l,m} \frac{X_{lm}(r,\omega)}{\sqrt{r^2+a^2}} S_{0lm}(\theta,\omega)e^{im\phi}e^{-i\omega t}\,, \tag{9.19}$$

$$4\pi\Sigma T = \int \mathrm{d}\omega \sum_{l,m} T_{lm}(r,\omega)S_{0lm}(\theta,\omega)e^{im\phi}e^{-i\omega t}\,. \tag{9.20}$$

This decomposition allows us to decouple the angular and radial dependence of the scalar field. Indeed, we obtain the standard inhomogeneous differential equation for the radial field $X_{lm}(r,\omega)$:

$$\left[\frac{\mathrm{d}^2}{\mathrm{d}r_*^2} + V\right] X_{lm}(r,\omega) = \frac{\Delta}{(r^2+a^2)^{3/2}} T_{lm}(r,\omega)\,, \tag{9.21}$$

where V is the effective potential and can be found, for example, in [429]. We can obtain T_{lm} as a function of T by inverting Eq. (9.20) using the properties of the spheroidal harmonics:

$$T_{lm}(r,\omega) = 2\int \mathrm{d}t\mathrm{d}\theta\mathrm{d}\phi\Sigma\sin\theta T S^*_{0lm}e^{-im\phi}e^{i\omega t}\,. \tag{9.22}$$

We can now substitute Eq. (9.17) into Eq. (9.22) and perform the integrals in θ and ϕ, through integration by parts and the properties of the δ function. We finally obtain

$$\begin{aligned} T_{lm} = \frac{4\pi\mu d}{|\dot{t}|}\delta(m\Omega_c-\omega)\Big[&S^*_{0lm}(\frac{\pi}{2},m\Omega_c)\delta r\partial_r\delta(r-r_0) - \frac{\mathrm{d}}{\mathrm{d}\theta}S^*_{0lm}(\frac{\pi}{2},m\Omega_c)\delta\theta\delta(r-r_0) \\ &+ (\delta\phi-\Omega_c\delta t)S^*_{0lm}(\frac{\pi}{2},m\Omega_c)im\delta(r-r_0)\Big]\,. \end{aligned} \tag{9.23}$$

Note that the displacements along the t and ϕ directions are proportional to each other[2]. This is a consequence of the chosen equatorial circular motion. In fact, for circular equatorial orbits, performing a displacement $\delta\phi$ corresponds to moving the particle along the orbit by an angle proportional to $\Omega_c\delta t$ and vice-versa. In particular, for *prograde* orbits such that $\Omega_c > 0$, by considering a positive displacement $\delta\phi = \Omega_c\delta t$ the sum of these two terms is zero. This is because the angular term $\delta\phi$, if positive, shifts the particle along the circular orbit in a clockwise way. A shift δt along time instead, corresponds to $\phi = \Omega_c(t+\delta t)$, i.e. $\phi - \Omega_c\delta t = \Omega_c t$, so that at time t the particle is actually displaced by an angle $-\Omega_c\delta t = -\delta\phi$ with respect to its original position in the counterclock direction. For *retrograde* orbits, the effect is clearly reversed. In general, as these terms are proportional, we can neglect from now on shifts along time, and simply re-absorb them as shifts along the ϕ direction.

9.3 Dipole-induced scalar fluxes

9.3.1 Analytic derivation

The solution of the inhomogeneous equation (9.21) can be found using the standard Green function in terms of two independent solutions of the corresponding homogeneous equation. The latter have the following asymptotic behavior:

$$X^{\infty,r_+}_{lm\omega} \sim e^{\pm i r_* k_{\infty,+}} \text{ as } r \to \infty, r_+ \tag{9.24}$$

where $k_+ = \omega - m\Omega_H$, Ω_H being the angular velocity of the BH horizon, and $k_\infty = \omega$. The solution of the inhomogeneous equation reads

$$X_{lm\omega}(r) = W^{-1} X^{\infty}_{lm\omega} \int_{r_+}^{r} \mathrm{d}s \frac{T_{lm\omega} X^{r_+}_{lm\omega}}{\sqrt{s^2+a^2}} + W^{-1} X^{r_+}_{lm\omega} \int_{r}^{\infty} \mathrm{d}s \frac{T_{lm\omega} X^{\infty}_{lm\omega}}{\sqrt{s^2+a^2}}\,, \tag{9.25}$$

where W is the Wronskian of the two homogeneous solutions. To evaluate the fluxes we are interested in the asymptotic behaviour of the solution (9.25) at infinity and at the horizon. Using Eqs. (9.23) and (9.24), we get

$$X^{\text{out}}_{lm\omega} = Z^{\infty}_{lm\omega}\delta(m\Omega_c - \omega)e^{im\Omega_c r_*},\,, \tag{9.26}$$

$$X^{\text{in}}_{lm\omega} = Z^{r_+}_{lm\omega}\delta(m\Omega_c - \omega)e^{im(\Omega_c-\Omega_H)r_*}. \tag{9.27}$$

where

$$Z^{\infty,r_+}_{lm\omega} = W^{-1}\frac{4\pi\mu d}{|\dot{t}|}(\mathcal{R}+\Theta+\tilde{\Phi})\frac{X^{r_+,\infty}_{lm\omega}(r)}{\sqrt{r^2+a^2}}\Bigg|_{r=r_0}\,, \tag{9.28}$$

with

$$\mathcal{R} = S^*_{0lm}(\frac{\pi}{2}, m\Omega_c)\delta r\partial_r, \tag{9.29}$$

$$\Theta = -\frac{\mathrm{d}S^*_{0lm}}{\mathrm{d}\theta}(\frac{\pi}{2}, m\Omega_c)\delta\theta, \tag{9.30}$$

$$\tilde{\Phi} = imS^*_{0lm}(\frac{\pi}{2}, m\Omega_c)\delta\phi. \tag{9.31}$$

---

[2] Note also that both terms are proportional to the azimuthal number m. While this is obvious for the derivative with respect to ϕ, it arises also for the time derivative because the latter brings a factor ω, and circular motion implies $\omega = m\Omega_c$.

The fluxes at infinity and at horizon can be computed from the $t-r$ component of the scalar field stress-energy tensor,

$$F_{\infty,r_+} = \frac{\mathrm{d}E_{\infty,r_+}}{\mathrm{d}t} = \lim_{r\to\infty,r_+} \int \mathrm{d}\Omega\ \Sigma {T^{(s)}}^{r}_{\ t}\,, \tag{9.32}$$

Finally, using Eq. (9.28), the fluxes read:

$$F_\infty = \frac{\mathrm{d}E_\infty}{\mathrm{d}t} = \sum_{l,m} |Z^\infty_{lm\omega}|^2 m^2 \Omega_c^2, \tag{9.33}$$

$$F_{r_+} = \frac{\mathrm{d}E_{r_+}}{\mathrm{d}t} = \sum_{l,m} |Z^{r_+}_{lm\omega}|^2 m^2 \Omega_c(\Omega_c - \Omega_H). \tag{9.34}$$

In the next section, we will compute numerically the dipole-induced scalar fluxes and highlight the differences with respect to the monopolar case. For an immediate comparison, we report here also the quantities $\tilde{Z}^{\infty,r_+}_{lm\omega}$ characterizing the monopolar case:

$$\tilde{Z}^{\infty,r_+}_{lm\omega} = W^{-1} \frac{4\pi\mu d}{|\dot{t}|} S^*_{0lm}\Big(\frac{\pi}{2}, m\Omega_c\Big) \frac{X^{r_+,\infty}_{lm\omega}(r)}{\sqrt{r^2+a^2}}\bigg|_{r=r_0}\,. \tag{9.35}$$

Even by a first qualitative analysis, a crucial difference can already be highlighted from dimensional considerations. From Eq. (9.28), one sees that the inhomogeneous solution, both at the horizon and at infinity, depends on the sum of three terms proportional to the components of the dipole moment vector, $\delta r d/\mu, \delta\theta d/\mu, \delta\phi d/\mu$, respectively. First, we point out that the radial displacement is of the order of the secondary length scale, $\delta r = \mathcal{O}(\mu)$. Moreover, the term (9.29) features ∂_r which is $\mathcal{O}(M^{-1})$. As for the angular displacements, they can be roughly estimated as $\delta\theta, \delta\phi \sim \arcsin(\mu/r_0) \approx \mu/r_0 \lesssim \mu/M$, from which $\delta\theta, \delta\phi = \mathcal{O}(q)$. Thus, the terms (9.29), (9.30), (9.31) are all of the order $\mathcal{O}(q)$. This immediately tells us that Eq. (9.28) scales as the mass ratio squared, q^2, and the fluxes are proportional to q^4.

In the case of a monopole instead, the fluxes are proportional to q^2. Therefore, *emission from a dipole is intrinsically suppressed by a factor of* q^2.

If we instead consider a configuration where both a scalar monopole and a scalar dipole are present (as we shall do in Sec. 9.3.4), the fluxes will be proportional to the square of the sum of the two terms (9.35) and (9.28). Hence, due to the double product of these two terms, the lowest order correction to the scalar monopolar flux due to the presence of the dipole will be proportional to q^3. This resembles the contribution of the spin of the secondary compact object to the gravitational fluxes [430, 431, 432], which also enters at next-to leading order in the mass-ratio.

9.3.2 Numerical results

In this section we discuss the numerical results for the fluxes in the purely dipolar case. We consider an EMRI around a nearly-extremal Kerr BH with spin $a = 0.99M$. As we shall discuss, even if this choice maximizes the effect of the dipole, the latter is typically negligible. In all cases we compute the fluxes by summing the multipolar contributions up to $l = 17$ and for all $m = -l, -l+1, ..., l-1, l$.

The GW emission is studied by varying the radial coordinate r_0 of the center of mass of the secondary, and therefore its tangential velocity $v = \Omega_c r_0$, which increases as r_0 decreases. We will confront the dipole fluxes with the ones obtained in the monopolar case in the same setting [312, 314].

Recalling that, without loss of generality, we can set $\delta t = 0$, we can focus on the fluxes given by the three main possible orientations for the dipole, which are $p^i = d(\delta r, 0, 0)/\mu$, $p^i = d(0, \delta\theta, 0)/\mu$, and $p^i = d(0, 0, \delta\phi)/\mu$, respectively (see Fig. 9.1).

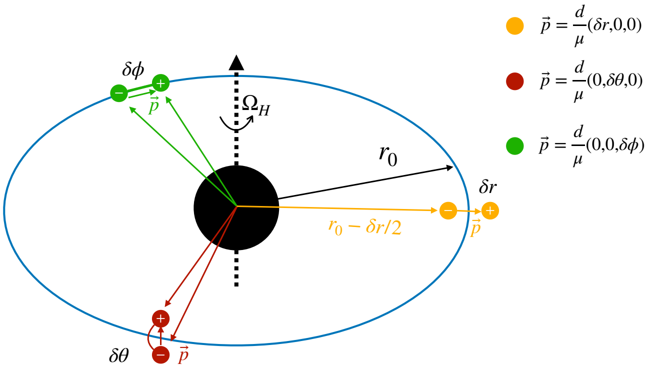

Figure 9.1. Schematic representation of an EMRI with a fundamental secondary dipole moment $\vec{p}$. We show the the three independent orientations of the dipole considered in this work. A generic orientation can be expressed as a linear combination of these three.

Given that the mass ratio enters the fluxes as an overall factor, it is convenient to normalize both the dipolar and monopolar fluxes normalized in a suitable way. For a given orientation of the dipole, we can define the normalized fluxes $\mathcal{F}_D$ and $\mathcal{F}_M$ as

$$F_M = (4\pi)^2 q^2 d^2 \mathcal{F}_M, \qquad F_D = (4\pi)^2 q^4 p^2 \mathcal{F}_D. \tag{9.36}$$

Here F_D (F_M) is the flux obtained from Eqs. (9.33) and (9.34) using the $Z_{lm\omega}$ given in Eq. (9.28) (Eq. (9.35)) for the dipolar (monopolar) case. Also, p is the magnitude of the dimensionless dipole vector, see Eq. (9.13). Using this normalization, $\mathcal{F}_D$ and $\mathcal{F}_M$ are independent of the dipole moment, charge, and mass ratio. However, for the purpose of a comparison one should keep in mind that, for the physical fluxes, $\mathcal{F}_D/\mathcal{F}_M = \mathcal{O}(q^2) \ll 1$.

Figure 9.2 shows the behaviour of normalized dipole emission (solid curves) in the $p^i = d(0, \delta\theta, 0)/\mu$ case (in which the dipole is orthogonal to the equatorial plane and therefore precession in absent) in comparison to the normalized monopolar emission (dashed curves). In this configuration, for any orbit, the dipole emits a normalized flux that is always smaller than in the monopolar setup at least by one order of magnitude, both at horizon and at infinity. This is due to the dependence on $\frac{\mathrm{d}S^*_{0lm}}{\mathrm{d}\theta}(\frac{\pi}{2}, m\Omega_c)$ in the dipole emission. Indeed, it is easy to see that when the derivative of the spheroidal harmonic is computed at $\theta = \pi/2$, the (polar) $m = \pm l$ contribution to the fluxes, which usually is the dominant one, is identically zero. The first non-zero contribution comes from the axial mode $m = \pm(l-1)$, which is typically smaller.

In Fig. 9.3 we show the behaviour of normalized dipole emission (solid curves) in the $p^i = d(\delta r, 0, 0)/\mu$ setting, where the dipole moment lays on the equatorial plane

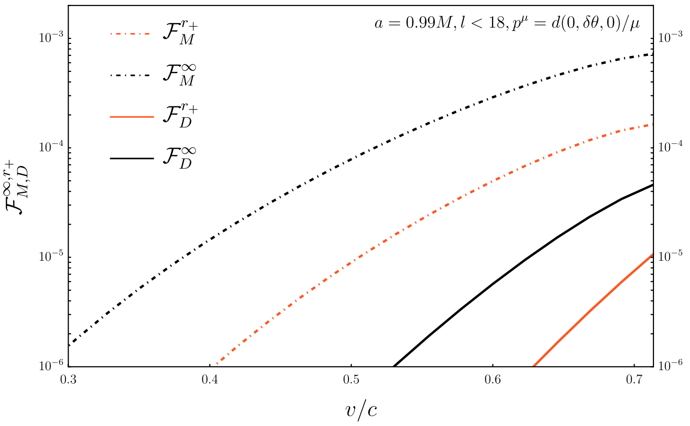

Figure 9.2. Solid curves: normalized scalar emission at infinity (black) and at horizon (orange) for a fundamental dipole with normalized moment $p^i = d(0, \delta\theta, 0)/\mu$, namely the case in which the dipole is parallel to the spin of the primary BH. Dashed curves: for comparison we show the normalized scalar emission at infinity (black) and at horizon (orange) for the case of a fundamental charge.

in radial direction. We notice that the relative importance of the dipolar flux with respect to the monopolar one increases in regions of the spacetime with a stronger gravitational field. The normalized flux at infinity peaks at the innermost-stable circular orbit (ISCO), where it is larger than the normalized monopolar one by almost two orders of magnitude.

Figure 9.4 shows the normalized dipole emission (solid curves) in the $p^i = d(0, 0, \delta\phi)/\mu$ setup. This trend shown in this plot is similar to the previous one. Overall the dipolar flux in this setting is always smaller than in the case of radially displaced dipole, but significantly larger than in the case of dipole aligned with the BH spin (Fig. 9.2).

Note that, as expected, in all three cases the fluxes increase as the small compact object gets closer to the ISCO since relativistic effects are amplified.

In the next section we will discuss the possible detectability of these fluxes, after restoring the normalization factors in Eq. (9.36).

9.3.3 Estimates for the fundamental dipole in various models

In order to give a rough estimate of the actual effects of fundamental dipole moments, we need to consider the physical fluxes in Eq. (9.36) and plugging in realistic values for the (dimensionless) scalar charge and dipole moment.

Using Eq. (9.36) and the numerical results of the previous section, we now wish to roughly estimate the minimum value of p that could possibly give detectable effects. An order-of-magnitude estimate can be obtained by computing the ratio between the physical dipolar and monopolar fluxes, $F_D/\ F_M$, and extract the minimum value of p for which the fluxes are comparable, $F_D/\ F_M \approx \mathcal{O}(1)$.

In the monopolar case, the smallest charge that would lead to a detectable effect for the scalar emission from a monopole is $d \approx 10^{-2}$. This was shown in [314] both by computing the GW dephasing due to the scalar emission and by performing a more rigorous parameter estimation. We can therefore estimate whether the

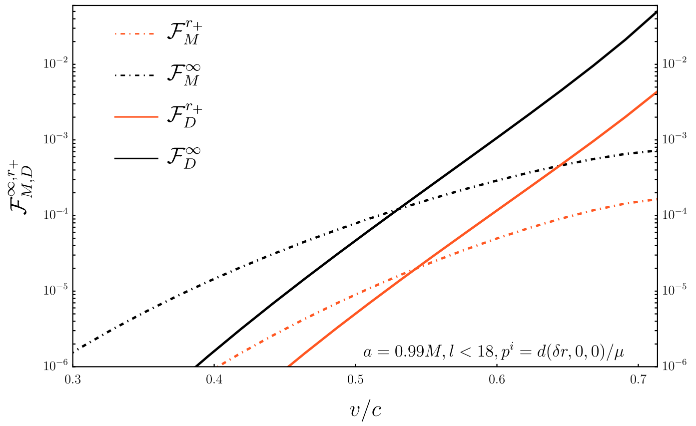

Figure 9.3. Same as Fig. 9.2 but for for the case of a radial dipole moment along the equatorial plane.

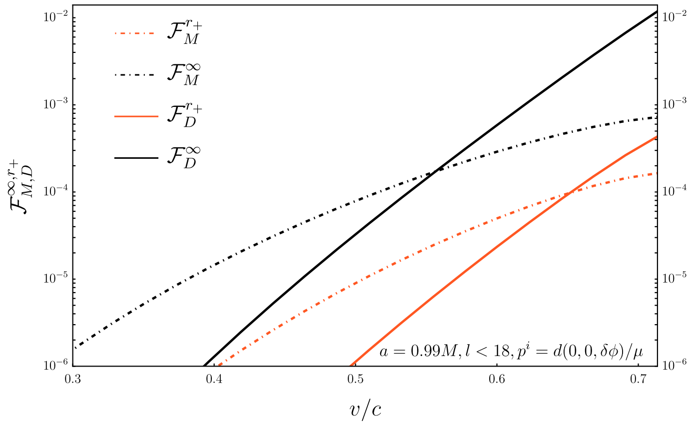

Figure 9.4. Same as Fig. 9.2 but for the case of a dipole moment with $\delta r = \delta\theta = 0$.

dipole emission is comparable to the flux generated by the monopole setup with this minimum detectable value for the scalar charge, using realistic values of p. We also assume a mass-ratio $q = 10^{-4}$ in order to minimize the suppression factor between dipole and monopole while remaining well within the extreme mass-ratio limit.

The fluxes ratio reads

$$\frac{F_D}{F_M} = \frac{\mathcal{F}_D}{\mathcal{F}_M}\left(\frac{pq}{d}\right)^2 = 10^{-4}\left(\frac{q}{10^{-4}}\right)^2\left(\frac{0.01}{d}\right)^2\frac{\mathcal{F}_D}{\mathcal{F}_M}p^2. \tag{9.37}$$

Near the ISCO, for nearly-extremal BHs, the maximum normalized ratio is $\mathcal{F}_D/\mathcal{F}_M \sim 10^2$, as shown in Fig. 9.3. This leads to

$$\frac{F_D}{F_M} \sim 10^{-2}\left(\frac{q}{10^{-4}}\right)^2\left(\frac{0.01}{d}\right)^2 p^2\,. \tag{9.38}$$

Therefore, in order to require a dipolar flux comparable to the monopolar one, $p \approx 10$.

To assess whether this value for our fundamental dipole is realistic, we consider a few significant examples. The first one is the magnetic dipole moment of a neutron star. Of course in this case the dipole moment is due to the electromagnetic field, but we will use the intuition from our scalar dipole as a proxy. The dipole moment of a neutron star can be estimated as BR^3, where B is the typical magnetic field and R the radius of the star [433]. If we assume standard parameters for a magnetar [411], $B \approx 10^{15}G$ and $R \approx 12$ km, we obtain a dipole moment $p \approx 10^{-2}$. Thus, from Eq. (9.38), even in the case of extreme magnetic fields and in the most optimistic scenario the dipole flux is 10^6 times smaller than the minimum detectable monopole flux.

The same occurs for the dipole moment of the recently constructed globally neutral topological solitons [434]. Such solutions are constructed by two opposite charges held at a given distance. While their dipole moment depends on the parameter space, in our units these solutions are characterized by $p \ll 1$ [434].

Furthermore, in the context of quadratic gravity theories with scalar fields coupled to quadratic curvature terms (which most notably include scalar Gauss-Bonnet and dynamical Chern-Simons theories) dipole hair can grow dynamically [413]. In this scenario the dipole moment is completely determined by the value of the monopole hair yielding $p \sim d$. In Chern-Simons gravity, dipole hair is proportional to the BH spin and is therefore bounded also in this case [413]. Likewise, fundamental dipoles can be produced in theories with spin-induced scalarization [414, 415, 416, 417] at the level of $p \sim d$.

Overall, for generic values of d, Eq. (9.38) implies a very large magnitude, $p \approx 10^3 d$, for the dipole flux to be comparable to the monopole one for $q = 10^{-4}$. Furthermore, the estimate (9.38) is already very optimistic, as it assumes the smallest detectable value of a scalar charge d, a moderate mass-ratio $q = 10^{-4}$, and the maximum possible normalized ratio $\mathcal{F}_D/\mathcal{F}_M$, obtained near the ISCO of a nearly extremal central BH. If these assumptions are relaxed (i.e., for smaller mass ratios, larger values of the charge, moderately spinning BHs, and less relativistic orbits), the flux ratio is even more severely suppressed.

We conclude that, for typical values of the dipole moment predicted in various models, the effect of a dipole flux is negligible.

9.3.4 Mixed case: charge+dipole

Until now, we have neglected the presence of a putative scalar charge and focused purely on the dipole contribution, assuming a globally neutral secondary. One might wonder if, in a scenario where both a scalar charge and a dipole are included, the corrections to the total flux due to the dipole are more significant. Indeed, as already mentioned, in this scenario the lowest order contribution from the dipole scales as q^3 instead of q^4. In this section, we will therefore compute the fluxes in this mixed case and show that, also in this case, one needs large values of the dipole moment ($p \approx 1$) in order to have appreciable deviations from the purely monopolar case.

We have studied the relative difference in the same optimistic scenario of the previous section, i.e. $a = 0.99M$, $q = 10^{-4}$, $d = 10^{-2}$, by considering different values of the dipole moment, namely $p = 10^{-2}, 0.1, 1, 10$. Moreover, we have considered the purely radial dipole case $p^i = d(\delta r, 0, 0)/\mu$, since our previous analysis showed that in this orientation the dipole contribution is maximized. Figure 9.5 shows the total fluxes (continuous lines) and the purely monopolar ones (dashed lines) as functions of the orbital velocity and for increasing values of p. Below each panel we also show the corresponding relative difference between monopole+dipole and purely monopole cases.

It is clear that also in this mixed case the presence of a nonvanishing dipole moment has a small impact on the total emission. For realistic values as $p \approx 0.01$, the total flux is larger than the the purely monopolar case at most by $\approx 0.1\%$. If we assume a larger dipole moment, $p \approx 1$, the maximum deviation from the purely monopolar case is at most 15%, whereas for $p \approx 10$ the monopolar and dipolar contributions are of the same order. Nevertheless, as already mentioned, such values of p are unrealistic and these corrections are obtained in the most optimistic scenario.

9.4 Conclusions

Motivated by various scenarios predicting globally neutral compact objects endowed with a dipole moment, we have developed a model-agnostic framework to compute the GW emission from a fundamental scalar dipole in EMRIs.

We found that the extra flux associated with the dipole moment is suppressed by the square of the mass ratio relative to the case of fundamental charges, making its detection with EMRIs very challenging for the typical values of the dipole predicted in various models. Even in the most optimistic scenarios, we estimated that, as long as the dimensionless dipole moment $p \lesssim 10$, its effect would be negligible for LISA.

This negative conclusion is based on a simple comparison between the dipole and monopole fluxes. Although the strong suppression suggests that our conclusion is solid, it would be important to confirm this expectation through a proper parameter estimation, along the lines of [314, 339] for the case of fundamental charges. In our case, however, this would come with the extra cost of properly taking into account the dipole precession during the evolution. Indeed, we have found that the only case in which precession is absent (when the dipole is parallel to the spin of the primary) is also the one in which dipole emission is more suppressed. For the most promising cases (any other orientation of the dipole) one needs to consistently evolve the dynamics of the dipole moment, similarly to the case of a secondary spin [435, 436, 437, 438]. It is also possible that precession helps make the effects of the dipole moment more prominent, as recently found in the context of post-Newtonian theory for comparable-mass binaries [439].

Although in our settings the effect of a fundamental dipole on the EMRI fluxes seems pessimistically small, for the same reason we estimate that if the secondary is endowed with both a charge and a dipole, the effect of the latter are typically negligible for constraints on and detectability of the former. This suggests that the estimates in [313, 314, 336, 337, 338, 339] should be robust against the inclusion of extra dipole effects. The mixed case is less suppressed by the mass ratio and is in fact very similar to that of an ordinary EMRIs with a spinning secondary [430, 432] for which the secondary spin is indeed not measurable with LISA, at least when neglecting precession [431]. In this context it would be interesting to include our effect in a more accurate self-force model, see [440] for very recent related work.

Finally, while the case of a fundamental scalar dipole might be interesting on its own in the context of modified gravity and physics beyond the Standard Model, we have also used it as a proxy for an intrinsic electromagnetic dipole, which is of direct astrophysical interest for magnetars. It would be very interesting to extend our work to the vector case, generalizing [338, 339] to the case of fundamental vector dipoles.

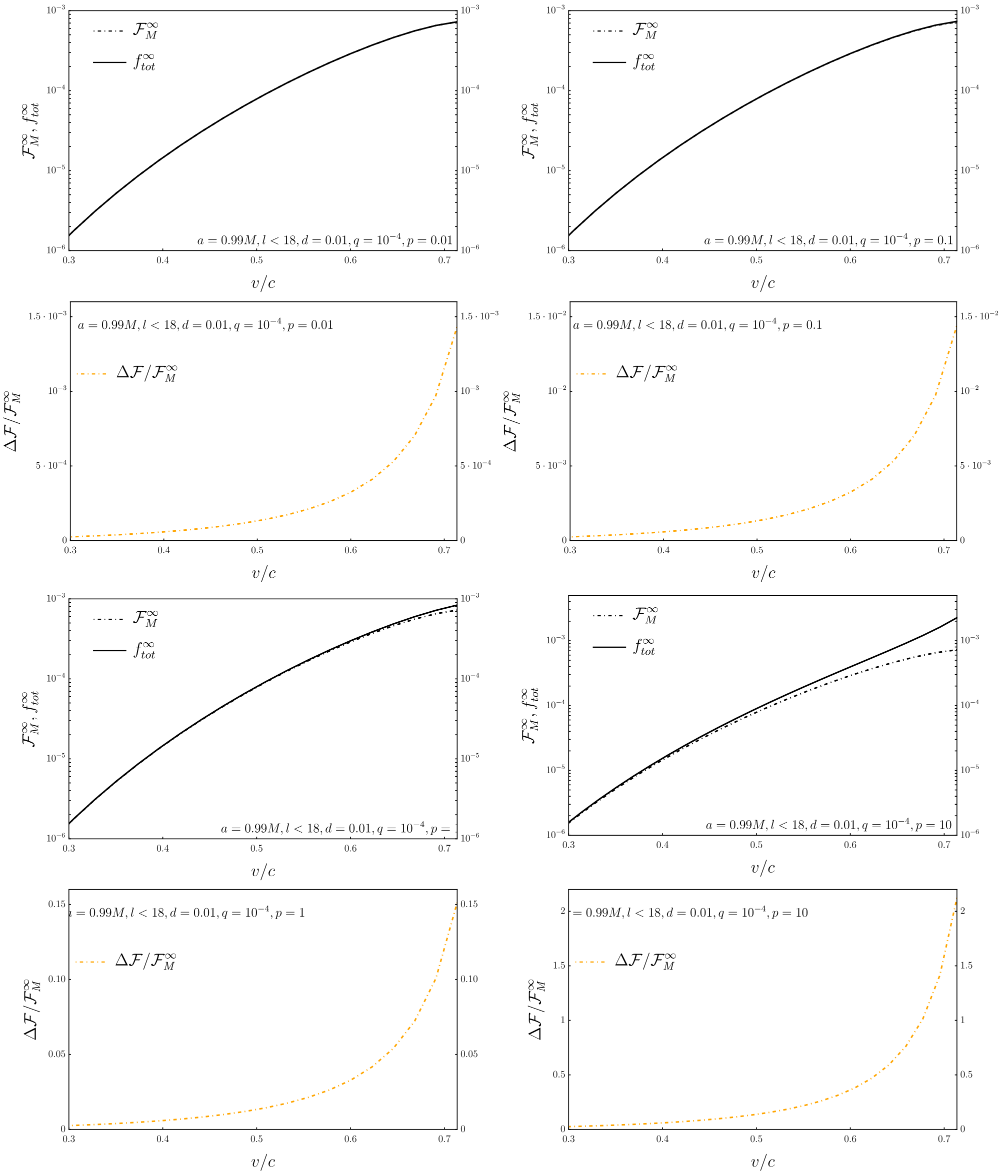

Figure 9.5. First and third row of panels: mixed case fluxes normalized by $(4\pi)^2\mu^2 d^2$ (solid lines) compared to normalized monopolar fluxes (dashed lines) for increasing values of p ($p = 0.01, 0.1, 1, 10$). Second and fourth row of panels: corresponding relative difference between the fluxes at infinity for the same values of p. The spin of the BH is fixed at $a = 0.99M$ and the orientation of the dipole is given by $p^i = d(\delta r, 0, 0)/\mu$.

Chapter 10

Novel tests of gravity using the stochastic GW background

Summary

Gravity theories that modify General Relativity in the slow-motion regime can introduce nonperturbative corrections to the stochastic gravitational-wave background (SGWB) from supermassive black-hole binaries in the nano-Hertz band, while remaining perturbative in the highly-relativistic regime and satisfying current post-Newtonian (PN) constraints. We present a model-agnostic formalism to map such theories into a modified tilt for the SGWB spectrum, showing that negative PN corrections (in particular -2PN) can alleviate the tension in the recent pulsar-timing-array data if the detected SGWB is interpreted as arising from supermassive binaries. Despite being preliminary, current data have already strong constraining power, for example they set a novel (conservative) upper bound on theories with time-varying Newton's constant (a -4PN correction) at least at the level of $\dot{G}/G \lesssim 10^{-5}\text{yr}^{-1}$ for redshift $z = [0.1 \div 1]$. We also show that NANOGrav data are best fitted by a broken power-law interpolating between a dominant -2PN or -3PN modification at low frequency, and the standard general-relativity scaling at high frequency. Nonetheless, a modified gravity explanation should be confronted with binary eccentricity, environmental effects, nonastrophysical origins of the signal, and scrutinized against statistical uncertainties. These novel tests of gravity will soon become more stringent when combining all pulsar-timing-array facilities and when collecting more data.

10.1 Tests of gravity using PTAs

Pulsar timing arrays (PTAs) offer a unique way to probe gravitational-wave (GW) astrophysics at the nano-Hertz (nHz) scale. In 2020, the NANOGrav collaboration first reported evidence in their 12.5 year dataset [352] for a common spectrum of a stochastic nature, which provided the first hint of a stochastic gravitational wave background (SGWB) signature. However, in these data, there was no statistical evidence for a quadrupolar spatial correlation (also denoted as Hellings-Down (HD) curve), necessary to interpret the signal as a GW background consistent with

General Relativity (GR). Remarkably, the more recent PTA data released in 2023 by the NANOGrav [298, 299], EPTA (in combination with InPTA) [300, 301, 302], PPTA [303, 304, 305] and CPTA [306] collaborations, found evidence for a HD angular correlation, typical of an homogeneous spin-2 GW background and consistent with the quadrupolar nature of GWs in GR [348].

The latest NANOGrav 15 yr (henceforth NANOGrav15) data found evidence for a smooth power law, $\Omega_{\rm GW} \propto f^{(1.6,2.3)}$ at 1σ. It is well known that a SGWB sourced by supermassive black hole (SMBH) binaries would be characterized by a scaling law $\Omega_{\rm GW} \propto f^{2/3}$ [349], which is currently disfavoured at 2σ by the NANOGrav15 data [326, 327]. Nevertheless, environmental and statistical effects may play a relevant role, and lead to a steeper scaling [321, 322, 323, 324, 325, 326, 327, 328, 329]. Even though with current data it is not possible to rule out a cosmological origin for the observed signal – such as coming from first-order phase transitions [353, 354, 355, 356, 357, 358, 359, 360, 361, 362, 363, 364, 365], cosmic strings and domain walls [366, 367, 368, 369, 370, 371, 372, 373, 374, 375, 376, 377, 378, 379, 380, 381, 382, 383], or scalar-induced GWs generated from primordial fluctuations [384, 385, 386, 387, 388, 389, 390, 391, 392, 393, 394, 395, 396, 397, 398, 399, 400, 401, 402, 403, 404, 405, 406] (see also [441, 442, 443, 444, 445, 446, 447]) – the SMBH hypothesis remains the leading explanation. Assuming the signal had astrophysical origin, one can greatly constrain the scenario and the physics governing SMBH binaries.

In principle, also modifications to GR (see, e.g., [34, 315, 17] for some reviews) may play a crucial role and lead to a different prediction than the standard scaling expected for SMBH binaries (including correlation patterns deviating from HD [448, 449, 450, 451]). Indeed, many known theories beyond GR induce new effects at negative post-Newtonian (PN) orders. Examples include dipole radiation in scalar-tensor theories at -1PN, or the effects of extra-dimensions or a time-varying Newton constant, both at -4PN (see e.g. [17, 18, 407]). Given that BH binaries in the PTA band have extremely large orbital separation during the early-inspiral phase, one could expect negative PN modifications to GR in this regime to play a much more relevant role than in the coalescence phase typically explored by ground- and space-based detectors [16, 452, 453, 297, 410].

In this work, we analyze the impact of generic effects at negative PN orders in light of the recent results of the PTA collaborations. We show that the recently detected SGWB allows for novel tests of GR. On the one hand, slow-motion modifications to GR can alleviate the current tension in PTA data and, on the other hand, we can use current data to place stringent upper bounds on putative negative-PN modifications, e.g. theories predicting a time-varying Newton's constant, $G(t)$, in an unconstrained region of their parameter space [454].

10.2 SGWB spectrum in modified gravity theories

The Hamiltonian of a binary system, corresponding to the centre of mass binding energy reads, at the Newtonian level,

$$E = \mu v^2/2 - G m_1 m_2/r \,, \tag{10.1}$$

where m_1, m_2 are the masses of the objects, r is the relative orbital separation, v is the relative orbital velocity, and μ is the reduced mass. Here we adopt a theory agnostic approach and consider model-independent modifications to GR. In particular, we consider *dissipative* corrections to the rate of change of the binding energy, at generic PN order[1]:

$$\dot{E} = \dot{E}_{\rm GR}\Big[1 + B\Big(\frac{Gm}{r}\Big)^q\Big]\,, \tag{10.2}$$

where $m = m_1 + m_2$ is the total mass and $\dot{E}_{\rm GR} = \frac{32}{5} G\mu^2\omega^6 r^4$ is the standard GR energy flux. This approach was widely considered in the literature in the contest of the parametrized post-Einsteinian (ppE) framework [455, 456, 407, 457]. Nevertheless, in the ppE formalism these corrections are always assumed to be much smaller than the GR term, and hence treated perturbatively. Here we remove this assumption, as we are interested in a seldom explored regime where these terms might dominate over the GR ones at the nHz scale. To compute the impact of this modification in the energy spectrum of GWs, we can simply express the latter as

$$\frac{dE_{\rm GW}}{d\omega} = \frac{\dot{E}_{\rm GR}}{\dot{\omega}}\,. \tag{10.3}$$

As we focused on purely dissipative corrections to GR, the binding energy is not modified, and one can therefore assume the standard Kepler's law relating the orbital radius to the frequency at the leading order, $r = (Gm/\omega^2)^{1/3}$. Using the latter, and combining Eqs. (10.1) and (10.2), we can compute the rate of change of the orbital frequency,

$$\dot{\omega} = \frac{96}{5}\mu G^{5/3} m^{2/3}\omega^{11/3}\Big[1 + B\Big(\frac{Gm}{r}\Big)^q\Big]\,. \tag{10.4}$$

Finally, the modified GW spectrum reads

$$\frac{dE_{\rm GW}}{d\omega} = -\frac{\frac{1}{3}G^{2/3}\mu m^{2/3}\omega^{-1/3}}{1 + B(Gm\omega)^{2q/3}}\,. \tag{10.5}$$

In the $B = 0$ limit this equation coincides with the standard GR one, where the only dissipation channel is ordinary GW emission, and leads to the standard scaling $\Omega_{\rm GW} \propto f dE_{\rm GW}/df \sim f^{2/3}$, where $f = \omega/\pi$ is the GW frequency. On the other hand, if

$$B(Gm\pi f)^{2q/3} \gg 1\,, \tag{10.6}$$

the modified scaling reads

$$\Omega_{\rm GW} \propto f^{\frac{2}{3}(1-q)}\,. \tag{10.7}$$

Modifications of the energy flux for *negative* PN orders ($q < 0$) lead to a steeper scaling, as expected. In particular, a dominant -2PN correction ($q = -2$) would give $\Omega_{\rm GW} \propto f^2$, compatible with the peak of NANOGrav15 posteriors for the tilt [298], as we shall also discuss later on. Taking $q = -2$ as an example, from Eq. (10.6) one has

$$B \gg 4\times 10^{-7}\left(\frac{m}{10^9 M_\odot}\right)^{4/3}\left(\frac{f}{\rm nHz}\right)^{4/3}\,. \tag{10.8}$$

---

[1] One can also include a similar parametrization for the *conservative* corrections to the binding energy of the binary [455, 456]. *For our purposes nevertheless, it is sufficient to focus only on dissipative corrections. Indeed, typically conservative corrections arise at higher post-Newtonian order and are therefore subdominant in the early inspiral [407, 18].*

On the other hand, the requirement that the same correction remains perturbative during the inspiral of a coalescing binary imposes $B \ll (Gm\omega_{\rm ISCO})^{-2q/3} \sim 0.03$ (for $q = -2$ and where $\omega_{\rm ISCO}$ is the reference frequency of the innermost stable circular orbit), regardless of the binary mass. Thus, there is a wide range in which the coupling B satisfies the inequality (10.8) while introducing a small correction in the coalescence phase. This range becomes even wider for more negative PN corrections.

Note that this general formalism includes several classes of gravity theories [18], but also several environmental effects that provide dissipation mechanisms at negative PN orders [33, 255, 458], leading to a steeper scaling [322, 459, 328]. Examples include accretion and dynamical friction ($q = -5.5$), stellar scattering ($q = -5$), and interaction with circumbinary gas ($q = -3.5$). Finally, large eccentricity ($e \gtrsim 0.6$) also provides a steeper scaling [350, 351] which can be fitted by multiple power-law phases with $q \approx -7.1$ and $q \approx -2.8$.

10.3 The case of varying G

Before delving into an actual confrontation with PTA data in the next section, let us discuss the strong constraining power of current data through a heuristic argument and considering a specific example. Alternatives to GR can violate the strong equivalence principle and in some case break local invariance [34]. Some of them predict a spacetime variation of the effective Newton constant, for example mediated by a scalar field on cosmological scales [36] or in the presence of energy leakage into small extra dimensions [460, 461]. Here we apply our formalism to the simplest and most studied case, promoting G to a function of time, $G(t)$, with G_0 being its present value [462, 463]. Several constraints to the first derivative of the Newton constant, $\dot{G}$, have been considered at different scales. At cosmological scales, bounds come from Big Bang nucleosynthesis [464, 465, 466] and cosmic microwave background [467], which estimated $\dot{G}/G_0 \lesssim 10^{-12}\,\mathrm{yr}^{-1}$, while in the solar system the most stringent constraint comes from a detailed analysis of Mercury's orbits, yielding $\dot{G}/G_0 \lesssim 10^{-14}\,\mathrm{yr}^{-1}$ [468]. Nevertheless, the former constraint assumes a linear scaling of $G(t)$ throughout the entire cosmic history, while the latter is obtained in the solar system at zero redshift. On the other hand, GWs offer a unique probe of *local* variation $\dot{G}$ at intermediate epochs [463, 469], being thus complementary to the aforementioned constraints. Depending on the specific GW source, one can place constraints at different redshift z. In particular, PTAs are sensible to systems at $z \approx [0.1 \div 1]$ [326], and hence they can provide complementary constraints to the low-redshift ones which were placed using binary pulsars [462, 470, 471] and LIGO [16]. On the other hand, the future space mission LISA will be able to provide bounds at similar redshifts [463, 472, 473, 469]. Here we show that using the recent PTA detection of the SGWB it is possible to place competitive bounds already with current data. The GW emission power in these theories depends on the time-varying Newton constant,

$$\dot{E}_{\rm GW} = \frac{32}{5G(t)}\Big[\pi\mathcal{M}_c G(t) f(t)\Big]^{10/3}\,, \tag{10.9}$$

where $\mathcal{M}_c$ is the binary chirp mass. Using Eq. (10.1) (with $G \to G(t)$) and the balance law, one can compute an expression for the secular variation of the GW

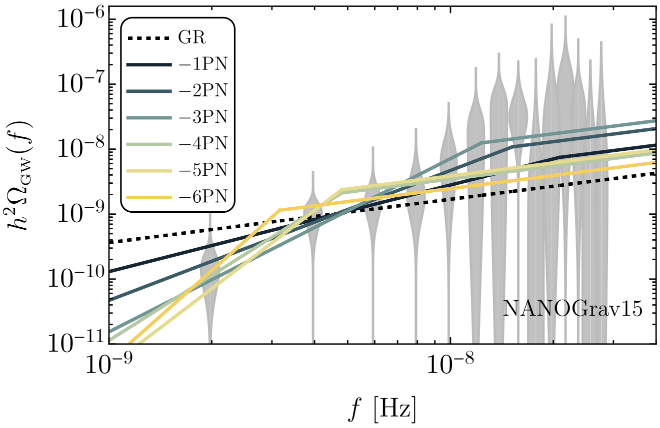

Figure 10.1. The posterior distribution for $\Omega_{\rm GW}$ in each frequency bin f_i reported by the NANOGrav collaboration, including HD correlations (gray violins). We also show the best fit spectra obtained by inserting a specific PN correction in the model, i.e. assuming a BPL spectrum with $n_T = 2/3(1-q)$ at $f < f_b$ and $n_T = 2/3$ at $f > f_b$. The black dashed line shows the best fit assuming GR scaling $\Omega_{\rm GW} \propto f^{2/3}$.

frequency valid at all orders in $\dot{G}$ [469]:

$$\dot{f} = \frac{96\pi^{8/3}}{5} G^{5/3}\mathcal{M}_c^{5/3} f^{11/3} - \left(\frac{\dot{G}}{G}\right) f \,. \tag{10.10}$$

The first term above is the standard GR one, while the second term is the modification due to the variation of G. Using the above relations, one can straightforwardly compute Eq. (10.3). If the first term dominates over the second one in Eq. (10.10), one obtains the standard scaling $\Omega_{\rm GW} \propto f^{2/3}$, while in the opposite regime, i.e. if $\dot{G}$ is large enough, one obtains the scaling

$$\Omega_{\rm GW} \propto f^{10/3} \,, \tag{10.11}$$

which corresponds to $q = -4$, i.e. to a −4PN order effect, in agreement with the ppE mapping of this correction in the perturbative regime [463, 18]. Hence, theories with a time-varying G can be directly mapped into our generic framework. The obtained scaling (10.11) deviates more than 3σ from the recent NANOGrav15 measurement, which can in turn be used to place constraints on $\dot{G}$. Assuming for simplicity that all binaries have same redshift and equal masses, $m_1 = m_2 = m/2$, one finds that the spectrum (10.11) is obtained if

$$\dot{G}/G_0 \gg 4.6 \times 10^{-9} {\rm yr}^{-1} \left(\frac{f}{\rm nHz}\right)^{8/3} \left(\frac{m}{10^9 M_\odot}\right)^{5/3} \,, \tag{10.12}$$

which is therefore excluded by PTA measurements.

10.4 Confrontation with NANOGrav 15 Dataset

After the heuristic analysis above, we now focus on the most constraining PTA dataset, which is the one reported by the NANOGrav collaboration [298]. Assuming

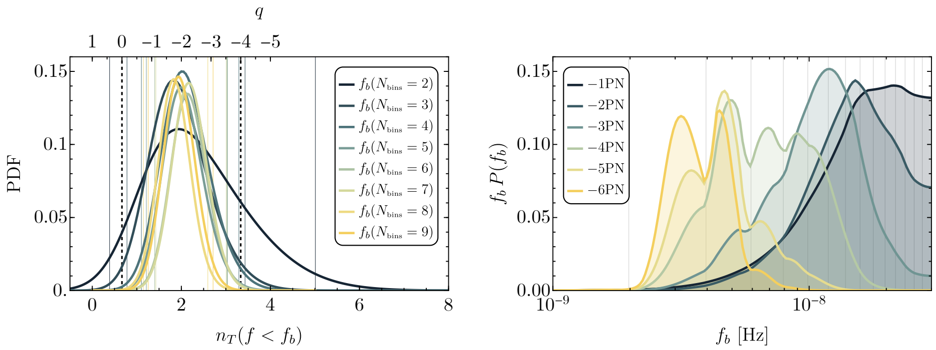

Figure 10.2. Fit of the NANOGrav15 dataset, assuming a BPL model with break frequency at f_b. For $f > f_b$ we always assume $n_T = 2/3$ as predicted by GW-driven, circular SMBH binaries in GR. *Left:* The low-frequency tilt n_T is left free to vary. As f_b increases, the constraint becomes more stringent, and converges towards the single power-law result. The colored vertical lines indicate the 2σ range for $n_T(f < f_b)$ while the dashed vertical lines indicate $n_T = 2/3$ and $10/3$ corresponding to GR and -4PN corrections, respectively. *Right:* The low frequency tilt is fixed assuming a given negative qPN correction, $n_T = 2/3(1-q)$ for $q = -1, \ldots, -6$. The posterior distribution for f_b indicates the preference for negative PN corrections (i.e. steeper spectra than $\propto f^{2/3}$). As a consequence, we always find lower bounds on f_b, while for $q \lesssim -3$ upper bounds are also obtained. The light vertical lines indicate the location of the NANOGrav frequency bins.

the signal to be a power-law (PL), this corresponds to a fraction energy density in GW today as [474]

$$\Omega_{\rm GW}(f) = \frac{2\pi^2 A^2 f_{\rm yr}^2}{3H_0^2}\left(\frac{f}{f_{\rm yr}}\right)^{n_T}, \tag{10.13}$$

where H_0 is the current Hubble rate, $f_{\rm yr} \equiv (1\ {\rm yr})^{-1} \simeq 32$ nHz, whereas A and n_T are the amplitude and spectral tilt, respectively. In Fig. 10.1, we show the posterior distribution for the SGWB abundance $\Omega_{\rm GW}(f)$ (gray violins), obtained by the NANOGrav collaboration fitting their data with the inclusion of HD correlations, in the first 14 bins.

We perform a maximum likelihood analysis to derive bounds on the tilt of the spectrum as a function of frequency, and compare this with the circular inspiral prediction $\Omega_{\rm GW} \propto f^{2/3}$. The full log-likelihood is computed as

$$\ln \mathcal{L}(\boldsymbol{\theta}) = \sum_k \ln p_k\left(\Omega_{\rm GW}(f_k|\boldsymbol{\theta})\right), \tag{10.14}$$

where $\boldsymbol{\theta}$ is the parameter vector characterising the models (e.g., amplitude and tilt for the power-law model), while p_k is the likelihood for each frequency bin k.

First, we assume that the SGWB spectrum is described by a power law in a certain number of the lowest frequency bins, hereafter denoted as $N_{\rm bin}$. We show the resulting 2σ range for the spectral tilt in Table 10.1 (PL case).

We can also assume the SGWB spectra to be described by a broken power-law (BPL) where the low-frequency tilt $(f < f_b)$ is fixed assuming a given negative PN

frequency [nHz]	$N_{\rm bin}$	$n_T^{\rm (PL)}$	$n_T^{\rm (BPL)}$
$f_2 = 3.96$	2	$3.0^{+2.9}_{-2.4}$	$2.2^{+2.8}_{-1.8}$
$f_3 = 5.93$	3	$2.3^{+1.7}_{-1.5}$	$1.9^{+1.5}_{-1.1}$
$f_4 = 7.92$	4	$2.0^{+1.4}_{-1.2}$	$2.1^{+1.2}_{-1.0}$
$f_5 = 9.88$	5	$2.1^{+1.2}_{-1.1}$	$2.0^{+0.1}_{-0.8}$
$f_6 = 11.9$	6	$2.1^{+1.2}_{-1.1}$	$2.2^{+0.9}_{-0.8}$
$f_7 = 13.9$	7	$2.1^{+1.2}_{-1.1}$	$2.2^{+0.8}_{-0.8}$
$f_8 = 15.8$	8	$2.4^{+1.0}_{-0.9}$	$1.8^{+0.8}_{-0.7}$
$f_9 = 17.8$	9	$2.2^{+0.9}_{-0.8}$	$2.0^{+0.8}_{-0.7}$

Table 10.1. We report the range of n_T at 2σ obtained fitting the first $N_{\rm bin}$ frequency bins with a power-law (PL), or with a broken power-law (BPL), where we set $n_T = 2/3$ only at $f_i > f_b$. The first frequency bin is at $f_1 = 1.98\,$nHz.

correction, $n_T = 2/3(1-q)$, while $\Omega_{\rm GW} \propto f^{2/3}$ for $f > f_b$. In our model (10.5), this occurs naturally: for fixed q and B, f_b corresponds to saturating Eq. (10.6), namely $f_b = B^{-\frac{3}{2q}}/(\pi G m)$.

The corresponding 2-σ range for n_T, assuming different values of f_b (corresponding to the location of each NANOGrav15 bin) are also shown in Table 10.1. This second version of the bounds are slightly more stringent, as additional information is brought by considering all NANOGrav15 posteriors, while assuming the high frequency range is described by the GW prediction. In Fig. 10.2 (left panel), we show the corresponding posterior distribution for $n_T(f < f_b)$, assuming the BPL model.

One can also perform a different analysis and focus on a single PN correction (i.e. fixing q) and derive the best fit parameters for the location of the break frequency f_b. The posterior distribution for f_b shown in the right panel of Fig. 10.2 has always significant support in the NANOGrav band, thus indicating the preference for negative PN corrections (i.e. steeper spectra than $f^{2/3}$). In all cases, we find lower bounds on f_b, while upper bounds are also obtained when $q \lesssim -3$.

The constraints set on f_b can be directly translated into constraints on the parameter B using Eq. (10.6). We show this in Fig. 10.3, assuming for simplicity that all binaries have the same total mass. The absence of support for $B = 0$ in all cases with $q < 0$ is due to the existing tension in PTA data with the standard scenario $\Omega_{\rm GW} \propto f^{2/3}$.

For $q = -4$ the posterior on B can be mapped into a bound on $\dot{G}/G_0$, assuming the latter to be approximately constant at the source's redshift $z \sim 0.5$ dominating the signal [326], see Fig. 10.4. Even in the most conservative scenario ($m = 10^9 M_\odot$), the bound on $\dot{G}/G_0$ is comparable to the projected bounds that LISA is expected to place using quasi-monochromatic sources [469]. Due to the $\dot{G} \propto m^{5/3}$ dependence, in more optimistic scenarios ($m < 10^9 M_\odot$) the bound is only slightly less stringent than what will be achievable in the LISA era by detecting SMBH coalescences

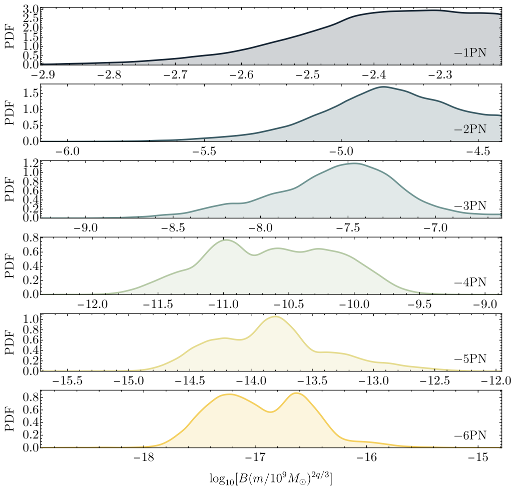

Figure 10.3. Posterior distribution of B derived assuming only one PN correction is active at the time. We left the explicit dependence on the total mass of the binaries, conservatively normalised to the value of $m = 10^9 M_\odot$. These constraints are derived from the BPL posteriors on f_b in Fig. 10.2.

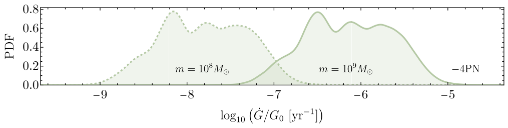

Figure 10.4. Posterior distribution of $\dot{G}/G_0$ assuming two values for the binary mass, $m = 10^9 M_\odot$ and $m = 10^8 M_\odot$.

and extreme mass-ratio inspirals [463, 472, 473] at similar redshift ($z \approx [0.1 \div 1]$). Overall, the bound on $\dot{G}/G_0$ is also several orders of magnitude better than the current bounds with LIGO/Virgo black-hole[2] binaries [18, 16], consistently with the fact that a small-velocity nonperturbative modification in the nHz band can become perturbatively small in the relativistic regime.

10.5 Conclusions and outlook

We argued that the recent groundbreaking PTA detection of a SGWB provides novel avenues to test gravity in the slow-motion regime. The novel constraints derived here are already competitive with those that the future LISA mission will place using nonrelativistic binaries. More accurate and stringent constraints should be derived by taking into account the mass distribution of SMBH binaries and its uncertainties. Furthermore, we expect that the upcoming joint analysis involving all collaborations within the International PTA framework will soon strengthen the constraints derived in this work. Likewise, the PTA posteriors on the tilt will shrink in time as longer duration datasets will be analyzed. Following the estimates provided in Ref. [476], one may expect the uncertainty on the spectral tilt to scale with the observation

---

[2] Neutron-star binary GW170817 sets a bound $\dot{G}/G_0 \lesssim 10^{-8}\,\mathrm{yr}^{-1}$ [475], which anyway refers to much smaller redshift, $z \approx 0.01$.

time as $\sigma_{n_T} \propto T_{\rm obs}^{-0.9(5-n_T)}$ ($\propto T_{\rm obs}^{-0.4}$) in the intermediate (weak) signal regime, with additional improvements given by the growing number of observed pulsars.

Depending on the specific modified gravity theory, binary pulsars [477, 17] can provide more stringent constraints on negative PN terms than PTAs. However, a direct comparison is challenging, since the coupling B can be source-dependent, for example being zero for pulsars and nonzero for SMBHs, as it happens in several theories for black-hole dipolar emission [407, 477]. As expected, PTA constraints are more stringent for more negative PN terms. For example, even if a -1PN modification were excluded at each frequency bin, the bounds derived from Eq. (10.6) at the nHz scale for $q = -1$ would be at most the level of $B \lesssim 6 \times 10^{-4}$. This is more stringent than those that can be obtained with LIGO at design sensitivity, but much less stringent than the projected bounds on B with LISA sources [407, 472, 473].

In addition to placing competitive constraints on modified gravity, a more ambitious possibility is to invoke slow-motion, beyond-GR effects to alleviate or solve the tension in the latest PTA data if the detected SGWB is interpreted as arising from SMBH binaries. While we showed that this is in principle possible without violating current constraints, one should be careful with degeneracies with astrophysical effects [321, 322, 323, 324, 325, 326, 327, 329], including large eccentricity [350, 351], and environmental modifications such as stellar scattering, interaction with circumbinary gas, and dynamical friction [322, 459, 328]. In this context, since our framework can accommodate both beyond-GR and environmental effects, it can be used to disentangle these modifications (which often enter at different negative PN order) through dedicated Bayesian inferences with more constraining future datasets. Finally, future work can be devoted to confront our general model with the hypothesis that the signal is due to, or contaminated by, sources of cosmological origin [327].

Chapter 11

General conclusions and future prospects

In this thesis, working on two parallel tracks, I discussed some systems where astrophysical black holes allow for a rich phenomenology beyond the SM and GR. In the first case, I focused on the role of environmental effects and interactions in BH superradiance. In particular, I showed how both features can dramatically change the evolution of superradiant instabilities in different scenarios.

Plasma-driven superradiant instabilities were poorly understood, as a rigorous application of plasma physics was never performed to describe the system. In chapter 3, I adopted a detailed plasma modeling that superseds the previous toy models and showed how an efficient instability can develop at a linear level. Nevertheless, I subsequently considered the fully non-linear system and shown how non-linearities alter the capability of the plasma to confine EM radiation, and completely quench the instability. The framework adopted to study linear photon-plasma effects in curved spacetime can be adapted to a number of different studies. For example, it is well known that plasma may hinder our ability to test BH charges using GWs, by suppressing the EM emission in the inspiral and in the ringdown [96]. Nevertheless, also in this case, current studies rely on toy models and lack a robust plasma modelling using consistent plasma physics. Hence, a future extension will be to employ the formalism outlined in section 3.2 to these systems. Most crucially, while in the SM case non-linear effects hamper the instability, in chapter 4 I discussed how a "dark" plasma can completely quench dark photon superradiant instabilities already at a linear level. Indeed in this case, an additional dark plasma effective mass, easily achievable in compelling dark matter models, alters the lifetime of the dark photon modes, rendering the instability ineffective. Also in this case a natural extension would be to generalize the analysis to the spinning case, possibly using the numerical tools for non-separable plasma profiles developed in section 6. Another outcome of the thesis is to highlight, in chapter 5, the importance of plasma in parametric instabilities triggered in the contest of axion superradiance. It was shown that plasma can inhibit the decay of an axion into two photos as it dresses the photons with an effective mass. Therefore, the presence of parametric EM instabilities induced by axion clouds can be strongly suppressed. The development of the instability depends on the ratio between the axionic coupling and the plasma density. Also in this scenario, an urgent and crucial extension would be to consider more realistic plasma geometries and to include in the analysis the already mentioned non-linear photon-plasma interactions. Most crucially, the presence of plasmas around an astrophysical BH also plays a pivotal role in scalar tensor theories. In chapter 6 I discussed how an accretion disk around a BH provides, in these theories, an effective mass for the scalar degree of freedom of the gravitational sector, and can therefore induce a superradiant instability. While the system resembles the plasma-driven instabilities discussed in chapter 3, most of the obstacles hampering the latter can be circumvented in this case. The linear analysis suggests that this effect can be used to impose competitive constrains on these theories. Nevertheless, a fully non-linear analysis is imperative to understand whether confinement can become ineffective in this regime, as in the plasma-photon case discussed in section 3.4. Finally, in chapter 7 I introduced a bilinear form for scalar perturbations under which quasi-bound states are orthogonal at a fully relativistic level. This bilinear form allows to develop a relativistic perturbation theory that supersedes the widely used non-relativistic approximation [92]. This framework opens a number of possible studies. For example, natural extensions would be to generalize it to spin-1 field , but also to perform a detailed study of relativistic transitions between energy levels of a BH-boson cloud in the presence of a binary companion [266].

In the second part of the thesis I discussed how EMRIs and supermassive BH binaries allow for novel tests of GR. In the first case, in chapter 9, I studied an EMRI system where the secondary object is endowed with a fundamental scalar dipole. I showed how during the inspiral the contribution to the fluxes from the scalar dipole is negligible, at variance with the well-known monopolar case [335, 312, 311, 313, 314, 336, 337]. In chapter 10 I focused instead on tests of gravity using PTAs. I showed how the recently detected SGWB allows for novel tests of gravity. In particular, I showed how it already allows to place stringent constrains on some beyond GR theories. Crucially, a notable feature of the introduced framework is the capacity to accommodate both beyond GR effects and environmental ones. Given that the latter are expected to play a prominent role in these systems [321, 322, 323, 324, 325, 326, 327, 328, 329], a natural extension of the study would be to disentangle them from beyond GR effects using future data through robust Bayesian inference.

Appendix A

Polar sector in the cold plasma, non-spinning limit

Here we derive the full potential for the photon-plasma polar sector in the different setups considered in section 3.2. We first consider a homogeneous plasma ($\omega_{\rm pl} =$ const) and then a generic radially-dependent density profile, i.e. $\omega_{\rm pl} = \omega_{\rm pl}(r)$. Finally, we generalize the equation for the polar sector in the collisional case.

A.1 Homogeneous plasma case

From Eq. (3.21), it is possible to find an expression for $u_{(2)}$ in terms of $u'_{(3)}$. This expression can be inserted in Eq. (3.22) to get a single second order equation for the decoupled variable $u_{(3)}$:

$$u''_{(3)} - u'_{(3)} \frac{2f^2 l(l+1)\omega^2 + (f-1)f^2 r^2 \omega_{\rm pl}^4 - f\omega_{\rm pl}^2\left(f(f+1)l(l+1) + 2(f-1)r^2\omega^2\right) + (f-1)r^2\omega^4}{fr\left(f\omega_{\rm pl}^2 - \omega^2\right)\left(f\left(l^2+l+r^2\omega_{\rm pl}^2\right) - r^2\omega^2\right)}$$
$$+ u_{(3)}\left(\omega^2 - \frac{f\left(l^2+l+r^2\omega_{\rm pl}^2\right)}{r^2}\right) f^{-2} = 0. \qquad \text{(A.1.1)}$$

Eq. (A.1.1) is still not in the form of a Schroedinger-like equation. We therefore perform the following substitution: $u_{(3)} = G(r)\psi(r)$, where G is an unknown function such that with this transformation equation Eq. (A.1.1) assumes the form $d^2\psi/dr_*^2 - V(r)\psi = 0$. We find $G(r) = r^{-1}\sqrt{fr(l^2+l+r^2\omega_{\rm pl}^2) - r^3\omega^2}\,\sqrt{r(f\omega_{\rm pl}^2 - \omega^2)}^{-1}$ and we finally arrive at a Schrodinger-like equation in terms of the tortoise coordinate where the potential has the following cumbersome form

$$V(r) = \frac{d(r)}{4\left(\omega^2 - f{\omega_{\rm pl}}^2\right)\left(fl(l+1)r + fr^3{\omega_{\rm pl}}^2 - r^3\omega^2\right)}\,, \qquad \text{(A.1.2)}$$

with

$$\begin{aligned}
d(r) = {} & -\omega^4 \Big[f^4 \Big(3l^2(l+1)^2 + 72l(l+1)r^2\omega_{\text{pl}}^2 \Big) + 2f^3 \Big(-18l(l+1) \Big(l^2+l+1 \Big) r^2\omega_{\text{pl}}^2 \\
& \quad - l^2(l+1)^2(2l(l+1)+1) - 36l(l+1)r^4\omega_{\text{pl}}^4 - 20r^6\omega_{\text{pl}}^6 \Big) - f^2 l^2 (l+1)^2 \Big] \\
& -\omega^8 \Big(-12fl(l+1)r^4 - 20fr^6\omega_{\text{pl}}^2 \Big) - 4r^6\omega^{10} - \omega^2 \Big[2f^5\omega_{\text{pl}}^2 \Big(-3l^2(l+1)^2 - 29l(l+1)r^2\omega_{\text{pl}}^2 \Big) \\
& + f^4 \Big(4l^2(l+1)^2(2l(l+1)+1)\omega_{\text{pl}}^2 + 48l(l+1)r^4\omega_{\text{pl}}^6 + 4l(l+1)(9l(l+1)+5)r^2\omega_{\text{pl}}^4 + 20r^6\omega_{\text{pl}}^8 \Big) \\
& \quad + 2f^3 \Big(l^2(l+1)^2\omega_{\text{pl}}^2 + l(l+1)r^2\omega_{\text{pl}}^4 \Big) \Big] - 4f^6 l(l+1)\omega_{\text{pl}}^4 \Big(l^2 + l + 4r^2\omega_{\text{pl}}^2 \Big) \\
& - 2f^5\omega_{\text{pl}}^2 \Big(-2l^2(l+1)^2 \Big(l^2+l+1 \Big) \omega_{\text{pl}}^2 - 6l(l+1)r^4\omega_{\text{pl}}^6 - 2l(l+1)(3l(l+1)+1)r^2\omega_{\text{pl}}^4 - 2r^6\omega_{\text{pl}}^8 \Big) \\
& - \omega^6 \Big(f^2 \Big(48l(l+1)r^4\omega_{\text{pl}}^2 + 4l(l+1)(3l(l+1)+5)r^2 + 40r^6\omega_{\text{pl}}^4 \Big) - 30f^3 l(l+1)r^2 - 2fl(l+1)r^2 \Big) \,.
\end{aligned} \tag{A.1.3}$$

Note that $V \to -\omega^2$ as $r \to 2M$ and $V \to \omega_{\text{pl}}^2 - \omega^2$ as $r \to \infty$.

A.2 Non-homogeneous plasma case

The case of a generic radially-dependent plasma density proceeds in the same fashion as the homogeneous case. We find the same expression for the function G with ω_{pl} replaced by $\omega_{\text{pl}}(r)$. As in the previous case we then arrive to a Schrodinger-like equation with an effective potential

$$V(r) = \frac{d(r)}{4\left(\omega^2 - f\omega_{\text{pl}}(r)^2\right)\left(fl(l+1)r + fr^3\omega_{\text{pl}}(r)^2 - r^3\omega^2\right)}\,, \tag{A.2.4}$$

where

$$
\begin{aligned}
d(r) = \omega^4 \Big[& 36 f^3 l(l+1) r^2 \left(-2f + l^2 + l + 1\right) \omega_{\rm pl}(r)^2 + f^2 l^2 (l+1)^2 (f(-3f + 4l(l+1) + 2) + 1) \\
& - 4 f^3 l(l+1) r \omega_{\rm pl}(r) \left((9f-5) r^2 \omega'_{\rm pl}(r) - f r^3 \omega''_{\rm pl}(r)\right) \\
& + 4 f^4 l(l+1) r^4 \omega'_{\rm pl}(r)^2 + 72 f^3 l(l+1) r^4 \omega_{\rm pl}(r)^4 + 40 f^3 r^6 \omega_{\rm pl}(r)^6 \Big] + \\
\omega^2 \Big[& 2 f \omega_{\rm pl}(r)^2 \left(f^2 l^2 (l+1)^2 (f(3f - 4l(l+1) - 2) - 1) + 4 f^4 l(l+1) r^4 \omega'_{\rm pl}(r)^2\right) \\
& - 4 f^5 l^2 (l+1)^2 r^2 \omega'_{\rm pl}(r)^2 + 4 f^4 l(l+1) r \omega_{\rm pl}(r)^3 \left(2(7f-3) r^2 \omega'_{\rm pl}(r) - 2 f r^3 \omega''_{\rm pl}(r)\right) \\
& - 48 f^4 l(l+1) r^4 \omega_{\rm pl}(r)^6 - 2 f^3 l(l+1) r^2 (f(-29f + 18 l(l+1) + 10) + 1) \omega_{\rm pl}(r)^4 \\
& - 4 f^3 l(l+1) r \omega_{\rm pl}(r) \left(f^2 l(l+1) r \omega''_{\rm pl}(r) + 2 f l(l+1) \omega'_{\rm pl}(r)\right) - 20 f^4 r^6 \omega_{\rm pl}(r)^8 \Big] \\
& - 2 f^2 \omega_{\rm pl}(r)^4 \left(6 f^4 l(l+1) r^4 \omega'_{\rm pl}(r)^2 - 2 f^3 l^2 (l+1)^2 \left(-f + l^2 + l + 1\right)\right) \\
+ \omega^6 & \left(-48 f^2 l(l+1) r^4 \omega_{\rm pl}(r)^2 - 40 f^2 r^6 \omega_{\rm pl}(r)^4 + 2 f l(l+1) r^2 (f(15f - 6l(l+1) - 10) + 1)\right) \\
& + 4 f^5 l(l+1) r^3 \omega_{\rm pl}(r)^5 \left((1-5f) \omega'_{\rm pl}(r) + f r \omega''_{\rm pl}(r)\right) + 12 f^5 l(l+1) r^4 \omega_{\rm pl}(r)^8 \\
& + 4 f^4 l(l+1) r \omega_{\rm pl}(r)^3 \left(f^2 l(l+1) r \omega''_{\rm pl}(r) + (f+1) f l(l+1) \omega'_{\rm pl}(r)\right) - 4 r^6 \omega^{10} \\
- 4 f^5 & l(l+1) r^2 (4f - 3l(l+1) - 1) \omega_{\rm pl}(r)^6 + 4 f^5 r^6 \omega_{\rm pl}(r)^{10} + \omega^8 \left(12 f l(l+1) r^4 + 20 f r^6 \omega_{\rm pl}(r)^2\right)
\end{aligned}
\tag{A.2.5}
$$

In this case the asymptotic behavior reads $V \to -\omega^2$ as $r \to 2M$ and $V \to \omega_{\rm pl}^2(r \to \infty) - \omega^2$ as $r \to \infty$. Obviously, the effective potential in Eq. (A.2.4) reduces to Eq. (A.1.2) when $\omega_{\rm pl} = \text{const}$.

A.3 Collisional plasma case

The polar sector in the presence of collisions on a nonspinning background depends on the function $F(r) \equiv G(r)/H(r)$, where

$$
\begin{aligned}
G(r) = & f \tau \omega_{\rm pl}^2 [(3f+1) f^{3/2} l(l+1) - 2i(f+1) f l(l+1) \tau \omega + 2i(f-1) f r^2 \tau \omega \omega_{\rm pl}^2 \\
& - 4i(f-1) r^2 \tau \omega^3 + 4(f-1) \sqrt{f} r^2 \omega^2] + 2i\omega(\tau\omega + i\sqrt{f})^2 \left[2 f^2 l(l+1) + (f-1) r^2 \omega^2\right]
\end{aligned}
\tag{A.3.6}
$$

$$
H(r) = 2r \left[f \tau \omega_{\rm pl}^2 - \omega(\tau\omega + i\sqrt{f})\right] \left[(\sqrt{f} - i\tau\omega) \left(f l(l+1) - r^2 \omega^2\right) - i f r^2 \tau \omega \omega_{\rm pl}^2\right] .
\tag{A.3.7}
$$

Appendix B

Field decomposition in Kerr

B.1 List of coefficients

In the following, we list the coefficients appearing in the decomposition of the plasma equations in a Kerr background, Eqs. (3.21), (3.22) and (3.23),

$$\tilde{A}_l = 0, \tag{B.1.1}$$

$$\eta_l = -\frac{2al(l+1)M\omega^2}{(r(r-2M))^{3/2}} u_{(4)}, \tag{B.1.2}$$

$$\begin{aligned} A_l = \frac{i}{r^{11/2}(r-2M)^{5/2}} \big[& -2amMr(M-r)(2M-r)^2 u''_{(3)} \\ & + (2M-r)(2amM\left(2M(M-r) - r^4\omega^2\right) + l(l+1)r^4\omega(2M-r))u'_{(3)} \\ & + 2amM(2M-r)r(2M^2 - 3Mr + r^2)u'_{(2)} + 2amMr^3\omega^2(r-M)u_{(3)} \\ & + (r-2M)(4amM\left(M^2 - Mr - r^4\omega^2\right) - r^4\omega(r-2M)\left(l^2 + l + r^2\omega_{\text{pl}}^2\right) + \\ & r^7\omega^3)u_{(2)} \big], \end{aligned} \tag{B.1.3}$$

$$\begin{aligned} B_l = -\frac{2aM}{r^{11/2}(r-2M)^{5/2}} \big[& r(2M-r)\left(2M^2 - 3Mr + r^2\right)u''_{(4)} + (2M-r)\left(-2M^2 + 2Mr + r^4\omega^2\right)u'_{(4)} \\ & + (M-r)\left(l^2(2M-r) + l(2M-r) + r^3\omega^2\right)u_{(4)} \big], \end{aligned} \tag{B.1.4}$$

$$\begin{aligned} \alpha_l = \frac{i\omega}{r^{3/2}(r-2M)^{3/2}} \big[& -r(r-2M)^2 u''_{(3)} + 2M(2M-r)u'_{(3)} + \left(r(r-2M)^2 u'_{(2)} + 2M(r-2M)\right)u_{(2)} \\ & + \omega\left(2amM - r^3\omega\right) + r^2(r-2M)\omega_{\text{pl}}^2 u_{(3)} \big], \end{aligned} \tag{B.1.5}$$

$$\begin{aligned} \zeta_l = -\frac{2aM}{r^{9/2}(r-2M)^{3/2}} \big[& -l(l+1)(M-r)(2M-r)u'_{(3)} - r^4\omega^2(2M-r)u'_{(2)} - l(l+1)r^3\omega^2 u_{(3)} \\ & + \left(l^2\left(2M^2 - 3Mr + r^2\right) + l\left(2M^2 - 3Mr + r^2\right) + r^3\omega^2(3M-2r)\right)u_{(2)} \big], \end{aligned} \tag{B.1.6}$$

$$\begin{aligned}\delta_l = &-\frac{4aM}{r^{9/2}(r-2M)^{3/2}}\big[r(r-2M)^2u''_{(4)}+2M(r-2M)u'_{(4)}\\&+\left(l^2(2M-r)+l(2M-r)+r^3\omega^2\right)u_{(4)}\big],\end{aligned} \tag{B.1.7}$$

$$\begin{aligned}\gamma_l = &\frac{4iamM}{r^{9/2}(r-2M)^{3/2}}\big[r(r-2M)^2u''_{(3)}+2M(r-2M)u'_{(3)}-r(r-2M)^2u'_{(2)}\\&+r^3\omega^2u_{(3)}+2M(2M-r)u_{(2)}\big],\end{aligned} \tag{B.1.8}$$

$$\begin{aligned}\beta_l = &-\frac{i\omega}{(r(r-2M))^{3/2}}\big[-r(r-2M)^2u''_{(4)}+2M(2M-r)u'_{(4)}\\&+\left(\omega\left(2amM-r^3\omega\right)+l^2(r-2M)+l(r-2M)+r^2(r-2M)\omega_{\rm pl}^2\right)u_{(4)}\big].\end{aligned} \tag{B.1.9}$$

B.2 Polar sector in Kerr

In the following, we outline the procedure to derive the polar potential from Eqs. (3.21), (3.22), by neglecting the terms multiplied by $Q_{l,m}$ and using the expressions given in Appendix B. From Eq. (3.21), it is possible to obtain an expression for $u'_{(2)}$ as a function of $u_{(2)}, u_{(3)}, u'_{(3)}$ and $u''_{(3)}$. This expression can be then inserted in Eq. (3.22), obtaining an equation that only contains $u_{(2)}$, $u_{(3)}$, $u'_{(3)}$ and $u''_{(3)}$. Thus, by solving this equation, it is possible to write $u_{(2)}$ as a function of the degree of freedom $u_{(3)}$ and its derivatives, $u_{(2)}(r)=\mathcal{F}[u_{(3)},u'_{(3)},u''_{(3)}]$. Inserting this in Eq. (3.22) allows us to obtain an equation for the decoupled variable $u_{(3)}$, which in general contains third-order radial derivatives. However, the latter are $\mathcal{O}(\tilde{a}^2)$ and can therefore be neglected to linear order in the BH spin. The resulting equation is a second-order equation for the decoupled variable $u_{(3)}$ in the form $a_2(r)u''_{(3)}+a_1(r)u'_{(3)}+a_0(r)u_{(3)}=0$, where the coefficients a_i are functions of r and are at most linear in the BH spin. As in the nonspinning case, therefore, only one degree of freedom is propagating in the polar sector.

The differential equation for $u_{(3)}$ can also be written in a Schrödinger-like form through a variable redefinition and in terms of the tortoise coordinate. At first order in the spin, $V\to-(\omega^2-2m\omega\Omega_H)$ near the horizon and $V\to\omega_{\rm pl}^2-\omega^2$ at infinity.

Appendix C

Derivation of the $3+1$ form of the plasma-photon equations

Here we perform the explicit computation to obtain the field equations in the $3+1$ form. For the EM field we avoid to rewrite the procedure and we refer directly to [152]. We will thus consider only Eqs. (3.4), (3.6).

C.1 Decomposition of Eq. (3.4)

Let us rewrite Eq. (3.4) for clarity:

$$u^\nu \nabla_\nu u^\mu = \frac{e}{m} F^{\mu\nu} u_\nu. \tag{C.1.1}$$

we have to project it separately on n^μ and on Σ_t.

Projection on n^μ

Contracting Eq. (3.4) with n_μ we obtain

$$n_\mu u^\nu \nabla_\nu u^\mu = \frac{e}{m} F^{\mu\nu} u_\nu n_\mu. \tag{C.1.2}$$

In the right hand side we have

$$\frac{e}{m} F^{\mu\nu} u_\nu n_\mu = -\frac{e}{m} E^\nu u_\nu = -\frac{e}{m} E^{\nu\,(3)} u_\nu, \tag{C.1.3}$$

where in the last step we used the fact that E^μ lies on Σ_t. The left hand side requires more manipulation. In particular we have that

$$\begin{aligned} n_\mu u^\nu \nabla_\nu u^\mu &= u^\nu \nabla_\nu (n_\mu u^\mu) - u^\mu u^\nu \nabla_\nu n_\mu \\ &= -u^\nu \nabla_\nu \Gamma - u^\mu u^\nu \nabla_\nu n_\mu. \end{aligned} \tag{C.1.4}$$

Let us now consider only the second term:

$$\begin{aligned}
u^\mu u^\nu \nabla_\nu n_\mu &= u^\mu u^\nu \delta^\lambda{}_\nu \nabla_\lambda n_\mu = u^\mu u^\nu (h^\lambda{}_\nu - n^\lambda n_\nu) \nabla_\lambda n_\mu \\
&= u^\nu u^\mu h^\lambda{}_\nu \nabla_\lambda n_\mu - u^\nu n_\nu u^\mu a_\mu \\
&= u^\nu u^\mu h^\lambda{}_\nu \delta^\sigma{}_\mu \nabla_\lambda n_\sigma + \Gamma u^\mu a_\mu \\
&= u^\nu u^\mu h^\lambda{}_\nu h^\sigma{}_\mu \nabla_\lambda n_\sigma - u^\nu u^\mu h^\lambda{}_\nu n^\sigma n_\mu \nabla_\lambda n_\sigma \\
&+ \Gamma u^\mu a_\mu . \qquad \text{(C.1.5)}
\end{aligned}$$

Here we used the definition of the projection operator $h^\mu{}_\nu = \delta^\mu{}_\nu + n^\mu n_\nu$, the definition of Γ, and defined the 4-acceleration of the Eulerian observer, $a_\mu = n^\nu \nabla_\nu n_\mu = D_\mu \ln \alpha$. Given that $n^\mu n_\mu = -1$ the second term in the last line vanishes. Furthermore, by recognizing that $K_{\mu\nu} = -h^\lambda{}_\nu h^\sigma{}_\mu \nabla_\lambda n_\sigma$, we can write the first term as $-K_{\mu\nu} u^\mu u^\nu$. Substituting all these terms in Eq. (C.1.2) we obtain

$$-u^\mu \nabla_\mu \Gamma + K_{\mu\nu} u^\mu u^\nu - \Gamma u^\mu D_\mu \ln \alpha = -\frac{e}{m} E^\mu \, {}^{(3)}u_\mu . \qquad \text{(C.1.6)}$$

Using now the decomposed form of u^μ (Eq. (3.71)) we can write

$$\partial_t \Gamma = \beta^i \partial_i \Gamma - \alpha \mathcal{U}^i \partial_i \Gamma + \alpha \Gamma K_{ij} \mathcal{U}^i \mathcal{U}^j - \Gamma \mathcal{U}^i \partial_i \alpha + \frac{e}{m} \alpha E^i \mathcal{U}_i . \qquad \text{(C.1.7)}$$

Projection on Σ_t

Let us now project Eq. (3.4) with $h^\mu{}_\nu$:

$$h^\mu{}_\sigma u^\nu \nabla_\nu u^\sigma = \frac{e}{m} h^\mu{}_\sigma F^{\sigma\nu} u_\nu . \qquad \text{(C.1.8)}$$

In the right hand side we have

$$\begin{aligned}
\frac{e}{m} h^\mu{}_\sigma F^{\sigma\nu} u_\nu &= \frac{e}{m} h^\mu{}_\sigma (n^\sigma E^\nu - n^\nu E^\sigma + {}^{(3)}\epsilon^{\sigma\nu\lambda} B_\lambda) u_\nu \\
&= -\frac{e}{m} n^\nu u_\nu E^\mu + \frac{e}{m} \, {}^{(3)}\epsilon^{\mu\nu\lambda} B_\lambda u_\nu = \frac{e}{m} \Gamma E^\mu + \frac{e}{m} \Gamma \, {}^{(3)}\epsilon^{\mu\nu\lambda} B_\lambda \mathcal{U}_\nu .
\end{aligned} \qquad \text{(C.1.9)}$$

In the left hand side, instead, we start by substituting the decomposition (3.71):

$$\begin{aligned}
h^\mu{}_\sigma u^\nu \nabla_\nu u^\sigma &= h^\mu{}_\sigma u^\nu \nabla_\nu (\Gamma n^\sigma + {}^{(3)}u^\sigma) = h^\mu{}_\sigma u^\nu n^\sigma \nabla_\nu \Gamma + \Gamma h^\mu{}_\sigma u^\nu \nabla_\nu n^\sigma + h^\mu{}_\sigma u^\nu \nabla_\nu \, {}^{(3)}u^\sigma \\
&= \Gamma h^\mu{}_\sigma (\Gamma n^\nu + {}^{(3)}u^\nu) \nabla_\nu n^\sigma + h^\mu{}_\sigma (\Gamma n^\nu + {}^{(3)}u^\nu) \nabla_\nu \, {}^{(3)}u^\sigma \\
&= \Gamma^2 h^\mu{}_\sigma a^\sigma - \Gamma K^\mu{}_\nu \, {}^{(3)}u^\nu + \Gamma h^\mu{}_\sigma n^\nu \nabla_\nu \, {}^{(3)}u^\sigma + h^\mu{}_\sigma \, {}^{(3)}u^\nu D_\nu \, {}^{(3)}u^\sigma ,
\end{aligned} \qquad \text{(C.1.10)}$$

where in the third step we used the orthogonality between n^μ and $h^\mu{}_\nu$, while on the fourth step we used the definition of the 4-acceleration a_μ and the extrinsic curvature $K_{\mu\nu}$. The covariant derivative D_μ has been introduced according to the definition $D_\nu\,{}^{(3)}u^\mu = h^\sigma{}_\nu h^\mu{}_\lambda \nabla_\sigma\,{}^{(3)}u^\lambda$. Let us now rewrite this equation in terms of $\mathcal{U}^\mu$:

$$\begin{aligned} h^\mu{}_\sigma u^\nu \nabla_\nu u^\sigma &= \Gamma^2 a^\mu - \Gamma^2 K^\mu{}_\nu \mathcal{U}^\nu + \Gamma \mathcal{U}^\mu n^\nu \nabla_\nu \Gamma \\ &+ \Gamma^2 h^\mu{}_\sigma n^\nu \nabla_\nu \mathcal{U}^\sigma + \mathcal{U}^\nu \mathcal{U}^\mu \Gamma D_\nu \Gamma \\ &+ \Gamma^2 h^\mu{}_\sigma \mathcal{U}^\nu D_\nu \mathcal{U}^\sigma . \end{aligned} \tag{C.1.11}$$

Now we wish to rewrite the spatial components of this equation in the form of an evolution equation, and for this purpose we use a procedure similar to the one in Eqs. (A14) - (A20) of [152]. First we note that for any 3-vector ${}^{(3)}V^\mu$, $\mathcal{L}_n\,{}^{(3)}V^\nu = n^\mu \nabla_\mu\,{}^{(3)}V^\nu - {}^{(3)}V^\mu \nabla_\mu n^\nu$, so that

$$\begin{aligned} h^\nu{}_\sigma n^\mu \nabla_\mu\,{}^{(3)}V^\sigma &= h^\nu{}_\sigma \mathcal{L}_n\,{}^{(3)}V^\sigma + h^\nu{}_\sigma\,{}^{(3)}V^\mu \nabla_\mu n^\sigma \\ &= h^\nu{}_\sigma \mathcal{L}_n\,{}^{(3)}V^\sigma - {}^{(3)}V^\mu K^\nu{}_\mu . \end{aligned} \tag{C.1.12}$$

Now, the Lie derivative can also be written in terms of partial derivatives, and setting $\nu = i$ we obtain

$$\begin{aligned} h^i{}_\sigma n^\mu \nabla_\mu\,{}^{(3)}V^\sigma &= h^i{}_\sigma \mathcal{L}_n\,{}^{(3)}V^\sigma - {}^{(3)}V^j K^i{}_j \\ &= \frac{1}{\alpha}\partial_t\,{}^{(3)}V^i - \frac{\beta^j}{\alpha}\partial_j\,{}^{(3)}V^i + \frac{{}^{(3)}V^j}{\alpha}\partial_j \beta^i \\ &- {}^{(3)}V^j K^i{}_j \,, \end{aligned} \tag{C.1.13}$$

where we made use of the explicit expressions of $h^\mu{}_\nu$ and n^μ.

If we now substitute Eq. (C.1.13) in the i-th component of Eq. (C.1.11), we get

$$\begin{aligned} h^i{}_\sigma u^\nu \nabla_\nu u^\sigma &= \Gamma^2 a^i + \Gamma \mathcal{U}^i n^\nu \nabla_\nu \Gamma + \mathcal{U}^i \mathcal{U}^j \Gamma D_j \Gamma \\ &+ \frac{\Gamma^2}{\alpha}\Big(\partial_t \mathcal{U}^i - \beta^j \partial_j \mathcal{U}^i + \mathcal{U}^j \partial_j \beta^i\Big) \\ &+ \Gamma^2 \mathcal{U}^j D_j \mathcal{U}^i - 2\Gamma^2 K^i{}_j \mathcal{U}^j \,. \end{aligned} \tag{C.1.14}$$

Next, $n^\nu \nabla_\nu \Gamma = \frac{1}{\alpha}[\partial_t \Gamma - \beta^i \partial_i \Gamma]$, which is given by Eq. (C.1.7). Substituting in Eq. (C.1.14) we obtain

$$\begin{aligned} h^i{}_\sigma u^\nu \nabla_\nu u^\sigma &= \Gamma^2 a^i + \Gamma^2 \mathcal{U}^i K_{jl} \mathcal{U}^j \mathcal{U}^l - \Gamma^2 \mathcal{U}^i \mathcal{U}^j \frac{\partial_j \alpha}{\alpha} \\ &+ \frac{\Gamma^2}{\alpha}\Big(\partial_t \mathcal{U}^i - \beta^j \partial_j \mathcal{U}^i + \mathcal{U}^j \partial_j \beta^i\Big) \\ &+ \frac{e}{m}\Gamma \mathcal{U}^i E^j \mathcal{U}_j + \Gamma^2 \mathcal{U}^j D_j \mathcal{U}^i - 2\Gamma^2 K^i{}_j \mathcal{U}^j \,. \end{aligned} \tag{C.1.15}$$

We are now ready to replace Eq. (C.1.15) and the spatial components of Eq. (C.1.9) in the original equation (C.1.8) and isolate the evolution operator. The result is:

$$\begin{aligned} \partial_t \mathcal{U}^i &= \beta^j \partial_j \mathcal{U}^i - \mathcal{U}^j \partial_j \beta^i - \alpha a^i - \alpha \mathcal{U}^i K_{jl} \mathcal{U}^j \mathcal{U}^l \\ &+ \frac{\alpha}{\Gamma}\frac{e}{m}\Big(-\mathcal{U}^i E^j \mathcal{U}_j + E^i + {}^{(3)}\epsilon^{ijl} B_l \mathcal{U}_j\Big) \\ &+ 2\alpha K^i{}_j \mathcal{U}^j + \mathcal{U}^i \mathcal{U}^j \partial_j \alpha - \alpha \mathcal{U}^j D_j \mathcal{U}^i \,. \end{aligned} \tag{C.1.16}$$

C.2 Continuity equation in $3+1$ variables

Let us now use the variables that we have introduced to rewrite the continuity equation Eq. (3.6). Using the decomposition $u^\mu = \Gamma(n^\mu + \mathcal{U}^\mu)$ and the definition of the electron density seen by the Eulerian observer, $n_{EL} = \Gamma n_e$, we can rewrite Eq. (3.6) as

$$\begin{aligned} 0 &= \nabla_\mu[n_e\Gamma(n^\mu + \mathcal{U}^\mu)] = \nabla_\mu[n_{EL}(n^\mu + \mathcal{U}^\mu)] \\ &= n^\mu\nabla_\mu n_{EL} + \mathcal{U}^\mu\nabla_\mu n_{EL} + n_{EL}\nabla_\mu n^\mu + n_{EL}\nabla_\mu\mathcal{U}^\mu \,. \end{aligned} \tag{C.2.17}$$

Expressing $n^\mu\nabla_\mu n_{EL}$ in terms of Lie derivatives, Eq. (C.2.17) can be written as an evolution equation for n_{EL}:

$$\partial_t n_{EL} = \beta^i\partial_i n_{EL} + \alpha K n_{EL} - \alpha\mathcal{U}^i\partial_i n_{EL} - \alpha n_{EL}\nabla_\mu\mathcal{U}^\mu. \tag{C.2.18}$$

Appendix D

Convergence and homogeneity of non-linear photon-plasma simulations

D.1 Convergence tests

We have evaluated the accuracy and the convergence properties of our code by checking how the constraint violations scale with the resolution in two test setups taken from the simulations presented in the main text.

Specifically, we considered the following quantities

$$CV_{\text{Gauss}} = \partial_i E^i - e n_{EL} + \rho_{(\text{ions})}, \tag{D.1.1}$$

$$CV_{\text{Plasma}} = \sqrt{\Gamma^2(1 - \mathcal{U}_i \mathcal{U}^i)} - 1, \tag{D.1.2}$$

which, whenever nonzero, represent the violations of the Gauss law (3.77) and of the normalization condition in Eq. (3.84), respectively.

In order to asses the reliability of our code we show here the convergence in the two most challenging nonlinear regimes: WB and blowout (although not shown, the convergence of the linear regime is excellent). Starting from the former, we repeated the simulation with $A_E = 1$ whose characteristic are described in Sec. 3.4.3, using a lower resolution $\Delta x = \Delta y = \Delta z = 0.4$, and increasing the grid size to $[-4, 4] \times [-4, 4] \times [-1450, 1150]$ in order to maintain 21 grid points along the x and y directions. We also doubled the time step to $\Delta t = 0.2$, in order to keep the CFL factor constant.

Figure D.1 shows the constraint violations CV_{Gauss} (left panel) and CV_{Plasma} (right panel) along the z axis at $t = 830$, slightly before WB happens (cf. lower panel of Fig. 3.15). In general, while for both the constraint violations there is a region where they are dominated by noise, in the central region they show an excellent fourth order scaling, and convergence is lost only for $65 \lesssim z \lesssim 75$, where the WB phenomenon is taking place.

We now move to consider the convergence in the blowout regime. We repeated the simulation with $A_E = 1000$ using grid steps $\Delta x = \Delta y = \Delta z = 0.4$ while maintaining the CFL factor constant. As in the previous case we extended the

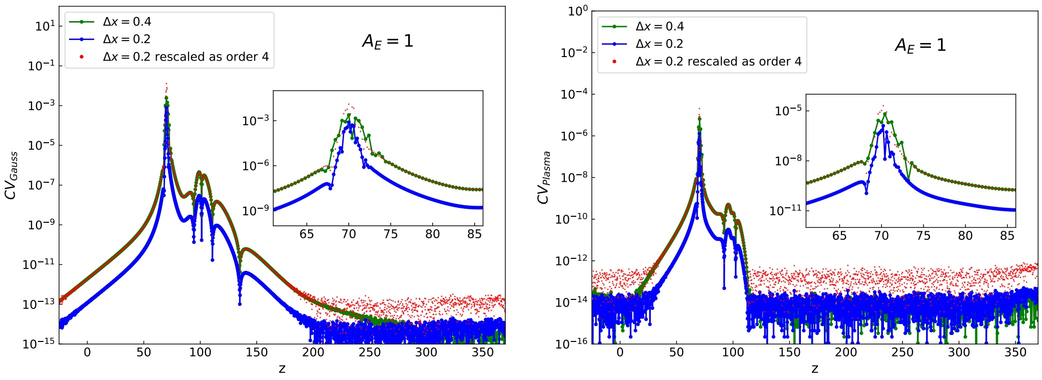

Figure D.1. Scaling of the violations of the Gauss Law (left panel) and the condition $u^\mu u_\mu = -1$ along the z axis, for the simulation in the nonlinear regime with $A_E = 1$. CV_{Gauss} and CV_{Plasma} are extracted at $t = 830$, when the WB phenomenon starts taking place. Overall the code converges extremely well, except in the region around the spike of n_{EL}, where the constraint violation displays a peak. The insets show a magnification of the constraint violations around this region.

grid to $[-4, 4] \times [-4, 4] \times [-750, 850]$ in order to have the same number of grid points along the transverse directions x and y. We show the scaling of CV_{Gauss} and CV_{Plasma} on the z axis at $t = 190$ in the left and right panel of Fig. D.2, respectively. We can see that the code converges extremely well, except in the region just behind the peak of the plasma density (cf. lowest panel of Fig. 3.13). However, we note that the extension of the region where convergence is lost decreases as the resolution increases, and that fourth-order scaling is restored in the plasma-depleted region.

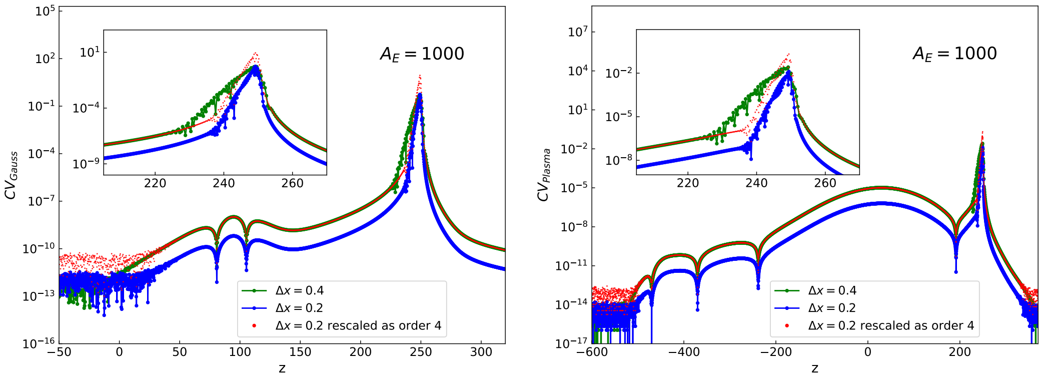

Figure D.2. Convergence of CV_{Gauss}(left panel) and CV_{Plasma}(right panel) along the z axis for the simulation in the nonlinear regime with $A_E = 1000$. The constraint violation is computed at $t = 190$, when the system is in the blowout regime. As we can see it satisfies fourth-order scaling except in the region close to the "transported" plasma and behind it, where the constraint violations have a peak. This can be better appreciated in the inset, that contains a magnification of the constraint violation around this region.

Given the excellent convergence properties in the nonlinear regime, we conclude that the code is reliable and produces accurate results at the resolutions used in this work.

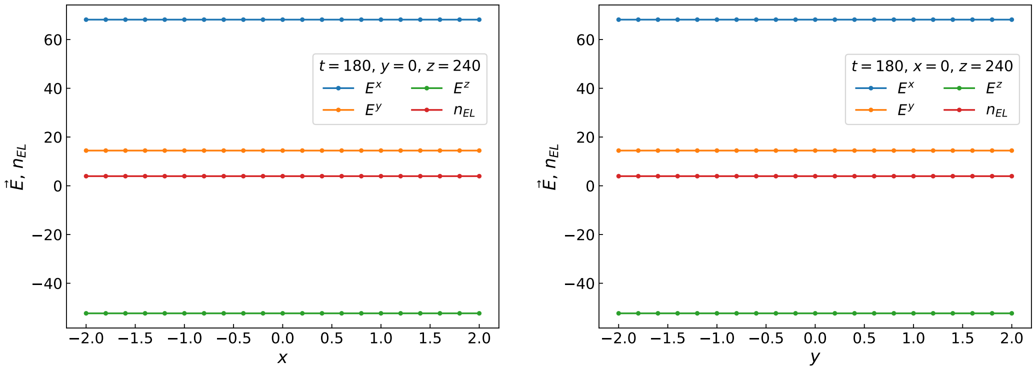

Figure D.3. Profiles of $\vec{E}$ and n_{EL} along the transverse directions x (left) and y (right) at $z = 240$ for the simulation with initial amplitude $A_E = 1000$. These data are extracted at $t = 180$, where the system is already in the blowout regime, and in the spatial region where the plasma density peaks. All the profiles are constant in x and y, with values consistent between the two plots. This confirms that the homogeneity property is conserved during the $3 + 1$ simulations.

D.2 Homogeneity of the fields along the transverse direction

Throughout all this work we used numerical grids whose extension along the transverse directions x and y is significantly smaller than in the z direction. This has the advantage of reducing considerably the computational cost, and can be done by exploiting the planar geometry of the system under consideration. In this appendix, we wish to show that homogeneity of the variables along the transverse directions is preserved also at late times during the evolution, so that this grid structure is compatible with the physical properties of the system for the entire duration of the simulations.

For this purpose we consider the simulation in the nonlinear regime with $A_E = 1000$, and we extract the profiles of E^x, E^y, E^z, and n_{EL} along the x and y axes at $z = 240$. This operation is performed at $t = 180$ when the system is already in a blowout state, and the value of the z coordinate is chosen to be where plasma is concentrated at this time.

We show the results in Fig. D.3, where the left and right panels represent the profiles along the x and y axes, respectively. We see that all the profiles are constant along the axes, and that the values are consistent between the two plots, confirming that the system maintains homogeneity along the transverse direction.

Appendix E

The master differential equation of spin-1 fields in plasma

E.1 The master differential equation

In the following, we will rearrange the system of Eqs. (4.6)-(4.8) into a single master equation for the DP field. To do so, let us define the following projection operator

$$h^{\alpha\beta} = g^{\alpha\beta} + u^\alpha u^\beta \,, \tag{E.1.1}$$

which projects vectors onto hypersurfaces whose normal vector is the fermionic four velocity. Then, we can decompose the derivative of the four-velocity as [130]

$$\nabla_\mu u^\nu = \theta^\nu{}_\mu + \omega^\nu{}_\mu - u_\mu u^\rho \nabla_\rho u^\nu \,, \tag{E.1.2}$$

where the tensors $\theta^{\alpha\beta}$ and $\omega^{\alpha\beta}$ are the deformation and vorticity tensors, defined as the symmetric and antisymmetric part of the tensor $v^{\mu\nu} = h^{\mu\alpha} h^{\nu\beta} u_{\alpha;\beta}$:

$$\theta_{\mu\nu} = \frac{1}{2}(v_{\mu\nu} + v_{\nu\mu}) \,, \tag{E.1.3}$$

$$\omega_{\mu\nu} = \frac{1}{2}(v_{\mu\nu} - v_{\nu\mu}) \,. \tag{E.1.4}$$

Finally, we can decompose the background field strength in to an electric component $E^\nu \equiv F^{\nu\mu} u_\mu$ and a magnetic one $B_{\mu\nu} \equiv h_\mu{}^\alpha h_\nu{}^\beta F_{\alpha\beta}$, which leads to a definition of the Larmor tensor for the DP: ${\omega_{\rm L}}^{\mu\nu} = -\frac{q_\chi}{m_\chi} B^{\mu\nu}$.

To reassemble the system of equations into a single one, we can express the perturbed four-velocity in terms of the DP field by projecting Eq. (4.6),

$$\tilde{u}^\rho = \frac{h^\rho{}_\nu}{q_\chi n} (\nabla_\mu \tilde{F}^{\nu\mu} + \mu^2 \tilde{V}^\nu) \,, \tag{E.1.5}$$

and insert it into Eq. (4.7) to obtain

$$h^\mu{}_\alpha (\nabla_\sigma \tilde{F}^{\alpha\sigma} + \mu^2 \tilde{V}^\alpha) \nabla_\mu u^\nu + u^\mu \nabla_\mu h^\nu{}_\alpha (\nabla_\sigma \tilde{F}^{\alpha\sigma} + \mu^2 \tilde{V}^\alpha) - \frac{1}{n} u^\mu \partial_\mu n \; h^\nu{}_\alpha (\nabla_\sigma \tilde{F}^{\alpha\sigma} + \mu^2 \tilde{V}^\alpha) = \tag{E.1.6}$$

$$\omega_{\rm pl}^{\chi\,2} \tilde{F}^{\nu\mu} u_\mu + \frac{q_\chi}{m_\chi} F^{\nu\mu} h_{\mu\alpha} (\nabla_\sigma \tilde{F}^{\alpha\sigma} + \mu^2 \tilde{V}^\alpha)$$

where we defined a plasma frequency for the oscillations induced by the DP propagation in the plasma, ${\omega_{\rm pl}^{\chi}}^2 = q_\chi^2 n/m_\chi$.

We still want to rearrange this equation into a more convenient form, to obtain Eq. (4.10). In the following, we provide a step-by-step calculation, focusing individually on each term of Eq. (E.1.6). Let us start by handling the first term: we decompose the first derivative of the four velocity in the standard way, via Eq. (E.1.2),

$$\begin{aligned}&(\nabla_\sigma \tilde{F}^{\alpha\sigma} + \mu^2 \tilde{V}^\alpha)(g^{\mu}{}_{\alpha} + u^\mu u_\alpha)\nabla_\mu u^\nu = \\ &(\nabla_\sigma \tilde{F}^{\alpha\sigma} + \mu^2 \tilde{V}^\alpha)(g^{\mu}{}_{\alpha} + u^\mu u_\alpha)(\theta^{\nu}{}_{\mu} + \omega^{\nu}{}_{\mu} - u_\mu u^\rho \nabla_\rho u^\nu)\,.\end{aligned} \tag{E.1.7}$$

Next, we use the following identities: $u^\mu \theta_{\mu}{}^{\nu} = u^\mu \omega_{\mu}{}^{\nu} = 0$ and $(g^{\mu}{}_{\alpha} + u^\mu u_\alpha)(-u_\mu u^\rho \nabla_\rho u^\nu) = 0$ (where the latter follows from $u^\mu u_\mu = -1$) so that the first term simply becomes

$$(\theta^{\nu}{}_{\alpha} + \omega^{\nu}{}_{\alpha})(\nabla_\sigma \tilde{F}^{\alpha\sigma} + \mu^2 \tilde{V}^\alpha)\,. \tag{E.1.8}$$

Now let us manipulate the second term of (E.1.6). We have

$$\begin{aligned}&u^\mu \nabla_\mu h^{\nu}{}_{\alpha}(\nabla_\sigma \tilde{F}^{\alpha\sigma} + \mu^2 \tilde{V}^\alpha) = u^\mu h^{\nu}{}_{\alpha} \nabla_\mu(\nabla_\sigma \tilde{F}^{\alpha\sigma} + \mu^2 \tilde{V}^\alpha) \\ &+ (\nabla_\sigma \tilde{F}^{\alpha\sigma} + \mu^2 \tilde{V}^\alpha) u^\mu (u^\alpha \nabla_\mu u^\nu + u^\nu \nabla_\mu u_\alpha)\,.\end{aligned} \tag{E.1.9}$$

As for the third term, we shall use the continuity equation (4.5) to get

$$\begin{aligned}&-\frac{1}{n} u^\mu \partial_\mu n\; h^{\nu}{}_{\alpha}(\nabla_\sigma \tilde{F}^{\alpha\sigma} + \mu^2 \tilde{V}^\alpha) = \frac{1}{n} n \nabla_\mu u^\mu\; h^{\nu}{}_{\alpha}(\nabla_\sigma \tilde{F}^{\alpha\sigma} + \mu^2 \tilde{V}^\alpha) \\ &= \theta h^{\nu}{}_{\alpha}(\nabla_\sigma \tilde{F}^{\alpha\sigma} + \mu^2 \tilde{V}^\alpha)\,,\end{aligned} \tag{E.1.10}$$

where $\theta = \theta^\mu_\mu$ is the trace of the deformation tensor. As for the fourth and fifth terms on the right side of Eq. (E.1.6), we just leave them in their original form.

Let us now apply the operator $h^{\xi}{}_{\nu}$ on every term. From (E.1.8) it is easy to see that the first term becomes simply $(\theta^{\xi}{}_{\alpha} + \omega^{\xi}{}_{\alpha})(\nabla_\sigma \tilde{F}^{\alpha\sigma} + \mu^2 \tilde{A}^\alpha)$, as the deformation and vorticity are orthogonal to the four-velocity. As for the second term, we can use $h^{\xi}{}_{\nu} u^\nu = 0$ and $h^{\xi}{}_{\nu} h^{\nu}{}_{\alpha} = h^{\xi}{}_{\alpha}$. We thus have

$$\begin{aligned}&u^\mu h^{\xi}{}_{\alpha} \nabla_\mu(\nabla_\sigma \tilde{F}^{\alpha\sigma} + \mu^2 \tilde{V}^\alpha) + (\nabla_\sigma \tilde{F}^{\alpha\sigma} + \mu^2 \tilde{V}^\alpha) u^\mu u_\alpha h^{\xi}{}_{\nu} \nabla_\mu u^\nu = \\ &u^\mu h^{\xi}{}_{\alpha} \nabla_\mu(\nabla_\sigma \tilde{F}^{\alpha\sigma} + \mu^2 \tilde{V}^\alpha) + (\nabla_\sigma \tilde{F}^{\alpha\sigma} + \mu^2 \tilde{V}^\alpha) u_\alpha u^\mu \nabla_\mu u^\xi\,,\end{aligned} \tag{E.1.11}$$

where we used $u^\nu \nabla_\mu u_\nu = 0$. By using the momentum equation on the second term $u^\mu \nabla_\mu u^\xi$ we obtain

$$h^{\xi}{}_{\alpha} u^\mu \nabla_\mu(\nabla_\sigma \tilde{F}^{\alpha\sigma} + \mu^2 \tilde{V}^\alpha) + \frac{q_\chi}{m_\chi} u_\alpha F^{\xi\beta} u_\beta (\nabla_\sigma \tilde{F}^{\alpha\sigma} + \mu^2 \tilde{V}^\alpha)\,. \tag{E.1.12}$$

As for the third term, from (E.1.10) it is simply

$$\theta h^{\xi}{}_{\alpha}(\nabla_\sigma \tilde{F}^{\alpha\sigma} + \mu^2 \tilde{V}^\alpha)\,, \tag{E.1.13}$$

where we used $h^{\xi}{}_{\nu} h^{\nu}{}_{\alpha} = h^{\xi}{}_{\alpha}$. The fourth term simply becomes

$$h^{\xi}{}_{\nu} {\omega_{\rm pl}^{\chi}}^2 \tilde{F}^{\nu\mu} u_\mu = {\omega_{\rm pl}^{\chi}}^2 \tilde{F}^{\xi\mu} u_\mu + {\omega_{\rm pl}^{\chi}}^2 u^\xi u_\nu \tilde{F}^{\nu\mu} u_\mu = {\omega_{\rm pl}^{\chi}}^2 \tilde{F}^{\xi\mu} u_\mu\,, \tag{E.1.14}$$

where we used the anti-symmetric nature of the field strength. As for the fifth and last term of Eq. E.1.6, upon projection it gives

$$\frac{q_\chi}{m_\chi} h^\xi{}_\nu F^{\nu\mu} h_{\mu\alpha} (\nabla_\sigma \tilde{F}^{\alpha\sigma} + \mu^2 \tilde{V}^\alpha) \,. \tag{E.1.15}$$

Since by the definition $B_{ab} = h_a{}^c h_b{}^d F_{cd}$ and $\omega_{L\ ab} = -\frac{e}{m} B_{ab}$, we can rewrite this term as

$$-\omega_L{}^\xi{}_\alpha (\nabla_\sigma \tilde{F}^{\alpha\sigma} + \mu^2 \tilde{V}^\alpha) \,. \tag{E.1.16}$$

Assembling all terms together leads to the final Eq. (4.10), describing the propagation of a massive spin-1 particle in a cold, collisionless plasmic medium in curved spacetime.

Appendix F

DP field equations in the multipolar expantion

F.1 Static case

We assume an unmagnetised background plasma, ${\omega_{\rm L}}^{\mu\nu} = 0$. The four velocity of a static plasma is $u^\alpha = (f^{-1/2}, \vec{0})$, satisfying the normalisation condition $u_\mu u^\mu = -1$. From Eq. (4.4), the electric field has then only one nonvanishing radial component $E^\alpha = (0, m_\chi/q_\chi\, \Gamma^r_{00}(u^0)^2, 0, 0)$, where $\Gamma^\mu_{\alpha\beta}$ are the Christoffel's symbols. In this case it can be seen that the vorticity and deformation tensors are both zero, $\omega^{\alpha\beta} = \theta^{\alpha\beta} = 0$. By performing the multipolar expantion and working in the frequency domain we obtain the following set of equations:

$$\begin{aligned}
-\omega(f(l(l+1)+r^2\mu^2) - r^2\omega^2 + fr^2{\omega^{\chi}_{\rm pl}}^2)u_{(2)}& \\
+ifr(\omega^2 - f{\omega^{\chi}_{\rm pl}}^2)u_{(1)}& \\
+fr(-ir(\omega^2 - f{\omega^{\chi}_{\rm pl}}^2)u'_{(1)} + f\omega u'_{(3)}) &= 0\,, \qquad \text{(F.1.1)}\\
-l(l+1)r(\omega^2 - f{\omega^{\chi}_{\rm pl}}^2)u_{(1)} - ifl(l+1)\omega u_{(2)}& \\
+ir^2\omega(f\mu^2 - \omega^2 + f{\omega^{\chi}_{\rm pl}}^2)u_{(3)}& \\
+if\omega(l(l+1)ru'_{(2)} - 2Mu'_{(3)} - fr^2u''_{(3)})) &= 0\,, \qquad \text{(F.1.2)}\\
(f(l+l^2+r^2\mu^2) - r^2\omega^2 + fr^2{\omega^{\chi}_{\rm pl}}^2)u_{(4)}& \\
-f(2Mu'_{(4)} + fr^2u''_{(4)}) &= 0\,. \qquad \text{(F.1.3)}
\end{aligned}$$

where $u'_{(i)} = \partial_r u_{(i)}$, we have suppressed the l superscript, and the radial dependence of $\omega^{\chi}_{\rm pl} = \omega^{\chi}_{\rm pl}(r)$. Now we have three equations for the four wavefunctions $u_{(1)}, u_{(2)}, u_{(3)}, u_{(4)}$. We can close the system with the Lorenz condition

$$-ir^2\omega u_{(1)} - rf(u_{(2)} - u_{(3)} + ru'_{(2)}) = 0\,. \qquad \text{(F.1.4)}$$

By solving the Lorenz equation for u_1 and plugging it in to the polar field equations we obtain Eqs. (4.13), (4.14).

F.2 Free-fall case

In the free-fall configuration, plasma particles follow geodesics, i.e. the background DP field is set to $F^{\mu\nu} = 0$, $E^{\alpha} = \omega_L^{\alpha\beta} = 0$.

A free-fall plasma does not have vorticity, $\omega^{\alpha\beta} = 0$, but has a nonvanishing deformation. The nonzero components are

$$\theta_0{}^0 = \frac{\sqrt{2}(M/r)^{3/2}}{2M - r}, \quad \theta_r{}^r = \frac{\sqrt{M/r}}{\sqrt{2}(r - 2M)}, \quad \theta_\theta{}^\theta = -\frac{\sqrt{2M}}{r^{3/2}},$$
$$\theta_\phi{}^\phi = -\frac{\sqrt{2M}}{r^{3/2}}, \quad \theta_0{}^r = \frac{M}{r^2}, \quad \theta_r{}^0 = -\frac{M}{(r-2M)^2}\,. \tag{F.2.5}$$

The trace of this tensor is also different from zero and therefore there are extra terms in Eq. (4.10) with respect to the static case. Working again in the frequency domain, we obtain the following set of equations:

$$A_1 u_{(4)} + A_2 u'_{(4)} + A_3 u''_{(4)} + A_4 u'''_{(4)} = 0 \tag{F.2.6}$$
$$B_1 u_{(2)} + B_2 u'_{(2)} + B_3 u''_{(2)} + B_4 u_{(1)} + B_5 u'_{(1)} + B_6 u''_{(1)} + B_7 u'''_{(1)} + B_8 u_{(3)} + B_9 u'_{(3)} + B_{10} u''_{(3)} = 0 \tag{F.2.7}$$
$$C_1 u_{(2)} + C_2 u'_{(2)} + C_3 u''_{(2)} + C_4 u_{(1)} + C_5 u'_{(1)} + C_6 u_{(3)} + C_7 u'_{(3)} + C_8 u''_{(3)} = 0 \tag{F.2.8}$$

These consist of a single, third-order axial equation for the wavefunction $u_{(4)}(r)$, and two equations for the polar wavefunctions $u_{(1)}(r)$, $u_{(2)}(r)$ and $u_{(3)}(r)$. The system can then be closed using the Lorenz condition given by Eq. (F.1.4). The coefficient of the above equations are listed in the following:

$$\begin{aligned} A_1 =& -4Mr^{5/2}(\lambda + r^2\mu^2)\omega + 2r^{7/2}\omega(\lambda + r^2(\mu^2 - \omega^2) \\ &+ 2i\sqrt{2}M^{3/2}r(-2\lambda + r^2(6\mu^2 - 5\omega^2)) + 4i\sqrt{2}M^{5/2}(\lambda - 3r^2\mu^2) \\ &+ i\sqrt{2M}r^2(\lambda + 3r^2(-\mu^2 + \omega^2)) + 2r^{11/2}\omega f\omega_{\mathrm{pl}}^{\chi\,2})\,, \end{aligned} \tag{F.2.9}$$

$$\begin{aligned} A_2 =& -2f\sqrt{M}r(-2\sqrt{2}iM^2 + 2\sqrt{M}r^{5/2}\omega + \sqrt{2}r^2 i(\lambda + r^2(\mu^2 - \omega^2) + r^2\omega_{\mathrm{pl}}^{D\,2}) \\ &- \sqrt{2}iMr(-1 + 2\lambda + 2r^2\mu^2 + 2r^2\omega_{\mathrm{pl}}^{\chi\,2}))\,, \end{aligned} \tag{F.2.10}$$

$$A_3 = f^2r^3(2\sqrt{2}iM^{3/2} + 3i\sqrt{2M}r - 2r^{5/2}\omega)\,, \tag{F.2.11}$$

$$A_4 = 2\sqrt{2}if^3\sqrt{M}r^5\,, \tag{F.2.12}$$

$$\begin{aligned} B_1 =& 6\sqrt{2}(Mr)^{3/2}\lambda - 4\sqrt{2}M^{5/2}\sqrt{r}\lambda + 4\sqrt{2}(Mr)^{5/2}\mu^2 - 8iM^3r\omega + 18iM^2r^2\omega \\ &- iMr^3(3 + 2\lambda + 2r^2\mu^2)\omega - 2\sqrt{2}M^{3/2}r^{7/2}(\mu^2 - 4\omega^2) \\ &- \sqrt{2M}r^{5/2}(2\lambda + r^2\omega^2) + ir^4\omega(\lambda + r^2(\mu^2 - \omega^2)) + if^2r^6\omega\omega_{\mathrm{pl}}^{\chi\,2}\,, \end{aligned} \tag{F.2.13}$$

$$\begin{aligned} B_2 =& -f\sqrt{M}r^{5/2}(2\sqrt{2}M(\lambda + r^2\mu^2) + 10iM^{3/2}\sqrt{r}\omega - i\sqrt{M}r^{3/2}\omega \\ &- \sqrt{2}r(\lambda + r^2(\mu^2 - 2\omega^2)))\,, \end{aligned} \tag{F.2.14}$$

$$B_3 = 2if^2Mr^5\omega\,, \tag{F.2.15}$$

$$\begin{aligned} B_4 =& -16M^2r\lambda + 4M^3(3\lambda - r^2\mu^2) - i\sqrt{2M}r^{7/2}(-1 + \lambda + r^2\mu^2)\omega \\ &+ 2\sqrt{2}iM^{3/2}r^{5/2}(\lambda + r^2\mu^2)\omega + r^5\omega^2 + Mr^2(5\lambda - 2\sqrt{2Mr}i\omega \\ &+ r^2(\mu^2 - 2\omega^2)) - f^3r^5\omega_{\mathrm{pl}}^{\chi\,2}\,, \end{aligned} \tag{F.2.16}$$

$$\begin{aligned} B_5 =& fr^2(4M^2(\lambda + r^2\mu^2) - 2Mr(\lambda + 2r^2\mu^2) - \sqrt{2M}ir^{5/2}\omega \\ &- r^4\omega^2 + f^2r^4\omega_{\mathrm{pl}}^{\chi\,2})\,, \end{aligned} \tag{F.2.17}$$

$$B_6 = f^2\sqrt{M}r^3(2M^{3/2} - \sqrt{M}r + 2\sqrt{2}ir^{5/2}\omega)\,, \tag{F.2.18}$$

$$B_7 = 2f^3Mr^5\,, \tag{F.2.19}$$

$$B_8 = -if\sqrt{M}r^2\omega(2M^{3/2} - 3\sqrt{M}r + i\sqrt{2}r^{5/2}\omega)\,, \tag{F.2.20}$$

$$B_9 = f^2r^{5/2}(-2\sqrt{2}M^{3/2} + \sqrt{2M}r - 2iMr^{3/2}\omega - i\omega r^{5/2}\,, \tag{F.2.21}$$

$$B_{10} = \sqrt{2M}r^{3/2}(8M^3 + 6Mr^2 - r^3 - 12M^{3/2}\sqrt{rM}r\,, \tag{F.2.22}$$

$$C_1 = fr\lambda(2\sqrt{2}M^{3/2} + 2i\omega r^{5/2} + \sqrt{2M}r(-1 + 2r^2\omega_{\mathrm{pl}}^{\chi\,2}))\,, \tag{F.2.23}$$

$$C_2 = r(-4\sqrt{2}\lambda M^{3/2}r + \sqrt{2M}\lambda r^2 + 4\sqrt{2}M^{5/2}\lambda + 4iMr^{5/2}\lambda\omega - 2ir^{7/2}\lambda\omega)\,, \tag{F.2.24}$$

$$C_3 = -2\sqrt{2M}r^2(\lambda r(-4M + r) + 4M^2\lambda)\,, \tag{F.2.25}$$

$$C_4 = r^2\lambda(\omega(i\sqrt{2M}(6M - r) + 2r^{5/2}\omega) - 2fr^{5/2}\omega_{\mathrm{pl}}^{\chi\,2})\,, \tag{F.2.26}$$

$$C_5 = -2\sqrt{2M}ifr^4\lambda\omega\,, \tag{F.2.27}$$

$$\begin{aligned} C_6 =& r^2(-12\sqrt{2}M^{5/2}\mu^2 + 2\sqrt{2}M^{3/2}r(6\mu^2 - 5\omega^2) + 3\sqrt{2M}r^2(-\mu^2 + \omega^2) \\ &+ 4iMr^{5/2}\omega(\mu^2 + \omega_{\mathrm{pl}}^{\chi\,2}) - 2ir^{7/2}\omega(\mu^2 + \omega_{\mathrm{pl}}^{\chi\,2} - \omega^2))\,, \end{aligned} \tag{F.2.28}$$

$$\begin{aligned} C_7 =& 2f\sqrt{M}r(2\sqrt{2}M^2 + 2i\sqrt{M}r^{5/2}\omega - \sqrt{2}r^4(\mu^2 + \omega_{\mathrm{pl}}^{\chi\,2} - \omega^2) \\ &+ \sqrt{2}Mr(-1 + 2r^2(\mu^2 + \omega_{\mathrm{pl}}^{\chi\,2}))\,, \end{aligned} \tag{F.2.29}$$

$$C_8 = f^2r^3(2\sqrt{2}M^{3/2} + 3\sqrt{2M}r + 2ir^{5/2}\omega)\,, \tag{F.2.30}$$

where for simplicity we defined $\lambda = l(l+1)$.

Appendix G

Benchmarks for evolution of scalar fields

The purpose of this appendix is to study in some detail the time evolution of free massive scalar fields in the vicinity of a Schwarzschild BH. Even though SR requires a spinning BH and thus the use of the Kerr metric, timescales are prohibitively large. Nevertheless, the main focus of our work is on physics related to the *existence* of scalar clouds, more than to what caused them in the first place.

As such, we mimic SR growth without the need of a spinning BH (see Section G.2 below) and therefore we consider a Schwarzschild spacetime for simplicity. We still need to guarantee that, on the required timescales, a bound state exists, so that it can mimic well the true SR clouds. Fortunately, massive scalars around non-spinning BHs do settle on quasi-bound states which, while not unstable, have extremely large lifetimes. Thus, we want to show first of all that our numerical framework reproduces well such states.

G.1 Bound states

The initial data whose time evolution we will study, are the quasi-bound states of a massive scalar field, which are solutions localised in the vicinity of the BH and prone to become unstable in the SR regime (if the BH is allowed to spin). There exist various methods to find such quasi-bound solutions, either by direct numerical integration or using continued fractions [269, 209, 69, 208]. In this work, we use Leaver's continued fraction approach [269]. It is crucial to have accurate solutions describing pure quasi-bound states, as deviations from such a pure state may trigger excitations of overtones, resulting in a beating pattern [84].

In Boyer-Lindquist (BL) coordinates ($t_{\rm BL}$, $r_{\rm BL}$, $\theta_{\rm BL}$, $\varphi_{\rm BL}$), the scalar field bound state is given by[1]

$$\Psi_{\ell m} = e^{-i\omega t_{\rm BL}} e^{-im\varphi_{\rm BL}} S_{\ell m}\left(\theta_{\rm BL}\right) R_{\ell m}\left(r_{\rm BL}\right) \,, \tag{G.1.1}$$

where $S_{\ell m}(\theta_{\rm BL})$ are the spheroidal harmonics. In a Schwarzschild geometry, the angular dependence is fully captured by the familiar spherical harmonics $S_{\ell m}(\theta_{\rm BL})e^{im\varphi_{\rm BL}} =$

---

[1] We include spin here for generality, although we evolve the scalar field in a Schwarzschild background

$Y_{\ell m}(\theta_{\rm BL},\varphi_{\rm BL})$. The radial dependence is given by

$$\begin{aligned} R_{\ell m}\left(r_{\rm BL}\right) = \left(r_{\rm BL}-r_{\rm BL,+}\right)^{-i\sigma}\left(r_{\rm BL}-r_{\rm BL,-}\right)^{i\sigma+\chi-1}\times \\ e^{r_{\rm BL}q}\sum_{n=0}^{\infty}a_n\left(\frac{r_{\rm BL}-r_{\rm BL,+}}{r_{\rm BL}-r_{\rm BL,-}}\right)^n\,, \end{aligned} \tag{G.1.2}$$

where

$$\begin{aligned} \sigma &= \frac{2Mr_{\rm BL,+}\left(\omega-\omega_{\rm c}\right)}{r_{\rm BL,+}-r_{\rm BL,-}}\,,\quad q=\pm\sqrt{\mu^2-\omega^2}\,,\\ \chi &= M\frac{\mu^2-2\omega^2}{q}\,. \end{aligned} \tag{G.1.3}$$

Here, $r_{\rm BL,\pm}=M\pm\sqrt{M^2-a_{\rm J}^2}$ are the inner ($-$) and outer ($+$) horizon, $\omega_{\rm c}=m\Omega_H=ma_{\rm J}/(2Mr_{\rm BL,+})$ is the critical SR frequency, $a_{\rm J}$ is the spin of the BH and to obtain quasi-bound states, one should consider the minus sign in the expression for q. Since all the terms in these expressions are known in closed form, we only need to solve for the frequency of the mode of interest, ω. This is found by solving the following condition for ω:

$$\beta_0-\frac{\alpha_0\gamma_1}{\beta_1-}\frac{\alpha_1\gamma_2}{\beta_2-}\cdots=0\,, \tag{G.1.4}$$

where all the coefficients can be found in e.g. [69]. In (G.1.2), the amplitude of the scalar field is defined arbitrarily (as long as one neglects the backreaction of the field on the background geometry). Hence, we must choose a suitable normalization. We will normalize the field by assigning a predetermined value to the maximum of the radial wavefunction. In previous works [172, 171], the hydrogenic approximation was used instead, where the wavefunction is defined as $\Psi=\Psi_0 r_{\rm BL}M\mu^2 e^{-r_{\rm BL}M\mu^2/2}\cos\left(\varphi_{\rm BL}-\omega_{\rm R}t\right)\sin\theta_{\rm BL}$, where $\omega_{\rm R}$ is the real part of the eigenfrequency. In order to allow for a direct comparison with those works, we relate our normalization, the maximum value of the real part of the field, $(R_{\ell m})_{\rm max}$, to this parameter Ψ_0. They are related by

$$(R_{\ell m})_{\rm max}=\frac{4\Psi_0\sqrt{2\pi/3}}{e}\,, \tag{G.1.5}$$

where the factor $\sqrt{2\pi/3}$ comes from the normalization of the spherical harmonics $\ell=1$ modes, and should be adapted accordingly for higher multipoles. We will introduce relevant quantities in terms of Ψ_0.

For numerical purposes, BL coordinates are not ideal due to the coordinate singularity at the horizon. Therefore, we employ Kerr-Schild coordinates, which are horizon penetrating coordinates [84]. The coordinate transformation from BL to Kerr-Schild (KS) coordinates is given by

$$\begin{aligned} {\rm d}t_{\rm KS} &= {\rm d}t_{\rm BL}+\frac{2Mr_{\rm BL}}{\Delta}{\rm d}r_{\rm BL}\,,\quad {\rm d}r_{\rm KS}={\rm d}r_{\rm BL}\,,\\ {\rm d}\theta_{\rm KS} &= {\rm d}\theta_{\rm BL}\,,\quad {\rm d}\varphi_{\rm KS}={\rm d}\varphi_{\rm BL}+\frac{a_{\rm J}}{\Delta}{\rm d}r_{\rm BL}\,, \end{aligned} \tag{G.1.6}$$

where $\Delta\equiv r^2-2Mr+a_{\rm J}^2$. Using this coordinate transformation in (G.1.1), we can construct the bound state scalar field as

$$\Psi_{\ell m} = e^{-i\omega t_{\rm KS}} \left(r_{\rm KS} - r_{\rm KS,+}\right)^P \left(r_{\rm KS} - r_{\rm KS,-}\right)^Q \left(\frac{r_{\rm KS} - r_{\rm KS,+}}{r_{\rm KS} - r_{\rm KS,-}}\right)^R Y_{\ell m}\left(\theta_{\rm KS}, \varphi_{\rm KS}\right) R_{\ell m}(r_{\rm KS})\,, \tag{G.1.7}$$

where $P = \frac{2i\omega M r_{\rm KS,+}}{r_{\rm KS,+} - r_{\rm KS,-}}$, $Q = -\frac{2i\omega M r_{\rm KS,-}}{r{\rm KS},+ - r_{\rm KS,-}}$, $R = \frac{i m a_{\rm J}}{r_{\rm KS,-} - r_{\rm KS,+}}$. Unless otherwise stated, we use KS coordinates without the subscript. In our non-spinning BH case, $Q = R = 0$. The remaining extra term instead exactly cancels the divergence of the field at the BH horizon. We test our numerical setup by constructing the bound state initial configurations for scalar fields with mass couplings $\mu M = 0.1$ and $\mu M = 0.3$ and evolving them in a Schwarzschild background.

In the left panel of Fig. G.1, we show the non-vanishing multipolar component of the field for $\mu M = 0.1$ and $\mu M = 0.3$, where we only display a fraction of the time evolution such that individual oscillations are visible. For $\mu M = 0.1$, the scalar field is exceptionally stable on timescales longer than $5000M$. For $\mu M = 0.3$, there is a decrease in the amplitude of a few percent on those timescales, which does not have severe consequences. In fact, this problem can be resolved by increasing the spatial resolution.

As a last check, we show in the right panel of Fig. G.1 the Fourier transform for both $\mu M = 0.1$ and $\mu M = 0.3$ and compare it with the real part of the eigenfrequency of the fundamental mode. We find an excellent comparison, showing that we are not triggering any overtones.

G.2 Artificial superradiance

Studying SR for scalars is numerically challenging, since timescales for SR growth are very large. Fortunately, an effective SR-like instability can be introduced by adding a simple $C\partial\Psi/\partial t$ term to the KG equation as shown in (5.4). This “trick” was first used by Zel’dovich [47, 48, 210] and it can mimic the correct description of many SR systems. The addition of this Lorentz-invariance violating term causes an instability on a timescale of the order $1/C$, where we can tune C to be within our numerical limits. For reference, let us report the timescales in our problem.
“*Normal SR*”:

$$t_{\rm SR} \sim 48 \left(\frac{a_{\rm J}}{M}(\mu M)^{-9}\right) M \quad \text{when} \quad \mu M \ll 1\,, \tag{G.2.8}$$

“*Artificial SR*”:

$$t_{\rm ASR} \sim \frac{1}{C} M\,, \tag{G.2.9}$$

“*EM instability*”:

$$t_{\rm EM} \sim 10 k_{\rm a}^{-1} \left(\frac{M}{M_{\rm c}}\right)^{1/2} (\mu M)^{-3} = 5(\mu M)^{-1} M\,, \tag{G.2.10}$$

which is the EM instability timescale that was found in [171] and where we used $k_{\rm a} \geq 2(\frac{M}{M_{\rm c}})^{1/2}(\mu M)^{-2} M^{-1}$.

Accordingly, for a reasonable mass coupling of $\mu M = 0.1$, and while optimizing SR growth with a maximally spinning BH, normal SR timescales are on the order

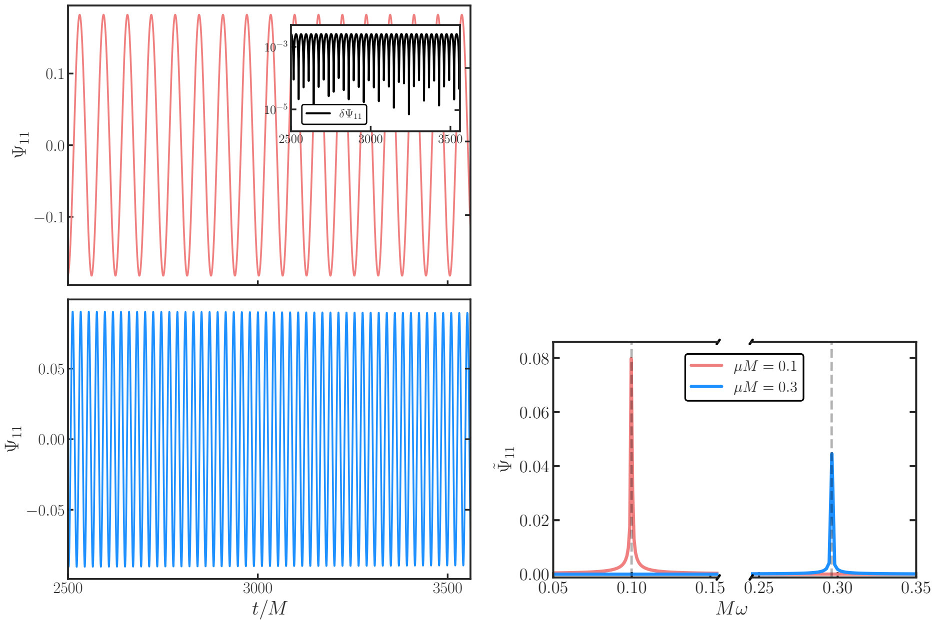

Figure G.1. **Left top Panel:** The $\ell = m = 1$ component of a scalar field around a Schwarzschild BH. Figure shows fraction of the time evolution of the initial conditions from (G.1.7). The field is extracted at $r_{\rm ex} = 100M$ and $\mu M = 0.1$. Inset shows $\delta\Psi_{11}$, which is the difference between the numerical output and the theoretically predicted fundamental mode $\Psi_{11}^{\rm Fund} \sim \cos(\omega_{\rm R} t) e^{-\omega_{\rm I} t}$, where $\omega_{\rm R}, \omega_{\rm I}$ are the real and imaginary part of the eigenfrequency, respectively. These were independently computed using Leaver's method. **Left bottom Panel:** Same for $\mu M = 0.3$ and extraction radius $r_{\rm ex} = 40M$. There is an apparent decay of the field on timescales shorter than those implied by the quasi-bound state decay. This effect is due to finite resolution, and its magnitude is small enough such that we can ignore it in our study. **Right Panel:**Fourier transform of the dipole component of the scalar field for $\mu M = 0.1$ and $\mu M = 0.3$ when the field is extracted at $r_{\rm ex} = 100M$ and $r_{\rm ex} = 40M$, respectively. Fourier transform is taken on the entire time evolution of Figure G.1. Dashed lines indicate the (real part of the) frequency of the fundamental mode for $\mu M = 0.1$ and $\mu M = 0.3$. Clearly, we are not triggering any overtones.

of $t_{\rm SR} \sim 10^{10}M$. This should be compared to the EM instability, which is on $t_{\rm EM} \sim 50M$.

To test whether we implemented the artificial SR growth in the correct way, we set $C = 5 \times 10^{-4}M^{-1}$ and evolve the scalar field. From Fig. G.2, we can see that the artificial SR is correctly implemented in the code, as it leads to the desired exponential evolution of the field.

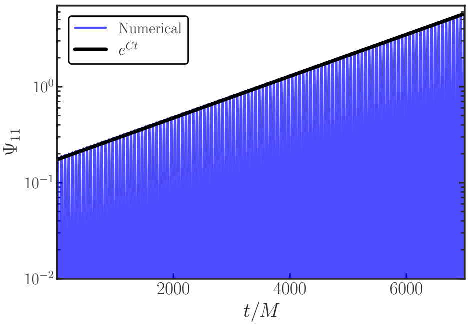

Figure G.2. The time evolution of Ψ_{11} extracted at $r_{\rm ex} = 100M$ with $C = 5 \times 10^{-4}M^{-1}$ and $\mu M = 0.1$. We show the growth of the scalar field from the initial conditions (G.1.7), using Zel'Dovich trick described in the main text.

Appendix H

Wave extraction

From the simulations, we extract the radiated scalar and vector waves at some radius $r = r_{\rm ex}$. For the scalar waves, we project the field Ψ and its conjugated momentum Π onto spheres of constant coordinate radius using the spherical harmonics with spin weight $s_{\rm w} = 0$:

$$\begin{aligned}\Psi_{\ell m}(t) &= \int \mathrm{d}\Omega\, \Psi(t,\theta,\varphi)\, {}_0Y^*_{\ell m}(\theta,\varphi), \\ \Pi_{\ell m}(t) &= \int \mathrm{d}\Omega\, \Pi(t,\theta,\varphi)\, {}_0Y^*_{\ell m}(\theta,\varphi)\,.\end{aligned} \tag{H.0.1}$$

To monitor the emitted EM (vector) waves, we use the Newman-Penrose formalism [478]. In this formalism, the radiative degrees of freedom are given by complex scalars. For EM, these are defined as contractions between the Maxwell tensor and vectors of a null tetrad $(k^\mu, \ell^\mu, m^\mu, \bar{m}^\mu)$, where $k^\mu \ell_\mu = -m^\mu \bar{m}_\mu = -1$. The null tetrad itself is constructed from the orthonormal timelike vector n^μ and a Cartesian orthonormal basis $\{u^i, v^i, w^i\}$ on the spatial hypersurface. Asymptotically, the basis vectors $\{u^i, v^i, w^i\}$ behave as the unit radial, polar and azimuthal vectors, respectively. For our purposes, the quantity of interest is the gauge-invariant Newman-Penrose scalar Φ_2, which captures the outgoing EM radiation at infinity and is defined as

$$\Phi_2 = F_{\mu\nu}\ell^\mu \bar{m}^\nu\,, \tag{H.0.2}$$

where $\ell^\mu = \frac{1}{\sqrt{2}}(n^\mu - u^\mu)$ and $\bar{m}^\mu = \frac{1}{\sqrt{2}}(v^\mu - i w^\mu)$. Decomposing the Maxwell tensor gives

$$F_{\mu\nu} = n_\mu E_\nu - n_\nu E_\mu + D_\mu \mathcal{A}_\nu - D_\nu \mathcal{A}_\mu\,, \tag{H.0.3}$$

where $E_\mu = F_{\mu\nu} n^\nu$ and $\mathcal{A}_\mu$ is the spatial part of the vector field A_μ. The real and imaginary components of Φ_2 are then given by

$$\begin{aligned}\Phi_2^{\rm R} &= -\frac{1}{2}\left[E_i^{\rm R} v^i + u^i v^j \left(D_i \mathcal{A}_j^{\rm R} - D_j \mathcal{A}_i^{\rm R}\right) + E_i^{\rm I} w^i + u^i w^j \left(D_i \mathcal{A}_j^{\rm I} - D_j \mathcal{A}_i^{\rm I}\right)\right], \\ \Phi_2^{\rm I} &= \frac{1}{2}\left[E_i^{\rm R} w^i + u^i w^j \left(D_i \mathcal{A}_j^{\rm R} - D_j \mathcal{A}_i^{\rm R}\right) - E_i^{\rm I} v^i - u^i v^j \left(D_i \mathcal{A}_j^{\rm I} - D_j \mathcal{A}_i^{\rm I}\right)\right].\end{aligned} \tag{H.0.4}$$

Similar to the scalar case, we obtain the multipoles of Φ_2 at a certain extraction radius $r_{\rm ex}$, by projecting Φ_2 onto the $s_{\rm w} = -1$ spin-weighted spherical harmonics.

$$\begin{aligned}(\Phi_2^{\rm R})_{\ell m}(t) &= \int \mathrm{d}\Omega \Big[\Phi_2^{\rm R}(t,\theta,\varphi)\ {}_{-1}Y_{\ell m}^{\rm R}(\theta,\varphi) + \Phi_2^{\rm I}(t,\theta,\varphi)\ {}_{-1}Y_{\ell m}^{\rm I}(\theta,\varphi)\Big]\,,\\ (\Phi_2^{\rm I})_{\ell m}(t) &= \int \mathrm{d}\Omega \Big[\Phi_2^{\rm I}(t,\theta,\varphi)\ {}_{-1}Y_{\ell m}^{\rm R}(\theta,\varphi) - \Phi_2^{\rm R}(t,\theta,\varphi)\ {}_{-1}Y_{\ell m}^{\rm I}(\theta,\varphi)\Big]\,.\end{aligned} \tag{H.0.5}$$

Throughout this work, we will often show $|(\Phi_2)_{\ell m}| = \sqrt{(\Phi_2)^*_{\ell m}(\Phi_2)_{\ell m}}$.

Appendix I

Formulation as a Cauchy problem

In this appendix, we formalize our equations of motion (5.2) as an (initial value) Cauchy problem and we discuss the initial data.

I.1 3+1 Decomposition

The equations of motion of our axion-photon-plasma system are given by (5.2). In this work, we will ignore the dynamics of gravity and solve the Klein-Gordon, Maxwell and plasma equations on a fixed spacetime background. In order to evolve the system in time, we use the standard 3+1 decomposition of the spacetime (see e.g. [479]). The metric then takes the following generic form:

$$\mathrm{d}s^2 = -\alpha^2 \mathrm{d}t^2 + \gamma_{ij}\left(\mathrm{d}x^i + \beta^i \mathrm{d}t\right)\left(\mathrm{d}x^j + \beta^j \mathrm{d}t\right) , \tag{I.1.1}$$

where α is the lapse function, β^i is the shift vector and γ_{ij} is the 3-metric on the spatial hypersurface. Furthermore, we introduce the scalar momentum as

$$\Pi = -n^\mu \nabla_\mu \Psi , \tag{I.1.2}$$

where n^μ is the unit normal vector to the spatial hypersurface, which takes on the form $n^\mu = (1/\alpha, -\beta^i/\alpha)$. The vector field A_μ can be decomposed as

$$A_\mu = \mathcal{A}_\mu + n_\mu A_\varphi , \tag{I.1.3}$$

where

$$\mathcal{A}_i = \gamma^j{}_i A_j \quad \text{and} \quad A_\varphi = -n^\mu A_\mu . \tag{I.1.4}$$

We also introduce the EM fields

$$E^i = \gamma^i{}_j F^{j\nu} n_\nu \quad \text{and} \quad B^i = \gamma^i{}_j {}^*F^{j\nu} n_\nu , \tag{I.1.5}$$

which are defined with respect to an Eulerian observer. As for the plasma quantities, we decompose the fluids' four velocities as [480]

$$u^\mu_{\mathrm{e}} = \Gamma_{\mathrm{e}}(n^\mu + \mathcal{U}^\mu), \quad u^\mu_{\mathrm{ion}} = \Gamma_{\mathrm{ion}}(n^\mu + \mathcal{V}^\mu) . \tag{I.1.6}$$

where $\mathcal{U}^\mu, \mathcal{V}^\mu$ are again defined with respect to an Eulerian observer. From the normalization of the four velocities, the Lorentz factor is then:

$$\Gamma_{\mathrm{e}} = -n_\mu u^\mu = \frac{1}{\sqrt{1-\mathcal{U}_\mu \mathcal{U}^\mu}}, \quad \Gamma_{\mathrm{ion}} = \frac{1}{\sqrt{1-\mathcal{V}_\mu \mathcal{V}^\mu}}\,. \tag{I.1.7}$$

Note that even though we include the ion quantities in (I.1.6) and (I.1.7) for generality, we do not actually use them in this work as we ignore the oscillations of the ions (assumption (ii)). Finally, we introduce the charge density as seen by an Eulerian observer as

$$\rho = -n_\mu j^\mu\,. \tag{I.1.8}$$

Since j^μ is the sum of the currents of the two fluids, we can express (I.1.8) also as $\rho = \rho_{\mathrm{e}} + \rho_{\mathrm{ion}}$.

Using the above definitions, we obtain the following evolution equations for the full axion-photon-plasma system (for the decomposition of the momentum equation, we refer to Appendix C; for the EM part, see e.g. [152]):

$$\begin{aligned}
\partial_t \Psi &= -\alpha\Pi + \mathcal{L}_\beta \Psi\,,\\
\partial_t \Pi &= \alpha\left(-D^2\Psi + \mu^2\Psi + K\Pi - 2k_{\mathrm{a}} E^i B_i\right) - D^i\alpha D_i \Psi + \mathcal{L}_\beta \Pi\,,\\
\partial_t \mathcal{A}_i &= -\alpha\left(E_i + D_i A_\varphi\right) - A_\varphi D_i \alpha + \mathcal{L}_\beta \mathcal{A}_i\,,\\
\partial_t E^i &= \alpha K E^i - \alpha D_j\left(D^j\mathcal{A}^i - D^i\mathcal{A}^j\right) - \left(D^i\mathcal{A}^j - D^j\mathcal{A}^i\right)D_j\alpha + \alpha\left(D^i\mathcal{Z} - j^i\right)\\
&\quad + 2k_{\mathrm{a}}\alpha\left(B^i\Pi + \epsilon^{ijk}E_k D_j\Psi\right) + \mathcal{L}_\beta E^i\,,\\
\partial_t A_\varphi &= -\mathcal{A}^i D_i\alpha + \alpha\left(KA_\varphi - D_i\mathcal{A}^i - \mathcal{Z}\right) + \mathcal{L}_\beta A_\varphi\,,\\
\partial_t(\Gamma_{\mathrm{e}}\mathcal{U}_i) &= \alpha\left(\frac{q_{\mathrm{e}}}{m_{\mathrm{e}}}E_i + \epsilon_{ijk}\mathcal{U}^j B^k - \Gamma_{\mathrm{e}} a_i - \mathcal{U}^j D_j\left(\Gamma_{\mathrm{e}}\mathcal{U}_i\right)\right) + \mathcal{L}_\beta \Gamma_{\mathrm{e}}\mathcal{U}_i\,,\\
\partial_t \rho_{\mathrm{e}} &= -D_i(\alpha j^i) + \alpha\rho_{\mathrm{e}} K + \mathcal{L}_\beta \rho_{\mathrm{e}}\,,\\
\partial_t \mathcal{Z} &= \alpha\left(D_i E^i + 2k_{\mathrm{a}} B^i D_i \Psi - \rho\right) - \kappa\alpha\mathcal{Z} + \mathcal{L}_\beta \mathcal{Z}\,,
\end{aligned} \tag{I.1.9}$$

where we have introduced a constraint damping variable $\mathcal{Z}$ to stabilize the numerical time evolution. Furthermore, we define D_i as the covariant derivative with respect to γ_{ij}, the extrinsic curvature as $K_{ij} = \frac{1}{2\alpha}\left[-\partial_t\gamma_{ij} + D_i\beta_j + D_j\beta_i\right]$ and K as its trace. Note that the absence of the evolution equations for the ions due to assumption (ii).

Finally, we get the following constraints:

$$\begin{aligned}
D_i B^i &= 0\,,\\
D_i E^i &= \rho - 2k_{\mathrm{a}} B_i D^i \Psi\,,\\
(n^\mu + \mathcal{U}^\mu)\nabla_\mu \Gamma_{\mathrm{e}} &= \Gamma_{\mathrm{e}}\mathcal{U}^i\mathcal{U}^j K_{ij} - \Gamma_{\mathrm{e}}\mathcal{U}^i a_i - \frac{q_{\mathrm{e}}}{m_{\mathrm{e}}}E^i\mathcal{U}_i\,.
\end{aligned} \tag{I.1.10}$$

Upon ignoring the gravitational term in the momentum evolution equation (assumption (v)), this last constraint is trivially satisfied on the linear level.

I.2 Background metric

As discussed in Appendix G.1, we employ Kerr-Schild coordinates in our numerical setup to avoid the coordinate singularity at the horizon. These are related to

Cartesian coordinates by

$$\begin{aligned} x &= r\cos\varphi\sin\theta - a_{\mathrm{J}}\sin\varphi\sin\theta\,, \\ y &= r\sin\varphi\sin\theta + a_{\mathrm{J}}\cos\varphi\sin\theta\,, \\ z &= r\cos\theta\,. \end{aligned} \tag{I.2.11}$$

In these coordinates, the metric takes on the following form:

$$\mathrm{d}s^2 = (\eta_{\mu\nu} + 2Hl_\mu l_\nu)\mathrm{d}x^\mu \mathrm{d}x^\nu\,, \tag{I.2.12}$$

where

$$\begin{aligned} H &= \frac{r^3 M}{r^4 + a_{\mathrm{J}}^2 z^2}\,, \\ l_\mu &= \left(1, \frac{rx + a_{\mathrm{J}}y}{r^2 + a_{\mathrm{J}}^2}, \frac{-a_{\mathrm{J}}x + ry}{r^2 + a_{\mathrm{J}}^2}, \frac{z}{r}\right)\,, \\ r &= \left[\frac{1}{2}\left(x^2 + y^2 + z^2 - a_{\mathrm{J}}^2 + \sqrt{(x^2+y^2+z^2)^2 + 4a_{\mathrm{J}}^2 z^2}\right)\right]^{1/2}\,, \end{aligned} \tag{I.2.13}$$

where we consider Schwarzschild, i.e., $a_{\mathrm{J}} = 0$. Furthermore, we define

$$\begin{aligned} \alpha &= \frac{1}{\sqrt{1+2H}}\,, \\ \beta_i &= 2Hl_i\,, \\ \gamma_{ij} &= \delta_{ij} + 2Hl_i l_j, \\ K_{ij} &= \frac{\partial_i\left(Hl_j\right) + \partial_j\left(Hl_i\right) + 2H(l^*)^k\partial_k\left(Hl_i l_j\right)}{\sqrt{1+2H}}\,, \end{aligned} \tag{I.2.14}$$

which are the lapse function, shift vector, spatial metric, and the extrinsic curvature, respectively.

I.3 Evolution without plasma

Since the simulations *with* and *without* plasma have a slightly different structure, we separate these clearly in the following sections. First, we consider the full set of equations in the absence of plasma. These belong to the simulations $\mathcal{I}_i$ and $\mathcal{J}_i$ from Sections 5.3 and 5.4. They are

$$\begin{aligned} \partial_t\Psi &= -\alpha\Pi + \mathcal{L}_\beta\Psi\,, \\ \partial_t\Pi &= \alpha\left(-D^2\Psi + \mu^2\Psi + K\Pi - 2k_{\mathrm{a}}E^iB_i\right) - D^i\alpha D_i\Psi + \mathcal{L}_\beta\Pi\,, \\ \partial_t\mathcal{A}_i &= -\alpha\left(E_i + D_iA_\varphi\right) - A_\varphi D_i\alpha + \mathcal{L}_\beta\mathcal{A}_i\,, \\ \partial_tE^i &= \alpha KE^i - \alpha D_j\left(D^j\mathcal{A}^i - D^i\mathcal{A}^j\right) - \left(D^i\mathcal{A}^j - D^j\mathcal{A}^i\right)D_j\alpha + \alpha D^i\mathcal{Z} \\ &\quad + 2k_{\mathrm{a}}\alpha\left(B^i\Pi + \epsilon^{ijk}E_kD_j\Psi\right) + \mathcal{L}_\beta E^i\,, \\ \partial_tA_\varphi &= -\mathcal{A}^iD_i\alpha + \alpha\left(KA_\varphi - D_i\mathcal{A}^i - \mathcal{Z}\right) + \mathcal{L}_\beta A_\varphi\,, \\ \partial_t\mathcal{Z} &= \alpha\left(D_iE^i + 2k_{\mathrm{a}}B^iD_i\Psi\right) - \kappa\alpha\mathcal{Z} + \mathcal{L}_\beta\mathcal{Z}\,. \end{aligned} \tag{I.3.15}$$

Note that these are the same as considered in [172, 171].

Initial Data – To construct the initial data for our simulations, we must solve the constraint equations (I.1.10). By doing so on the initial time-slice, the Bianchi identity will ensure they are satisfied throughout the evolution. As explained in Appendix G.1, we use Leaver's method to construct the scalar field bound state. For the electric field, we use initial data analogous to [172, 171]. In particular, we choose a Gaussian profile defined in (5.5).

I.4 Evolution with plasma

In the simulations *with* plasma, we linearize the axion-photon-plasma system due to the complexity of the problem, and we neglect ion perturbations. We express the perturbed quantities with a tilde, such that

$$\begin{aligned} &\mathcal{A}^i = \mathcal{A}^i_{\rm b} + \varepsilon\tilde{\mathcal{A}}_i, \quad E^i = E^i_{\rm b} + \varepsilon\tilde{E}_i, \quad A_\varphi = A_{{\rm b},\varphi} + \varepsilon\tilde{A}_\varphi\,, \\ &\mathcal{U}^i = U^i_{\rm b} + \varepsilon\tilde{\mathcal{U}}_i, \quad \Gamma_{\rm e} = 1\,, \quad \rho = \rho_{\rm b,e} + \rho_{\rm b,ion} + \varepsilon\tilde{\rho}_{\rm e}\,. \end{aligned} \tag{I.4.16}$$

where we denote background quantities with a subscript b and where ε is the arbitrarily small parameter in the perturbation scheme. For simplicity, we consider a quasi-neutral, field-free background plasma, i.e., $E^i_{\rm b} = A^i_{\rm b} = A_{{\rm b},\varphi} = 0$, and $\rho_{\rm b,e} = -\rho_{\rm b,ion}$. The problem at hand naturally introduces two distinct reference frames: the Eulerian observer rest frame and the plasma rest frame. The relative velocity between the two is the background quantity $\mathcal{U}^i$. We consider a plasma co-moving with the Eulerian observer, such that the plasma is static in the spacetime foliation. Since the background field of the electron charge density does not vanish, according to (I.1.9) it should evolve as

$$\partial_t\rho_{\rm b} = \alpha\rho_{\rm b,e}K + \mathcal{L}_\beta\rho_{\rm b,e}\,. \tag{I.4.17}$$

We are mainly interested in the evolution of this variable in a localized region of spacetime far away from the BH, i.e., the axion cloud, and thus the evolution of (I.4.17) due to strong gravity terms is extremely slow compared to the linear system. Therefore, we neglect its evolution similarly to the gravitational influence on the evolution of the background velocity (assumption (v)).

Before proceeding, there is one other subtlety. The plasma response to the perturbing EM field is proportional to the electron charge-to-mass ratio, which is extremely large $q_{\rm e}/m_{\rm e} \approx 10^{22}$. Nevertheless, as we are linearizing the system, and therefore neglecting the backreaction of the EM field onto the axion field, the amplitude of the former is arbitrary in our scheme. If we were to consider the full problem including backreaction instead, the amplitude of the axion field would clearly introduce a scale. Due to this freedom, we rescale the EM variables as

$$\begin{aligned} \bar{E}^i &= \frac{q_{\rm e}}{m_{\rm e}}\tilde{E}^i\,, \\ \bar{A}_i &= \frac{q_{\rm e}}{m_{\rm e}}\tilde{A}_i\,, \\ \bar{\mathcal{Z}} &= \frac{q_{\rm e}}{m_{\rm e}}\mathcal{Z}\,. \end{aligned} \tag{I.4.18}$$

Then, we can write down the full set of equations *including* the plasma as

$$\begin{aligned}
\partial_t\Psi &= -\alpha\Pi + \mathcal{L}_\beta\Psi\,,\\
\partial_t\Pi &= \alpha\left(-D^2\Psi + \mu^2\Psi + K\Pi\right) - D^i\alpha D_i\Psi + \mathcal{L}_\beta\Pi\,,\\
\partial_t\bar{\mathcal{A}}_i &= -\alpha\left(\bar{E}_i + D_i\bar{A}_\varphi\right) - \bar{A}_\varphi D_i\alpha + \mathcal{L}_\beta\bar{\mathcal{A}}_i\,,\\
\partial_t\bar{E}^i &= \alpha K\bar{E}^i - \alpha D_j\left(D^j\bar{\mathcal{A}}^i - D^i\bar{\mathcal{A}}^j\right) - \left(D^i\bar{\mathcal{A}}^j - D^j\bar{\mathcal{A}}^i\right)D_j\alpha + \alpha\left(D^i\bar{\mathcal{Z}} - \omega_{\mathrm{pl}}^2\tilde{\mathcal{U}}^i\right)\\
&\qquad + 2k_{\mathrm{a}}\alpha\left(\bar{B}^i\Pi + \epsilon^{ijk}\bar{E}_k D_j\Psi\right) + \mathcal{L}_\beta\bar{E}^i\,,\\
\partial_t\bar{A}_\varphi &= -\bar{\mathcal{A}}^i D_i\alpha + \alpha(K\bar{\mathcal{A}}_\varphi - D_i\bar{\mathcal{A}}^i - \bar{\mathcal{Z}}) + \mathcal{L}_\beta\bar{A}_\varphi\,,\\
\partial_t\tilde{U}_i &= \alpha\bar{E}_i + \mathcal{L}_\beta\tilde{U}_i\,,\\
\partial_t\tilde{\omega}_{\mathrm{pl}}^2 &= -D_i(\alpha\omega_{\mathrm{pl}}^2\tilde{U}^i) + \alpha\tilde{\omega}_{\mathrm{p}}^2K + \mathcal{L}_\beta\tilde{\omega}_{\mathrm{pl}}^2\,,\\
\partial_t\bar{\mathcal{Z}} &= \alpha\left(D_i\bar{E}^i + 2k_{\mathrm{a}}\bar{B}^iD_i\Psi - \tilde{\omega}_{\mathrm{p}}^2\right) - \kappa\alpha\bar{\mathcal{Z}} + \mathcal{L}_\beta\bar{\mathcal{Z}}\,,
\end{aligned} \tag{I.4.19}$$

where ω_{pl}^2 is the plasma frequency, and $\tilde{\omega}_{\mathrm{pl}}^2$ its perturbation:

$$\begin{aligned}
\omega_{\mathrm{pl}}^2 &= \frac{q_{\mathrm{e}}}{m_{\mathrm{e}}}\rho_{\mathrm{b,e}}\,,\\
\tilde{\omega}_{\mathrm{pl}}^2 &= \frac{q_{\mathrm{e}}}{m_{\mathrm{e}}}\tilde{\rho}_{\mathrm{e}}\,.
\end{aligned} \tag{I.4.20}$$

Note that due to the rescaling, there is no charge-to-mass ratio of the electrons and the field equations are written only in terms of the plasma frequency, which is $\mathcal{O}(1/M)$.

As we detail in the following subsection, including a linearized fluid model in the equations of motion, causes the system (I.4.19) to become ill-posed upon using a damping variable.[1] However, this damping variable is essential in constraining Gauss' law and without it, the simulations diverge for large EM values. As a resolution, we slightly adjust our equations by not including the perturbed plasma frequency, $\tilde{\omega}_{\mathrm{p}}$, in the evolution equation of the damping variable $\mathcal{Z}$, i.e.,

$$\partial_t\bar{\mathcal{Z}} = \alpha\left(D_i\bar{E}^i + 2k_{\mathrm{a}}\bar{B}^iD_i\Psi\right) - \kappa\alpha\bar{\mathcal{Z}} + \mathcal{L}_\beta\bar{\mathcal{Z}}\,. \tag{I.4.21}$$

This is a minimal change as the perturbed plasma frequency does not enter any other evolution equation of the system in the linearized regime, yet it does restore the well-posedness of our setup. We justify this approach in two ways; (i) we evolve the system *with* and *without* the damping variable for large plasma frequencies (where the EM values remain small) and we find excellent agreement between the two, and (ii) for small plasma frequencies, where the EM field is allowed to grow, the effects of the plasma are negligible, and therefore ignoring $\tilde{\omega}_{\mathrm{p}}$ leads to a subleading error compared to the EM values.

Initial Data – For the plasma part, we assume quasi-neutrality (cf. assumption (iii)), i.e., $\rho = -n_\mu(en_{\mathrm{e}}u_{\mathrm{e}}^\mu - Zen_{\mathrm{ion}}u_{\mathrm{ion}}^\mu) = en_{\mathrm{e}} - Zen_{\mathrm{ion}} = 0$. As shown in (I.1.10), the constraint equation for the plasma is trivially satisfied on the linear level, and

---

[1] The ill-posedness originates from the linearization of the fluid equation, whereas the full non-linear system of equations is strongly hyperbolic and thus well-posed [481, 482]

thus the initial data listed in the previous section solves all of our constraints. As for the electronic density, in principle, depending on the specific environment we are interested in, we can assume different spatial profiles [115, 116, 32], which correspond to a space-dependent effective mass for the photon. However, the length-scale of interest to us, i.e., the size of the axion cloud, is typically much shorter than length-scale on which the effective mass varies. Hence, for simplicity, we assume a constant density plasma.

I.5 Hyperbolicity of fluid model

The evolution equations (I.4.19) are not strongly hyperbolic and therefore do not form a well-posed system. Consequently, the existence of a unique solution that depends continuously on the initial data is not guaranteed and any numerical approach is bound to fail. In this appendix, we proof that our system is not strongly hyperbolic.

Based on [483], we introduce an arbitrary unit vector s^i and consider the principal part of the system, i.e., we consider only the highest derivative terms from (I.4.19):

$$\begin{aligned}
\partial_t[\partial_s^2\psi] &\sim -\alpha\partial_s\left(\partial_s\bar{A}_\varphi\right) + \beta^s\partial_s[\partial_t^2\psi]\,,\\
\partial_t(\partial_s\bar{\mathcal{A}}_A) &\sim -\alpha\partial_s\bar{E}_A + \beta^s\partial_s(\partial_s\bar{\mathcal{A}}_A)\,,\\
\partial_t(\partial_s\bar{A}_\varphi) &\sim \beta^s(\partial_s\bar{A}_\varphi) - \alpha\partial_s[\partial_s^2\psi]\,,\\
\partial_t\bar{E}_A &\sim -\alpha\partial_s(\partial_s\bar{\mathcal{A}}_A) + \beta^s\partial_s\bar{E}_A\,,\\
\partial_t\bar{E}_s &\sim \alpha\partial_s\bar{\mathcal{Z}} + \beta^s\partial_s\bar{E}_s\,,\\
\partial_t\bar{\mathcal{Z}} &\sim \alpha\partial_s\bar{E}^s + \beta^s\partial_s\bar{\mathcal{Z}}\,,\\
\partial_t\tilde{U}_s &\sim \beta^s\partial_s\tilde{U}_s\,,\\
\partial_t\tilde{U}_A &\sim \beta^s\partial_s\tilde{U}_A\,,\\
\partial_t\tilde{\omega}_{\rm pl}^2 &\sim -\alpha\omega_{\rm pl}^2\partial_s\tilde{U}_s + \beta^s\partial_s\tilde{\omega}_{\rm pl}^2\,,
\end{aligned} \tag{I.5.22}$$

where the index A denotes the component projected into the surface orthogonal to s^i, and $[\partial_s^2\psi]$ can be written as

$$[\partial_s^2\psi] = \partial_s\bar{\mathcal{A}}_s + \bar{\mathcal{Z}}\,. \tag{I.5.23}$$

Defining the principal symbol of $([\partial_s^2\psi], \bar{A}_\varphi)$ $(\bar{\mathcal{Z}}, E_s)$, $(\partial_s\bar{\mathcal{A}}_A, \bar{E}_A)$, and $(\tilde{U}_s, \tilde{\omega}_{\rm pl}^2)$ as $P_\mathcal{G}$, $P_\mathcal{C}$, $P_\mathcal{P}$, and $P_\mathcal{F}$, respectively, we get:

$$\begin{aligned}
P_\mathcal{G} &= \begin{pmatrix} \beta^s & -\alpha \\ -\alpha & \beta^s \end{pmatrix}, \qquad P_\mathcal{C} = \begin{pmatrix} \beta^s & \alpha \\ \alpha & \beta^s \end{pmatrix},\\
P_\mathcal{P} &= \begin{pmatrix} \beta^s & -\alpha \\ -\alpha & \beta^s \end{pmatrix}, \qquad P_\mathcal{F} = \begin{pmatrix} \beta^s & 0 \\ -\alpha\omega_{\rm pl}^2 & \beta^s \end{pmatrix}.
\end{aligned} \tag{I.5.24}$$

We see that the eigenvalue for $P_\mathcal{F}$ is degenerate with β^s *and* the eigenvector is $(0, b)^T$, where b is an arbitrary value. Therefore, the principal symbol does not have a complete set of eigenvectors, and the system is not strongly hyperbolic. If we ignore $\tilde{\omega}_{\rm pl}^2$ in $\mathcal{Z}$, it becomes decoupled from Maxwell's equations, and the only relevant variable for the fluid part that remains, is the linearized four velocity $\tilde{U}_i$. As is shown in (I.5.22), the principal part for $\tilde{U}_i$ is just canonical the advection term.

I.6 The 3+1 linearized momentum equation

The full computation of the 3+1 split of the momentum equation was already showed in Appendix C. The final form of the equation is (C.1.16). As explained earlier nevertheless, we now simplify the plasma to make it more suitable to our numerical setup. By linearizing this equation, which also implies $\Gamma \sim 1$, we are left with

$$\partial_t \mathcal{U}_i = \alpha \left(\frac{q}{m} E_i - a_i \right) + \mathcal{L}_\beta \mathcal{U}_i \,. \tag{I.6.25}$$

Finally, we also neglect gravity, which brings us to our final equation:

$$\partial_t \mathcal{U}_i = \alpha \frac{q}{m} E_i + \mathcal{L}_\beta \mathcal{U}_i \,. \tag{I.6.26}$$

Appendix J

Numerical convergence and higher multipoles

J.1 Numerical convergence

In our numerical framework, we employ the method-of-lines, where spatial derivatives are approximated by a fourth-order accurate finite-difference scheme and we integrate using a fourth-order Runge-Kutta method. Furthermore, Kreiss-Oliger dissipation is applied to evolved quantities in order to suppress high-frequency modes that come from the boundaries between adjacent refinement regions. The numerical simulations are performed using the open source `Einstein Toolkit` [484, 485]. For the evolution of the scalar and vector field, we extent the `ScalarEvolve` [486, 487, 488] and `ProcaEvolve` thorns [489, 490], respectively. We use `Multipatch` to interpolate between different grids in our numerical domain [491, 492]. In particular, to connect the central Cartesian grid with the spherical wavezone. Additionally, `Carpet` communicates between refinement levels with second-order and fifth-order accuracy in time and space, respectively. The Courant number in all our simulations is 0.2, such that the CFL condition is satisfied. To check whether our numerical results respect the required convergence, we evolve the same configuration with a coarse ($h_{\rm c}$), medium ($h_{\rm m}$) and fine ($h_{\rm f}$) resolution. The convergence factor can then be calculated according to

$$Q_n = \frac{f_{h_{\rm c}} - f_{h_{\rm m}}}{f_{h_{\rm m}} - f_{h_{\rm f}}} = \frac{h_{\rm c}^n - h_{\rm m}^n}{h_{\rm m}^n - h_{\rm f}^n}\,, \tag{J.1.1}$$

where n is the expected convergence order. In our case, we take as the coarsest level $h_{\rm c} = 1.8M$, then $h_{\rm m} = 1.2M$ and $h_{\rm f} = 1.0M$. As can be seen in Fig. J.1, we obtain a convergence order between 3 and 4. We have performed similar tests for the other simulations in this work (*with* or *without* C and *with* or *without* the plasma) and we find similar conclusions.

J.2 Higher multipoles

In the main text, we have shown the dominant contribution coming from the dipole $\ell = m = 1$ mode (cf. Figs. 5.2-5.4). In general however, higher order multipoles

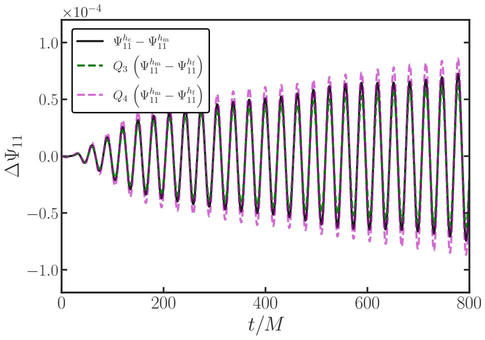

Figure J.1. Convergence analysis of the $\ell = m = 1$ multipole of Ψ, extracted at $r_{\rm ex} = 20M$ for $\mu M = 0.2$ and $C = 10^{-3}$. The green line shows the expected result for third-order convergence ($Q_3 = 5.64$), while the purple line is the expected result for fourth-order convergence ($Q_4 = 7.85$).

are also produced. In Figs. J.2 and J.3, we show a subset of those from the scalar and vector field, respectively. In both figures, we consider simulation $\mathcal{I}_3$, where SR is turned off and we start in the supercritical regime. Three features are worth noting; (i) only axion modes with odd ℓ can be produced from our initial data. An explanation for this selection rule is provided in Appendix L; (ii) the Fourier transform of the vector field shows additional peaks with a frequency slightly lower than $\mu/2$ and two near $3\mu/2$. As discussed in the main text, these should be interpreted as "photon echos" created by outwards traveling photons that interact with the axion cloud; (iii) in Fig. J.2, we observe that some of these up-scattered photons can recombine with "normal" photons ($\omega \sim \mu/2$) to form axion waves with a frequency of twice the boson mass.

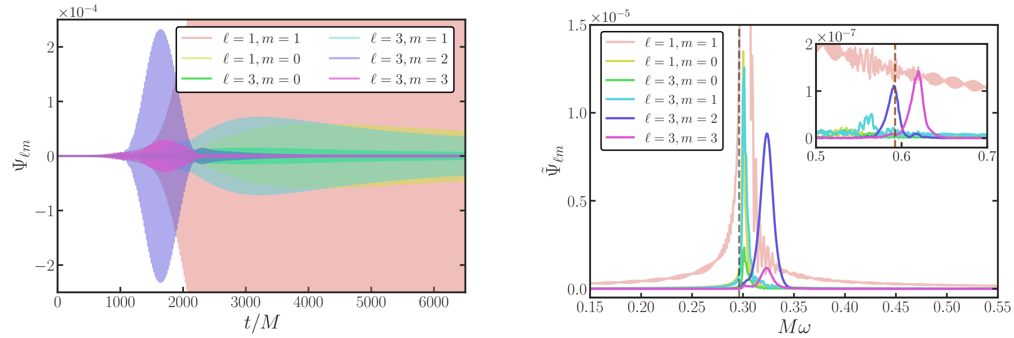

Figure J.2. Top Panel: Time evolution of various multipole modes of the scalar field in the supercritical case (simulation $\mathcal{I}_3$). The field is extracted at $r_{\rm ex} = 400M$ and $\mu M = 0.3$. Interestingly, even ℓ modes are not excited, while odd ℓ modes are, which we explain in Appendix L. **Bottom Panel:** The Fourier transform of the multipole modes shown in the top panel, where the gray dashed line denotes the frequency of the fundamental mode (ω_0). The peaks around $\omega = 2\omega_0$ (brown dashed line) seen in the inset originate from interactions between "up-scattered" photons ($\omega = 3\omega_0/2$) with "normal" photons ($\omega = \omega_0/2$).

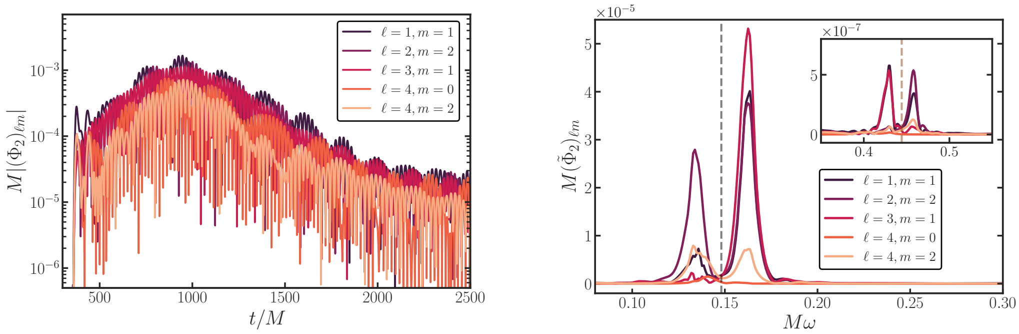

Figure J.3. Top Panel: Time evolution of various multipole modes of the Newman-Penrose scalar $|(\Phi_2)_{\ell m}|$ in the supercritical regime. Considered simulation is $\mathcal{I}_3$. Field is extracted at $r_{\rm ex} = 400M$ and $\mu M = 0.3$. **Bottom Panel:** Fourier transform of the multipole modes shown in the top panel. The gray and brown dashed line indicate the frequencies at $\omega_0/2$ and $3\omega_0/2$, respectively.

Appendix K

Superradiant and Plasma Mathieu equation

K.1 Superradiant Mathieu equation

By solving the superradiant Mathieu equation (5.8) numerically for different values of C, we are able to find a growth rate (5.9) for the EM field in flat spacetime, while assuming a homogeneous axion condensate. Remarkably, this estimate is even accurate in describing the super-exponential growth of the EM field in presence of SR, when considering the full setup on a Schwarzschild background (including the finite-size effects of the cloud with $\lambda_{\rm esc}$). In this appendix, we show a few examples of the numerical solutions to (5.8) and we use a multiple-scale method to derive the growth rate analytically.

Figure K.1 shows various numerical solutions to the superradiant Mathieu equation (5.8). For $C = 0$, the solution is well-described by the standard Mathieu growth rate (red dashed line). For non-zero values of C instead, the standard Mathieu prediction becomes inaccurate and the numerical solutions are well fitted by the super-exponential growth rate (5.9) (black dashed lines).

Multiple-scale analysis – Regular perturbation theory fails to describe some types of problems at late times. This is due to the presence of secular terms, causing non-uniformities to appear between consecutive orders in the perturbation series. An example of this happening is when solving the Mathieu equation, where a multiple-scale analysis is more suitable (see e.g. [493]). In the following, we will show its effectiveness for solving the superradiant Mathieu equation and with that, provide an analytical explanation of the numerically fitted growth rate (5.9).

Let us consider the superradiant Mathieu equation (5.8), where we expand the exponential as

$$\frac{\mathrm{d}^2 y}{\mathrm{d}T^2} + \left(b + 2\delta(1 + CT)\cos T\right) y = 0\,, \tag{K.1.1}$$

and we assume δ to be small. We can introduce two timescales, a *fast* timescale T, and a *slow* one, $\mathcal{T} = \delta T$, which we treat as independent variables. By assuming a dependence on both variables, i.e., $y(T) \to y(T, \mathcal{T})$ and expanding all the parameters, i.e., $y = y_0(T, \mathcal{T}) + \delta y_1(T, \mathcal{T})$ and $b = b_0 + \delta b_1$, we can use the additional freedom from treating $\mathcal{T}$ as a new variable to eliminate secular terms. This causes the solution

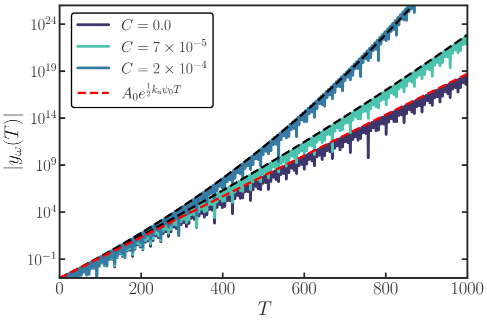

Figure K.1. Numerical solutions to the superradiant Mathieu equation (5.8) for different values of C. Horizontal axis shows the rescaled time $T = \mu t$. Red dashed line shows the "standard" Mathieu growth rate, while black dashed lines are obtained from the analytic growth rate (5.9) and describe the numerical solutions well. Chosen parameters are $\mu = 0.2, p_z = 0.1, k_{\rm a}\psi_0 = 0.1$.

to hold for longer times compared to a "normal" perturbative approach. Assuming the SR term also to be small, i.e., $C = \delta\mathfrak{C}$, we can introduce yet another timescale, the *very slow* one, $\mathfrak{T} = \delta^2 T$. Upon expanding again $b = b_0 + \delta b_1 + \delta^2 b_2$, we obtain

$$\frac{\mathrm{d}^2 y}{\mathrm{d}T^2} + \Big(b + \delta(b_1 + 2\cos T) + \delta^2(b_2 + 2\mathfrak{C}T\cos T)\Big)\, y = 0\,. \tag{K.1.2}$$

In the spirit of the multiple-scale method, we "promote" y to depend on all the timescales as independent variables and then expand, i.e., $y(T, \mathcal{T}, \mathfrak{T}) = y_0(T, \mathcal{T}, \mathfrak{T}) + \delta y_1(T, \mathcal{T}, \mathfrak{T}) + \delta^2 y_2(T, \mathcal{T}, \mathfrak{T})$.

We can now consider (K.1.2) order-by-order. At zeroth order, we have:

$$\partial_T^2 y_0 + b_0 y_0 = 0\,, \tag{K.1.3}$$

where $b_0 = 1/4$ at the inset of the first unstable Mathieu band. Consequently, at this order, we obtain the solution: $y_0 = A(\mathcal{T}, \mathfrak{T})e^{iT/2} + \text{c.c.}$ Hence, the solution at the fast timescale T just describes the harmonic behavior. At first-order, we have

$$\partial_T^2 y_1 + \frac{1}{4} y_1 = -2\partial_T \partial_{\mathcal{T}} y_0 - (b_1 + 2\cos T)\, y_0\,. \tag{K.1.4}$$

The right-hand side of this equation contains secular terms. However, we can use the extra dependence of y_0 on the slow timescale to remove it, namely by requiring $i\partial_{\mathcal{T}} A(\mathcal{T}, \mathfrak{T}) = -b_1 A(\mathcal{T}, \mathfrak{T}) + A^*(\mathcal{T}, \mathfrak{T})$. Solving this leads to the dependence of the zeroth-order solution on the slow timescale, i.e., $y_0 = A(\mathfrak{T})e^{\sqrt{1-b_1^2}\mathcal{T}} e^{iT/2} + \text{c.c.}$ Similarly, the dependence on the very slow timescale can be used to eliminate secular terms in the second-order equation.[1] Following this procedure, we obtain for the zeroth-order solution:

$$y_0 \approx e^{\sqrt{1-b_1^2}\mathcal{T}} e^{iT/2} e^{\mathfrak{C}T\mathfrak{T}} + \text{c.c.} \tag{K.1.5}$$

At sufficiently large times ($T \gg 1/\mathfrak{C}$), the growth rate is thus dominated by $e^{\mathfrak{C}T\mathfrak{T}} = e^{\delta C T^2}$.

---

[1] As these computations become quite cumbersome, we do not report them here.

Finally, by comparing (K.1.1) with (5.8), we identify $\delta = p_z\psi_0 k_\mathrm{a}/\mu^2$ and $p_z = \mu/2$, such that, after rescaling the physical time $t = T/\mu$, the growth rate is $e^{\lambda t}$ with

$$\lambda t = \frac{\mu}{2} k_\mathrm{a}\psi_0 C t^2 \,, \tag{K.1.6}$$

which is the dominant growth rate at late times we found in (5.10) (up to a factor of 2).

The multiple-scale method thus produces a solution with three timescales; (i) the "fast" timescale that corresponds to the harmonic oscillations with a frequency at half the boson mass, (ii) the "slow" timescale belonging to the standard Mathieu growth rate, and (iii) the "very slow" timescale which originates from the super-exponential growth induced by SR and becomes dominant at late times. In conclusion, the Mathieu equation provides us, once again, with a simple analytical explanation to the behavior of the full system.

K.2 Plasma Mathieu equation

In this appendix, we study the axion-photon-plasma system in flat spacetime. This analysis closely follows [199], yet now in the context of a Mathieu-like equation. Furthermore, we generalize their work by including a momentum equation rather than assuming Ohm's law.

The starting point is the equations of motion (5.2) in Minkowski. Similar to Section 5.4.2, we assume the wave vector to be along the $\hat{z}$ direction, i.e., $\vec{p} = (0, 0, p_z)$, the EM ansatz (5.6), and a homogeneous axion condensate defined as

$$\Psi = \frac{1}{2}(\psi_0 e^{-i\mu t} + \psi_0^* e^{i\mu t}) \,. \tag{K.2.7}$$

By linearizing (5.2), one can straightforwardly solve the momentum equation and find the velocity of the electrons with respect to the EM field. Once again, due to their large inertia, we neglect the perturbations of the ions and treat them as a neutralizing background. Since the longitudinal and transverse modes in linear photon-plasma theory in flat spacetime are decoupled, we focus on the latter, obtaining

$$u^k = -\frac{q_\mathrm{e}}{m_\mathrm{e}} \alpha^k e^{i(\vec{p}\cdot\vec{x} - \omega t)} \,, \tag{K.2.8}$$

where $k = \hat{x}, \hat{y}$ are the transverse directions. We can now insert this expression in the current that appears on the right-hand side of Maxwell's equations, i.e., $j^k = q_\mathrm{e} n_\mathrm{e} u_\mathrm{e}^k$, to obtain two decoupled equations for the transverse polarizations, α^k. Finally, by adopting the field redefinition $y_k = e^{i\omega t}\alpha_k$, rescaling the time as $T = \mu t$ and projecting along a circular polarization basis $e_\pm$ such that $y = y_\omega e_\pm$, we find the Mathieu equation in the presence of plasma to be [212]

$$\partial_T^2 y_\omega + \frac{1}{\mu^2}\Big(p_z^2 + \omega_\mathrm{pl}^2 - 2\mu p_z \psi_0 k_\mathrm{a} \sin T\Big) y_\omega = 0 \,. \tag{K.2.9}$$

One can readily see that in the absence of a plasma, i.e., $\omega_\mathrm{pl} = 0$, the vacuum Mathieu equation is recovered [172].

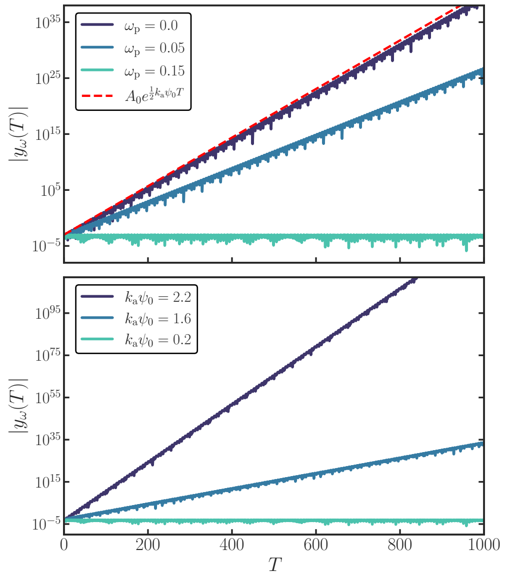

Figure K.2. Top Panel: Solutions of the plasma Mathieu equation (K.2.9) for different values of the plasma frequency. Here, we choose $\mu = 0.2, p_z = 0.1$ and $k_\mathrm{a}\psi_0 = 0.2$. **Bottom Panel:** A similar setup as above, yet now the axionic coupling is varied and $\omega_\mathrm{pl} = 0.15 > \mu/2$. The other parameters are the same as above. As can be seen, for large values of $k_\mathrm{a}\psi_0$ the instability is restored.

The top panel of Fig. K.2 shows numerical solutions to the plasma Mathieu equation (K.2.9) for different values of the plasma frequency. For $\omega_\mathrm{pl} = 0$, the solution develops an instability which is well described by the analytic solution of the vacuum Mathieu equation (red dashed line). By increasing ω_pl, the growth rate of the instability becomes smaller as the interval of the momentum corresponding to the instability shrinks until the solution becomes stable when $\omega_\mathrm{pl} \geq \mu/2$. We find good agreement with the instability interval predicted in equation (19) from [199], by exploring a wide region of the parameter space. Interestingly, even when $\omega_\mathrm{pl} \geq \mu/2$, the instability band can be widened by increasing the value of $k_\mathrm{a}\psi_0$, making it possible to restore the instability even for dense plasmas. This effect can be seen in the bottom panel of Fig. K.2. By fixing $\omega_\mathrm{pl} = 0.15$ (with $\mu = 0.2$), the instability is restored for large enough values of $k_\mathrm{a}\psi_0$.

Band analysis – In [199], the maximum growth rate in the low axionic coupling regime is found where the condition $p_z^2 + \omega_\mathrm{pl}^2 = \mu^2/4$ holds. While in [199], this result does not have an immediate interpretation, our redefinition of the system in terms of the Mathieu equation provides a simple explanation to this condition; from (K.2.9), it follows immediately that the instability bands are located where

$$p_z^2 + \omega_\mathrm{pl}^2 = n^2 \, \frac{\mu^2}{4} \quad \text{with} \quad n \in \mathbb{N} \, . \tag{K.2.10}$$

Therefore, the maximum growth rate of [199] can be interpreted as the first, dominant instability band, i.e., where $n = 1$. Note that, as long as the axionic coupling is sufficiently low, the dispersion relation of the photon is not modified by the condensate, and thus $\omega^2 \approx p_z^2 + \omega_\mathrm{pl}^2$, with ω the frequency of the photon. Therefore,

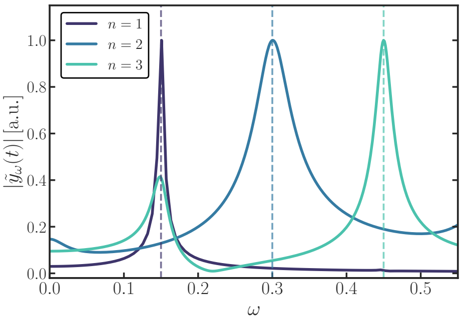

Figure K.3. The Fourier transforms of three numerical solutions to the plasma Mathieu equation (K.2.9) with $\mu = 0.3$ and $p_z = 0.15$. The peaks have been arbitrarily normalized and we revert $t = \mu^{-1}T$ for the Fourier transform. The considered parameters for the plasma frequency and the axionic coupling for $n = 1, 2, 3$ are $\omega_{\rm pl} = 0, 0.2, 0.43$ and $k_{\rm a}\psi_0 = 0.02, 2, 2.8$, respectively. The dashed lines indicate $n\mu/2$ and show that each of the solutions lies in a different instability band.

similar to the vacuum case, the instability bands correspond to frequencies which are multiples of $\mu/2$.

For large enough $\omega_{\rm pl}$, i.e., when $\omega_{\rm pl} \geq \mu/2$, the condition (K.2.10) can never be satisfied for $n = 1$. However, crucially, it can still be satisfied for $n > 1$, which corresponds to exciting higher bands and thus restoring the instability.[2] In Fig. K.3, we show that this is indeed the case by numerically solving (K.2.9) and taking the Fourier transform. The dark-blue line which peaks at $\mu/2$, has $\omega_{\rm pl} = 0$ and a moderate value of $k_{\rm a}\psi_0 = 0.02$, and thus behaves according to the parametric mechanism by triggering the first band. When we consider a higher plasma frequency, $\omega_{\rm pl} = 0.2 > \mu/2$, it is not possible to excite the first instability band anymore. However, as we increase the axionic coupling to $k_{\rm a}\psi_0 = 2$, the instability is restored in the second band with a frequency μ (blue line). We can continue for even higher plasma frequencies, e.g. $\omega_{\rm pl} = 0.43$, which for an axionic coupling of $k_{\rm a}\psi_0 = 2.8$, triggers the third instability band at $\omega = 3/2\mu$ (turquoise line). Note that the chosen values of $\omega_{\rm pl}$ in the three solutions approximately satisfy (K.2.10) for $n = 1, 2$ and 3.

---

[2] Higher bands of the Mathieu equation are narrower than the first one, making the available parameter space for an instability smaller. However, since these bands widen for large values of the axionic coupling $k_{\rm a}\psi_0$, even for $n > 1$ an efficient instability can be triggered.

Appendix L

Selection rules

Using spherical harmonics, the equations of motion can be decomposed, and, as we will show, allows us to predict which modes are excited from the axionic coupling. This approach yields a consistency check of our simulations in the case where SR growth is absent. Using the electric field E_i and the magnetic field B_i, the Maxwell equations can be written as

$$\begin{aligned}\partial_t E^i &= \alpha K E^i + \beta^j \partial_j E^i - E^j \partial_j \beta^i - \epsilon^{ijk} D_j(\alpha B_k) \\ &\quad + 2k_{\mathrm{a}}\alpha \left(\epsilon^{ijk} E_k D_j \Psi + B^i n^\alpha \partial_\alpha \Psi\right) , \\ \partial_t B^i &= \beta^j \partial_j B^i - B^j \partial_j \beta^i + \alpha K B^i + \epsilon^{ijk} D_j(\alpha E_k) ,\end{aligned} \tag{L.0.1}$$

where $\epsilon^{ijk} = -\frac{1}{\sqrt{\gamma}} E^{ijk}$ and E^{ijk} is the totally anti-symmetric tensor with $E^{123} = 1$. We focus on a Schwarzschild BH which has the following metric:

$$\mathrm{d}s^2 = -f(r)\mathrm{d}t^2 + \frac{1}{f(r)}(r)\mathrm{d}r^2 + r^2 \hat{\gamma}_{AB}\mathrm{d}x^A \mathrm{d}x^B , \tag{L.0.2}$$

where $f(r) = 1 - \frac{2M}{r}$, and $\hat{\gamma}_{AB}\mathrm{d}x^A\mathrm{d}x^B = \mathrm{d}\theta^2 + \sin^2\theta \mathrm{d}\varphi^2$. From the spacetime symmetry, the electric and magnetic field can be decomposed using the scalar spherical harmonics $Y_{\ell m}(\theta, \varphi)$ and the vector spherical harmonics $\hat{\nabla}_A Y_{\ell m}$ and $V_{\ell m,A} = \hat{\epsilon}_A^B \hat{\nabla}_B Y_{\ell m}$. Here, $\hat{\epsilon}_{AB}$ is the anti-symmetric tensor with $\hat{\epsilon}_{\theta\varphi} = \sin\theta$. Using these harmonics functions, we expand the electric, magnetic and scalar field as follows:

$$\begin{aligned} E_r &= \sum_{\ell m} \mathcal{E}_{\ell m,r} Y_{\ell m} + \text{c.c.} , \\ E_A &= \sum_{\ell m} \left\{ \mathcal{E}_{\ell m,S} \frac{\hat{\nabla}_A Y_{\ell m}}{\sqrt{\ell(\ell+1)}} + \mathcal{E}_{\ell m,V} V_{\ell m,A} + \text{c.c.} \right\} , \\ B_r &= \sum_{\ell m} \mathcal{B}_{\ell m,r} Y_{\ell m} + \text{c.c.} , \\ B_A &= \sum_{\ell m} \left\{ \mathcal{B}_{\ell m,S} \frac{\hat{\nabla}_A Y_{\ell m}}{\sqrt{\ell(\ell+1)}} + \mathcal{B}_{\ell m,V} V_{\ell m,A} + \text{c.c.} \right\} , \\ \Psi &= \sum_{\ell m} \Psi_{\ell m} Y_{\ell m} + \text{c.c.} , \end{aligned} \tag{L.0.3}$$

where $A = \{\theta, \varphi\}$ and $\mathcal{E}_{\ell m,r}$, $\mathcal{E}_{\ell m,S}$, $\mathcal{E}_{\ell m,V}$, $\mathcal{B}_{\ell m,r}$, $\mathcal{B}_{\ell m,S}$, $\mathcal{B}_{\ell m,V}$, and $\Psi_{\ell m}$ are all coefficients that depend on t and r only. Time or space derivatives are denoted with a dot or prime, respectively. Since both the scalar and vector spherical harmonics are orthogonal functions, the Maxwell equations with axionic coupling can be decomposed. We find the coefficients for the electric field to be:

$$\begin{aligned}
\dot{\mathcal{E}}_{\ell m,r} &= -\frac{\ell(\ell+1)}{r^2}\mathcal{B}_{\ell m,V} - \frac{2k_{\mathrm{a}}}{\sqrt{f}r^2}\sum_{\substack{\ell' m'\\ \ell'' m''}}\sum_{I=1}^{4} C^{(r,I)}_{\ell m\ell' m'\ell'' m''}X_{(I),\ell m\ell' m'\ell'' m''}\,,\\
\dot{\mathcal{E}}_{\ell m,S} &= -\frac{\sqrt{\ell(\ell+1)}}{2}(f'\mathcal{B}_{\ell m,V} + 2f\mathcal{B}'_{\ell m,V}) - 2k_{\mathrm{a}}\sqrt{\ell(\ell+1)}\sum_{\substack{\ell' m'\\ \ell'' m''}}\sum_{I=1}^{4} C^{(S,I)}_{\ell m\ell' m'\ell'' m''}X_{(I),\ell m\ell' m'\ell'' m''}\,,\\
\dot{\mathcal{E}}_{\ell m,V} &= -f\mathcal{B}_{\ell m,r} + \frac{f'\mathcal{B}_{\ell m,S} + 2f\mathcal{B}'_{\ell m,S}}{2\sqrt{\ell(\ell+1)}} - 2k_{\mathrm{a}} \times \sum_{\substack{\ell' m'\\ \ell'' m''}}\sum_{I=1}^{4} C^{(V,I)}_{\ell m\ell' m'\ell'' m''}X_{(I),\ell m\ell' m'\ell'' m''}\,.
\end{aligned} \tag{L.0.4}$$

Then, we proceed with the coefficients for the magnetic field:

$$\begin{aligned}
\dot{\mathcal{B}}_{\ell m,r} &= \frac{\ell(\ell+1)}{r^2}\mathcal{E}_{\ell m,V}\,,\\
\dot{\mathcal{B}}_{\ell m,S} &= \frac{\sqrt{\ell(\ell+1)}}{2}\left(f'\mathcal{E}_{\ell m,V} + 2f\mathcal{E}'_{\ell m,V}\right)\,,\\
\dot{\mathcal{B}}_{\ell m,V} &= f\mathcal{E}_{\ell m,r} - \frac{f'\mathcal{E}_{\ell m,S} + 2f\mathcal{E}'_{\ell m,S}}{2\sqrt{\ell(\ell+1)}}\,,
\end{aligned} \tag{L.0.5}$$

and finally the coefficients for the scalar field:

$$\begin{aligned}
\ddot{\Psi}_{\ell m} &= -f\left(\frac{2}{r} + f'\right)\Psi'_{\ell m}\\
&\quad - f^2\Psi''_{\ell m} + f\left(\frac{\ell(\ell+1)}{r^2} + \mu^2\right)\Psi_{\ell m} - 2k_{\mathrm{a}}f\\
&\quad \times \sum_{\substack{\ell' m'\\ \ell'' m''}}\sum_{I=1}^{4} C^{(\Psi,I)}_{\ell m\ell' m'\ell'' m''}X_{(I),\ell m\ell' m'\ell'' m''}\,,
\end{aligned} \tag{L.0.6}$$

where $X_{(I),\ell m\ell' m'\ell'' m''}$ is found by

$$\begin{aligned}
X_{(1),\ell m\ell' m'\ell'' m''} &= \int \mathrm{d}^2\Omega Y^*_{\ell m}Y_{\ell'' m''}Y_{\ell' m'}\,,\\
X_{(2),\ell m\ell' m'\ell'' m''} &= \int \mathrm{d}^2\Omega Y^*_{\ell m}Y^*_{\ell'' m''}Y_{\ell' m'}\,,\\
X_{(3),\ell m\ell' m'\ell'' m''} &= \int \mathrm{d}^2\Omega Y^*_{\ell m}\hat{\nabla}^A Y_{\ell'' m''}V_{\ell' m',A}\,,\\
X_{(4),\ell m\ell' m'\ell'' m''} &= \int \mathrm{d}^2\Omega Y^*_{\ell m}\hat{\nabla}^A Y^*_{\ell'' m''}V_{\ell' m',A}\,.
\end{aligned} \tag{L.0.7}$$

Upon defining the prefactor

$$Q_{\ell\ell'\ell''} = \frac{\ell(\ell+1) + \ell'(\ell'+1) - \ell''(\ell''+1)}{2}\,, \tag{L.0.8}$$

we find for $C^{(r,I)}$:

$$\begin{aligned}
C^{(r,1)}_{\ell m\ell' m'\ell'' m''} &= Q_{\ell''\ell'\ell}\mathcal{E}_{\ell'' m'',V}\Psi_{\ell' m'} - r^2\mathcal{B}_{\ell'' m'',r}\dot{\Psi}_{\ell' m'}\ , \\
C^{(r,2)}_{\ell m\ell' m'\ell'' m''} &= Q_{\ell''\ell'\ell}\mathcal{E}^*_{\ell'' m'',V}\Psi_{\ell' m'} - r^2\mathcal{B}^*_{\ell'' m'',r}\dot{\Psi}_{\ell' m'}\ , \\
C^{(r,3)}_{\ell m\ell' m'\ell'' m''} &= \frac{\mathcal{E}_{\ell'' m'',S}\Psi_{\ell' m'}}{\sqrt{\ell''(\ell''+1)}}\ , \\
C^{(r,4)}_{\ell m\ell' m'\ell'' m''} &= \frac{\mathcal{E}^*_{\ell'' m'',S}\Psi_{\ell' m'}}{\sqrt{\ell''(\ell''+1)}}\ ,
\end{aligned} \tag{L.0.9}$$

for $C^{(S,I)}$:

$$\begin{aligned}
C^{(S,1)}_{\ell m\ell' m'\ell'' m''} &= -Q_{\ell''\ell\ell'}\left(f\mathcal{E}_{\ell'' m'',V}\Psi'_{\ell' m'} + \frac{\mathcal{B}_{\ell'' m'',S}\dot{\Psi}_{\ell' m'}}{\sqrt{\ell''(\ell''+1)}}\right), \\
C^{(S,2)}_{\ell m\ell' m'\ell'' m''} &= -Q_{\ell''\ell\ell'}\left(f\mathcal{E}^*_{\ell'' m'',V}\Psi'_{\ell' m'} + \frac{\mathcal{B}^*_{\ell'' m'',S}\dot{\Psi}_{\ell' m'}}{\sqrt{\ell''(\ell''+1)}}\right), \\
C^{(S,3)}_{\ell m\ell' m'\ell'' m''} &= f\mathcal{E}_{\ell'' m'',r}\Psi_{\ell' m'} - \frac{f}{\sqrt{\ell''(\ell''+1)}} \\
&\quad \times \mathcal{E}_{\ell'' m'',S}\Psi'_{\ell' m'} + \mathcal{B}_{\ell'' m'',V}\dot{\Psi}_{\ell' m'}\ , \\
C^{(S,4)}_{\ell m\ell' m'\ell'' m''} &= f\mathcal{E}^*_{\ell'' m'' m,r}\Psi_{\ell' m'} - \frac{f}{\sqrt{\ell''(\ell''+1)}} \\
&\quad \times \mathcal{E}^*_{\ell'' m'',S}\Psi'_{\ell' m'} + \mathcal{B}^*_{\ell'' m'',V}\dot{\Psi}_{\ell' m'}\ ,
\end{aligned} \tag{L.0.10}$$

for $C^{(V,I)}$:

$$\begin{aligned}
C^{(V,1)}_{\ell m\ell' m'\ell'' m''} &= -Q_{\ell'\ell\ell''}f\mathcal{E}_{\ell'' m'',r}\Psi_{\ell' m'} + Q_{\ell''\ell\ell'}\left(\frac{f}{\sqrt{\ell''(\ell''+1)}}\mathcal{E}_{\ell'' m'',S}\Psi'_{\ell' m'} - \mathcal{B}_{\ell'' m'',V}\dot{\Psi}_{\ell' m'}\right), \\
C^{(V,2)}_{\ell m\ell' m'\ell'' m''} &= -Q_{\ell'\ell\ell''}f\mathcal{E}^*_{\ell'' m'',r}\Psi_{\ell' m'} + Q_{\ell''\ell\ell'}\left(\frac{f}{\sqrt{\ell''(\ell''+1)}}\mathcal{E}_{\ell'' m'',S}\Psi'_{\ell' m'} - \mathcal{B}_{\ell'' m''}\dot{\Psi}_{\ell' m'}\right), \\
C^{(V,3)}_{\ell m\ell' m'\ell'' m''} &= -\left(f\mathcal{E}_{\ell'' m'',V}\Psi'_{\ell' m'} + \frac{\mathcal{B}_{\ell'' m'',S}\dot{\Psi}_{\ell' m'}}{\sqrt{\ell''(\ell''+1)}}\right), \\
C^{(V,4)}_{\ell m\ell' m'\ell'' m''} &= -\left(f\mathcal{E}^*_{\ell'' m'',V}\Psi'_{\ell' m'} + \frac{\mathcal{B}^*_{\ell'' m'',S}\dot{\Psi}_{\ell' m'}}{\sqrt{\ell''(\ell''+1)}}\right),
\end{aligned} \tag{L.0.11}$$

and finally for $C^{(\Psi,I)}$:

$$\begin{aligned}
C^{(\Psi,1)}_{\ell m\ell' m'\ell'' m''} &= f\mathcal{E}_{\ell' m',r}\mathcal{B}_{\ell'' m'',r} + \frac{Q_{\ell''\ell'\ell}}{r^2}\left(\frac{\mathcal{E}_{\ell' m',S}\mathcal{B}_{\ell'' m'' S,}}{\sqrt{\ell'\ell''(\ell'+1)(\ell''+1)}} + \mathcal{E}_{\ell' m',V}\mathcal{B}_{\ell'' m'',V}\right), \\
C^{(\Psi,2)}_{\ell m\ell' m'\ell'' m''} &= f\mathcal{E}_{\ell' m',r}\mathcal{B}^*_{\ell'' m'',r}\frac{Q_{\ell''\ell'\ell}}{r^2}\left(\frac{\mathcal{E}_{\ell' m' S}\mathcal{B}^*_{\ell'' m'',S}}{\sqrt{\ell'\ell''(\ell'+1)(\ell''+1)}} + \mathcal{E}_{\ell' m',V}\mathcal{B}^*_{\ell'' m'',V}\right), \\
C^{(\Psi,3)}_{\ell m\ell' m'\ell'' m''} &= \frac{1}{r^2}\left(\mathcal{E}_{\ell' m',V}\frac{\mathcal{B}_{\ell'' m'',S}}{\sqrt{\ell''(\ell''+1)}} \qquad + \frac{\mathcal{E}_{\ell' m' S}}{\sqrt{\ell'(\ell'+1)}}\mathcal{B}_{\ell'' m'' V}\right), \\
C^{(\Psi,4)}_{\ell m\ell' m'\ell'' m''} &= \frac{1}{r^2}\left(\mathcal{E}_{\ell' m',V}\frac{\mathcal{B}^*_{\ell'' m'',S}}{r^2\sqrt{\ell''(\ell''+1)}} \qquad + \frac{\mathcal{E}_{\ell' m' S}}{\sqrt{\ell'(\ell'+1)}}\mathcal{B}^*_{\ell' m' V}\right).
\end{aligned} \tag{L.0.12}$$

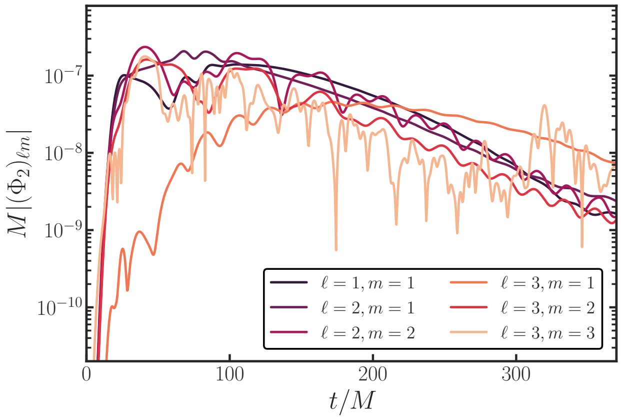

Figure L.1. The time evolution of various multipole modes of the Newman-Penrose scalar Φ_2 in the subcritical regime. The considered simulation is $\mathcal{I}_2$, where the field is extracted at $r_{\rm ex} = 20M$ and $\mu M = 0.3$. Each of the curves has been rescaled according to the order found in (L.0.15).

In our simulations, we monitor the Newman-Penrose variable Φ_2, and the coefficient for spin-weighted spherical harmonics is

$$(\Phi_2)_{\ell m} = \frac{\sqrt{\ell(\ell+1)}}{2r}\left\{-\left(\mathcal{B}_{\ell m,V} + \frac{\mathcal{E}_{\ell m,S}}{\sqrt{\ell(\ell+1)}}\right) + i\left(-\mathcal{E}_{\ell m,V} + \frac{\mathcal{B}_{\ell m,S}}{\sqrt{\ell(\ell+1)}}\right)\right\}\,. \tag{L.0.13}$$

The non-vanishing components of our initial data (see Appendix I.3) are

$$\begin{aligned} \Psi_{1,\pm 1} &\sim \Psi_0\,, \\ \mathcal{E}_{10,V}(t=0,r) &= \frac{1}{2}\sqrt{\frac{\pi}{3}}E^{\varphi}(r)\,, \end{aligned} \tag{L.0.14}$$

where $E^{\varphi}(r)$ is defined in (5.5). Since this is a perturbative approach, we focus on the subcritical regime and assume $E^{\varphi}(r)$ is order $\mathcal{O}(\epsilon)$. Using the above equations, we can obtain the order of each mode of $(\Phi_2)_{\ell m}$ as

$$\begin{aligned} (\Phi_2)_{1,0} &\sim \mathcal{O}(\epsilon)\,, \\ (\Phi_2)_{1,\pm 1} &\sim \mathcal{O}(k_{\rm a}\Psi_0\epsilon)\,, \\ (\Phi_2)_{2,\pm 1} &\sim \mathcal{O}(k_{\rm a}\Psi_0\epsilon)\,, \\ (\Phi_2)_{2,\pm 2} &\sim \mathcal{O}((k_{\rm a}\Psi_0)^2\epsilon)\,, \\ (\Phi_2)_{3,\pm 3} &\sim \mathcal{O}((k_{\rm a}\Psi_0)^3\epsilon)\,. \end{aligned} \tag{L.0.15}$$

In Fig. L.1, we show $|(\Phi_2)_{\ell m}|$ in the subcritical regime ($\mathcal{I}_2$), and rescale all multipoles according to (L.0.15). As can be seen, using the rescaling, all curves are on the same order, demonstrating that our simulations show consistent behaviour.

As alluded to in Section 5.3, from our initial data only odd ℓ scalar multipoles can be produced. We can now proof this. From $Y_{\ell m}(\pi-\theta,\varphi+\pi) = (-1)^{\ell}Y_{\ell m}(\theta,\varphi)$, we find that $X_{(1),\ell m\ell' m'\ell'' m''}$ and $X_{(2),\ell m\ell' m'\ell'' m''}$ are non-zero when $\ell+\ell'+\ell''$ is an *even* number, and $X_{(3),\ell m\ell' m'\ell'' m''}$ and $X_{(4),\ell m\ell' m'\ell'' m''}$ are non-zero when $\ell + \ell' + \ell''$ is *odd* number.

Then, equations (L.0.9)-(L.0.11) show that the non-vanishing modes of our initial data, $\Psi_{\ell m}$ and $\mathcal{E}_{\ell m,V}$ (see (L.0.14)) with odd ℓ can *only* excite $\mathcal{E}_{\ell m,r}$ and $\mathcal{E}_{\ell m,S}$ with even ℓ, while it excites $\mathcal{E}_{\ell m,V}$ with odd ℓ.

Next, (L.0.5) implies that the non-vanishing component of $\mathcal{E}_{\ell m,r}$ and $\mathcal{E}_{\ell m,S}$ with even ℓ excites $\mathcal{B}_{\ell m,V}$ with even ℓ, while the non-vanishing component of $\mathcal{E}_{\ell m,V}$ with odd ℓ excites $\mathcal{B}_{\ell m,r}$ and $\mathcal{B}_{\ell m,S}$ with odd ℓ.

Finally, (L.0.12) shows that the non-vanishing component of $\mathcal{E}_{\ell m,r}$, $\mathcal{E}_{\ell m,S}$ and $\mathcal{B}_{\ell m,V}$ with even ℓ, and $\mathcal{E}_{\ell m,V}$, $\mathcal{B}_{\ell m,r}$ and $\mathcal{B}_{\ell m,S}$ with odd ℓ *only* excites $\Psi_{\ell m}$ with odd ℓ. Therefore, the non-vanishing components of the simulation starting from initial data (L.0.14), only excite $\Psi_{\ell m}$ with odd ℓ. These results are consistent with our simulations, see Fig. J.2.

Bibliography

[1] G. Bertone, D. Hooper, and J. Silk, “Particle dark matter: Evidence, candidates and constraints,” *Phys. Rept.* **405** (2005) 279–390, `arXiv:hep-ph/0404175`.

[2] K. G. Begeman, A. H. Broeils, and R. H. Sanders, “Extended rotation curves of spiral galaxies : dark haloes and modified dynamics.,” MNRAS **249** (Apr., 1991) 523.

[3] V. C. Rubin and J. Ford, W. Kent, “Rotation of the Andromeda Nebula from a Spectroscopic Survey of Emission Regions,” ApJ **159** (Feb., 1970) 379.

[4] E. Corbelli and P. Salucci, “The Extended Rotation Curve and the Dark Matter Halo of M33,” *Mon. Not. Roy. Astron. Soc.* **311** (2000) 441–447, `arXiv:astro-ph/9909252`.

[5] D. Clowe, M. Bradac, A. H. Gonzalez, M. Markevitch, S. W. Randall, C. Jones, and D. Zaritsky, “A direct empirical proof of the existence of dark matter,” *Astrophys. J. Lett.* **648** (2006) L109–L113, `arXiv:astro-ph/0608407`.

[6] R. Massey, T. Kitching, and J. Richard, “The dark matter of gravitational lensing,” *Rept. Prog. Phys.* **73** (2010) 086901, `arXiv:1001.1739 [astro-ph.CO]`.

[7] Planck Collaboration, N. Aghanim, Y. Akrami, M. Ashdown, J. Aumont, C. Baccigalupi, M. Ballardini, A. J. Banday, R. B. Barreiro, N. Bartolo, S. Basak, R. Battye, K. Benabed, J. P. Bernard, M. Bersanelli, P. Bielewicz, J. J. Bock, J. R. Bond, J. Borrill, F. R. Bouchet, F. Boulanger, M. Bucher, C. Burigana, R. C. Butler, E. Calabrese, J. F. Cardoso, J. Carron, A. Challinor, H. C. Chiang, J. Chluba, L. P. L. Colombo, C. Combet, D. Contreras, B. P. Crill, F. Cuttaia, P. de Bernardis, G. de Zotti, J. Delabrouille, J. M. Delouis, E. Di Valentino, J. M. Diego, O. Doré, M. Douspis, A. Ducout, X. Dupac, S. Dusini, G. Efstathiou, F. Elsner, T. A. Enßlin, H. K. Eriksen, Y. Fantaye, M. Farhang, J. Fergusson, R. Fernandez-Cobos, F. Finelli, F. Forastieri, M. Frailis, A. A. Fraisse, E. Franceschi, A. Frolov, S. Galeotta, S. Galli, K. Ganga, R. T. Génova-Santos, M. Gerbino, T. Ghosh, J. González-Nuevo, K. M. Górski, S. Gratton, A. Gruppuso, J. E. Gudmundsson, J. Hamann, W. Handley, F. K. Hansen, D. Herranz, S. R. Hildebrandt, E. Hivon, Z. Huang, A. H. Jaffe,

W. C. Jones, A. Karakci, E. Keihänen, R. Keskitalo, K. Kiiveri, J. Kim, T. S. Kisner, L. Knox, N. Krachmalnicoff, M. Kunz, H. Kurki-Suonio, G. Lagache, J. M. Lamarre, A. Lasenby, M. Lattanzi, C. R. Lawrence, M. Le Jeune, P. Lemos, J. Lesgourgues, F. Levrier, A. Lewis, M. Liguori, P. B. Lilje, M. Lilley, V. Lindholm, M. López-Caniego, P. M. Lubin, Y. Z. Ma, J. F. Macías-Pérez, G. Maggio, D. Maino, N. Mandolesi, A. Mangilli, A. Marcos-Caballero, M. Maris, P. G. Martin, M. Martinelli, E. Martínez-González, S. Matarrese, N. Mauri, J. D. McEwen, P. R. Meinhold, A. Melchiorri, A. Mennella, M. Migliaccio, M. Millea, S. Mitra, M. A. Miville-Deschênes, D. Molinari, L. Montier, G. Morgante, A. Moss, P. Natoli, H. U. Nørgaard-Nielsen, L. Pagano, D. Paoletti, B. Partridge, G. Patanchon, H. V. Peiris, F. Perrotta, V. Pettorino, F. Piacentini, L. Polastri, G. Polenta, J. L. Puget, J. P. Rachen, M. Reinecke, M. Remazeilles, A. Renzi, G. Rocha, C. Rosset, G. Roudier, J. A. Rubiño-Martín, B. Ruiz-Granados, L. Salvati, M. Sandri, M. Savelainen, D. Scott, E. P. S. Shellard, C. Sirignano, G. Sirri, L. D. Spencer, R. Sunyaev, A. S. Suur-Uski, J. A. Tauber, D. Tavagnacco, M. Tenti, L. Toffolatti, M. Tomasi, T. Trombetti, L. Valenziano, J. Valiviita, B. Van Tent, L. Vibert, P. Vielva, F. Villa, N. Vittorio, B. D. Wandelt, I. K. Wehus, M. White, S. D. M. White, A. Zacchei, and A. Zonca, "Planck 2018 results. VI. Cosmological parameters," A&A **641** (Sept., 2020) A6, `arXiv:1807.06209 [astro-ph.CO]`.

[8] **Supernova Search Team** Collaboration, A. G. Riess *et al.*, "Observational evidence from supernovae for an accelerating universe and a cosmological constant," *Astron. J.* **116** (1998) 1009–1038, `arXiv:astro-ph/9805201`.

[9] K. Hinterbichler and J. Khoury, "Symmetron Fields: Screening Long-Range Forces Through Local Symmetry Restoration," *Phys. Rev. Lett.* **104** (2010) 231301, `arXiv:1001.4525 [hep-th]`.

[10] J. Khoury and A. Weltman, "Chameleon fields: Awaiting surprises for tests of gravity in space," *Phys. Rev. Lett.* **93** (2004) 171104, `arXiv:astro-ph/0309300`.

[11] G. Raffelt, *Stars as laboratories for fundamental physics: The astrophysics of neutrinos, axions, and other weakly interacting particles.* 5, 1996.

[12] M. Baryakhtar *et al.*, "Dark Matter In Extreme Astrophysical Environments," in *Snowmass 2021.* 3, 2022. `arXiv:2203.07984 [hep-ph]`.

[13] **LIGO Scientific, Virgo** Collaboration, B. P. Abbott *et al.*, "Observation of Gravitational Waves from a Binary Black Hole Merger," *Phys. Rev. Lett.* **116** no. 6, (2016) 061102, `arXiv:1602.03837 [gr-qc]`.

[14] **LIGO Scientific, Virgo** Collaboration, B. P. Abbott *et al.*, "Tests of general relativity with GW150914," *Phys. Rev. Lett.* **116** no. 22, (2016) 221101, `arXiv:1602.03841 [gr-qc]`. [Erratum: Phys.Rev.Lett. 121, 129902 (2018)].

[15] **LIGO Scientific, Virgo** Collaboration, R. Abbott *et al.*, "Tests of general relativity with binary black holes from the second LIGO-Virgo

gravitational-wave transient catalog," *Phys. Rev. D* **103** no. 12, (2021) 122002, `arXiv:2010.14529 [gr-qc]`.

[16] **LIGO Scientific, VIRGO, KAGRA** Collaboration, R. Abbott *et al.*, "Tests of General Relativity with GWTC-3," `arXiv:2112.06861 [gr-qc]`.

[17] E. Berti *et al.*, "Testing General Relativity with Present and Future Astrophysical Observations," *Class. Quant. Grav.* **32** (2015) 243001, `arXiv:1501.07274 [gr-qc]`.

[18] N. Yunes, K. Yagi, and F. Pretorius, "Theoretical Physics Implications of the Binary Black-Hole Mergers GW150914 and GW151226," *Phys. Rev. D* **94** no. 8, (2016) 084002, `arXiv:1603.08955 [gr-qc]`.

[19] R. D. Peccei and H. R. Quinn, "CP conservation in the presence of pseudoparticles," *Phys. Rev. Lett.* **38** (Jun, 1977) 1440–1443. `https://link.aps.org/doi/10.1103/PhysRevLett.38.1440`.

[20] S. Weinberg, "A new light boson?," *Phys. Rev. Lett.* **40** (Jan, 1978) 223–226. `https://link.aps.org/doi/10.1103/PhysRevLett.40.223`.

[21] M. Fairbairn, R. Hogan, and D. J. E. Marsh, "Unifying inflation and dark matter with the Peccei-Quinn field: observable axions and observable tensors," *Phys. Rev. D* **91** no. 2, (2015) 023509, `arXiv:1410.1752 [hep-ph]`.

[22] D. J. E. Marsh, D. Grin, R. Hlozek, and P. G. Ferreira, "Tensor Interpretation of BICEP2 Results Severely Constrains Axion Dark Matter," *Phys. Rev. Lett.* **113** no. 1, (2014) 011801, `arXiv:1403.4216 [astro-ph.CO]`.

[23] D. J. E. Marsh, "Axion Cosmology," *Phys. Rept.* **643** (2016) 1–79, `arXiv:1510.07633 [astro-ph.CO]`.

[24] A. Arvanitaki, S. Dimopoulos, S. Dubovsky, N. Kaloper, and J. March-Russell, "String Axiverse," *Phys. Rev.* **D81** (2010) 123530, `arXiv:0905.4720 [hep-th]`.

[25] V. M. Mehta, M. Demirtas, C. Long, D. J. E. Marsh, L. Mcallister, and M. J. Stott, "Superradiance Exclusions in the Landscape of Type IIB String Theory," `arXiv:2011.08693 [hep-th]`.

[26] L. Ackerman, M. R. Buckley, S. M. Carroll, and M. Kamionkowski, "Dark Matter and Dark Radiation," *Phys. Rev. D* **79** (2009) 023519, `arXiv:0810.5126 [hep-ph]`.

[27] M. Goodsell, J. Jaeckel, J. Redondo, and A. Ringwald, "Naturally Light Hidden Photons in LARGE Volume String Compactifications," *JHEP* **11** (2009) 027, `arXiv:0909.0515 [hep-ph]`.

[28] K. Nakayama, "Vector Coherent Oscillation Dark Matter," *JCAP* **10** (2019) 019, `arXiv:1907.06243 [hep-ph]`.

[29] J. Jaeckel and A. Ringwald, "The Low-Energy Frontier of Particle Physics," *Ann. Rev. Nucl. Part. Sci.* **60** (2010) 405–437, `arXiv:1002.0329 [hep-ph]`.

[30] R. Brito, V. Cardoso, and P. Pani, *Superradiance: New Frontiers in Black Hole Physics*, vol. 971. Springer, 2020. `arXiv:1501.06570 [gr-qc]`.

[31] N. I. Shakura and R. A. Sunyaev, "Reprint of 1973A&A....24..337S. Black holes in binary systems. Observational appearance.," A&A **500** (June, 1973) 33–51.

[32] M. A. Abramowicz and P. C. Fragile, "Foundations of black hole accretion disk theory," *Living Reviews in Relativity* **16** no. 1, (Jan, 2013) . `http://dx.doi.org/10.12942/lrr-2013-1`.

[33] E. Barausse, V. Cardoso, and P. Pani, "Can environmental effects spoil precision gravitational-wave astrophysics?," *Phys. Rev. D* **89** no. 10, (2014) 104059, `arXiv:1404.7149 [gr-qc]`.

[34] C. M. Will, "The Confrontation between General Relativity and Experiment," *Living Rev. Rel.* **17** (2014) 4, `arXiv:1403.7377 [gr-qc]`.

[35] D. Psaltis, "Probes and Tests of Strong-Field Gravity with Observations in the Electromagnetic Spectrum," *Living Rev. Rel.* **11** (2008) 9, `arXiv:0806.1531 [astro-ph]`.

[36] Y. Fujii and K. Maeda, *The scalar-tensor theory of gravitation.* Cambridge Monographs on Mathematical Physics. Cambridge University Press, 7, 2007.

[37] V. Faraoni, *Cosmology in scalar tensor gravity.* 2004.

[38] A. S. Goldhaber and M. M. Nieto, "Photon and graviton mass limits," *Rev. Mod. Phys.* **82** (Mar, 2010) 939–979. `https://link.aps.org/doi/10.1103/RevModPhys.82.939`.

[39] K. Hinterbichler, "Theoretical aspects of massive gravity," *Rev. Mod. Phys.* **84** (May, 2012) 671–710. `https://link.aps.org/doi/10.1103/RevModPhys.84.671`.

[40] C. de Rham, "Massive Gravity," *Living Rev. Rel.* **17** (2014) 7, `arXiv:1401.4173 [hep-th]`.

[41] R. H. Dicke, "Coherence in spontaneous radiation processes," *Phys. Rev.* **93** (Jan, 1954) 99–110. `https://link.aps.org/doi/10.1103/PhysRev.93.99`.

[42] V. L. Ginzburg, "Radiation by uniformly moving sources (vavilov–cherenkov effect, transition radiation, and other phenomena)," *Physics-Uspekhi* **39** no. 10, (Oct, 1996) 973. `https://dx.doi.org/10.1070/PU1996v039n10ABEH000171`.

[43] O. Klein, "Die reflexion von elektronen an einem potentialsprung nach der relativistischen dynamik von dirac.," *Z. Physik 117, 53, 157–165* **39** no. 10, (Oct, 1929) 973. `https://doi.org/10.1007/BF01339716`.

[44] F. Hund, "Materieerzeugung im anschaulichen und im gequantelten wellenbild der materie," *Z. Physik 117, 1–17* **39** no. 10, (Oct, 1941) 973. `https://doi.org/10.1007/BF01337403`.

[45] R. G. Winter, "Klein Paradox for the Klein-Gordon Equation," *American Journal of Physics* **27** no. 5, (May, 1959) 355–358.

[46] C. A. Manogue, "The klein paradox and superradiance," *Annals of Physics* **181** no. 2, (1988) 261–283. `https://www.sciencedirect.com/science/article/pii/0003491688901674`.

[47] Y. B. Zel'Dovich, "Generation of Waves by a Rotating Body," *ZhETF Pisma Redaktsiiu* **14** (Aug., 1971) 270.

[48] Y. B. Zel'Dovich, "Amplification of Cylindrical Electromagnetic Waves Reflected from a Rotating Body," *Soviet Journal of Experimental and Theoretical Physics* **35** (Jan., 1972) 1085.

[49] S. A. Teukolsky, "Rotating black holes: Separable wave equations for gravitational and electromagnetic perturbations," *Phys. Rev. Lett.* **29** (Oct, 1972) 1114–1118. `https://link.aps.org/doi/10.1103/PhysRevLett.29.1114`.

[50] W. H. Press and S. A. Teukolsky, "Floating Orbits, Superradiant Scattering and the Black-hole Bomb," *Nature* **238** (1972) 211–212.

[51] W. Unruh, "Separability of the neutrino equations in a kerr background," *Phys. Rev. Lett.* **31** (Nov, 1973) 1265–1267. `https://link.aps.org/doi/10.1103/PhysRevLett.31.1265`.

[52] S. Chandrasekhar, "The Solution of Dirac's Equation in Kerr Geometry," *Proceedings of the Royal Society of London Series A* **349** no. 1659, (June, 1976) 571–575.

[53] B. R. Iyer and A. Kumar, "Note on the absence of massive fermion superradiance from a kerr black hole," *Phys. Rev. D* **18** (Dec, 1978) 4799–4801. `https://link.aps.org/doi/10.1103/PhysRevD.18.4799`.

[54] T. Damour, N. Deruelle, and R. Ruffini, "On Quantum Resonances in Stationary Geometries," *Lett. Nuovo Cim.* **15** (1976) 257–262.

[55] S. L. Detweiler, "Resonant oscillations of a rapidly rotating black hole," *Proc. Roy. Soc. Lond. A* **352** (1977) 381–395.

[56] T. J. M. Zouros and D. M. Eardley, "Instabilities of massive scalar perturbations of a rotating black hole," *Annals Phys.* **118** (1979) 139–155.

[57] T. Torres, S. Patrick, A. Coutant, M. Richartz, E. W. Tedford, and S. Weinfurtner, "Observation of superradiance in a vortex flow," *Nature Phys.* **13** (2017) 833–836, `arXiv:1612.06180 [gr-qc]`.

[58] G. W. Gibbons, "Vacuum Polarization and the Spontaneous Loss of Charge by Black Holes," *Commun. Math. Phys.* **44** (1975) 245–264.

[59] P. Goldreich and W. H. Julian, "Pulsar Electrodynamics," ApJ **157** (Aug., 1969) 869.

[60] M. A. Ruderman and P. G. Sutherland, "Theory of pulsars: polar gaps, sparks, and coherent microwave radiation.," ApJ **196** (Feb., 1975) 51–72.

[61] D. M. Eardley and W. H. Press, "Astrophysical processes near black holes," *Ann. Rev. Astron. Astrophys.* **13** (1975) 381–422.

[62] V. Cardoso, C. F. B. Macedo, P. Pani, and V. Ferrari, "Black holes and gravitational waves in models of minicharged dark matter," *JCAP* **05** (2016) 054, `arXiv:1604.07845 [hep-ph]`.

[63] R. P. Kerr, "Gravitational field of a spinning mass as an example of algebraically special metrics," *Phys. Rev. Lett.* **11** (1963) 237–238.

[64] R. Penrose, "Gravitational Collapse: the Role of General Relativity," *Nuovo Cimento Rivista Serie* **1** (Jan., 1969) 252.

[65] R. Vicente, V. Cardoso, and J. C. Lopes, "Penrose process, superradiance, and ergoregion instabilities," *Phys. Rev.* **D97** no. 8, (2018) 084032, `arXiv:1803.08060 [gr-qc]`.

[66] T. Hartman, W. Song, and A. Strominger, "The Kerr-Fermi Sea," `arXiv:0912.4265 [hep-th]`.

[67] V. Cardoso, M. Cavaglia, and L. Gualtieri, "Hawking emission of gravitons in higher dimensions: Non-rotating black holes," *JHEP* **02** (2006) 021, `arXiv:hep-th/0512116`.

[68] A. A. Starobinskij and S. M. Churilov, "Amplification of electromagnetic and gravitational waves scattered by a rotating black hole.," *Zhurnal Eksperimentalnoi i Teoreticheskoi Fiziki* **65** (1973) 3–11.

[69] S. R. Dolan, "Instability of the massive Klein-Gordon field on the Kerr spacetime," *Phys.Rev.* **D76** (2007) 084001, `arXiv:0705.2880 [gr-qc]`.

[70] S. R. Dolan, "Superradiant instabilities of rotating black holes in the time domain," *Phys.Rev.* **D87** (2013) 124026, `arXiv:1212.1477 [gr-qc]`.

[71] P. Pani, "Advanced Methods in Black-Hole Perturbation Theory," *Int. J. Mod. Phys.* **A28** (2013) 1340018, `arXiv:1305.6759 [gr-qc]`.

[72] D. Baumann, H. S. Chia, J. Stout, and L. ter Haar, "The Spectra of Gravitational Atoms," *JCAP* **1912** no. 12, (2019) 006, `arXiv:1908.10370 [gr-qc]`.

[73] S. L. Detweiler, "Klein-Gordon equation and rotating black holes," *Phys. Rev. D* **22** (1980) 2323–2326.

[74] J. G. Rosa, "The Extremal black hole bomb," *JHEP* **06** (2010) 015, `arXiv:0912.1780 [hep-th]`.

[75] J. G. Rosa and S. R. Dolan, "Massive vector fields on the Schwarzschild spacetime: quasi-normal modes and bound states," *Phys. Rev. D* **85** (2012) 044043, `arXiv:1110.4494 [hep-th]`.

[76] P. Pani, V. Cardoso, L. Gualtieri, E. Berti, and A. Ishibashi, "Perturbations of slowly rotating black holes: massive vector fields in the Kerr metric," *Phys. Rev. D* **86** (2012) 104017, `arXiv:1209.0773 [gr-qc]`.

[77] R. Brito, V. Cardoso, and P. Pani, "Massive spin-2 fields on black hole spacetimes: Instability of the Schwarzschild and Kerr solutions and bounds on the graviton mass," *Phys. Rev.* **D88** (2013) 023514, `arXiv:1304.6725 [gr-qc]`.

[78] O. J. C. Dias, G. Lingetti, P. Pani, and J. E. Santos, "Black hole superradiant instability for massive spin-2 fields," *Phys. Rev. D* **108** no. 4, (2023) L041502, `arXiv:2304.01265 [gr-qc]`.

[79] P. Pani, V. Cardoso, L. Gualtieri, E. Berti, and A. Ishibashi, "Black hole bombs and photon mass bounds," *Phys. Rev. Lett.* **109** (2012) 131102, `arXiv:1209.0465 [gr-qc]`.

[80] W. E. East, "Superradiant instability of massive vector fields around spinning black holes in the relativistic regime," *Phys. Rev. D* **96** no. 2, (2017) 024004, `arXiv:1705.01544 [gr-qc]`.

[81] W. E. East and F. Pretorius, "Superradiant Instability and Backreaction of Massive Vector Fields around Kerr Black Holes," *Phys. Rev. Lett.* **119** no. 4, (2017) 041101, `arXiv:1704.04791 [gr-qc]`.

[82] V. P. Frolov, P. Krtous, D. Kubiznak, and J. E. Santos, "Massive Vector Fields in Rotating Black-Hole Spacetimes: Separability and Quasinormal Modes," *Phys. Rev. Lett.* **120** (2018) 231103, `arXiv:1804.00030 [hep-th]`.

[83] M. Baryakhtar, R. Lasenby, and M. Teo, "Black Hole Superradiance Signatures of Ultralight Vectors," *Phys. Rev.* **D96** no. 3, (2017) 035019, `arXiv:1704.05081 [hep-ph]`.

[84] H. Witek, V. Cardoso, A. Ishibashi, and U. Sperhake, "Superradiant instabilities in astrophysical systems," *Phys. Rev. D* **87** no. 4, (2013) 043513, `arXiv:1212.0551 [gr-qc]`.

[85] R. Brito, S. Grillo, and P. Pani, "Black Hole Superradiant Instability from Ultralight Spin-2 Fields," *Phys. Rev. Lett.* **124** no. 21, (2020) 211101, `arXiv:2002.04055 [gr-qc]`.

[86] W. E. East and N. Siemonsen, "Instability and backreaction of spin-2 fields around black holes," `arXiv:2309.05096 [gr-qc]`.

[87] R. Brito, V. Cardoso, and P. Pani, “Black holes as particle detectors: evolution of superradiant instabilities,” *Class. Quant. Grav.* **32** no. 13, (2015) 134001, `arXiv:1411.0686 [gr-qc]`.

[88] W. E. East, “Massive Boson Superradiant Instability of Black Holes: Nonlinear Growth, Saturation, and Gravitational Radiation,” *Phys. Rev. Lett.* **121** no. 13, (2018) 131104, `arXiv:1807.00043 [gr-qc]`.

[89] A. Arvanitaki and S. Dubovsky, “Exploring the String Axiverse with Precision Black Hole Physics,” *Phys.Rev.* **D83** (2011) 044026, `arXiv:1004.3558 [hep-th]`.

[90] R. Brito, S. Ghosh, E. Barausse, E. Berti, V. Cardoso, I. Dvorkin, A. Klein, and P. Pani, “Gravitational wave searches for ultralight bosons with LIGO and LISA,” *Phys. Rev.* **D96** no. 6, (2017) 064050, `arXiv:1706.06311 [gr-qc]`.

[91] V. Cardoso, O. J. Dias, G. S. Hartnett, M. Middleton, P. Pani, and J. E. Santos, “Constraining the mass of dark photons and axion-like particles through black-hole superradiance,” *JCAP* **03** (2018) 043, `arXiv:1801.01420 [gr-qc]`.

[92] D. Baumann, H. S. Chia, and R. A. Porto, “Probing Ultralight Bosons with Binary Black Holes,” *Phys. Rev. D* **99** no. 4, (2019) 044001, `arXiv:1804.03208 [gr-qc]`.

[93] D. Baumann, H. S. Chia, R. A. Porto, and J. Stout, “Gravitational Collider Physics,” *Phys. Rev. D* **101** no. 8, (2020) 083019, `arXiv:1912.04932 [gr-qc]`.

[94] D. Baumann, G. Bertone, J. Stout, and G. M. Tomaselli, “Ionization of gravitational atoms,” *Phys. Rev. D* **105** no. 11, (2022) 115036, `arXiv:2112.14777 [gr-qc]`.

[95] G. M. Tomaselli, T. F. M. Spieksma, and G. Bertone, “Dynamical friction in gravitational atoms,” *JCAP* **07** (2023) 070, `arXiv:2305.15460 [gr-qc]`.

[96] V. Cardoso, F. Duque, and T. Ikeda, “Tidal effects and disruption in superradiant clouds: a numerical investigation,” *Phys. Rev. D* **101** no. 6, (2020) 064054, `arXiv:2001.01729 [gr-qc]`.

[97] E. Berti, R. Brito, C. F. B. Macedo, G. Raposo, and J. L. Rosa, “Ultralight boson cloud depletion in binary systems,” *Phys. Rev. D* **99** no. 10, (2019) 104039, `arXiv:1904.03131 [gr-qc]`.

[98] V. De Luca and P. Pani, “Tidal deformability of dressed black holes and tests of ultralight bosons in extended mass ranges,” *JCAP* **08** (2021) 032, `arXiv:2106.14428 [gr-qc]`.

[99] H. Yoshino and H. Kodama, “Probing the string axiverse by gravitational waves from Cygnus X-1,” *PTEP* **2015** no. 6, (2015) 061E01, `arXiv:1407.2030 [gr-qc]`.

[100] R. Brito, S. Ghosh, E. Barausse, E. Berti, V. Cardoso, I. Dvorkin, A. Klein, and P. Pani, "Stochastic and resolvable gravitational waves from ultralight bosons," *Phys. Rev. Lett.* **119** no. 13, (2017) 131101, `arXiv:1706.05097 [gr-qc]`.

[101] L. Tsukada, T. Callister, A. Matas, and P. Meyers, "First search for a stochastic gravitational-wave background from ultralight bosons," *Phys. Rev. D* **99** no. 10, (2019) 103015, `arXiv:1812.09622 [astro-ph.HE]`.

[102] O. A. Hannuksela, K. W. K. Wong, R. Brito, E. Berti, and T. G. F. Li, "Probing the existence of ultralight bosons with a single gravitational-wave measurement," *Nature Astron.* (2019) , `arXiv:1804.09659 [astro-ph.HE]`.

[103] M. Isi, L. Sun, R. Brito, and A. Melatos, "Directed searches for gravitational waves from ultralight bosons," `arXiv:1810.03812 [gr-qc]`.

[104] L. Tsukada, R. Brito, W. E. East, and N. Siemonsen, "Modeling and searching for a stochastic gravitational-wave background from ultralight vector bosons," *Phys. Rev. D* **103** no. 8, (2021) 083005, `arXiv:2011.06995 [astro-ph.HE]`.

[105] N. Siemonsen and W. E. East, "Gravitational wave signatures of ultralight vector bosons from black hole superradiance," *Phys. Rev. D* **101** no. 2, (2020) 024019, `arXiv:1910.09476 [gr-qc]`.

[106] W. H. Press, "Table-Top Model for Black Hole Electromagnetic Instabilities," in *Frontiers Science Series 23: Black Holes and High Energy Astrophysics*, H. Sato and N. Sugiyama, eds., p. 235. 1998.

[107] J. P. Conlon and C. A. Herdeiro, "Can black hole superradiance be induced by galactic plasmas?," *Phys. Lett. B* **780** (2018) 169–173, `arXiv:1701.02034 [astro-ph.HE]`.

[108] P. Pani and A. Loeb, "Constraining Primordial Black-Hole Bombs through Spectral Distortions of the Cosmic Microwave Background," *Phys. Rev. D* **88** (2013) 041301, `arXiv:1307.5176 [astro-ph.CO]`.

[109] C. Done, M. Gierliński, and A. Kubota, "Modelling the behaviour of accretion flows in x-ray binaries," *The Astronomy and Astrophysics Review* **15** no. 1, (Aug, 2007) 1–66. `http://dx.doi.org/10.1007/s00159-007-0006-1`.

[110] J. Poutanen and A. Veledina, "Modelling spectral and timing properties of accreting black holes: The hybrid hot flow paradigm," *Space Science Reviews* **183** no. 1-4, (Jan, 2014) 61–85. `http://dx.doi.org/10.1007/s11214-013-0033-3`.

[111] F. Yuan and R. Narayan, "Hot accretion flows around black holes," *Annual Review of Astronomy and Astrophysics* **52** no. 1, (Aug, 2014) 529–588. `http://dx.doi.org/10.1146/annurev-astro-082812-141003`.

[112] A. A. Esin, J. E. McClintock, and R. Narayan, "Advection-dominated accretion and the spectral states of black hole x-ray binaries: Application to

nova muscae 1991," *The Astrophysical Journal* **489** no. 2, (Nov, 1997) 865–889. `http://dx.doi.org/10.1086/304829`.

[113] B. F. Liu, "Coupling of the accretion disk and corona around black holes," in *Feeding Compact Objects: Accretion on All Scales*, C. M. Zhang, T. Belloni, M. Méndez, and S. N. Zhang, eds., vol. 290, pp. 62–65. Feb., 2013.

[114] V. Cardoso, I. P. Carucci, P. Pani, and T. P. Sotiriou, "Black holes with surrounding matter in scalar-tensor theories," *Phys. Rev. Lett.* **111** (2013) 111101, `arXiv:1308.6587 [gr-qc]`.

[115] A. Dima and E. Barausse, "Numerical investigation of plasma-driven superradiant instabilities," *Class. Quant. Grav.* **37** no. 17, (2020) 175006, `arXiv:2001.11484 [gr-qc]`.

[116] Z. Wang, T. Helfer, K. Clough, and E. Berti, "Superradiance in massive vector fields with spatially varying mass," `arXiv:2201.08305 [gr-qc]`.

[117] L. D. Landau, "On the vibrations of the electronic plasma," *J. Phys. (USSR)* **10** (1946) 25–34.

[118] C. K. Birdsall and A. B. Langdon, *Plasma Physics via Computer Simulation.* 1991.

[119] T. D. Arber, K. Bennett, C. S. Brady, A. Lawrence-Douglas, M. G. Ramsay, N. J. Sircombe, P. Gillies, R. G. Evans, H. Schmitz, A. R. Bell, and C. P. Ridgers, "Contemporary particle-in-cell approach to laser-plasma modelling," *Plasma Physics and Controlled Fusion* **57** no. 11, (Nov., 2015) 113001.

[120] N. Krall and A. Trivelpiece, *Principles of Plasma Physics.* International series in pure and applied physics. McGraw-Hill, 1973. `https://books.google.dk/books?id=b0BRAAAAMAAJ`.

[121] K. S. Thorne and R. D. Blandford, *Modern Classical Physics: Optics, Fluids, Plasmas, Elasticity, Relativity, and Statistical Physics.* 2017.

[122] U. S. Inan and M. Gołkowski, *Principles of Plasma Physics for Engineers and Scientists.* Cambridge University Press, 2010.

[123] B. V. Somov, *Plasma Astrophysics, Part I: Fundamentals and Practice.* 2006.

[124] J. P. Freidberg, *Ideal MHD.* 2014.

[125] R. Kulsrud and A. Loeb, "Dynamics and gravitational interaction of waves in nonuniform media," *Phys. Rev. D* **45** (Jan, 1992) 525–531. `https://link.aps.org/doi/10.1103/PhysRevD.45.525`.

[126] J. T. Mendonça, A. M. Martins, and A. Guerreiro, "Field quantization in a plasma: Photon mass and charge," *Phys. Rev. E* **62** (Aug, 2000) 2989–2991. `https://link.aps.org/doi/10.1103/PhysRevE.62.2989`.

[127] D. N. Page and K. S. Thorne, "Disk-Accretion onto a Black Hole. Time-Averaged Structure of Accretion Disk," ApJ **191** (July, 1974) 499–506.

[128] M. A. Abramowicz and P. Fragile, "Foundations of Black Hole Accretion Disk Theory," *Living Rev. Rel.* **16** (2013) 1, `arXiv:1104.5499 [astro-ph.HE]`.

[129] R. A. Breuer and J. Ehlers, "Propagation of electromagnetic waves through magnetized plasmas in arbitrary gravitational fields," A&A **96** no. 1-2, (Mar., 1981) 293–295.

[130] G. Ellis, "Relativistic cosmology," *Gen. Rel. Grav.* **41** (2009) 581–660.

[131] D. Gal'tsov, G. Pomerantseva, and G. Chizhov, "Behavior of massive vector particles in a Schwarzschild field," *Sov. Phys. J.* **27** (1984) 697–700.

[132] S. R. Dolan, "Instability of the Proca field on Kerr spacetime," *Phys. Rev.* **D98** no. 10, (2018) 104006, `arXiv:1806.01604 [gr-qc]`.

[133] H. Bondi, "On spherically symmetrical accretion," MNRAS **112** (Jan., 1952) 195.

[134] V. Ferrari, L. Gualtieri, and S. Marassi, "A New approach to the study of quasi-normal modes of rotating stars," *Phys. Rev. D* **76** (2007) 104033, `arXiv:0709.2925 [gr-qc]`.

[135] C. B. Schroeder and E. Esarey, "Relativistic warm plasma theory of nonlinear laser-driven electron plasma waves," *Phys. Rev. E* **81** (May, 2010) 056403. `https://link.aps.org/doi/10.1103/PhysRevE.81.056403`.

[136] S. Dubovsky and G. Hernández-Chifflet, "Heating up the Galaxy with Hidden Photons," *JCAP* **1512** no. 12, (2015) 054, `arXiv:1509.00039 [hep-ph]`.

[137] V. Cardoso, W.-d. Guo, C. F. Macedo, and P. Pani, "The tune of the universe: the role of plasma in tests of strong-field gravity," `arXiv:2009.07287 [gr-qc]`.

[138] D. Blas and S. J. Witte, "Quenching Mechanisms of Photon Superradiance," `arXiv:2009.10075 [hep-ph]`.

[139] B. B. Ahmedov, "Ohm's Law for Plasma in General Relativity and Cowling's Theorem," *Astrophys. Space Sci.* **331** (2011) 565–573, `arXiv:1008.3025 [astro-ph.SR]`.

[140] R. A. Konoplya, "Massive vector field perturbations in the schwarzschild background: Stability and quasinormal spectrum," *Phys. Rev. D* **73** (Jan, 2006) 024009. `https://link.aps.org/doi/10.1103/PhysRevD.73.024009`.

[141] R. H. Price, "Nonspherical perturbations of relativistic gravitational collapse. 1. Scalar and gravitational perturbations," *Phys. Rev.* **D5** (1972) 2419–2438.

[142] V. Perlick, O. Y. Tsupko, and G. S. Bisnovatyi-Kogan, "Influence of a plasma on the shadow of a spherically symmetric black hole," Phys. Rev. D **92** no. 10, (Nov., 2015) 104031, `arXiv:1507.04217 [gr-qc]`.

[143] J. Daniel and T. Tajima, “Electromagnetic waves in a strong schwarzschild plasma,” *Phys. Rev. D* **55** (Apr, 1997) 5193–5204. `https://link.aps.org/doi/10.1103/PhysRevD.55.5193`.

[144] V. L. Ginzburg, *The propagation of electromagnetic waves in plasmas, by V. L. Ginzburg. Translated by J. B. Sykes and R. J. Tayler.* Pergamon Press Oxford, New York, 2d ed., rev. and enl. ed., 1970.

[145] J. P. Freidberg, R. W. Mitchell, R. L. Morse, and L. I. Rudsinski, “Resonant absorption of laser light by plasma targets,” *Phys. Rev. Lett.* **28** (Mar, 1972) 795–799. `https://link.aps.org/doi/10.1103/PhysRevLett.28.795`.

[146] D. W. Forslund, J. M. Kindel, K. Lee, E. L. Lindman, and R. L. Morse, “Theory and simulation of resonant absorption in a hot plasma,” *Phys. Rev. A* **11** (Feb, 1975) 679–683. `https://link.aps.org/doi/10.1103/PhysRevA.11.679`.

[147] D. E. Hinkel-Lipsker, B. Fried, and G. Morales, “Analytic expressions for mode conversion in a plasma with a linear density profile,” *Physics of fluids. B, Plasma physics* **4** (1992) 559–575.

[148] R. Dragila, “Relativistic limit on resonance at oblique incidence,” *Physics of Fluids* **24** (1981) 1099–1103.

[149] Y. Kojima, “Coupled Pulsations between Polar and Axial Modes in a Slowly Rotating Relativistic Star,” *Progress of Theoretical Physics* **90** no. 5, (Nov., 1993) 977–990.

[150] P. Kaw and J. Dawson, “Relativistic Nonlinear Propagation of Laser Beams in Cold Overdense Plasmas,” *Physics of Fluids* **13** no. 2, (Feb., 1970) 472–481.

[151] F. Cattani, A. Kim, D. Anderson, and M. Lisak, “Threshold of induced transparency in the relativistic interaction of an electromagnetic wave with overdense plasmas,” *Physical review. E, Statistical physics, plasmas, fluids, and related interdisciplinary topics* **62** (08, 2000) 1234–7.

[152] M. Alcubierre, J. C. Degollado, and M. Salgado, “The Einstein-Maxwell system in 3+1 form and initial data for multiple charged black holes,” *Phys. Rev. D* **80** (2009) 104022, `arXiv:0907.1151 [gr-qc]`.

[153] I. D. Novikov and K. S. Thorne, “Astrophysics and black holes,” in *Proceedings, Ecole d’Eté de Physique Théorique: Les Astres Occlus*, pp. 343–550. 1973.

[154] https://web.uniroma1.it/gmunu/.

[155] E. Esarey, C. B. Schroeder, and W. P. Leemans, “Physics of laser-driven plasma-based electron accelerators,” *Rev. Mod. Phys.* **81** (Aug, 2009) 1229–1285. `https://link.aps.org/doi/10.1103/RevModPhys.81.1229`.

[156] P. Sprangle, E. Esarey, and A. Ting, "Nonlinear theory of intense laser-plasma interactions," *Phys. Rev. Lett.* **64** (Apr, 1990) 2011–2014. `https://link.aps.org/doi/10.1103/PhysRevLett.64.2011`.

[157] T. Tajima and J. M. Dawson, "Laser electron accelerator," *Phys. Rev. Lett.* **43** (Jul, 1979) 267–270. `https://link.aps.org/doi/10.1103/PhysRevLett.43.267`.

[158] J. M. Dawson, "Nonlinear electron oscillations in a cold plasma," *Phys. Rev.* **113** (Jan, 1959) 383–387. `https://link.aps.org/doi/10.1103/PhysRev.113.383`.

[159] A. I. Akhiezer and R. V. Polovin, "Theory of wave motion of an electron plasma," *Soviet Phys. JETP* **3** (1956) . `https://www.osti.gov/biblio/4361348`.

[160] A. Pukhov and J. Meyer-ter Vehn, "Laser wake field acceleration: the highly non-linear broken-wave regime," *Appl. Phys. B* **74** no. 4-5, (2002) 355–361.

[161] A. Bergmann and P. Mulser, "Breaking of resonantly excited electron plasma waves," *Phys. Rev. E* **47** (May, 1993) 3585–3589. `https://link.aps.org/doi/10.1103/PhysRevE.47.3585`.

[162] E. Siminos, B. Svedung Wettervik, M. Grech, and T. Fülöp, "Kinetic effects on the transition to relativistic self-induced transparency in laser-driven ion acceleration," in *APS Division of Plasma Physics Meeting Abstracts*, vol. 2016 of *APS Meeting Abstracts*, p. TO6.007. Oct., 2016.

[163] M. Tushentsov, A. Kim, F. Cattani, D. Anderson, and M. Lisak, "Electromagnetic energy penetration in the self-induced transparency regime of relativistic laser-plasma interactions," *Phys. Rev. Lett.* **87** (Dec, 2001) 275002. `https://link.aps.org/doi/10.1103/PhysRevLett.87.275002`.

[164] V. I. Berezhiani, D. P. Garuchava, S. V. Mikeladze, K. I. Sigua, N. L. Tsintsadze, S. M. Mahajan, Y. Kishimoto, and K. Nishikawa, "Fluid-Maxwell simulation of laser pulse dynamics in overdense plasma," *Physics of Plasmas* **12** no. 6, (05, 2005) , `https://pubs.aip.org/aip/pop/article-pdf/doi/10.1063/1.1924708/12598311/062308_1` `https://doi.org/10.1063/1.1924708`. 062308.

[165] A. Pukhov and J. Meyer-ter Vehn, "Laser hole boring into overdense plasma and relativistic electron currents for fast ignition of icf targets," *Phys. Rev. Lett.* **79** (Oct, 1997) 2686–2689. `https://link.aps.org/doi/10.1103/PhysRevLett.79.2686`.

[166] A. Macchi, "Theory of light sail acceleration by intense lasers: an overview," *High Power Laser Science and Engineering* **2** (2014) e10.

[167] S. S. Bulanov, E. Esarey, C. B. Schroeder, S. V. Bulanov, T. Z. Esirkepov, M. Kando, F. Pegoraro, and W. P. Leemans, "Radiation pressure acceleration: The factors limiting maximum attainable ion energy," *Physics of Plasmas* **23** no. 5, (Apr, 2016) 056703. `https://doi.org/10.1063%2F1.4946025`.

[168] G. Lingetti, E. Cannizzaro, and P. Pani, "Superradiant instabilities by accretion disks in scalar-tensor theories," *Phys. Rev. D* **106** no. 2, (2022) 024007, `arXiv:2204.09335 [gr-qc]`.

[169] M. Baryakhtar, M. Galanis, R. Lasenby, and O. Simon, "Black hole superradiance of self-interacting scalar fields," *Phys. Rev. D* **103** no. 9, (2021) 095019, `arXiv:2011.11646 [hep-ph]`.

[170] K. Clough, T. Helfer, H. Witek, and E. Berti, "The problem with Proca: ghost instabilities in self-interacting vector fields," `arXiv:2204.10868 [gr-qc]`.

[171] T. Ikeda, R. Brito, and V. Cardoso, "Blasts of Light from Axions," *Phys. Rev. Lett.* **122** no. 8, (2019) 081101, `arXiv:1811.04950 [gr-qc]`.

[172] M. Boskovic, R. Brito, V. Cardoso, T. Ikeda, and H. Witek, "Axionic instabilities and new black hole solutions," *Phys. Rev. D* **99** no. 3, (2019) 035006, `arXiv:1811.04945 [gr-qc]`.

[173] E. Cannizzaro, A. Caputo, L. Sberna, and P. Pani, "Plasma-photon interaction in curved spacetime I: formalism and quasibound states around nonspinning black holes," *Phys. Rev. D* **103** (2021) 124018, `arXiv:2012.05114 [gr-qc]`.

[174] E. Cannizzaro, A. Caputo, L. Sberna, and P. Pani, "Plasma-photon interaction in curved spacetime. II. Collisions, thermal corrections, and superradiant instabilities," *Phys. Rev. D* **104** no. 10, (2021) 104048, `arXiv:2107.01174 [gr-qc]`.

[175] A. Caputo, S. J. Witte, D. Blas, and P. Pani, "Electromagnetic Signatures of Dark Photon Superradiance," `arXiv:2102.11280 [hep-ph]`.

[176] N. Siemonsen, C. Mondino, D. Egana-Ugrinovic, J. Huang, M. Baryakhtar, and W. E. East, "Dark photon superradiance: Electrodynamics and multimessenger signals," *Phys. Rev. D* **107** no. 7, (2023) 075025, `arXiv:2212.09772 [astro-ph.HE]`.

[177] E. V. Stenson, J. Horn-Stanja, M. R. Stoneking, and T. S. Pedersen, "Debye length and plasma skin depth: two length scales of interest in the creation and diagnosis of laboratory pair plasmas," *Journal of Plasma Physics* **83** (2017) .

[178] V. Perlick, O. Y. Tsupko, and G. S. Bisnovatyi-Kogan, "Influence of a plasma on the shadow of a spherically symmetric black hole," *Phys. Rev. D* **92** no. 10, (2015) 104031, `arXiv:1507.04217 [gr-qc]`.

[179] D. Ghosh and D. Sachdeva, "Constraining Light Dark Photons from GW190517 and GW190426_152155," *Phys. Rev. D* **103** no. 9, (2021) 095028, `arXiv:2102.08857 [astro-ph.HE]`.

[180] M. Kaplinghat, S. Tulin, and H.-B. Yu, "Dark Matter Halos as Particle Colliders: Unified Solution to Small-Scale Structure Puzzles from Dwarfs to Clusters," *Phys. Rev. Lett.* **116** no. 4, (2016) 041302, `arXiv:1508.03339 [astro-ph.CO]`.

[181] M. Pospelov, A. Ritz, and M. B. Voloshin, "Secluded WIMP Dark Matter," *Phys. Lett. B* **662** (2008) 53–61, `arXiv:0711.4866 [hep-ph]`.

[182] T. Lin, "Dark matter models and direct detection," *PoS* **333** (2019) 009, `arXiv:1904.07915 [hep-ph]`.

[183] K. E. Andrade, J. Fuson, S. Gad-Nasr, D. Kong, Q. Minor, M. G. Roberts, and M. Kaplinghat, "A stringent upper limit on dark matter self-interaction cross-section from cluster strong lensing," *Mon. Not. Roy. Astron. Soc.* **510** no. 1, (2021) 54–81, `arXiv:2012.06611 [astro-ph.CO]`.

[184] K. Schutz and T. R. Slatyer, "Self-Scattering for Dark Matter with an Excited State," *JCAP* **01** (2015) 021, `arXiv:1409.2867 [hep-ph]`.

[185] M. Vogelsberger, J. Zavala, K. Schutz, and T. R. Slatyer, "Evaporating the Milky Way halo and its satellites with inelastic self-interacting dark matter," `arXiv:1805.03203 [astro-ph.GA]`.

[186] A. Arvanitaki, S. Dimopoulos, M. Galanis, D. Racco, O. Simon, and J. O. Thompson, "Dark QED from inflation," *JHEP* **11** (2021) 106, `arXiv:2108.04823 [hep-ph]`.

[187] P. Ullio, H. Zhao, and M. Kamionkowski, "A Dark matter spike at the galactic center?," *Phys. Rev. D* **64** (2001) 043504, `arXiv:astro-ph/0101481`.

[188] P. Gondolo and J. Silk, "Dark matter annihilation at the galactic center," *Phys. Rev. Lett.* **83** (1999) 1719–1722, `arXiv:astro-ph/9906391`.

[189] A. Caputo, A. J. Millar, C. A. J. O'Hare, and E. Vitagliano, "Dark photon limits: A handbook," *Phys. Rev. D* **104** no. 9, (2021) 095029, `arXiv:2105.04565 [hep-ph]`.

[190] A. Caputo, H. Liu, S. Mishra-Sharma, and J. T. Ruderman, "Dark Photon Oscillations in Our Inhomogeneous Universe," *Phys. Rev. Lett.* **125** no. 22, (2020) 221303, `arXiv:2002.05165 [astro-ph.CO]`.

[191] A. Caputo, H. Liu, S. Mishra-Sharma, and J. T. Ruderman, "Modeling Dark Photon Oscillations in Our Inhomogeneous Universe," *Phys. Rev. D* **102** no. 10, (2020) 103533, `arXiv:2004.06733 [astro-ph.CO]`.

[192] K. Bondarenko, J. Pradler, and A. Sokolenko, "Constraining dark photons and their connection to 21 cm cosmology with CMB data," *Phys. Lett. B* **805** (2020) 135420, `arXiv:2002.08942 [astro-ph.CO]`.

[193] K. K. Y. Ng, O. A. Hannuksela, S. Vitale, and T. G. F. Li, "Searching for ultralight bosons within spin measurements of a population of binary black hole mergers," *Phys. Rev. D* **103** no. 6, (2021) 063010, `arXiv:1908.02312 [gr-qc]`.

[194] N. Fernandez, A. Ghalsasi, and S. Profumo, "Superradiance and the Spins of Black Holes from LIGO and X-ray binaries," `arXiv:1911.07862 [hep-ph]`.

[195] K. Belczynski, C. Done, and J. P. Lasota, "All Apples: Comparing black holes in X-ray binaries and gravitational-wave sources," `arXiv:2111.09401 [astro-ph.HE]`.

[196] H. Davoudiasl and P. B. Denton, "Ultralight Boson Dark Matter and Event Horizon Telescope Observations of M87*," *Phys. Rev. Lett.* **123** no. 2, (2019) 021102, `arXiv:1904.09242 [astro-ph.CO]`.

[197] **LIGO Scientific, KAGRA, Virgo** Collaboration, R. Abbott *et al.*, "Constraints on dark photon dark matter using data from LIGO's and Virgo's third observing run," *Phys. Rev. D* **105** no. 6, (2022) 063030, `arXiv:2105.13085 [astro-ph.CO]`.

[198] J. a. G. Rosa and T. W. Kephart, "Stimulated Axion Decay in Superradiant Clouds around Primordial Black Holes," *Phys. Rev. Lett.* **120** no. 23, (2018) 231102, `arXiv:1709.06581 [gr-qc]`.

[199] S. Sen, "Plasma effects on lasing of a uniform ultralight axion condensate," *Phys. Rev. D* **98** no. 10, (2018) 103012, `arXiv:1805.06471 [hep-ph]`.

[200] D. E. Kaplan and R. Rattazzi, "Large field excursions and approximate discrete symmetries from a clockwork axion," *Phys. Rev. D* **93** no. 8, (2016) 085007, `arXiv:1511.01827 [hep-ph]`.

[201] M. Farina, D. Pappadopulo, F. Rompineve, and A. Tesi, "The photo-philic QCD axion," *JHEP* **01** (2017) 095, `arXiv:1611.09855 [hep-ph]`.

[202] A. V. Sokolov and A. Ringwald, "Photophilic hadronic axion from heavy magnetic monopoles," *JHEP* **06** (2021) 123, `arXiv:2104.02574 [hep-ph]`.

[203] A. V. Sokolov and A. Ringwald, "Electromagnetic Couplings of Axions," `arXiv:2205.02605 [hep-ph]`.

[204] H. Yoshino and H. Kodama, "Bosenova collapse of axion cloud around a rotating black hole," *Prog. Theor. Phys.* **128** (2012) 153–190, `arXiv:1203.5070 [gr-qc]`.

[205] H. Omiya, T. Takahashi, T. Tanaka, and H. Yoshino, "Impact of multiple modes on the evolution of self-interacting axion condensate around rotating black holes," `arXiv:2211.01949 [gr-qc]`.

[206] H. S. Chia, C. Doorman, A. Wernersson, T. Hinderer, and S. Nissanke, "Self-interacting gravitational atoms in the strong-gravity regime," *JCAP* **04** (2023) 018, `arXiv:2212.11948 [gr-qc]`.

[207] C. A. R. Herdeiro, E. Radu, and N. M. Santos, "A bound on energy extraction (and hairiness) from superradiance," *Phys. Lett. B* **824** (2022) 136835, `arXiv:2111.03667 [gr-qc]`.

[208] E. Berti, V. Cardoso, and A. O. Starinets, "Quasinormal modes of black holes and black branes," *Class. Quantum Grav.* **26** (2009) 163001, `arXiv:0905.2975 [gr-qc]`.

[209] V. Cardoso and S. Yoshida, "Superradiant instabilities of rotating black branes and strings," *JHEP* **07** (2005) 009, `arXiv:hep-th/0502206`.

[210] V. Cardoso, R. Brito, and J. L. Rosa, "Superradiance in stars," *Phys. Rev. D* **91** no. 12, (2015) 124026, `arXiv:1505.05509 [gr-qc]`.

[211] T. W. Kephart and T. J. Weiler, "Stimulated radiation from axion cluster evolution," *Phys. Rev. D* **52** (Sep, 1995) 3226–3238. `https://link.aps.org/doi/10.1103/PhysRevD.52.3226`.

[212] M. P. Hertzberg and E. D. Schiappacasse, "Dark Matter Axion Clump Resonance of Photons," *JCAP* **11** (2018) 004, `arXiv:1805.00430 [hep-ph]`.

[213] P. Carenza, A. Mirizzi, and G. Sigl, "Dynamical evolution of axion condensates under stimulated decays into photons," *Phys. Rev. D* **101** no. 10, (2020) 103016, `arXiv:1911.07838 [hep-ph]`.

[214] **LIGO Scientific, Virgo, KAGRA** Collaboration, R. Abbott *et al.*, "All-sky search for gravitational wave emission from scalar boson clouds around spinning black holes in LIGO O3 data," *Phys. Rev. D* **105** no. 10, (2022) 102001, `arXiv:2111.15507 [astro-ph.HE]`.

[215] C. Palomba *et al.*, "Direct constraints on ultra-light boson mass from searches for continuous gravitational waves," *Phys. Rev. Lett.* **123** (2019) 171101, `arXiv:1909.08854 [astro-ph.HE]`.

[216] C. Yuan, Y. Jiang, and Q.-G. Huang, "Constraints on an ultralight scalar boson from Advanced LIGO and Advanced Virgo's first three observing runs using the stochastic gravitational-wave background," *Phys. Rev. D* **106** no. 2, (2022) 023020, `arXiv:2204.03482 [astro-ph.CO]`.

[217] K. K. Y. Ng, M. Isi, C.-J. Haster, and S. Vitale, "Multiband gravitational-wave searches for ultralight bosons," *Phys. Rev. D* **102** no. 8, (2020) 083020, `arXiv:2007.12793 [gr-qc]`.

[218] A. Arvanitaki, M. Baryakhtar, and X. Huang, "Discovering the QCD Axion with Black Holes and Gravitational Waves," *Phys. Rev.* **D91** no. 8, (2015) 084011, `arXiv:1411.2263 [hep-ph]`.

[219] M. J. Stott, "Ultralight Bosonic Field Mass Bounds from Astrophysical Black Hole Spin," `arXiv:2009.07206 [hep-ph]`.

[220] K. K. Y. Ng, S. Vitale, O. A. Hannuksela, and T. G. F. Li, "Constraints on Ultralight Scalar Bosons within Black Hole Spin Measurements from the LIGO-Virgo GWTC-2," *Phys. Rev. Lett.* **126** no. 15, (2021) 151102, `arXiv:2011.06010 [gr-qc]`.

[221] S. Wen, P. G. Jonker, N. C. Stone, and A. I. Zabludoff, "Mass, Spin, and Ultralight Boson Constraints from the Intermediate-mass Black Hole in the Tidal Disruption Event 3XMM J215022.4–055108," *Astrophys. J.* **918** no. 2, (2021) 46, `arXiv:2104.01498 [astro-ph.HE]`.

[222] D. Baumann, G. Bertone, J. Stout, and G. M. Tomaselli, "Sharp Signals of Boson Clouds in Black Hole Binary Inspirals," *Phys. Rev. Lett.* **128** no. 22, (2022) 221102, `arXiv:2206.01212 [gr-qc]`.

[223] P. S. Cole, G. Bertone, A. Coogan, D. Gaggero, T. Karydas, B. J. Kavanagh, T. F. M. Spieksma, and G. M. Tomaselli, "Disks, spikes, and clouds: distinguishing environmental effects on BBH gravitational waveforms," *Nature Astron.* (2023) , `arXiv:2211.01362 [gr-qc]`.

[224] J. Zhang and H. Yang, "Gravitational floating orbits around hairy black holes," *Phys. Rev. D* **99** no. 6, (2019) 064018, `arXiv:1808.02905 [gr-qc]`.

[225] J. Zhang and H. Yang, "Dynamic Signatures of Black Hole Binaries with Superradiant Clouds," *Phys. Rev. D* **101** no. 4, (2020) 043020, `arXiv:1907.13582 [gr-qc]`.

[226] I. Kovacic, R. H. Rand, and S. M. Sah, "Mathieu's Equation and Its Generalizations: Overview of Stability Charts and Their Features," *Applied Mechanics Reviews* **70** (2018) 020802.

[227] C. O'Hare, "cajohare/axionlimits: Axionlimits." `https://cajohare.github.io/AxionLimits/`, July, 2020.

[228] K. M. Ferriere, "The interstellar environment of our galaxy," *Rev. Mod. Phys.* **73** (2001) 1031–1066, `arXiv:astro-ph/0106359`.

[229] J. Burns, G. Hallinan, J. Lux, A. Romero-Wolf, T.-C. Chang, J. Kocz, J. Bowman, R. MacDowall, J. Kasper, R. Bradley, M. Anderson, and D. Rapetti, "Farside: A low radio frequency interferometric array on the lunar farside," `arXiv:1907.05407 [astro-ph.IM]`.

[230] S. M. Carroll, G. B. Field, and R. Jackiw, "Limits on a Lorentz and Parity Violating Modification of Electrodynamics," *Phys. Rev. D* **41** (1990) 1231.

[231] D. Harari and P. Sikivie, "Effects of a Nambu-Goldstone boson on the polarization of radio galaxies and the cosmic microwave background," *Phys. Lett. B* **289** (1992) 67–72.

[232] Y. Chen, J. Shu, X. Xue, Q. Yuan, and Y. Zhao, "Probing Axions with Event Horizon Telescope Polarimetric Measurements," *Phys. Rev. Lett.* **124** no. 6, (2020) 061102, `arXiv:1905.02213 [hep-ph]`.

[233] Y. Chen, Y. Liu, R.-S. Lu, Y. Mizuno, J. Shu, X. Xue, Q. Yuan, and Y. Zhao, "Stringent axion constraints with Event Horizon Telescope polarimetric measurements of M87*," *Nature Astron.* **6** no. 5, (2022) 592–598, `arXiv:2105.04572 [hep-ph]`.

[234] Y. Chen, C. Li, Y. Mizuno, J. Shu, X. Xue, Q. Yuan, Y. Zhao, and Z. Zhou, "Birefringence tomography for axion cloud," *JCAP* **09** (2022) 073, `arXiv:2208.05724 [hep-ph]`.

[235] T. Clifton, P. G. Ferreira, A. Padilla, and C. Skordis, "Modified Gravity and Cosmology," *Phys. Rept.* **513** (2012) 1–189, `arXiv:1106.2476 [astro-ph.CO]`.

[236] V. Cardoso, I. P. Carucci, P. Pani, and T. P. Sotiriou, "Matter around Kerr black holes in scalar-tensor theories: scalarization and superradiant instability," *Phys. Rev. D* **88** (2013) 044056, `arXiv:1305.6936 [gr-qc]`.

[237] T. P. Sotiriou and V. Faraoni, "Black holes in scalar-tensor gravity," *Phys. Rev. Lett.* **108** (2012) 081103, `arXiv:1109.6324 [gr-qc]`.

[238] R. Narayan, I. V. Igumenshchev, and M. A. Abramowicz, "Magnetically arrested disk: an energetically efficient accretion flow," *Publ. Astron. Soc. Jap.* **55** (2003) L69, `arXiv:astro-ph/0305029`.

[239] G. S. Bisnovatyi-Kogan and S. I. Blinnikov, "Old models for cygnus x-1 and agn," *Sov. Astron. Lett.* **2** (1976) 191, `arXiv:astro-ph/0003275`.

[240] J.-P. De Villiers, J. F. Hawley, and J. H. Krolik, "Magnetically driven accretion flows in the kerr metric I: models and overall structure," *Astrophys. J.* **599** (2003) 1238, `arXiv:astro-ph/0307260`.

[241] J.-P. De Villiers, J. F. Hawley, J. H. Krolik, and S. Hirose, "Magnetically driven accretion in the Kerr metric. 3. Unbound outflows," *Astrophys. J.* **620** (2005) 878–888, `arXiv:astro-ph/0407092`.

[242] E. Meyer-Hofmeister, B. F. Liu, and E. Qiao, "Interaction of the accretion flows in corona and disk near the black hole in active galactic nuclei," *Astron. Astrophys.* **607** (2017) A94, `arXiv:1712.02031 [astro-ph.HE]`.

[243] E. Meyer-Hofmeister, B. F. Liu, and F. Meyer, "Coronae above accretion disks around black holes: The effect of Compton cooling," *Astron. Astrophys.* **544** (2012) A87, `arXiv:1208.0265 [astro-ph.HE]`.

[244] R. Narayan and I. Yi, "Advection-dominated Accretion: Underfed Black Holes and Neutron Stars," ApJ **452** (Oct., 1995) 710, `arXiv:astro-ph/9411059 [astro-ph]`.

[245] V. Cardoso, O. J. C. Dias, J. P. S. Lemos, and S. Yoshida, "The Black hole bomb and superradiant instabilities," *Phys. Rev. D* **70** (2004) 044039, `arXiv:hep-th/0404096`. [Erratum: Phys.Rev.D 70, 049903 (2004)].

[246] S. Güttel and F. Tisseur, "The nonlinear eigenvalue problem," *Acta Numerica* **26** (2017) 1–94.

[247] J.-P. Berrut and L. N. Trefethen, "Barycentric lagrange interpolation," *SIAM Review* **46** (2004) 501–517.

[248] N. J. Higham, "The numerical stability of barycentric lagrange interpolation," *IMA Journal of Numerical Analysis* **24** no. 4, (2004) 547–556.

[249] M. Kramer *et al.*, "Strong-Field Gravity Tests with the Double Pulsar," *Phys. Rev. X* **11** no. 4, (2021) 041050, `arXiv:2112.06795 [astro-ph.HE]`.

[250] A.-C. Davis, B. Li, D. F. Mota, and H. A. Winther, "Structure Formation in the Symmetron Model," *Astrophys. J.* **748** (2012) 61, `arXiv:1108.3081 [astro-ph.CO]`.

[251] A.-C. Davis, R. Gregory, R. Jha, and J. Muir, "Astrophysical black holes in screened modified gravity," *JCAP* **08** (2014) 033, `arXiv:1402.4737 [astro-ph.CO]`.

[252] K. Hinterbichler, J. Khoury, A. Levy, and A. Matas, "Symmetron Cosmology," *Phys. Rev. D* **84** (2011) 103521, `arXiv:1107.2112 [astro-ph.CO]`.

[253] B. F. de Aguiar, R. F. P. Mendes, and F. T. Falciano, "Neutron Stars in the Symmetron Model," *Universe* **8** no. 1, (2021) 6, `arXiv:2112.03823 [gr-qc]`.

[254] C. Max and F. Perkins, "Strong Electromagnetic Waves in Overdense Plasmas," Phys. Rev. Lett. **27** no. 20, (Nov., 1971) 1342–1345.

[255] E. Barausse, V. Cardoso, and P. Pani, "Environmental Effects for Gravitational-wave Astrophysics," *J. Phys. Conf. Ser.* **610** no. 1, (2015) 012044, `arXiv:1404.7140 [astro-ph.CO]`.

[256] V. Cardoso, E. Franzin, and P. Pani, "Is the gravitational-wave ringdown a probe of the event horizon?," *Phys. Rev. Lett.* **116** no. 17, (2016) 171101, `arXiv:1602.07309 [gr-qc]`. [Erratum: Phys.Rev.Lett. 117, 089902 (2016)].

[257] V. Cardoso and P. Pani, "Testing the nature of dark compact objects: a status report," *Living Rev. Rel.* **22** no. 1, (2019) 4, `arXiv:1904.05363 [gr-qc]`.

[258] T. Regge and J. A. Wheeler, "Stability of a Schwarzschild singularity," *Phys. Rev.* **108** (1957) 1063–1069.

[259] F. Zerilli, "Gravitational field of a particle falling in a schwarzschild geometry analyzed in tensor harmonics," *Phys. Rev.* **D2** (1970) 2141–2160.

[260] S. A. Teukolsky, "Rotating black holes - separable wave equations for gravitational and electromagnetic perturbations," *Phys. Rev. Lett.* **29** (1972) 1114–1118.

[261] S. A. Teukolsky, "Perturbations of a rotating black hole. 1. Fundamental equations for gravitational electromagnetic and neutrino field perturbations," *Astrophys. J.* **185** (1973) 635–647.

[262] K. D. Kokkotas and B. G. Schmidt, "Quasi-normal modes of stars and black holes," *Living Reviews in Relativity* **2** no. 1, (Sep, 1999) . `https://doi.org/10.12942%2Flrr-1999-2`.

[263] N. Siemonsen, T. May, and W. E. East, "Modeling the black hole superradiance gravitational waveform," *Phys. Rev. D* **107** no. 10, (2023) 104003, `arXiv:2211.03845 [gr-qc]`.

[264] M. H.-Y. Cheung *et al.*, "Nonlinear Effects in Black Hole Ringdown," *Phys. Rev. Lett.* **130** no. 8, (2023) 081401, `arXiv:2208.07374 [gr-qc]`.

[265] K. Mitman *et al.*, "Nonlinearities in Black Hole Ringdowns," *Phys. Rev. Lett.* **130** no. 8, (2023) 081402, `arXiv:2208.07380 [gr-qc]`.

[266] R. Brito and S. Shah, "Extreme mass-ratio inspirals into black holes surrounded by scalar clouds," (7, 2023) , `arXiv:2307.16093 [gr-qc]`.

[267] X. Tong, Y. Wang, and H.-Y. Zhu, "Termination of superradiance from a binary companion," *Phys. Rev. D* **106** no. 4, (2022) 043002, `arXiv:2205.10527 [gr-qc]`.

[268] S. R. Green, S. Hollands, L. Sberna, V. Toomani, and P. Zimmerman, "Conserved currents for a Kerr black hole and orthogonality of quasinormal modes," *Phys. Rev. D* **107** no. 6, (2023) 064030, `arXiv:2210.15935 [gr-qc]`.

[269] E. W. Leaver, "An Analytic representation for the quasi normal modes of Kerr black holes," *Proc. Roy. Soc. Lond. A* **402** (1985) 285–298.

[270] R. A. Konoplya and A. Zhidenko, "Stability and quasinormal modes of the massive scalar field around Kerr black holes," *Phys. Rev. D* **73** (2006) 124040, `arXiv:gr-qc/0605013`.

[271] E. W. Leaver, "Spectral decomposition of the perturbation response of the Schwarzschild geometry," *Phys. Rev. D* **34** (1986) 384–408.

[272] H.-P. Nollert and R. H. Price, "Quantifying excitations of quasinormal mode systems," *J. Math. Phys.* **40** (1999) 980–1010, `arXiv:gr-qc/9810074`.

[273] E. Berti and V. Cardoso, "Quasinormal ringing of Kerr black holes. I. The Excitation factors," *Phys. Rev. D* **74** (2006) 104020, `arXiv:gr-qc/0605118`.

[274] L. Sberna, P. Bosch, W. E. East, S. R. Green, and L. Lehner, "Nonlinear effects in the black hole ringdown: Absorption-induced mode excitation," *Phys. Rev. D* **105** no. 6, (2022) 064046, `arXiv:2112.11168 [gr-qc]`.

[275] D. J. Griffiths, *Introduction to Quantum Mechanics (2nd Edition)*. Pearson Prentice Hall, 2nd ed., Apr., 2004. `http://www.amazon.com/exec/obidos/redirect?tag=citeulike07-20&path=ASIN/0131118927`.

[276] A. Zimmerman, H. Yang, Z. Mark, Y. Chen, and L. Lehner, "Quasinormal Modes Beyond Kerr," *Astrophys. Space Sci. Proc.* **40** (2015) 217–223, `arXiv:1406.4206 [gr-qc]`.

[277] Z. Mark, H. Yang, A. Zimmerman, and Y. Chen, "Quasinormal modes of weakly charged Kerr-Newman spacetimes," *Phys. Rev. D* **91** no. 4, (2015) 044025, `arXiv:1409.5800 [gr-qc]`.

[278] A. Hussain and A. Zimmerman, "Approach to computing spectral shifts for black holes beyond Kerr," *Phys. Rev. D* **106** no. 10, (2022) 104018, `arXiv:2206.10653 [gr-qc]`.

[279] “Black Hole Perturbation Toolkit.” (bhptoolkit.org).

[280] O. Lunin, “Maxwell’s equations in the Myers-Perry geometry,” *JHEP* **12** (2017) 138, `arXiv:1708.06766 [hep-th]`.

[281] S. R. Green, S. Hollands, and P. Zimmerman, “Teukolsky formalism for nonlinear Kerr perturbations,” *Class. Quant. Grav.* **37** no. 7, (2020) 075001, `arXiv:1908.09095 [gr-qc]`.

[282] A. Spiers, A. Pound, and J. Moxon, “Second-order Teukolsky formalism in Kerr spacetime: Formulation and nonlinear source,” *Phys. Rev. D* **108** no. 6, (2023) 064002, `arXiv:2305.19332 [gr-qc]`.

[283] M. Giesler, M. Isi, M. A. Scheel, and S. Teukolsky, “Black Hole Ringdown: The Importance of Overtones,” *Phys. Rev. X* **9** no. 4, (2019) 041060, `arXiv:1903.08284 [gr-qc]`.

[284] V. Baibhav, M. H.-Y. Cheung, E. Berti, V. Cardoso, G. Carullo, R. Cotesta, W. Del Pozzo, and F. Duque, “Agnostic black hole spectroscopy: quasinormal mode content of numerical relativity waveforms and limits of validity of linear perturbation theory,” `arXiv:2302.03050 [gr-qc]`.

[285] P. J. Nee, S. H. Völkel, and H. P. Pfeiffer, “Role of black hole quasinormal mode overtones for ringdown analysis,” *Phys. Rev. D* **108** no. 4, (2023) 044032, `arXiv:2302.06634 [gr-qc]`.

[286] **LIGO Scientific, Virgo** Collaboration, B. P. Abbott *et al.*, “GWTC-1: A Gravitational-Wave Transient Catalog of Compact Binary Mergers Observed by LIGO and Virgo during the First and Second Observing Runs,” `arXiv:1811.12907 [astro-ph.HE]`.

[287] **LIGO Scientific, Virgo** Collaboration, R. Abbott *et al.*, “GWTC-2: Compact Binary Coalescences Observed by LIGO and Virgo During the First Half of the Third Observing Run,” *Phys. Rev. X* **11** (2021) 021053, `arXiv:2010.14527 [gr-qc]`.

[288] **LIGO Scientific, VIRGO, KAGRA** Collaboration, R. Abbott *et al.*, “GWTC-3: Compact Binary Coalescences Observed by LIGO and Virgo During the Second Part of the Third Observing Run,” `arXiv:2111.03606 [gr-qc]`.

[289] M. Punturo *et al.*, “The Einstein Telescope: A third-generation gravitational wave observatory,” *Class. Quant. Grav.* **27** (2010) 194002.

[290] B. Sathyaprakash *et al.*, “Scientific Objectives of Einstein Telescope,” *Class. Quant. Grav.* **29** (2012) 124013, `arXiv:1206.0331 [gr-qc]`. [Erratum: Class.Quant.Grav. 30, 079501 (2013)].

[291] S. Dwyer, D. Sigg, S. W. Ballmer, L. Barsotti, N. Mavalvala, and M. Evans, “Gravitational wave detector with cosmological reach,” *Physical Review D* **91** no. 8, (Apr, 2015) . `https://doi.org/10.1103%2Fphysrevd.91.082001`.

[292] P. Amaro-Seoane, H. Audley, S. Babak, J. Baker, E. Barausse, P. Bender, E. Berti, P. Binetruy, M. Born, D. Bortoluzzi, J. Camp, C. Caprini, V. Cardoso, M. Colpi, J. Conklin, N. Cornish, C. Cutler, K. Danzmann, R. Dolesi, L. Ferraioli, V. Ferroni, E. Fitzsimons, J. Gair, L. G. Bote, D. Giardini, F. Gibert, C. Grimani, H. Halloin, G. Heinzel, T. Hertog, M. Hewitson, K. Holley-Bockelmann, D. Hollington, M. Hueller, H. Inchauspe, P. Jetzer, N. Karnesis, C. Killow, A. Klein, B. Klipstein, N. Korsakova, S. L. Larson, J. Livas, I. Lloro, N. Man, D. Mance, J. Martino, I. Mateos, K. McKenzie, S. T. McWilliams, C. Miller, G. Mueller, G. Nardini, G. Nelemans, M. Nofrarias, A. Petiteau, P. Pivato, E. Plagnol, E. Porter, J. Reiche, D. Robertson, N. Robertson, E. Rossi, G. Russano, B. Schutz, A. Sesana, D. Shoemaker, J. Slutsky, C. F. Sopuerta, T. Sumner, N. Tamanini, I. Thorpe, M. Troebs, M. Vallisneri, A. Vecchio, D. Vetrugno, S. Vitale, M. Volonteri, G. Wanner, H. Ward, P. Wass, W. Weber, J. Ziemer, and P. Zweifel, "Laser interferometer space antenna," 2017.

[293] E. Berti, A. Sesana, E. Barausse, V. Cardoso, and K. Belczynski, "Spectroscopy of Kerr black holes with Earth- and space-based interferometers," *Phys. Rev. Lett.* **117** no. 10, (2016) 101102, `arXiv:1605.09286 [gr-qc]`.

[294] **LIGO Scientific** Collaboration, B. P. Abbott *et al.*, "Exploring the Sensitivity of Next Generation Gravitational Wave Detectors," *Class. Quant. Grav.* **34** no. 4, (2017) 044001, `arXiv:1607.08697 [astro-ph.IM]`.

[295] R. Essick, S. Vitale, and M. Evans, "Frequency-dependent responses in third generation gravitational-wave detectors," *Phys. Rev.* **D96** no. 8, (2017) 084004, `arXiv:1708.06843 [gr-qc]`.

[296] S. Hild *et al.*, "Sensitivity Studies for Third-Generation Gravitational Wave Observatories," *Class. Quant. Grav.* **28** (2011) 094013, `arXiv:1012.0908 [gr-qc]`.

[297] E. Barausse *et al.*, "Prospects for Fundamental Physics with LISA," *Gen. Rel. Grav.* **52** no. 8, (2020) 81, `arXiv:2001.09793 [gr-qc]`.

[298] **NANOGrav** Collaboration, G. Agazie *et al.*, "The nanograv 15-year data set: Evidence for a gravitational-wave background," `arXiv:2306.16213 [astro-ph.HE]`.

[299] **NANOGrav** Collaboration, G. Agazie *et al.*, "The nanograv 15-year data set: Observations and timing of 68 millisecond pulsars," `arXiv:2306.16217 [astro-ph.HE]`.

[300] **EPTA** Collaboration, J. Antoniadis *et al.*, "The second data release from the european pulsar timing array iii. search for gravitational wave signals," `arXiv:2306.16214 [astro-ph.HE]`.

[301] **EPTA** Collaboration, J. Antoniadis *et al.*, "The second data release from the european pulsar timing array i. the dataset and timing analysis," `arXiv:2306.16224 [astro-ph.HE]`.

[302] **EPTA** Collaboration, J. Antoniadis *et al.*, "The second data release from the european pulsar timing array: V. implications for massive black holes, dark matter and the early universe," `arXiv:2306.16227 [astro-ph.HE]`.

[303] **PPTA** Collaboration, D. Reardon *et al.*, "Search for an isotropic gravitational-wave background with the parkes pulsar timing array," `arXiv:2306.16215 [astro-ph.HE]`.

[304] **PPTA** Collaboration, A. Zic *et al.*, "The parkes pulsar timing array third data release," `arXiv:2306.16230 [astro-ph.HE]`.

[305] **PPTA** Collaboration, D. Reardon *et al.*, "The gravitational-wave background null hypothesis: Characterizing noise in millisecond pulsar arrival times with the parkes pulsar timing array," `arXiv:2306.16229 [astro-ph.HE]`.

[306] **CPTA** Collaboration, H. Xu *et al.*, "Searching for the nano-hertz stochastic gravitational wave background with the chinese pulsar timing array data release i," `arXiv:2306.16216 [astro-ph.HE]`.

[307] E. D. Hall and M. Evans, "Metrics for next-generation gravitational-wave detectors," *Classical and Quantum Gravity* **36** no. 22, (Oct., 2019) 225002. `http://dx.doi.org/10.1088/1361-6382/ab41d6`.

[308] K. S. Stelle, "Renormalization of Higher Derivative Quantum Gravity," *Phys. Rev.* **D16** (1977) 953–969.

[309] S. Alexander and N. Yunes, "Chern-Simons Modified General Relativity," *Phys. Rept.* **480** (2009) 1–55, `arXiv:0907.2562 [hep-th]`.

[310] K. Yagi, N. Yunes, and T. Tanaka, "Gravitational Waves from Quasi-Circular Black Hole Binaries in Dynamical Chern-Simons Gravity," *Phys. Rev. Lett.* **109** (2012) 251105, `arXiv:1208.5102 [gr-qc]`. [Erratum: Phys.Rev.Lett. 116, 169902 (2016), Erratum: Phys.Rev.Lett. 124, 029901 (2020)].

[311] P. Pani, V. Cardoso, and L. Gualtieri, "Gravitational waves from extreme mass-ratio inspirals in Dynamical Chern-Simons gravity," *Phys. Rev. D* **83** (2011) 104048, `arXiv:1104.1183 [gr-qc]`.

[312] N. Yunes, P. Pani, and V. Cardoso, "Gravitational Waves from Quasicircular Extreme Mass-Ratio Inspirals as Probes of Scalar-Tensor Theories," *Phys. Rev. D* **85** (2012) 102003, `arXiv:1112.3351 [gr-qc]`.

[313] A. Maselli, N. Franchini, L. Gualtieri, and T. P. Sotiriou, "Detecting scalar fields with Extreme Mass Ratio Inspirals," *Phys. Rev. Lett.* **125** no. 14, (2020) 141101, `arXiv:2004.11895 [gr-qc]`.

[314] A. Maselli, N. Franchini, L. Gualtieri, T. P. Sotiriou, S. Barsanti, and P. Pani, "Detecting fundamental fields with LISA observations of gravitational waves from extreme mass-ratio inspirals," *Nature Astron.* **6** no. 4, (2022) 464–470, `arXiv:2106.11325 [gr-qc]`.

[315] N. Yunes and X. Siemens, "Gravitational-Wave Tests of General Relativity with Ground-Based Detectors and Pulsar Timing-Arrays," *Living Rev. Rel.* **16** (2013) 9, `arXiv:1304.3473 [gr-qc]`.

[316] Y. Pan, A. Buonanno, A. Taracchini, M. Boyle, L. E. Kidder, A. H. Mroué, H. P. Pfeiffer, M. A. Scheel, B. Szilágyi, and A. Zenginoglu, "Stability of nonspinning effective-one-body model in approximating two-body dynamics and gravitational-wave emission," *Phys. Rev. D* **89** no. 6, (2014) 061501, `arXiv:1311.2565 [gr-qc]`.

[317] R. Sturani, S. Fischetti, L. Cadonati, G. M. Guidi, J. Healy, D. Shoemaker, and A. Vicere, "Phenomenological gravitational waveforms from spinning coalescing binaries," in *CAPRA and NRDA 2010: Theory Meets Data Analysis at Comparable and Extreme Mass Ratios.* 12, 2010. `arXiv:1012.5172 [gr-qc]`.

[318] R. Sturani, S. Fischetti, L. Cadonati, G. M. Guidi, J. Healy, D. Shoemaker, and A. Vicere, "Complete phenomenological gravitational waveforms from spinning coalescing binaries," *J. Phys. Conf. Ser.* **243** (2010) 012007, `arXiv:1005.0551 [gr-qc]`.

[319] M. Hannam, P. Schmidt, A. Bohé, L. Haegel, S. Husa, F. Ohme, G. Pratten, and M. Pürrer, "Simple Model of Complete Precessing Black-Hole-Binary Gravitational Waveforms," *Phys. Rev. Lett.* **113** no. 15, (2014) 151101, `arXiv:1308.3271 [gr-qc]`.

[320] P. Schmidt, F. Ohme, and M. Hannam, "Towards models of gravitational waveforms from generic binaries II: Modelling precession effects with a single effective precession parameter," *Phys. Rev. D* **91** no. 2, (2015) 024043, `arXiv:1408.1810 [gr-qc]`.

[321] A. Sesana, A. Vecchio, and C. N. Colacino, "The stochastic gravitational-wave background from massive black hole binary systems: implications for observations with Pulsar Timing Arrays," *Mon. Not. Roy. Astron. Soc.* **390** (2008) 192, `arXiv:0804.4476 [astro-ph]`.

[322] B. Kocsis and A. Sesana, "Gas driven massive black hole binaries: signatures in the nHz gravitational wave background," *arXiv e-prints* (Feb., 2010) arXiv:1002.0584, `arXiv:1002.0584 [astro-ph.CO]`.

[323] L. Z. Kelley, L. Blecha, and L. Hernquist, "Massive Black Hole Binary Mergers in Dynamical Galactic Environments," *Mon. Not. Roy. Astron. Soc.* **464** no. 3, (2017) 3131–3157, `arXiv:1606.01900 [astro-ph.HE]`.

[324] D. Perrodin and A. Sesana, "Radio pulsars: testing gravity and detecting gravitational waves," *Astrophys. Space Sci. Libr.* **457** (2018) 95–148, `arXiv:1709.02816 [astro-ph.HE]`.

[325] J. Ellis, M. Fairbairn, G. Hütsi, M. Raidal, J. Urrutia, V. Vaskonen, and H. Veermäe, "Prospects for Future Binary Black Hole GW Studies in Light of PTA Measurements," `arXiv:2301.13854 [astro-ph.CO]`.

[326] **NANOGrav** Collaboration, G. Agazie *et al.*, “The nanograv 15-year data set: Constraints on supermassive black hole binaries from the gravitational wave background,” `arXiv:2306.16220 [astro-ph.HE]`.

[327] **NANOGrav** Collaboration, A. Afzal *et al.*, “The nanograv 15-year data set: Search for signals from new physics,” `arXiv:2306.16219 [astro-ph.HE]`.

[328] A. Ghoshal and A. Strumia, “Probing the Dark Matter density with gravitational waves from super-massive binary black holes,” `arXiv:2306.17158 [astro-ph.CO]`.

[329] M. Bonetti, A. Sesana, E. Barausse, and F. Haardt, “Post-Newtonian evolution of massive black hole triplets in galactic nuclei – III. A robust lower limit to the nHz stochastic background of gravitational waves,” *Mon. Not. Roy. Astron. Soc.* **477** no. 2, (2018) 2599–2612, `arXiv:1709.06095 [astro-ph.GA]`.

[330] R. Genzel, F. Eisenhauer, and S. Gillessen, “The Galactic Center Massive Black Hole and Nuclear Star Cluster,” *Rev. Mod. Phys.* **82** (2010) 3121–3195, `arXiv:1006.0064 [astro-ph.GA]`.

[331] C. P. L. Berry, S. A. Hughes, C. F. Sopuerta, A. J. K. Chua, A. Heffernan, K. Holley-Bockelmann, D. P. Mihaylov, M. C. Miller, and A. Sesana, “The unique potential of extreme mass-ratio inspirals for gravitational-wave astronomy,” `arXiv:1903.03686 [astro-ph.HE]`.

[332] L. Barack and A. Pound, “Self-force and radiation reaction in general relativity,” *Rept. Prog. Phys.* **82** no. 1, (2019) 016904, `arXiv:1805.10385 [gr-qc]`.

[333] L. Barack and C. Cutler, “LISA capture sources: Approximate waveforms, signal-to-noise ratios, and parameter estimation accuracy,” *Phys. Rev. D* **69** (2004) 082005, `arXiv:gr-qc/0310125`.

[334] S. Babak, J. Gair, A. Sesana, E. Barausse, C. F. Sopuerta, C. P. L. Berry, E. Berti, P. Amaro-Seoane, A. Petiteau, and A. Klein, “Science with the space-based interferometer LISA. V: Extreme mass-ratio inspirals,” *Phys. Rev.* **D95** no. 10, (2017) 103012, `arXiv:1703.09722 [gr-qc]`.

[335] V. Cardoso, S. Chakrabarti, P. Pani, E. Berti, and L. Gualtieri, “Floating and sinking: The Imprint of massive scalars around rotating black holes,” *Phys. Rev. Lett.* **107** (2011) 241101, `arXiv:1109.6021 [gr-qc]`.

[336] S. Barsanti, N. Franchini, L. Gualtieri, A. Maselli, and T. P. Sotiriou, “Extreme mass-ratio inspirals as probes of scalar fields: Eccentric equatorial orbits around Kerr black holes,” *Phys. Rev. D* **106** no. 4, (2022) 044029, `arXiv:2203.05003 [gr-qc]`.

[337] S. Barsanti, A. Maselli, T. P. Sotiriou, and L. Gualtieri, “Detecting massive scalar fields with Extreme Mass-Ratio Inspirals,” `arXiv:2212.03888 [gr-qc]`.

[338] D. Liang, R. Xu, Z.-F. Mai, and L. Shao, "Probing vector hair of black holes with extreme-mass-ratio inspirals," *Phys. Rev. D* **107** no. 4, (2023) 044053, `arXiv:2212.09346 [gr-qc]`.

[339] C. Zhang, H. Guo, Y. Gong, and B. Wang, "Detecting vector charge with extreme mass ratio inspirals onto Kerr black holes," `arXiv:2301.05915 [gr-qc]`.

[340] N. Yunes, B. Kocsis, A. Loeb, and Z. Haiman, "Imprint of Accretion Disk-Induced Migration on Gravitational Waves from Extreme Mass Ratio Inspirals," *Phys. Rev. Lett.* **107** (2011) 171103, `arXiv:1103.4609 [astro-ph.CO]`.

[341] B. Kocsis, N. Yunes, and A. Loeb, "Observable signatures of extreme mass-ratio inspiral black hole binaries embedded in thin accretion disks," *Phys. Rev. D* **84** (Jul, 2011) 024032. `https://link.aps.org/doi/10.1103/PhysRevD.84.024032`.

[342] L. Speri, A. Antonelli, L. Sberna, S. Babak, E. Barausse, J. R. Gair, and M. L. Katz, "Probing Accretion Physics with Gravitational Waves," *Phys. Rev. X* **13** no. 2, (2023) 021035, `arXiv:2207.10086 [gr-qc]`.

[343] J. P. W. Verbiest, M. Bailes, W. van Straten, G. B. Hobbs, R. T. Edwards, R. N. Manchester, N. D. R. Bhat, J. M. Sarkissian, B. A. Jacoby, and S. R. Kulkarni, "Precision Timing of PSR J0437-4715: An Accurate Pulsar Distance, a High Pulsar Mass, and a Limit on the Variation of Newton's Gravitational Constant," ApJ **679** no. 1, (May, 2008) 675–680, `arXiv:0801.2589 [astro-ph]`.

[344] M. Maggiore, *Gravitational Waves. Vol. 1: Theory and Experiments.* Oxford University Press, 2007.

[345] M. L. Jones, M. A. McLaughlin, M. T. Lam, J. M. Cordes, L. Levin, S. Chatterjee, Z. Arzoumanian, K. Crowter, P. B. Demorest, T. Dolch, J. A. Ellis, R. D. Ferdman, E. Fonseca, M. E. Gonzalez, G. Jones, T. J. W. Lazio, D. J. Nice, T. T. Pennucci, S. M. Ransom, D. R. Stinebring, I. H. Stairs, K. Stovall, J. K. Swiggum, and W. W. Zhu, "The NANOGrav Nine-year Data Set: Measurement and Analysis of Variations in Dispersion Measures," ApJ **841** no. 2, (June, 2017) 125, `arXiv:1612.03187 [astro-ph.HE]`.

[346] M. V. Sazhin, "Opportunities for detecting ultralong gravitational waves," Soviet Ast. **22** (Feb., 1978) 36–38.

[347] S. Detweiler, "Pulsar timing measurements and the search for gravitational waves," ApJ **234** (Dec., 1979) 1100–1104.

[348] R. W. Hellings and G. S. Downs, "Upper limits on the isotropic gravitational radiation background from pulsar timing analysis.," *The Astrophysical Journal Letters* **265** (Feb., 1983) L39–L42.

[349] E. S. Phinney, “A Practical theorem on gravitational wave backgrounds,” `arXiv:astro-ph/0108028`.

[350] M. Enoki and M. Nagashima, “The Effect of Orbital Eccentricity on Gravitational Wave Background Radiation from Cosmological Binaries,” *Prog. Theor. Phys.* **117** (2007) 241, `arXiv:astro-ph/0609377`.

[351] S. Chen, A. Sesana, and W. Del Pozzo, “Efficient computation of the gravitational wave spectrum emitted by eccentric massive black hole binaries in stellar environments,” *Mon. Not. Roy. Astron. Soc.* **470** no. 2, (2017) 1738–1749, `arXiv:1612.00455 [astro-ph.CO]`.

[352] **NANOGrav** Collaboration, Z. Arzoumanian *et al.*, “The NANOGrav 12.5 yr Data Set: Search for an Isotropic Stochastic Gravitational-wave Background,” *Astrophys. J. Lett.* **905** no. 2, (2020) L34, `arXiv:2009.04496 [astro-ph.HE]`.

[353] **NANOGrav** Collaboration, Z. Arzoumanian *et al.*, “Searching for Gravitational Waves from Cosmological Phase Transitions with the NANOGrav 12.5-Year Dataset,” *Phys. Rev. Lett.* **127** no. 25, (2021) 251302, `arXiv:2104.13930 [astro-ph.CO]`.

[354] X. Xue *et al.*, “Constraining Cosmological Phase Transitions with the Parkes Pulsar Timing Array,” *Phys. Rev. Lett.* **127** no. 25, (2021) 251303, `arXiv:2110.03096 [astro-ph.CO]`.

[355] Y. Nakai, M. Suzuki, F. Takahashi, and M. Yamada, “Gravitational Waves and Dark Radiation from Dark Phase Transition: Connecting NANOGrav Pulsar Timing Data and Hubble Tension,” *Phys. Lett. B* **816** (2021) 136238, `arXiv:2009.09754 [astro-ph.CO]`.

[356] P. Di Bari, D. Marfatia, and Y.-L. Zhou, “Gravitational waves from first-order phase transitions in Majoron models of neutrino mass,” *JHEP* **10** (2021) 193, `arXiv:2106.00025 [hep-ph]`.

[357] A. S. Sakharov, Y. N. Eroshenko, and S. G. Rubin, “Looking at the NANOGrav signal through the anthropic window of axionlike particles,” *Phys. Rev. D* **104** no. 4, (2021) 043005, `arXiv:2104.08750 [hep-ph]`.

[358] S.-L. Li, L. Shao, P. Wu, and H. Yu, “NANOGrav signal from first-order confinement-deconfinement phase transition in different QCD-matter scenarios,” *Phys. Rev. D* **104** no. 4, (2021) 043510, `arXiv:2101.08012 [astro-ph.CO]`.

[359] A. Ashoorioon, K. Rezazadeh, and A. Rostami, “NANOGrav signal from the end of inflation and the LIGO mass and heavier primordial black holes,” *Phys. Lett. B* **835** (2022) 137542, `arXiv:2202.01131 [astro-ph.CO]`.

[360] M. Benetti, L. L. Graef, and S. Vagnozzi, “Primordial gravitational waves from NANOGrav: A broken power-law approach,” *Phys. Rev. D* **105** no. 4, (2022) 043520, `arXiv:2111.04758 [astro-ph.CO]`.

[361] J. Barir, M. Geller, C. Sun, and T. Volansky, "Gravitational Waves from Incomplete Inflationary Phase Transitions," `arXiv:2203.00693 [hep-ph]`.

[362] M. Hindmarsh and J. Kume, "Multi-messenger constraints on Abelian-Higgs cosmic string networks," *JCAP* **04** (2023) 045, `arXiv:2210.06178 [astro-ph.CO]`.

[363] Y. Gouttenoire and T. Volansky, "Primordial Black Holes from Supercooled Phase Transitions," `arXiv:2305.04942 [hep-ph]`.

[364] I. Baldes, M. Dichtl, Y. Gouttenoire, and F. Sala, "Bubbletrons," `arXiv:2306.15555 [hep-ph]`.

[365] S.-P. Li and K.-P. Xie, "A collider test of nano-Hertz gravitational waves from pulsar timing arrays," `arXiv:2307.01086 [hep-ph]`.

[366] J. Ellis and M. Lewicki, "Cosmic String Interpretation of NANOGrav Pulsar Timing Data," *Phys. Rev. Lett.* **126** no. 4, (2021) 041304, `arXiv:2009.06555 [astro-ph.CO]`.

[367] S. Datta, A. Ghosal, and R. Samanta, "Baryogenesis from ultralight primordial black holes and strong gravitational waves from cosmic strings," *JCAP* **08** (2021) 021, `arXiv:2012.14981 [hep-ph]`.

[368] R. Samanta and S. Datta, "Gravitational wave complementarity and impact of NANOGrav data on gravitational leptogenesis," *JHEP* **05** (2021) 211, `arXiv:2009.13452 [hep-ph]`.

[369] W. Buchmuller, V. Domcke, and K. Schmitz, "From NANOGrav to LIGO with metastable cosmic strings," *Phys. Lett. B* **811** (2020) 135914, `arXiv:2009.10649 [astro-ph.CO]`.

[370] S. Blasi, V. Brdar, and K. Schmitz, "Has NANOGrav found first evidence for cosmic strings?," *Phys. Rev. Lett.* **126** no. 4, (2021) 041305, `arXiv:2009.06607 [astro-ph.CO]`.

[371] S. Ramazanov, E. Babichev, D. Gorbunov, and A. Vikman, "Beyond freeze-in: Dark matter via inverse phase transition and gravitational wave signal," *Phys. Rev. D* **105** no. 6, (2022) 063530, `arXiv:2104.13722 [hep-ph]`.

[372] E. Babichev, D. Gorbunov, S. Ramazanov, and A. Vikman, "Gravitational shine of dark domain walls," *JCAP* **04** no. 04, (2022) 028, `arXiv:2112.12608 [hep-ph]`.

[373] M. Gorghetto, E. Hardy, and H. Nicolaescu, "Observing invisible axions with gravitational waves," *JCAP* **06** (2021) 034, `arXiv:2101.11007 [hep-ph]`.

[374] W. Buchmuller, V. Domcke, and K. Schmitz, "Stochastic gravitational-wave background from metastable cosmic strings," *JCAP* **12** no. 12, (2021) 006, `arXiv:2107.04578 [hep-ph]`.

[375] J. J. Blanco-Pillado, K. D. Olum, and J. M. Wachter, "Comparison of cosmic string and superstring models to NANOGrav 12.5-year results," *Phys. Rev. D* **103** no. 10, (2021) 103512, `arXiv:2102.08194 [astro-ph.CO]`.

[376] R. Z. Ferreira, A. Notari, O. Pujolas, and F. Rompineve, "Gravitational waves from domain walls in Pulsar Timing Array datasets," *JCAP* **02** (2023) 001, `arXiv:2204.04228 [astro-ph.CO]`.

[377] H. An and C. Yang, "Gravitational Waves Produced by Domain Walls During Inflation," `arXiv:2304.02361 [hep-ph]`.

[378] Z.-Y. Qiu and Z.-H. Yu, "Gravitational waves from cosmic strings associated with pseudo-Nambu-Goldstone dark matter," `arXiv:2304.02506 [hep-ph]`.

[379] Z.-M. Zeng, J. Liu, and Z.-K. Guo, "Enhanced curvature perturbations from spherical domain walls nucleated during inflation," `arXiv:2301.07230 [astro-ph.CO]`.

[380] S. F. King, D. Marfatia, and M. H. Rahat, "Towards distinguishing Dirac from Majorana neutrino mass with gravitational waves," `arXiv:2306.05389 [hep-ph]`.

[381] E. Babichev, D. Gorbunov, S. Ramazanov, R. Samanta, and A. Vikman, "NANOGrav spectral index $\gamma = 3$ from melting domain walls," `arXiv:2307.04582 [hep-ph]`.

[382] N. Kitajima, J. Lee, K. Murai, F. Takahashi, and W. Yin, "Nanohertz Gravitational Waves from Axion Domain Walls Coupled to QCD," `arXiv:2306.17146 [hep-ph]`.

[383] B. Barman, D. Borah, S. Jyoti Das, and I. Saha, "Scale of Dirac leptogenesis and left-right symmetry in the light of recent PTA results," `arXiv:2307.00656 [hep-ph]`.

[384] V. Vaskonen and H. Veermäe, "Did NANOGrav see a signal from primordial black hole formation?," *Phys. Rev. Lett.* **126** no. 5, (2021) 051303, `arXiv:2009.07832 [astro-ph.CO]`.

[385] V. De Luca, G. Franciolini, and A. Riotto, "NANOGrav Data Hints at Primordial Black Holes as Dark Matter," *Phys. Rev. Lett.* **126** no. 4, (2021) 041303, `arXiv:2009.08268 [astro-ph.CO]`.

[386] N. Bhaumik and R. K. Jain, "Small scale induced gravitational waves from primordial black holes, a stringent lower mass bound, and the imprints of an early matter to radiation transition," *Phys. Rev. D* **104** no. 2, (2021) 023531, `arXiv:2009.10424 [astro-ph.CO]`.

[387] K. Inomata, M. Kawasaki, K. Mukaida, and T. T. Yanagida, "NANOGrav Results and LIGO-Virgo Primordial Black Holes in Axionlike Curvaton Models," *Phys. Rev. Lett.* **126** no. 13, (2021) 131301, `arXiv:2011.01270 [astro-ph.CO]`.

[388] K. Kohri and T. Terada, "Solar-Mass Primordial Black Holes Explain NANOGrav Hint of Gravitational Waves," *Phys. Lett. B* **813** (2021) 136040, `arXiv:2009.11853 [astro-ph.CO]`.

[389] G. Domènech and S. Pi, "NANOGrav hints on planet-mass primordial black holes," *Sci. China Phys. Mech. Astron.* **65** no. 3, (2022) 230411, `arXiv:2010.03976 [astro-ph.CO]`.

[390] S. Vagnozzi, "Implications of the NANOGrav results for inflation," *Mon. Not. Roy. Astron. Soc.* **502** no. 1, (2021) L11–L15, `arXiv:2009.13432 [astro-ph.CO]`.

[391] R. Namba and M. Suzuki, "Implications of Gravitational-wave Production from Dark Photon Resonance to Pulsar-timing Observations and Effective Number of Relativistic Species," *Phys. Rev. D* **102** (2020) 123527, `arXiv:2009.13909 [astro-ph.CO]`.

[392] S. Sugiyama, V. Takhistov, E. Vitagliano, A. Kusenko, M. Sasaki, and M. Takada, "Testing Stochastic Gravitational Wave Signals from Primordial Black Holes with Optical Telescopes," *Phys. Lett. B* **814** (2021) 136097, `arXiv:2010.02189 [astro-ph.CO]`.

[393] Z. Zhou, J. Jiang, Y.-F. Cai, M. Sasaki, and S. Pi, "Primordial black holes and gravitational waves from resonant amplification during inflation," *Phys. Rev. D* **102** no. 10, (2020) 103527, `arXiv:2010.03537 [astro-ph.CO]`.

[394] J. Lin, S. Gao, Y. Gong, Y. Lu, Z. Wang, and F. Zhang, "Primordial black holes and scalar induced gravitational waves from Higgs inflation with noncanonical kinetic term," *Phys. Rev. D* **107** no. 4, (2023) 043517, `arXiv:2111.01362 [gr-qc]`.

[395] K. Rezazadeh, Z. Teimoori, S. Karimi, and K. Karami, "Non-Gaussianity and secondary gravitational waves from primordial black holes production in α-attractor inflation," *Eur. Phys. J. C* **82** no. 8, (2022) 758, `arXiv:2110.01482 [gr-qc]`.

[396] M. Kawasaki and H. Nakatsuka, "Gravitational waves from type II axion-like curvaton model and its implication for NANOGrav result," *JCAP* **05** (2021) 023, `arXiv:2101.11244 [astro-ph.CO]`.

[397] W. Ahmed, M. Junaid, and U. Zubair, "Primordial black holes and gravitational waves in hybrid inflation with chaotic potentials," *Nucl. Phys. B* **984** (2022) 115968, `arXiv:2109.14838 [astro-ph.CO]`.

[398] Z. Yi and Q. Fei, "Constraints on primordial curvature spectrum from primordial black holes and scalar-induced gravitational waves," *Eur. Phys. J. C* **83** no. 1, (2023) 82, `arXiv:2210.03641 [astro-ph.CO]`.

[399] Z. Yi, "Primordial black holes and scalar-induced gravitational waves from the generalized Brans-Dicke theory," *JCAP* **03** (2023) 048, `arXiv:2206.01039 [gr-qc]`.

[400] V. Dandoy, V. Domcke, and F. Rompineve, "Search for scalar induced gravitational waves in the International Pulsar Timing Array Data Release 2 and NANOgrav 12.5 years dataset," `arXiv:2302.07901 [astro-ph.CO]`.

[401] J.-X. Zhao, X.-H. Liu, and N. Li, "Primordial black holes and scalar-induced gravitational waves from the perturbations on the inflaton potential in peak theory," *Phys. Rev. D* **107** no. 4, (2023) 043515, `arXiv:2302.06886 [astro-ph.CO]`.

[402] G. Ferrante, G. Franciolini, A. Iovino, Junior., and A. Urbano, "Primordial black holes in the curvaton model: possible connections to pulsar timing arrays and dark matter," *JCAP* **06** (2023) 057, `arXiv:2305.13382 [astro-ph.CO]`.

[403] Y. Cai, M. Zhu, and Y.-S. Piao, "Primordial black holes from null energy condition violation during inflation," `arXiv:2305.10933 [gr-qc]`.

[404] G. Franciolini, A. Iovino, Junior., V. Vaskonen, and H. Veermae, "The recent gravitational wave observation by pulsar timing arrays and primordial black holes: the importance of non-gaussianities," `arXiv:2306.17149 [astro-ph.CO]`.

[405] S. Balaji, G. Domènech, and G. Franciolini, "Scalar-induced gravitational wave interpretation of PTA data: the role of scalar fluctuation propagation speed," `arXiv:2307.08552 [gr-qc]`.

[406] L. Liu, Z.-C. Chen, and Q.-G. Huang, "Implications for the non-Gaussianity of curvature perturbation from pulsar timing arrays," `arXiv:2307.01102 [astro-ph.CO]`.

[407] E. Barausse, N. Yunes, and K. Chamberlain, "Theory-Agnostic Constraints on Black-Hole Dipole Radiation with Multiband Gravitational-Wave Astrophysics," *Phys. Rev. Lett.* **116** no. 24, (2016) 241104, `arXiv:1603.04075 [gr-qc]`.

[408] L. Barack *et al.*, "Black holes, gravitational waves and fundamental physics: a roadmap," *Class. Quant. Grav.* **36** no. 14, (2019) 143001, `arXiv:1806.05195 [gr-qc]`.

[409] **LISA** Collaboration, P. Amaro-Seoane *et al.*, "Laser Interferometer Space Antenna," `arXiv:1702.00786 [astro-ph.IM]`.

[410] **LISA** Collaboration, K. G. Arun *et al.*, "New horizons for fundamental physics with LISA," *Living Rev. Rel.* **25** no. 1, (2022) 4, `arXiv:2205.01597 [gr-qc]`.

[411] V. M. Kaspi and A. Beloborodov, "Magnetars," *Ann. Rev. Astron. Astrophys.* **55** (2017) 261–301, `arXiv:1703.00068 [astro-ph.HE]`.

[412] E. Barausse, T. Jacobson, and T. P. Sotiriou, "Black holes in Einstein-aether and Horava-Lifshitz gravity," *Phys. Rev. D* **83** (2011) 124043, `arXiv:1104.2889 [gr-qc]`.

[413] A. H. K. R, E. R. Most, J. Noronha, H. Witek, and N. Yunes, "How do axisymmetric black holes grow monopole and dipole hair?," *Phys. Rev. D* **107** no. 10, (2023) 104047, `arXiv:2212.02039 [gr-qc]`.

[414] A. Dima, E. Barausse, N. Franchini, and T. P. Sotiriou, "Spin-induced black hole spontaneous scalarization," *Phys. Rev. Lett.* **125** no. 23, (2020) 231101, `arXiv:2006.03095 [gr-qc]`.

[415] E. Berti, L. G. Collodel, B. Kleihaus, and J. Kunz, "Spin-induced black-hole scalarization in Einstein-scalar-Gauss-Bonnet theory," *Phys. Rev. Lett.* **126** no. 1, (2021) 011104, `arXiv:2009.03905 [gr-qc]`.

[416] C. A. R. Herdeiro, E. Radu, H. O. Silva, T. P. Sotiriou, and N. Yunes, "Spin-induced scalarized black holes," *Phys. Rev. Lett.* **126** no. 1, (2021) 011103, `arXiv:2009.03904 [gr-qc]`.

[417] M. Elley, H. O. Silva, H. Witek, and N. Yunes, "Spin-induced dynamical scalarization, descalarization, and stealthness in scalar-Gauss-Bonnet gravity during a black hole coalescence," *Phys. Rev. D* **106** no. 4, (2022) 044018, `arXiv:2205.06240 [gr-qc]`.

[418] D. D. Doneva, F. M. Ramazanoğlu, H. O. Silva, T. P. Sotiriou, and S. S. Yazadjiev, "Scalarization," `arXiv:2211.01766 [gr-qc]`.

[419] D. R. Mayerson, "Fuzzballs and Observations," *Gen. Rel. Grav.* **52** no. 12, (2020) 115, `arXiv:2010.09736 [hep-th]`.

[420] I. Bena, E. J. Martinec, S. D. Mathur, and N. P. Warner, "Fuzzballs and Microstate Geometries: Black-Hole Structure in String Theory," `arXiv:2204.13113 [hep-th]`.

[421] I. Bena, E. J. Martinec, S. D. Mathur, and N. P. Warner, "Snowmass White Paper: Micro- and Macro-Structure of Black Holes," `arXiv:2203.04981 [hep-th]`.

[422] I. Bah and P. Heidmann, "Topological Stars and Black Holes," *Phys. Rev. Lett.* **126** no. 15, (2021) 151101, `arXiv:2011.08851 [hep-th]`.

[423] I. Bah and P. Heidmann, "Smooth bubbling geometries without supersymmetry," *JHEP* **09** (2021) 128, `arXiv:2106.05118 [hep-th]`.

[424] S. W. Hawking, "Black holes in the Brans-Dicke theory of gravitation," *Commun. Math. Phys.* **25** (1972) 167–171.

[425] D. M. Eardley, "Observable effects of a scalar gravitational field in a binary pulsar.," ApJ **196** (Mar., 1975) L59–L62.

[426] T. Damour and G. Esposito-Farese, "Tensor multiscalar theories of gravitation," *Class. Quant. Grav.* **9** (1992) 2093–2176.

[427] F.-L. Julié, "Reducing the two-body problem in scalar-tensor theories to the motion of a test particle : a scalar-tensor effective-one-body approach," *Phys. Rev. D* **97** no. 2, (2018) 024047, `arXiv:1709.09742 [gr-qc]`.

[428] A. Stavridis and C. M. Will, "Bounding the mass of the graviton with gravitational waves: Effect of spin precessions in massive black hole binaries," *Phys. Rev. D* **80** (2009) 044002, `arXiv:0906.3602 [gr-qc]`.

[429] A. Ohashi, H. Tagoshi, and M. Sasaki, "Post-Newtonian Expansion of Gravitational Waves from a Compact Star Orbiting a Rotating Black Hole in Brans-Dicke Theory: Circular Orbit Case," *Progress of Theoretical Physics* **96** no. 4, (10, 1996) 713–728, `https://academic.oup.com/ptp/article-pdf/96/4/713/5446219/96-4-713.pdf`. `https://doi.org/10.1143/PTP.96.713`.

[430] G. A. Piovano, A. Maselli, and P. Pani, "Extreme mass ratio inspirals with spinning secondary: a detailed study of equatorial circular motion," *Phys. Rev. D* **102** no. 2, (2020) 024041, `arXiv:2004.02654 [gr-qc]`.

[431] G. A. Piovano, R. Brito, A. Maselli, and P. Pani, "Assessing the detectability of the secondary spin in extreme mass-ratio inspirals with fully relativistic numerical waveforms," *Phys. Rev. D* **104** no. 12, (2021) 124019, `arXiv:2105.07083 [gr-qc]`.

[432] G. A. Piovano, *Spinning compact objects in extreme-mass-ratio inspirals.* PhD thesis, Rome U., 2022.

[433] J. G. Coelho and M. Malheiro, "Magnetic dipole moment of soft gamma-ray repeaters and anomalous X-ray pulsars described as massive and magnetic white dwarfs," *Publications of the Astronomical Society of Japan* **66** no. 1, (02, 2014) 14, `https://academic.oup.com/pasj/article-pdf/66/1/14/4421927/pst014.pdf`. `https://doi.org/10.1093/pasj/pst014`.

[434] I. Bah, P. Heidmann, and P. Weck, "Schwarzschild-like topological solitons," *JHEP* **08** (2022) 269, `arXiv:2203.12625 [hep-th]`.

[435] S. R. Dolan, N. Warburton, A. I. Harte, A. Le Tiec, B. Wardell, and L. Barack, "Gravitational self-torque and spin precession in compact binaries," *Phys. Rev. D* **89** no. 6, (2014) 064011, `arXiv:1312.0775 [gr-qc]`.

[436] G. Lukes-Gerakopoulos, E. Harms, S. Bernuzzi, and A. Nagar, "Spinning test-body orbiting around a Kerr black hole: circular dynamics and gravitational-wave fluxes," *Phys. Rev. D* **96** no. 6, (2017) 064051, `arXiv:1707.07537 [gr-qc]`.

[437] S. Akcay, D. Dempsey, and S. R. Dolan, "Spin–orbit precession for eccentric black hole binaries at first order in the mass ratio," *Class. Quant. Grav.* **34** no. 8, (2017) 084001, `arXiv:1608.04811 [gr-qc]`.

[438] S. Akcay, "Self-force correction to geodetic spin precession in Kerr spacetime," *Phys. Rev. D* **96** no. 4, (2017) 044024, `arXiv:1705.03282 [gr-qc]`.

[439] N. Loutrel, R. Brito, A. Maselli, and P. Pani, "Relevance of Precession for Tests of the Black Hole No Hair Theorems," `arXiv:2309.17404 [gr-qc]`.

[440] A. Spiers, A. Maselli, and T. P. Sotiriou, “Measuring scalar charge with compact binaries: High accuracy modelling with self-force,” `arXiv:2310.02315 [gr-qc]`.

[441] G. Franciolini, D. Racco, and F. Rompineve, “Footprints of the QCD Crossover on Cosmological Gravitational Waves at Pulsar Timing Arrays,” `arXiv:2306.17136 [astro-ph.CO]`.

[442] E. Madge, E. Morgante, C. P. Ibáñez, N. Ramberg, W. Ratzinger, S. Schenk, and P. Schwaller, “Primordial gravitational waves in the nano-hertz regime and pta data – towards solving the gw inverse problem,” `arXiv:2306.14856 [hep-ph]`.

[443] D. G. Figueroa, M. Pieroni, A. Ricciardone, and P. Simakachorn, “Cosmological Background Interpretation of Pulsar Timing Array Data,” `arXiv:2307.02399 [astro-ph.CO]`.

[444] J. Garcia-Bellido, A. Papageorgiou, M. Peloso, and L. Sorbo, “A flashing beacon in axion inflation: recurring bursts of gravitational waves in the strong backreaction regime,” `arXiv:2303.13425 [astro-ph.CO]`.

[445] K. Murai and W. Yin, “A Novel Probe of Supersymmetry in Light of Nanohertz Gravitational Waves,” `arXiv:2307.00628 [hep-ph]`.

[446] R. A. Konoplya and A. Zhidenko, “Asymptotic tails of massive gravitons in light of pulsar timing array observations,” `arXiv:2307.01110 [gr-qc]`.

[447] **EPTA** Collaboration, C. Smarra *et al.*, “The second data release from the European Pulsar Timing Array: VI. Challenging the ultralight dark matter paradigm,” `arXiv:2306.16228 [astro-ph.HE]`.

[448] S. J. Chamberlin and X. Siemens, “Stochastic backgrounds in alternative theories of gravity: overlap reduction functions for pulsar timing arrays,” *Phys. Rev. D* **85** (2012) 082001, `arXiv:1111.5661 [astro-ph.HE]`.

[449] W. Qin, K. K. Boddy, and M. Kamionkowski, “Subluminal stochastic gravitational waves in pulsar-timing arrays and astrometry,” *Phys. Rev. D* **103** no. 2, (2021) 024045, `arXiv:2007.11009 [gr-qc]`.

[450] Q. Liang, M.-X. Lin, and M. Trodden, “A Test of Gravity with Pulsar Timing Arrays,” `arXiv:2304.02640 [astro-ph.CO]`.

[451] R. C. Bernardo and K.-W. Ng, “Testing gravity with cosmic variance-limited pulsar timing array correlations,” `arXiv:2306.13593 [gr-qc]`.

[452] M. Maggiore *et al.*, “Science Case for the Einstein Telescope,” *JCAP* **03** (2020) 050, `arXiv:1912.02622 [astro-ph.CO]`.

[453] M. Branchesi *et al.*, “Science with the Einstein Telescope: a comparison of different designs,” `arXiv:2303.15923 [gr-qc]`.

[454] Throughout this work, we adopt natural units instead of geometric ones, as we shall eventually promote G to a time dependent quantity.

[455] N. Yunes and F. Pretorius, "Fundamental Theoretical Bias in Gravitational Wave Astrophysics and the Parameterized Post-Einsteinian Framework," *Phys. Rev. D* **80** (2009) 122003, `arXiv:0909.3328 [gr-qc]`.

[456] K. Chatziioannou, N. Yunes, and N. Cornish, "Model-Independent Test of General Relativity: An Extended post-Einsteinian Framework with Complete Polarization Content," *Phys. Rev. D* **86** (2012) 022004, `arXiv:1204.2585 [gr-qc]`. [Erratum: Phys.Rev.D 95, 129901 (2017)].

[457] A. Maselli, S. Marassi, V. Ferrari, K. Kokkotas, and R. Schneider, "Constraining Modified Theories of Gravity with Gravitational-Wave Stochastic Backgrounds," *Phys. Rev. Lett.* **117** no. 9, (2016) 091102, `arXiv:1606.04996 [gr-qc]`.

[458] V. Cardoso and A. Maselli, "Constraints on the astrophysical environment of binaries with gravitational-wave observations," *Astron. Astrophys.* **644** (2020) A147, `arXiv:1909.05870 [astro-ph.HE]`.

[459] L. Sampson, N. J. Cornish, and S. T. McWilliams, "Constraining the Solution to the Last Parsec Problem with Pulsar Timing," *Phys. Rev. D* **91** no. 8, (2015) 084055, `arXiv:1503.02662 [gr-qc]`.

[460] C. Deffayet and K. Menou, "Probing Gravity with Spacetime Sirens," *Astrophys. J. Lett.* **668** (2007) L143–L146, `arXiv:0709.0003 [astro-ph]`.

[461] K. Yagi, N. Tanahashi, and T. Tanaka, "Probing the size of extra dimension with gravitational wave astronomy," *Phys. Rev. D* **83** (2011) 084036, `arXiv:1101.4997 [gr-qc]`.

[462] T. Damour, G. W. Gibbons, and J. H. Taylor, "Limits on the Variability of G Using Binary-Pulsar Data," *Phys. Rev. Lett.* **61** (1988) 1151–1154.

[463] N. Yunes, F. Pretorius, and D. Spergel, "Constraining the evolutionary history of Newton's constant with gravitational wave observations," *Phys. Rev. D* **81** (2010) 064018, `arXiv:0912.2724 [gr-qc]`.

[464] C. J. Copi, A. N. Davis, and L. M. Krauss, "A New nucleosynthesis constraint on the variation of G," *Phys. Rev. Lett.* **92** (2004) 171301, `arXiv:astro-ph/0311334`.

[465] C. Bambi, M. Giannotti, and F. L. Villante, "The Response of primordial abundances to a general modification of G(N) and/or of the early Universe expansion rate," *Phys. Rev. D* **71** (2005) 123524, `arXiv:astro-ph/0503502`.

[466] J. Alvey, N. Sabti, M. Escudero, and M. Fairbairn, "Improved BBN Constraints on the Variation of the Gravitational Constant," *Eur. Phys. J. C* **80** no. 2, (2020) 148, `arXiv:1910.10730 [astro-ph.CO]`.

[467] F. Wu and X. Chen, "Cosmic microwave background with Brans-Dicke gravity II: constraints with the WMAP and SDSS data," *Phys. Rev. D* **82** (2010) 083003, `arXiv:0903.0385 [astro-ph.CO]`.

[468] A. Genova, E. Mazarico, S. Goossens, F. G. Lemoine, G. A. Neumann, D. E. Smith, and M. T. Zuber, "Solar system expansion and strong equivalence principle as seen by the NASA MESSENGER mission," *Nature Communications* **9** (Jan., 2018) 289.

[469] R. Barbieri, S. Savastano, L. Speri, A. Antonelli, L. Sberna, O. Burke, J. Gair, and N. Tamanini, "Constraining the evolution of Newton's constant with slow inspirals observed from spaceborne gravitational-wave detectors," *Phys. Rev. D* **107** no. 6, (2023) 064073, `arXiv:2207.10674 [gr-qc]`.

[470] V. M. Kaspi, J. H. Taylor, and M. F. Ryba, "High-Precision Timing of Millisecond Pulsars. III. Long-Term Monitoring of PSRs B1855+09 and B1937+21," *The Astrophysical Journal* **428** (June, 1994) 713.

[471] S. E. Thorsett, "The Gravitational constant, the Chandrasekhar limit, and neutron star masses," *Phys. Rev. Lett.* **77** (1996) 1432–1435, `arXiv:astro-ph/9607003`.

[472] K. Chamberlain and N. Yunes, "Theoretical Physics Implications of Gravitational Wave Observation with Future Detectors," *Phys. Rev. D* **96** no. 8, (2017) 084039, `arXiv:1704.08268 [gr-qc]`.

[473] S. E. Perkins, N. Yunes, and E. Berti, "Probing Fundamental Physics with Gravitational Waves: The Next Generation," *Phys. Rev. D* **103** no. 4, (2021) 044024, `arXiv:2010.09010 [gr-qc]`.

[474] B. Allen and J. D. Romano, "Detecting a stochastic background of gravitational radiation: Signal processing strategies and sensitivities," *Phys. Rev. D* **59** (1999) 102001, `arXiv:gr-qc/9710117`.

[475] A. Vijaykumar, S. J. Kapadia, and P. Ajith, "Constraints on the time variation of the gravitational constant using gravitational-wave observations of binary neutron stars," *Phys. Rev. Lett.* **126** no. 14, (2021) 141104, `arXiv:2003.12832 [gr-qc]`.

[476] **NANOGrav** Collaboration, N. S. Pol *et al.*, "Astrophysics Milestones for Pulsar Timing Array Gravitational-wave Detection," *Astrophys. J. Lett.* **911** no. 2, (2021) L34, `arXiv:2010.11950 [astro-ph.HE]`.

[477] R. Nair and N. Yunes, "Improved binary pulsar constraints on the parametrized post-einsteinian framework," *Phys. Rev. D* **101** (May, 2020) 104011. `https://link.aps.org/doi/10.1103/PhysRevD.101.104011`.

[478] E. Newman and R. Penrose, "An Approach to Gravitational Radiation by a Method of Spin Coefficients," *Journal of Mathematical Physics* **3** no. 3, (1962) 566–578.

[479] M. Alcubierre, *Introduction to 3+1 Numerical Relativity.* Oxford University Press, 2008.

[480] E. Gourgoulhon, "3+1 formalism and bases of numerical relativity," (3, 2007) , `arXiv:gr-qc/0703035`.

[481] C.-D. Munz, P. Omnes, R. Schneider, E. Sonnendrücker, and U. Voss, "Divergence correction techniques for maxwell solvers based on a hyperbolic model," *Journal of Computational Physics* **161** no. 2, (2000) 484–511. `https://www.sciencedirect.com/science/article/pii/S0021999100965070`.

[482] R. Abgrall and H. Kumar, "Robust Finite Volume Schemes for Two-Fluid Plasma Equations," *Journal of Scientific Computing* **60** no. 3, (2014) 584–611.

[483] D. Hilditch, "An Introduction to Well-posedness and Free-evolution," *Int. J. Mod. Phys. A* **28** (2013) 1340015, `arXiv:1309.2012 [gr-qc]`.

[484] F. Löffler, J. Faber, E. Bentivegna, T. Bode, P. Diener, R. Haas, I. Hinder, B. C. Mundim, C. D. Ott, E. Schnetter, G. Allen, M. Campanelli, and P. Laguna, "The Einstein Toolkit: A Community Computational Infrastructure for Relativistic Astrophysics," *Class. Quantum Grav.* **29** no. 11, (2012) 115001, `arXiv:1111.3344 [gr-qc]`.

[485] M. Zilhão and F. Löffler, "An Introduction to the Einstein Toolkit," *Int. J. Mod. Phys. A* **28** (2013) 1340014, `arXiv:1305.5299 [gr-qc]`.

[486] L. Bernard, V. Cardoso, T. Ikeda, and M. Zilhão, "Physics of black hole binaries: Geodesics, relaxation modes, and energy extraction," *Phys. Rev. D* **100** no. 4, (2019) 044002, `arXiv:1905.05204 [gr-qc]`.

[487] T. Ikeda, L. Bernard, V. Cardoso, and M. Zilhão, "Black hole binaries and light fields: Gravitational molecules," *Phys. Rev. D* **103** no. 2, (2021) 024020, `arXiv:2010.00008 [gr-qc]`.

[488] P. V. P. Cunha, J. A. Font, C. Herdeiro, E. Radu, N. Sanchis-Gual, and M. Zilhão, "Lensing and dynamics of ultracompact bosonic stars," *Phys. Rev.* **D96** no. 10, (2017) 104040, `arXiv:1709.06118 [gr-qc]`.

[489] M. Zilhão, H. Witek, and V. Cardoso, "Nonlinear interactions between black holes and Proca fields," *Class. Quant. Grav.* **32** (2015) 234003, `arXiv:1505.00797 [gr-qc]`.

[490] N. Sanchis-Gual, M. Zilhão, and V. Cardoso, "Electromagnetic emission from axionic boson star collisions," *Phys. Rev. D* **106** no. 6, (2022) 064034, `arXiv:2207.05494 [gr-qc]`.

[491] D. Pollney, C. Reisswig, E. Schnetter, N. Dorband, and P. Diener, "High accuracy binary black hole simulations with an extended wave zone," *Phys. Rev. D* **83** (2011) 044045, `arXiv:0910.3803 [gr-qc]`.

[492] C. Reisswig, R. Haas, C. D. Ott, E. Abdikamalov, P. Mösta, D. Pollney, and E. Schnetter, “Three-Dimensional General-Relativistic Hydrodynamic Simulations of Binary Neutron Star Coalescence and Stellar Collapse with Multipatch Grids,” *Phys. Rev. D* **87** no. 6, (2013) 064023, `arXiv:1212.1191 [astro-ph.HE]`.

[493] C. M. Bender and S. A. Orszag, *Advanced Mathematical Methods for Scientists and Engineers.* McGraw-Hill, 1978.